



ESCOLA POLITÉCNICA DA UNIVERSIDADE DE SÃO PAULO
PROGRAMA DE PÓS-GRADUAÇÃO EM ENGENHARIA CIVIL

RAMOEL SERAFINI

**The effect of fire on pre-cast steel fiber reinforced concrete for tunnel
linings: from microstructure to structural simulation**

São Paulo

2021

RAMOEL SERAFINI

**The effect of fire on pre-cast steel fiber reinforced concrete for tunnel
linings: from microstructure to structural simulation**

Revised version

Doctoral thesis presented to the Polytechnic School of the University of São Paulo as a requirement for obtaining the Doctorate Degree in Science.

Area of concentration: Civil and Urban Engineering

Advisor:

Prof. Dr. Antonio Domingues de Figueiredo

Co-advisor:

Prof. Dr. Alberto de la Fuente Antequera

São Paulo

2021

Autorizo a reprodução e divulgação total ou parcial deste trabalho, por qualquer meio convencional ou eletrônico, para fins de estudo e pesquisa, desde que citada a fonte.

Este exemplar foi revisado e corrigido em relação à versão original, sob responsabilidade única do autor e com anuência de seu orientador.

São Paulo, _____ de _____ de _____

Assinatura do autor: _____

Assinatura do orientador: _____

Catálogo-na-publicação

Serafini, Ramoel

The effect of fire on pre-cast steel fiber reinforced concrete for tunnel linings: from microstructure to structural simulation / R. Serafini -- versão corr. -- São Paulo, 2021.

283 p.

Tese (Doutorado) – Escola Politécnica da Universidade de São Paulo. Departamento de Construção Civil.

1. Steel fiber reinforced concrete 2. High temperature 3. Numerical modeling 4. Fire exposure 5. Tunnel structures. I. Universidade de São Paulo. Escola Politécnica. Departamento de Engenharia de Construção Civil II. t.

SERAFINI, R. **The effect of fire on pre-cast steel fiber reinforced concrete for tunnel linings:** from microstructure to structural simulation. 2021. 283 f. Tese (Doutorado em Engenharia Civil) – Escola Politécnica, Universidade de São Paulo, São Paulo, 2021.

Aprovado em:

Banca Examinadora

Prof. Dr. André Pacheco de Assis
Universidade de Brasília
Julgamento: _____

Prof. Dr. Flávio de Andrade Silva
Pontifícia Universidade Católica do Rio de Janeiro
Julgamento: _____

Prof. Dr. Giovanni Plizzari
Università degli Studi di Brescia
Julgamento: _____

Prof. Dr. Luiz Carlos Pinto da Silva Filho
Universidade Federal do Rio Grande do Sul
Julgamento: _____

Prof. Dr. Antonio Domingues de Figueiredo
Universidade de São Paulo (orientador)
Julgamento: _____

DEDICATION

This doctoral thesis is specially dedicated to my beloved parents, Leomar and Marilene; my loyal friend and brother, Junior; and my partner in life, Bárbara Elisa.

Esta tese de doutorado é especialmente dedicada aos meus amados pais, Leomar e Marilene; ao meu leal amigo e irmão, Junior; e a minha companheira de vida, Bárbara Elisa.

AGRADECIMENTOS

É incrível a inexorável necessidade humana de expressar-se por meio das mais diversas formas, símbolos, desenhos, letras e números. Penso que a tarefa de externar vivências permanece complexa e imprecisa, mesmo depois de milênios carregados de avanços linguísticos e tecnológicos. Assim, escrevo estes agradecimentos na esperança que as ferramentas que disponho sejam suficientes para transmitir a minha enorme gratidão àqueles que foram fundamentais para o desenvolvimento desta tese.

Por isso, agradeço:

Ao **Prof. Antonio Domingues de Figueiredo**, pela orientação e pelo constante estímulo e apoio durante o desenvolvimento do doutorado. É engraçado e nostálgico lembrar que, há alguns anos, um rapaz até então desconhecido e com um nome “peculiar” (eu!) bate na sua porta interessado em linhas de pesquisa correlatas à concreto com fibras: cheio de ideias, cheio de perguntas, cheio de incertezas. Como gostamos de caracterizar na física: “pura energia potencial”. Hoje, ao findar desta árdua jornada, é nítido o quanto trabalhar ao seu lado foi engrandecedor para meu crescimento pessoal e profissional. Em especial, sou muito grato pela confiança em mim depositada; pela liberdade que me foi concedida como pesquisador; e pelo valioso conjunto de valores e virtudes que desenvolvi neste últimos quatro anos sob sua orientação. Acima de tudo, sou muito grato pela inestimável amizade que desenvolvemos e que permanecerá comigo durante toda a minha existência.

Ao **Prof. Albert de la Fuente**, pela orientação, pelos valiosos ensinamentos durante o desenvolvimento da tese, e também pelo apoio técnico, financeiro e emocional durante a minha estadia na *Universitat Politècnica de Catalunya* (UPC), em Barcelona. Sou muito grato pelas orientações leves e proveitosas, com um grande clima de confiança e paciência – e que resultavam em centenas de “rascunhos” com representações e explicações sobre o modelo numérico. Estes “rascunhos” hoje estão guardados como lembrança dos momentos únicos que passei na UPC sob orientação do senhor! Mais do que isso, eu agradeço pela enorme confiança e pelos desafios estimulados pela sua atuação como orientador. Os estímulos e a confiança no meu potencial catalizaram (e muito!) o meu desenvolvimento como engenheiro e pesquisador. Tenho no senhor uma grande referência profissional a ser seguida, por isso me traz muita alegria tê-lo como orientador e, acima de tudo, como um grande amigo.

Ao **Instituto de Pesquisas Tecnológicas e seus pesquisadores** pela inestimável contribuição técnica e laboratorial que viabilizou e catalizou o desenvolvimento desta tese. Em especial, meus agradecimentos aos engenheiros **Me. Antonio Fernando Berto e Carlos Roberto Metzker de Oliveira** pelas valiosas discussões técnicas a respeito dos ensaios de exposição ao fogo. Ao **Dr. Valdecir Angelo Quarcioni** pelas discussões a respeito da cinética de hidratação/desidratação do cimento Portland, durabilidade das estruturas, e concreto reforçado com fibras. À **Ma. Priscila Rodrigues Melo Leal** pelas discussões a respeito dos resultados de MEV-EDS da interface fibra-matriz. À **Dra. Ana Paola Villalva Braga** pelas contribuições relativas às alterações microestruturais do aço exposto às elevadas temperaturas.

Aos **docentes e pesquisadores do Programa de Pós-Graduação em Engenharia Civil** da Universidade de São Paulo (PPGEC - USP) pelos ensinamentos e conhecimentos compartilhados, e também por serem fonte de inspiração profissional. Em especial, ao **Prof. Antonio Carlos Vieira Coelho** pela abertura para conversas técnicas e também por ter me recebido de forma tão gentil durante o meu primeiro dia no PPGEC-USP. À **Profª. Maria Alba Cincotto** pelas valiosas discussões e ensinamentos sobre química do cimento, além de nossas prazerosas conversas nos corredores da Escola Politécnica. Ao **Prof. Luís Bitencourt Jr.** pelas diversas reuniões, conversas técnicas, e discussões sobre os resultados obtidos pelos modelos numéricos desta tese.

Aos meus amigos/irmãos **Me. Ronney Rodrigues Agra e Dr. Sérgio Roberto Andrade Dantas** por dividir o peso da rotina, das betonadas e das centenas de corpos de prova que precisavam ser ensaiados. Obrigado pela nossa amizade que permeia desde assuntos pessoais até discussões técnicas sobre os resultados dos nossos trabalhos. Embora esta tese tenha o meu nome, eu certamente não seria capaz de desenvolvê-la sem o apoio diário e descomunal de cada um de vocês!

Ao **Fiber Team** por auxiliarem sempre que possível nas atividades e por tornarem os momentos laboratoriais mais leves e divertidos. Em especial, ao **Dr. Renan Pícolo Salvador** pelos enormes ensinamentos, excelentes discussões técnicas e pelas cirúrgicas alterações no texto dos artigos. Ao **Dr. Dimas Alan Strauss Rambo** por catalisar o meu desenvolvimento ao chegar no PPGEC-USP e me introduzir ao universo do fogo em estruturas de concreto. À **Dra. Renata Monte** pelas discussões técnicas que muito contribuíram para reflexão a cerca dos assuntos da tese. À **Ma. Lígia Vitória Real** por ser um exemplo profissional e por confiar e fomentar o meu potencial como pesquisador.

Aos **amigos que fiz pelo caminho** e que muito alegraram meus dias de trabalho: Leonardo, Pedro, Paula, Felipe, Alan, Tiago, Guilherme, César, Daniel, Amanda, Victor (PUC-RJ), Fábio, Andreia, João Paulo, César, Natália, Joelma, Luana, André, Roberto,

Lívia, Estevão, Jéssica, Danilo, Julie, Daniele, Heitor, José Augusto, Marcel, Carol, e Gustavo.

Aos **técnicos e funcionários do Hall Tecnológico**, em especial ao Jenício, Adilson, Jéssica e Mário pela enorme assistência em todas as etapas deste trabalho. Aos **funcionários do departamento** Wandréa, Carla, Engracia, Eliany, Milton e Paulinho pelos esclarecimentos e auxílio em relação aos questionamentos administrativos.

À **Fundação de Apoio ao Instituto de Pesquisas Tecnológicas e seus gestores** pelo apoio financeiro através do programa Novos Talentos.

Aos **professores da Banca Examinadora** por aceitarem o convite para participar da avaliação desta tese. Certamente os apontamentos valiosos contribuíram para a melhoria deste trabalho.

Por fim, o mais importante de todos os agradecimentos é para a minha família. Aos **meus pais, Leomar e Marilene**, que certamente devem receber o maior dos agradecimentos contidos nesta seção, maior ainda do que seria possível descrever em palavras. Eu cresci tendo vocês como grandes exemplos por serem pessoas justas, honestas, idôneas, batalhadoras e dedicadas. Mais do que isso, eu sou eternamente grato pelos duros sacrifícios que vocês fizeram cuidar dos sérios problemas de saúde que tive quando criança e também para possibilitar o meu acesso à educação de qualidade. Posso dizer com muito orgulho que, no berço familiar, aprendi tudo aquilo que é necessário para uma vida honesta e virtuosa – e isso é a melhor herança que um filho pode receber de seus pais. Eu sou eternamente grato por ser seu filho e, por toda a vida, eu irei honrar a educação e as virtudes que aprendi pelo exemplo de vocês. À **minha tia, Isabel Ceratto**, pelo constante cuidado, carinho e dedicação ao zelar por mim durante toda a minha vida, dos primeiros passos à vida adulta. Ao **meu irmão, Junior Serafini**, por sempre confiar no meu potencial pessoal e profissional e por dividir comigo todas as fases da minha vida. Pela irmandade que vai além do sangue e que, embora seja meu irmão mais novo, é uma das pessoas que eu mais admiro e respeito no mundo. À **minha outra parte, Bárbara Elisa Somacal**, por ser a mulher mais incrível que eu poderia ter ao meu lado. Por todo o apoio, encorajamento, carinho e incentivo incondicional em cada etapa deste trabalho, mesmo que estes culminassem na necessidade de resistir às dificuldades impostas pela distância física. Por fazer a minha jornada em São Paulo muito mais leve e tolerável, através do contato diário e do acolhimento das minhas dificuldades. O seu lugar no meu coração é único! Sem todos vocês, **família**, a conquista do doutorado não seria possível. Por isso, quero que vocês vejam nesta tese um pedacinho de cada um de vocês!

Muito obrigado!

“We can judge our progress by the courage of our questions and the depth of our answers, our willingness to embrace what is true rather than what feels good.”

“Nós podemos julgar o nosso progresso pela coragem de nossas perguntas e pela profundidade de nossas respostas, nossa disposição em aceitar o que é verdadeiro em detrimento daquilo que parece bom.” (tradução livre)

Carl Edward Sagan

ABSTRACT

SERAFINI, R. **The effect of fire on pre-cast steel fiber reinforced concrete for tunnel linings:** from microstructure to structural simulation. 2021. 283 f. Thesis (Doctorate in Civil Engineering) – Polytechnic School, University of São Paulo, São Paulo, 2021.

The occurrence of fire in fiber reinforced concrete structures is one of the main concerns regarding the use of this material. Although fire is a deleterious event, limitations are found in studies focused on evaluating the effect of elevated temperatures on the mechanical properties of the composite, as well as in terms of extrapolating the results to design. In this context, this thesis aims to understand the tendencies in the mesoscale behavior of steel fiber reinforced concretes (SFRC) after temperature exposure and simulate the fire-related stability condition of tunnel sections built with this material. The changes in the microstructure of steel fibers, cementitious matrix, and fiber-matrix interfacial transition zone were evaluated as a function of temperature. Later, the effect of elevated temperatures on the tensile strength of fibers; bond-slip behavior of fibers embedded in the cementitious matrix; and the compressive, tensile, and post-crack parameters were evaluated. Furthermore, the composite was exposed to a large-scale fire test to experimentally determine the distribution of temperatures and the post-fire tensile properties of the material. At last, a numerical model was developed to compute the effect of a fire and thermal spalling on the bending capacity of reinforced concrete, fiber reinforced concrete, and hybrid solutions. The thermal spalling model was based on a simplified approach that shutdown the layers spalled. The results show that the the post-crack parameters f_{ts} and f_{tu} were more considerably influenced by the properties of the fiber-matrix ITZ than the bulk matrix properties. In terms of f_{tu} , no statistically significant change was observed for $T \leq 300$ °C, which as explained based on the mineralogical changes in the fiber-matrix ITZ and the changes in the pull-out kinetics due to the expansion of iron oxides and shrinkage of the cement paste. Moreover, the bond-slip mechanism have shown to prevail, without fiber rupture, up to ~600 °C. Considering the

numerical simulation without thermal spalling, FRC and RC-FRC solutions have shown to be less sensitive than the RC30 solution, while the increase in concrete cover in RC50 solution considerably mitigated the reductions in terms of bending capacity. Nevertheless, the increase in concrete cover has negligible influence on mitigating the reductions caused by thermal spalling, being the FRC and RC-FRC the least sensitive solutions due to the diffuse reinforcing capacity of fibers in the cross-section. In this sense, the advances acquired in this thesis supported a tool for assessing the bearing capacity of tunnel sections exposed to fire with and without thermal spalling and contributed to improving the safety conditions for this type of structure.

Keywords: 1. Steel fiber reinforced concrete. 2. Elevated temperature. 3. Fire exposure. 4. Post-crack behavior. 5. Tunnel structures. 6. Numerical modeling. 7. Structural simulation.

SERAFINI, R. **O efeito do fogo em concretos pré-moldados reforçados com fibras de aço para túneis:** da microestrutura à simulação numérica. 2021. 283 f. Tese (Doutorado em Engenharia Civil) – Escola Politécnica, Universidade de São Paulo, São Paulo, 2020.

A ocorrência de incêndio em estruturas feitas com esse compósito é uma das principais preocupações relacionadas ao uso deste material. Embora incêndios sejam eventos deletérios, limitações são encontradas no estudo das elevadas temperaturas nas propriedades mecânicas do compósito, bem como em termos de extrapolação destes resultados para o projeto estrutural. Nesse contexto, esta tese tem por objetivo compreender as tendências comportamentais do concreto reforçado com fibras de aço (CRFA) após a exposição a elevadas temperaturas e simular numericamente as condições de estabilidade durante incêndios em túneis constituídos com esse material. As alterações microestruturais das fibras de aço, da matriz cimentícia, e da interface fibra-matriz foram avaliadas em função da temperatura. Posteriormente, o efeito das elevadas temperaturas foi avaliado por meio de ensaios de mesoescala na resistência à tração das fibras de aço; aderência e deslizamento das fibras embutidas na matriz cimentícia; na resistência à compressão e tração da matriz; e nas propriedades pós-fissuração do concreto com fibras de aço. Além disso, o compósito foi exposto a um ensaio de incêndio de larga escala a fim de verificar a distribuição interna de temperaturas gerada e o efeito do incêndio nas propriedades mecânicas de pós-fissuração do material, o que foi posteriormente utilizado para validação do modelo numérico. Por fim, um modelo numérico foi desenvolvido a fim de prever os efeitos do incêndio e da ocorrência de fragmentação térmica na capacidade resistente de seções de concreto armado, concreto com fibras, e híbridos de concreto armado com fibras. O modelo de fragmentação térmica foi concebido de forma simplificada através do desligamento das camadas afetadas. Os resultados mostram que os parâmetros f'_{ts} e f'_{tu} foram mais influenciados pelas propriedades da interface fibra-matriz do que pelas

propriedades da matriz cimentícia. Em termos de f_{tu} , não houve alteração significativa para $T \leq 300$ °C, o que foi explicado pelas alterações mineralógicas na zona de transição fibra-pasta e nas mudanças na cinética de arrancamento devido ao processo expansivo do óxido de ferro e retração da pasta de cimento. Considerando a simulação numérica, soluções de CRF e RC-CRF se mostraram menos sensíveis que a solução RC30, enquanto o aumento de cobrimento mitigou as reduções em termos de capacidade à flexão. Entretanto, o aumento do cobrimento não favoreceu a mitigação das reduções causadas pela fragmentação explosiva, sendo as soluções de CRF e RC-FRC as opções menos sensíveis devido a capacidade de reforço difuso das fibras. Nesse sentido, os avanços gerados nesta tese subsidiam uma ferramenta de verificação da capacidade à flexão de seções de túneis expostas ao fogo com e sem fragmentação explosiva, contribuindo para aprimorar as condições de segurança deste tipo de estrutura.

Palavras-chave: 1. Concreto reforçado com fibras 2. Elevadas temperaturas 3. Modelagem numérica 4. Exposição ao fogo 5. Comportamento pós-fissuração 6. Estrutura de túneis 7. Simulação estrutural.

LIST OF FIGURES

Figure 1.1 – Structure of the doctoral thesis	30
Figure 2.1 – Dimensional change of (a) Portland cement paste and (b) various rock types exposed to elevated temperatures (adapted from Bazant & Kaplan [69])	39
Figure 2.2 – Illustration of the ITZ between steel fiber and the cementitious matrix [101].....	42
Figure 2.3 – The effect of temperature on the k_b of hooked-end steel fibers.....	43
Figure 2.4 – Changes in (a) compressive and (b) elastic properties of SFRC as a function of temperature	45
Figure 2.5 – Effect of temperature on the (a) f'_c and (b) f'_{tu} of SFRC.....	48
Figure 2.6 – Thermal-field in concrete elements affected by uniaxial fire [68]	51
Figure 2.7 – Thermal stresses generated during an uniaxial fire exposure	52
Figure 2.8 – Differences between the isotherm and exact methods (Bamonte & Meda [128]).	54
Figure 3.1 – Illustration of the (a) rotary sample divider (b) manual sampler	58
Figure 3.2 – Procedure adopted to determine the particle size distribution of grained materials.....	58
Figure 3.3 – Particle size distribution for: (a) cementitious materials, and (b) fine and coarse aggregates	59
Figure 3.4 – Molding procedure: (a) pull-out molds used and (b) fixation frame and molding procedure	64
Figure 3.5 – (a) prismatic specimens, (b) cylindrical and cubic specimens, and (c) wooden tool for the fixation of thermocouples.....	65
Figure 3.6 – DEWS test: (a) prismatic specimen cutting procedure, and (b) the triangular grooves and notches.....	65
Figure 3.7 – Fire simulation: (a) positioning of prismatic specimens, and (b) the vertical fire simulator	67
Figure 3.8 – Experimental fire simulation compared to the hydrocarbon fire curve ..	67
Figure 3.9 – SEM-EDS analysis for the target temperatures of (a) 25 °C, (b) 150 °C, (c) 300 °C, (d) 450 °C, (e) 600 °C, and (f) 750 °C	69
Figure 3.10 – Test setup adopted for the three-point bending test.....	72
Figure 3.11 – Schematic (a) drawing and (b) illustration of the DEWS test setup ...	73
Figure 3.12 – Illustration of the heat transfer model developed.....	77

Figure 3.13 – Illustration of the mechanical model implemented.....	80
Figure 3.14 – Reduction factors employed in the numerical simulation.....	81
Figure 4.1 – Effect of temperature on external and effective diameters.....	86
Figure 4.2 – Effect of temperature on the grain size of steel	86
Figure 4.3 – Effect of temperature on the steel fiber’s tensile strength and rupture strain	87
Figure 4.4 – (a) average load-displacement curves and (b) the maximum P_{L1} , P_{L2} , and P_{L3} values.	88
Figure 4.5 – Effect of temperature on the steel fiber’s tensile strength and rupture strain	89
Figure 4.6 – (a) average load-displacement curves and (b) the maximum P_{L1} , P_{L2} , and P_{L3} values.	90
Figure 4.7 – (a) average stress-strain curve and (b) compressive strength and elastic modulus as a function of temperature	92
Figure 4.8 – (a) stress-COD average results and (b) tensile and post-crack tensile strength results	93
Figure 4.9 – Comparison with guidelines and literature results in terms of (a) K_{ft} and (b) K_{ftu}	93
Figure 4.10 – Sample size required as a function of the admissible error for the (a) f_{ft} and (b) f_{ftu} values	94
Figure 4.11 – Experimental and numerical results for the thermal field in the SFRC96	
Figure 4.12 – Experimental and numerical results for the thermal field in the SFRC97	
Figure 4.13 – (a) bending stress-CMOD curves and (b) DEWS stress-COD curves before and after fire	97
Figure 4.14 – Bending capacity with fire affecting specimens in (a) sagging bending (b) hogging bending.....	98
Figure 4.15 – Stress-COD results obtained after fire exposure and temperature exposure.....	99
Figure 4.16 – Distribution of f_{ftu} as a function of z for the DEWS test.....	100
Figure 4.17 – Bending capacity of the sections exposed to (a) the ISO 834 and (b) the HFC fire curves	101
Figure 4.18 – Effect of fire on the ductility of the reinforcing solutions affected by HFC.....	102
Figure 4.19 – Effect of spalling parameters on the bending capacity of (a) FRC, (b) RC30, (c) RC50 solutions	103

Figure 4.20 – Effect of spalling parameters on the bending capacity of (a) RC30-FRC and (b) RC50-FRC hybrid solutions 105

LIST OF TABLES

Table 1.1 – Specific objectives of the doctoral thesis	29
Table 2.1 – Brief summary of fire events in tunnels (adapted from Schütz [59]).....	36
Table 2.2 – Changes in the physical, chemical, and mineralogical properties of SFRC with temperature	41
Table 3.1 – The complete mix design used to produce 1 m ³ of SFRC	56
Table 3.2 – Manufacturer data for steel fibers and micro-synthetic fibers.....	57
Table 3.3 – Results of d ₁₀ , d ₅₀ , d ₉₀ , fineness modulus, and specific surface area of materials.....	60
Table 3.4 – Results of real density and specific surface area of grained materials	61
Table 3.5 – Mineralogical composition of the cement powder.....	62
Table 3.6 – Input parameters adopted for the thermo-mechanical simulations	84

NOTATIONS

Symbols

Greek lowercase letters

α_c	convective heat transfer coefficient
β_1	variable to compute the contribution of rebars in the stability equations
β_2	variable to compute the contribution of rebars in the stability equations
χ	curvature of the section
δ_F	partial safety factor
ε	emissivity of concrete
ε_c	total strain field
ε_{cg}	strain at the center of gravity
ε_m	mechanical strain
ρ	density of concrete
σ	Steffan-Boltzman constant
$\tau_{b,25^\circ C}$	fiber-matrix bond strength at room temperature
$\tau_{b,T}$	fiber-matrix bond strength at temperature T

Roman lowercase letters

\dot{h}_c	convection heat flux
\dot{h}_{net}	net heat flux
\dot{h}_r	radiation heat flux
d_{10}	diameter in which 10% of the distribution has smaller particle size
d_{50}	diameter in which 50% of the distribution has smaller particle size
d_{90}	diameter in which 90% of the distribution has smaller particle size

d_{max}	maximum diameter of aggregate
d_{sl}	concrete cover at the intrados
d_{su}	concrete cover at the extrados
$E_{c,T}$	elastic modulus at temperature T
$f_{c,25^{\circ}C}$	compressive strength at room temperature
$f_{c,T}$	compressive strength at temperature T
f_{cd}	design compressive strength
$f_{cd,T}$	design compressive strength at temperature T
f_{ck}	design compressive strength at room temperature
f_{LOP}	limit of proportionality in EN 14651 bending test
f_{R1}	post-crack tensile strength relative to serviceability conditions of fiber reinforced concrete
f_{R3}	post-crack tensile strength relative to ultimate conditions of fiber reinforced concrete
$f_{ft,25^{\circ}C}$	matrix tensile strength at room temperature
$f_{ft,T}$	matrix tensile strength at temperature T
$f_{ftu,25^{\circ}C}$	ultimate limit state post-crack tensile strength at room temperature
$f_{ftu,T}$	ultimate limit state post-crack tensile strength at temperature T
f_{Ftud}	design ULS post-crack tensile strength
$f_{Ftud,T}$	design ULS post-crack tensile strength at temperature T
$f_{sd,T}$	design yield strength of steel at temperature T
f_{syk}	characteristic yield strength of steel
h_{lig}	height of the ligament in the DEWS test
h_{sp}	distance between the tip of the notch to the top of the specimen in bending test
k_b	relative bond strength
k_c	relative compressive strength
k_{Ec}	relative elastic modulus
k_{ft}	relative matrix tensile strength

k_{ftu}	relative post-crack tensile strength at the ultimate limit state condition
m	number of time instants in the discretized time domain
n	number of points in the discretized space domain
n_s	number of subsections in the cross-section
n_{sc}	number of compressed subsections in the cross-section
n_{sl}	number of rebars in the lower portion of the section (intrados)
n_{st}	number of subsections subjected to tensile stresses in the cross-section
n_{su}	number of rebars in the upper portion of the section (extrados)
s_L	maximum section lost due to thermal spalling
t_{fire}	maximum duration of the fire
z	distance from the heating surface (depth)

Roman capital letters

A_s	total area of steel rebar
A_{sl}	area of one rebar located in the lower region of the cross-section
A_{su}	area of one rebar located in the upper region of the cross-section
C	specific heat of concrete
H	height of the cross-section
K	thermal conductivity of concrete
K_c	temperature dependant reduction in concrete compressive strength
K_{Ftu}	temperature dependant reduction in the ULS post-crack tensile strength
K_L	lower limit for the thermal conductivity
K_{sv}	temperature dependant reduction in the yield strength of steel
K_U	upper limit for the thermal conductivity
P_{ef}	splitting load that acts on the fracture surface of the DEWS test
R_{sp}	rate of thermal spalling
T	temperature
T_f	temperature of the fire at a given time

T_s temperature of the concrete surface at a given time

Abbreviations

<i>ABECE</i>	brazilian association of structural engineering and consulting
<i>ABNT</i>	brazilian national standards organization
<i>ACI</i>	american concrete institute
<i>C-H</i>	portlandite
<i>CMOD</i>	crack mouth opening displacement
<i>COD</i>	crack-opening displacement
<i>C-S-H</i>	calcium silicate hydrate
<i>CTMM</i>	center for metallurgical and materials technology
<i>DEWS</i>	double edge wedge splitting
<i>DPT</i>	double punch test
E_c	elastic modulus
<i>EDS</i>	energy dispersive spectroscopy
f_c	compressive strength
<i>FDM</i>	finite difference method
f_{ft}	tensile strength of the cementitious matrix
f_{fts}	post-crack tensile strength associated with the service condition
f_{ftu}	post-crack tensile strength associated with the ultimate condition
<i>FM</i>	fineness modulus
<i>FRC</i>	fiber reinforced concrete
f_{sy}	yield strength of steel
<i>HFC</i>	hydrocarbon fire curve
<i>IBRACON</i>	brazilian concrete institute
<i>IPT</i>	institute for technological research
<i>ISO</i>	international organization for standardization
<i>ITA</i>	international tunneling and underground space association

<i>ITZ</i>	interfacial transition zone
<i>M-N</i>	moment-axial force
<i>MVD</i>	Montevideo test
<i>MSFRC</i>	macro-synthetic fiber reinforced concrete
<i>NIST</i>	national institute of standards and technology
<i>OM</i>	optical microscopy
P_{L1}	peak load value in the pullout load-displacement curves
P_{L2}	second peak load value in the pullout load-displacement curves
P_{L3}	load value at a 10 mm displacement in the pullout load-displacement curves
<i>PP</i>	polypropylene
<i>RC</i>	reinforced concrete
<i>RC30</i>	reinforced concrete with 30 mm of concrete cover
<i>RC50</i>	reinforced concrete with 50 mm of concrete cover
<i>SCSFRC</i>	self consolidating steel fiber reinforced concrete
<i>SEM</i>	scanning electron microscopy
<i>SFRC</i>	steel fiber reinforced concrete
<i>TBM</i>	tunnel boring machine
<i>UHPRC</i>	ultra-high performance fiber reinforced concrete
<i>ULS</i>	ultimate limit state
<i>US</i>	ultrasonic
<i>XRD</i>	x-ray diffraction

SUMMARY

Chapter 1. Introduction	26
1.1 Scope of the research	26
1.2 Research significance	28
1.3 Objectives.....	29
1.4 Structure of the thesis	30
Chapter 2. Literature review	34
2.2 Effect of temperature on the SFRC.....	38
2.2.1 Physical, chemical, and mineralogical changes	38
2.2.2 Bond-slip behavior of fibers.....	42
2.2.3 Compressive parameters.....	44
2.2.4 Tensile parameters	46
2.3 The effect of fire on SFRC tunnel linings.....	49
2.3.1 Fire curve and thermal field.....	50
2.3.2 Thermal stresses and bearing capacity.....	51
Chapter 3. Methodology	56
3.1 Characterization of materials	56
3.1.1 Grained materials sampling.....	57
3.1.2 Particle size distribution	58
3.1.3 Real density and specific surface area	60
3.1.4 Mineralogical composition	61

3.2	Mixing, casting, and production procedures	62
3.2.1	Cement paste	62
3.2.2	Mortar	63
3.2.3	Steel fiber reinforced concrete (SFRC)	64
3.3	Heating of specimens	66
3.3.1	Oven heating procedure	66
3.3.2	Fire simulation procedure.....	66
3.4	Microstructural characterizations	68
3.4.1	Optical microscopy.....	68
3.4.2	Scanning electron microscopy.....	68
3.4.2	X-Ray diffraction technique	69
3.5	Mechanical characterizations.....	70
3.5.1	Tensile strength of steel fibers.....	70
3.5.2	Pullout test	70
3.5.3	Compressive strength and elastic modulus.....	71
3.5.4	Ultrasonic propagation speed	71
3.5.5	Three-point bending test	72
3.5.6	Tensile properties by means of DEWS test	72
3.5.7	Determination of DEWS sample size	74
3.6	Numerical model.....	74
3.6.1	Heat transfer model.....	75
3.6.2	Initial and boundary conditions	76
3.6.3	Thermal and physical properties of FRC	78
3.6.4	FRC constitutive law	79
3.6.5	Cross-sectional modelling	81
Chapter 4.	Results and analysis	85
4.1	Thermal effects on the bond-slip mechanism.....	85
4.2	Thermal-related changes in SFRC mechanical properties	91

4.3 Effect of fire on SFRC sections.....	94
4.3.1 Results of the experimental campaign.....	95
4.3.2 Results of the parametric study	100
Chapter 5. Conclusions.....	106
5.1 Prospective research topics.....	109
References	111
Attachments.....	122
Appendix A.....	282

CHAPTER 1.

INTRODUCTION

1.1 SCOPE OF THE RESEARCH

Tunnels play an important role in the development of society because they are capable of solving mobility problems in urban environments by taking advantage of the underground space in a sustainable manner [1]. The use of tunnels to expand urban infrastructure contributes to improving the quality of life in these areas [2] as well as reducing social inequality [3,4]. According to the International Tunneling and Underground Space Association (ITA), tunnels are infrastructure systems capable of providing urban mass transit in a safe and unobstrusive manner, while also reducing the traffic on surface streets, the traffic noise, and the air pollution [5].

In this context, the use of steel fiber reinforced concrete (SFRC) is increasingly seen as a promising construction material to be employed in the production of precast elements. Although SFRC is commonly employed in the production of pavements, sprayed concrete, and concrete pipes [6–8], the use of SFRC is expected to expand based on the considerable advances in research [9–12] and the publication of several design codes and guidelines, especially after the publication of the *fib* Model Code 2010 [13]. The production of segments for tunnel linings built with Tunnel Boring Machine (TBM) technology is one of the sectors that benefits from the use of SFRC as partial or total substitution to the conventional reinforced concrete (RC).

The benefits of using SFRC for the production of precast segments are associated with the increased production efficiency and economic competitiveness of the industrial plant, the reduction of short-term maintenance of segments, and the improved corrosion resistance [14–17]. Moreover, the use of SFRC improves the material's response to the diffused loads that may occur during the production stage

(e.g. storage, transportation, handling), to the concentrated loads that may occur during the installation phase (e.g. thrust of the jacks), and during the service life of the structure (e.g. irregular loads resulting from the contact between the tunnel lining and the soil).

Although the fire safety design of concrete structures have shown some progress in the last decades, very limited information is available regarding the fire safety of tunnel structures built with SFRC in guidelines and codes worldwide [18]. The *fib* Model Code 2010 and the *fib Bulletin* 38 provide tools for the design and assessment of RC structures regarding fire events, however the approach in terms of design of fiber reinforced concrete (FRC) structures is given only for regular conditions of usage. The *fib Bulletin* 46 is limited to stating that the steel fibers provide some post-crack tensile strength and increases the energy absorption of plain concrete after heat exposure. Although the *fib Bulletin* 83 provides some insight regarding a numerical tool for the assessment of fire damage on tunnels, the state-of-the-art report does not provide any spalling-related parameter to evaluate the fire resistance of tunnels. Additionally, several other references fail to provide an adequate approach for the fire design of SFRC structures, such as the ACI comitee 544 [19], the Eurocode 2 [20], and the French [21], Italian [22], and Brazilian [23] standards, reports, and guidelines.

A state of the art report published by the ITA discussed the use of fibers as total or partial substitution to RC in tunnel linings for precast fiber reinforced concrete segments [24]. Although the use of SFRC is discussed, the effect of fire is limited to a qualitative approach to the occurrence of spalling in SFRC segments, which highlights the lack of fire safety parameters for design and post-fire assessment of these structures. This is a result of the lack of experimental campaigns that study the effect of temperature and fire on the properties of SFRC, as well as the limited amount of reliable models capable of simulating the behavior of structures built with this composite.

This means that experimental campaigns and numerical models dedicated to the effect of fire on SFRC tunnels are required, especially regarding the occurrence of thermal spalling. In this sense, this thesis come with the motivation of conducting an experimental program to characterize the mechanical properties of SFRC after exposure to several target temperatures (from 25 to 750 °C) and to a fire simulation following the hydrocarbon fire curve (HFC). The methodology adopted aimed to

quantify the effects of temperature on the properties of the fibers, the fiber-matrix interaction, and the mesoscale properties of the SFRC. Based on the experimental results, a numerical model was implemented and validated to simulate the influence of a fire event in the bending capacity of FRC and hybrid RC-FRC sections considering the occurrence of thermal spalling. Therefore, this thesis provides a tool for the design and assessment of SFRC tunnels.

The advances of this thesis compared to results found in literature are related to the deeper investigation of the factors that explain the effects of temperature on the fiber-matrix interaction; the changes in the post-crack behavior of SFRC after exposure to elevated temperatures; the effect of a unifacial fire event on the properties of the composite; and the effect of thermal spalling on the bending capacity of FRC and RC-FRC sections.

1.2 RESEARCH SIGNIFICANCE

The demand for the use of SFRC in elements with structural responsibility is at rise, either in partial or total substitution to RC [10–13]. The use of SFRC as a structural material requires a deep understanding of the behavior in the mesoscale level, as well as reliable models to evaluate the structural behavior in case of a fire event.

The most recent codes discuss the guidelines to prevent the occurrence of thermal spalling in high temperature environments and the effect of temperature on the compressive strength (f_c) and elastic modulus (E_c) of the SFRC, which have been extensively studied [25–32]. Nevertheless, studies regarding the effect of temperature on the post-crack behavior of the composite remain fairly limited, while the effect of temperature on the bond-slip mechanism of steel fibers still need to be deeply investigated [29,33–37]. Moreover, investigations regarding the effect of fire on the bending capacity of FRC and RC-FRC sections is scarce in literature [38,39], especially considering the occurrence of thermal spalling. The incorporation of these contributions benefits aspects related both to the design procedure and the post-fire assessment of structures built with SFRC, thus contributing to the consolidation of SFRC as a construction material. Moreover, civil engineers would have tools to compute the effect of fire on the bending capacity of tunnel structures made with FRC and RC-FRC segments, which results in economical and social benefits.

1.3 OBJECTIVES

Based on the previous discussion, this thesis aims to understand the tendencies in the mesoscale behavior of steel fiber reinforced concretes after temperature exposure and simulate the fire-related stability condition of RC and RC-FRC tunnel sections built with this material. In order to achieve the main goal, several specific objectives are defined. Table 1.1 shows the main specific objectives for each subject treated in this doctoral thesis.

Table 1.1 – Specific objectives of the doctoral thesis

Subject	Specific objectives
Hooked-end steel fiber	<ul style="list-style-type: none"> ▪ Assess the effect of temperature on the physical properties and tensile strength of steel fibers, while correlating the results with the changes in the fiber's cross-sectional area and grain size.
Fiber-matrix interaction	<ul style="list-style-type: none"> ▪ Investigate the effect of temperature in the mineralogical properties in the fiber-matrix interfacial transition zone. ▪ Explain the effect of temperature on the bond-slip behavior of hooked-end steel fibers based on the microstructural changes evidenced. ▪ Develop an analytical formulation to predict the bond-slip behavior of hooked-end steel fibers after heat exposure. ▪ Validate the applicability of the analytical formulation in a numerical model capable of representing the steel fibers in a explicit and discrete manner inside the SFRC.
Mechanical properties of the SFRC after heat exposure	<ul style="list-style-type: none"> ▪ Investigate the effect of temperature on the mineralogical properties of the cementitious matrix. ▪ Assess the effect of temperature on the compressive strength and elastic modulus of the SFRC, correlating the results with the mineralogical characterization. ▪ Evaluate the suitability of the Double Edge Wedge Splitting (DEWS) test for the determination of the tensile properties of the SFRC after heat exposure. ▪ Develop a simplified analytical formulation to predict the effect of elevated temperatures on the tensile behavior of SFRC, which may be used as input for future numerical models.

Subject	Specific objectives
Tensile properties of the SFRC after fire exposure	<ul style="list-style-type: none"> ▪ Determine the thermal field and the distribution of mechanical properties in the SFRC during the exposure to a fire simulation test. ▪ Evaluate the differences in the tensile response obtained by the DEWS test and the three-point bending test before and after fire exposure.
Structural behavior of tunnels built with SFRC	<ul style="list-style-type: none"> ▪ Implement a numerical model that reproduces the effect of fire on the bending capacity of a FRC and RC-FRC sections considering thermal spalling effects. ▪ Perform a parametric study varying the reinforcement type, the fire curve, the rebar's concrete cover, and the thermal spalling parameters on the bending capacity of RC and RC-FRC sections.

1.4 STRUCTURE OF THE THESIS

The structure of the thesis is subdivided in five chapters that compose the main body of the document. The main body of the thesis is supported by five articles that compose the attachment section, as shown in Figure 1.1.

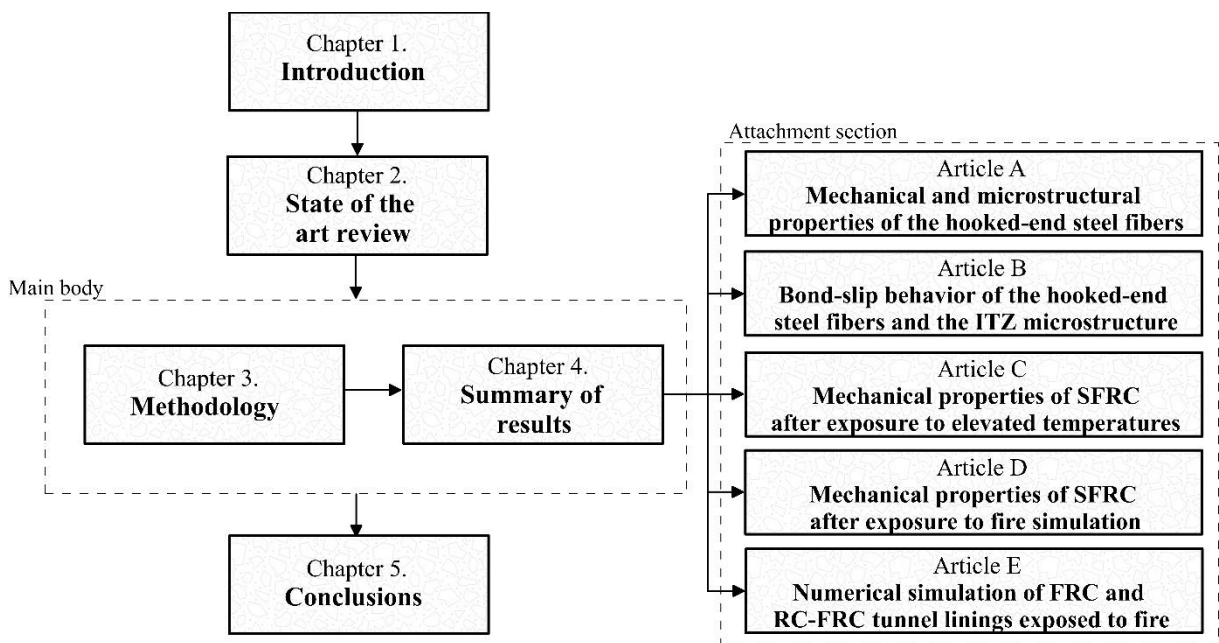


Figure 1.1 – Structure of the doctoral thesis

The chapters presented in this doctoral thesis serve specific purposes and are structured according to the following order:

- **Chapter 1. Introduction:** this chapter introduces the fundamental concepts on the development and utilization of steel fibre reinforced concrete, as well as identifies the problems and challenges to be addressed. The motivations and the objectives of the thesis are described based on the discussion proposed in this chapter and the literature review presented in Chapter 2.
- **Chapter 2. Literature review:** this chapter presents a literature review regarding the relevant subjects addressed in this thesis. Fundamental concepts about the applicability of fiber reinforced concrete in tunnels and the effects of elevated temperatures on the properties of cement paste, aggregates, and fibers are presented. This chapter also discusses previous works regarding experimental and numerical modelling of steel fiber reinforced concretes.
- **Chapter 3. Methodology:** this is the first chapter that composes the main body of this thesis. This chapter presents a detailed description of the methodologies presented in the articles attached in this thesis. The characterization of the materials and a detailed description of the sample preparations and testing procedures adopted are presented. The relevant information about the testing equipments and standards used for each test are provided. Moreover, a throughout description of the procedures implemented in the numerical model are described.
- **Chapter 4. Summary of results:** in this topic, the main results obtained in each one of the articles is presented. The main contributions of each article are summarized in a single chapter that highlights the relevance of the results to achieve the objectives of the thesis.
- **Chapter 5. Conclusions:** this topic serves as a mean to aggregate the results discussed in Chapter 4 and in the articles presented in the attachment section. This chapter summarizes the contribution of the research, the impact of the results to the engineering parameters regarding fire safety, and the social benefits that arise from this doctoral thesis.

The **attachments section** contains a total of five attached documents in the form of articles. The article A, B, C, and D are related to experimental studies that investigated the effect of temperature on the properties of the composite, whereas article E discusses the results of a parametric study using the numerical model implemented in this thesis. Each article is briefly introduced bellow:

The properties of steel fibers (Article A)

This paper was published in the *Magazine of Concrete Research* journal and discusses aspects related to the effect of elevated temperatures on the mechanical, physical, and microstructural properties of steel fibers. In this sense, the tensile strength and rupture strain were determined as a function of temperature and the results obtained for the physical and microstructural characterization were used as base to describe the changes in the tensile behavior of fibers.

The bond-slip behavior of steel fibers (Article B)

This paper was published in the *Composite Structures* journal and discusses aspects related to the effect of elevated temperatures on the bond-slip mechanism between fibers and the cementitious matrix, while also providing a microstructural analysis of the fiber-matrix interface. Therefore, the bond-slip behavior of steel fibers embedded in a cementitious matrix was evaluated as a function of temperature and the results obtained by the microstructural characterization of the interfacial transition zone were used to explain the tendencies evidenced.

The mechanical properties of SFRC as a function of temperature (Article C)

This paper was published in the *ASCE Journal of Materials in Civil Engineering* and discusses aspects related to the effect of elevated temperatures on the compressive, elastic, and tensile properties of SFRC. A refined mineralogical characterization of the cementitious matrix is conducted and correlated with the mechanical results obtained. Therefore, the mechanical behavior of SFRC is characterized as a function of temperature and the tendencies evidenced were explained based on the characterization conducted in *Articles A and B*.

The mechanical properties of SFRC after fire exposure (Article D)

This paper was submitted to the *Fire Safety Journal* and discusses aspects related to the effect of a experimental fire test on the distribution of temperatures and mechanical properties of SFRC. In this sense, the mechanical behavior of SFRC after fire exposure is characterized and the tendencies evidenced were discussed. A case study applied to a Subway Line of the city of São Paulo is conducted and presented.

The effect of fire on the bending capacity of FRC hybrid sections (Article E)

This paper was submitted to the *Materials and Structures* journal and discusses the effect of fire on the bending capacity of RC, FRC, and RC-FRC sections for TBM tunnels. A sectional analysis is conducted using a numerical model implemented in this thesis. The results show that the bending capacity of RC sections with lower concrete cover are greatly affected by fire, while FRC and hybrid RC-FRC may be suitable options to mitigate the reductions in bending capacity of the tunnel. Also, the effect of thermal spalling on the bending capacity of the solutions is evaluated and discussed.

CHAPTER 2.

LITERATURE REVIEW

Concrete has been widely used as a construction material in the modern civilization, especially when combined with steel reinforcing bars (rebars) [40]. In structural applications, these rebars are positioned in zones where the tensile or shear stresses occur as a countermeasure to the low tensile strength and the quasi-brittle behavior of concrete. This process results in a composite that is successfully used as structural material under quasi-static loading conditions due to the enhanced tensile and shear strength in a specific region of elements, called RC [41]. Although RC is widely used in the construction industry, the demand for specific applications has led to the development of alternative construction materials, such as FRC.

The FRC is a composite material produced by the addition of discontinuous fibers in the cementitious matrix, which can be used as a partial or total substitution to the rebars [13]. In this sense, the fibers interact with the cementitious matrix by delaying the opening and unstable growth of micro- and macro-cracks [42]. This interaction results in a composite material with a pseudo-ductile behavior and enhanced mechanical properties. The benefits from the material standpoint are mostly associated with the enhancements in terms of post-crack response and toughness [9,12], resistance to corrosion [14], and fatigue and impact resistance [43–46]. Among the various types of fibers, the steel fiber is the most commonly used for structural purposes [47].

During the last fifty years, the applications of SFRC in the construction industry have progressively increased, partially because of the significant advances in the constituent materials and the understanding of the mechanics of the material [48]. Historically, the vast majority of applications of SFRC were associated with elements of relatively low risk of structural failure, such as sanitary pipes or industrial floors [6]. However, the publication of design codes and guidelines, such as the *fib* Model Code 2010 [13], promoted an expansion in the number of applications for SFRC. In

case of tunnel linings, the use of SFRC has been a reality for the last decades, even before the publication of the Model Code. However, a considerable increase in applications could be verified after the publication of the Model Code, since the technical community gained a solid design basis for such structures [49].

The production of pre-cast elements is among one of the sectors that benefit from the use of SFRC, especially the production of concrete segments for tunnel linings built by TBM technology. A considerable amount of experiences using precast concrete segments reinforced only with fibers have been conducted in national and international levels [11]. The advantages of producing tunnel segments with SFRC are related to the material's response to impact and the diffused loads that may occur during production (*e.g.* storage, transportation, handling), concentrated loads (*e.g.* thrust of the jacks), and service stage (*e.g.* irregular loads resulting from the contact between the tunnel lining and the soil).

More than the enhanced properties, the production efficiency of the industrial plant is boosted since the use of steel fibers considerably reduces the space required for stocking of materials, as well as eliminate some production steps – such as the assembly, positioning, and verification of steel rebars in the forms. Literature results show that, under TBM jack loads, the cracking strength and resistance to damage propagation of SFRC are superior to RC both in serviceability and ultimate limit states [50]. Moreover, the use of this composite material have shown a significant reduction in repair costs since the use of SFRC minimize the damages associated with transport, stock, and installation of the segments [44,51–53], reduced storage costs [54], while also providing increased ultimate load capacity [15].

Although the use of fibers enhance the properties of plain concrete, the behavior of SFRC depends on several fiber-related variables, such as the material type, geometry, content, aspect ratio, and length, as well as variables related to the concrete properties and the manufacturing techniques adopted [55–57]. In this sense, SFRC is a composite material with an intrinsically bound variability that is influenced by factors that have a complex interaction between them, especially in terms of post-crack parameters (after matrix cracks). Therefore, the use of safety factors that account for this intrinsically bound variability are required because the design of structures made with SFRC rely on the assumption that the fibers have a homogeneous and isotropic reinforcement contribution in the elements, which is not

the case of most applications. Even with those considerations, the variability in post-crack parameters is expected to be more stable when the SFRC is used in structural applications [58].

An investigation conducted by Schütz [59] have shown that a total of 177 fire events were reported in 29 different countries between 1866 and 2014, and a summary is provided in Table 2.1. More severe fire scenarios tend to occur in road tunnels due to the type and quantity of combustible material, the reduced compartment dimensions and ventilation conditions. As an example, the Mont Blanc tunnel fire occurred in the year of 1999 when the engine of a transport truck caught fire several kilometers into the tunnel. The fire rapidly developed and spread, generating toxic smoke and increasing the temperature, reaching over 1000 °C and lasting for over 50 hours [60]. The incident resulted in 39 casualties, over 300 million dollars in repair costs, and 3 years of tunnel closure. The temperature inside the tunnel reached more than 1100 °C and required over 50 firefighters to control the blaze [61].

Table 2.1 – Brief summary of fire events in tunnels (adapted from Schütz [59])

Fire events	Structural integrity	Repair cost (in dollars)	Casualties/ Injured (C)/(I)	Year
Sangju Road Tunnel (KR)	Structural damage	N.S.	00C/21I	2015
Oslofjord Road Tunnel (NO)	Structural damage	N.S.	31C/34I	2014
Rodoanel Road Tunnel (BR)	Minor damage	N.S.	00C/00I	2012
Channel Rail Tunnel (FR)	Structural damage	~ 250 million	N.S.	2008
Los Angeles Road Tunnel (USA)	Structural damage	N.S.	03C/10I	2007
Burnley Road Tunnel (AUS)	Minor damage	N.S.	03C/02I	2007
Daegu Subway Train (KR)	Structural damage	N.S.	130C/140I	2003
São Paulo Line Red Subway (BR)	N.S.	N.S.	01C/26I	2001
Kitzsteinhorn Train Tunnel (AT)	Structural damage	N.S.	155C/N.S.	2000
Mont-Blanc Tunnel (FR)	Structural damage	~350 million	39C/M.I.	1999
Tauern Road Tunnel (AUS)	Structural damage	~25 million	12C/49I	1996
Channel Rail Tunnel (UK)	Structural damage	~220 million	N.S.	1996

N.S. – not specified; M.I. – multiple injuries

Although the aforementioned fire events were ignited by accident, fires may be intentionally induced. A typical example of this is the arson attack occurred in Daegu, South Korea, in 2003, where a man set fire to a couch in a subway train using volatile materials. The arson attack resulted in 151 people injured, more than 190 people dead, and over 40 million dollars in property damage [62,63]. Therefore, these examples denote how fire events can impose severe consequences in social, economical, and technical aspects of engineering.

As a result, an increase in the amount of research projects, recommendations, and actions aiming to increase the fire safety of structures have been driven by the unquantifiable cost associated with the loss of human lives and the high social and monetary costs due to the repair and temporary closure of tunnels. The risk is increased for tunnels built in urban areas since the damages could affect the surrounding area, which could involve third party buildings, roadways, and even heritage buildings. Even with those concerns, the study of the effects of fire on the structural behavior of tunnels built with SFRC segments is very scarce in standards and guidelines, as well as in research articles in literature [32,64].

The concern regarding the use of SFRC as a structural material began to be tackled in Brazil in 2015, when the IBRACON/ABECE Committee 303 was created to produce a national guideline for the use of this composite material. Later, in 2021, the first Brazilian guidelines regarding the design and quality control of fiber reinforced composites was published by the Brazilian National Standards Organization (ABNT) [65–67]. Although this represented a milestone for the regulamentation of this composite material, a profound lack of parameters for the fire design of such structures is verified. This is not only a drawback of the national guidelines, but also in the current international design procedures, such as the ACI committee 544 [19], Eurocode 2 [20], and in French [21] and Italian [22] guidelines.

It is important to remark that the occurrence of a fire induces several temperature related effects on SFRC that changes the overall behavior of the composite, both in meso- and structural scale. Therefore, the first concept that needs to be conceived is that a unifacial fire event induces a wide range of internal temperatures, which results in a wide range of mechanical properties inside the composite [68]. These changes in the mechanical properties can be correlated to the changes in microstructural properties of the cement paste, steel fibers, aggregates, and the interfaces between the different phases of the composite. In this sense, the

next subsections seek to briefly summarize the state of the knowledge regarding the behavior SFRC exposed to high temperatures.

2.2 EFFECT OF TEMPERATURE ON THE SFRC

The exposure of the SFRC to elevated temperatures affects the chemical composition, physical structure, and water content of the composite. These changes are primarily associated with the hardened cement paste, although it affects the aggregates to a certain extent. The pore structure and pore distribution of the hardened cement paste are modified with the increase in temperature, while cracking is generated, in most cases, by the superposition of the non-uniform volume expansions of various types (*e.g.* thermal, crystalline conversion) and the non-linear thermal strains generated fire. Although a mathematical approach can be given to describe these thermal-related phenomena [69], this subchapter is focused on a descriptive approach to the effect of temperature on SFRC.

2.2.1 Physical, chemical, and mineralogical changes

The majority of the thermal-related changes that occur in plain concrete can be extrapolated to SFRC, specially regarding the hardened cement paste and the aggregates [68]. The increase in temperature affects the thermal properties [70–72] and density [68,71] of Portland cement based materials. The Eurocode [20] prescribes analytical equations capable of estimating the density (ρ), thermal conductivity (K), and the specific heat (C) of plain concrete as a function of temperature, which are commonly employed in SFRC applications [38,39]. In general lines, the increase in temperature results in an increase in C , as well as a decrease in ρ and a K values.

The cement paste is known to expand for temperatures up to ~ 150 °C and to have a expansion-free stabilization period for temperatures between 150-300 °C. After this brief stabilization, the hardened cement paste begins to shrink for temperatures up to 800 °C [69,73–76]. Contrary to the cement paste, most aggregates tend to expand as temperature increases (Fig. 2.1). Therefore, this thermal expansion/shrinkage mismatch between cement paste and aggregates results in stresses that lead to the formation of micro-cracks in the aggregate-paste ITZ. Another relevant aspect is that a reversible expansion of siliceous aggregates occurs at the temperature of 573 °C due to the changes in the crystal structure of quartz,

from α -trigonal to β -hexagonal, which results in the expansion and cracking of concrete [71].

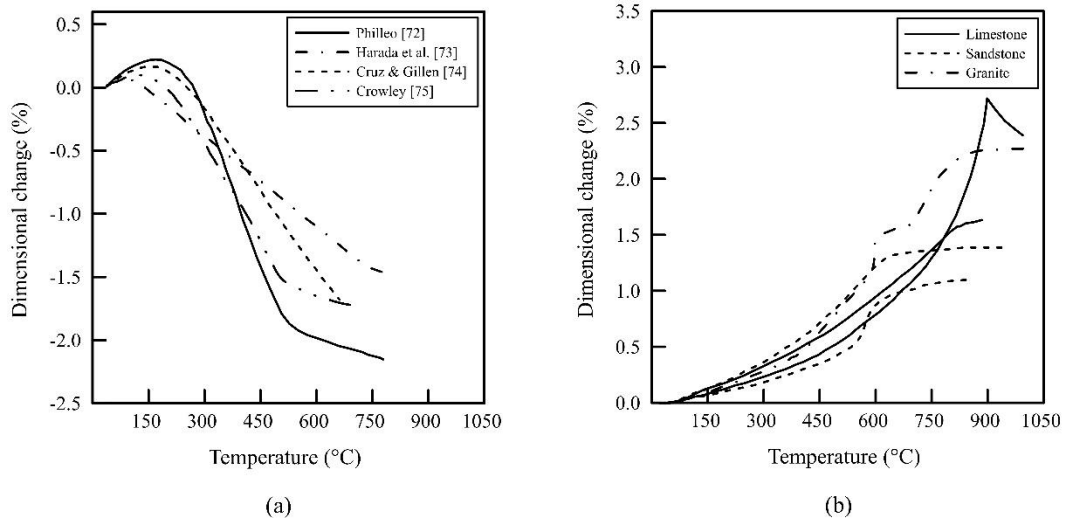


Figure 2.1 – Dimensional change of (a) Portland cement paste and (b) various rock types exposed to elevated temperatures (adapted from Bazant & Kaplan [69])

The mineralogical composition of the cement paste is also affected by temperature, mostly due to the dehydration and decarbonation of hydrated products. The free and the physically absorbed water present in the cement paste evaporates completely for temperatures around 105 °C, and the chemically bond water begins to evaporate after this temperature [77]. The AFt/AFm phases dehydrate in the initial range of heating, for temperatures between 110 °C and 150 °C [78]. This dehydration process results in the amorphization of ettringite and is one of the main reasons behind the use of solvent-exchange methods to stop the hydration of cement pastes instead of elevated temperatures or vacuum drying [79].

The dehydroxylation and loss of interlayer water of calcium silicate hydrate (C-S-H) occurs over a wide range of temperatures. The C-S-H begins to decompose into nesosilicates in the form of belite (C_2S) for temperatures of 150-200 °C, however with a significantly different morphology than the silicates found in anhydrous cement paste [68]. Additionally, the inherent crystal structure of this nesosilicates results in variable Ca-Ca bond length [80], which may significantly affect the rehydration kinetics due to differences in terms of hydraulic activity. For temperatures greater than 600 °C, the decomposition of C-S-H results in the formation of wollastonite ($CaSiO_3$) and the metastable merwinite, larnite, and

melilite [68,71,81]. The dehydration of portlandite occurs at ~ 450 °C and the decarbonation of CaCO_3 occur for temperatures of ~ 600 °C [78].

As temperature increases, the specific surface area of hydration products reduces and pore structure becomes coarser [82,83]. This leads to increase in capillary pore size and the generation of fine cracks. Also, microcracks formation is the main factor affecting permeability evolution, while changes in capillary pore size is less influent [84]. Therefore, the elevation of temperature increases porosity and pore size of the cement paste as a result of the water evaporation and the chemical changes in the hydrated products [71]. Moreover, a total loss of water of hydration is verified for temperatures greater than 800 °C [85–89].

The knowledge regarding the effect of temperature on the physical and mechanical properties of steel may be considered consolidated in current literature, especially regarding parameters of grain-size changes, thermal oxidation, and recrystallization processes [90–93]. It is known that cold-drawn steel experiences a recrystallization and grain-growth processes at temperatures ~ 450 °C [94], which is a process known to affect the tensile strength and ductility of steel. Additionally, the thermal oxidation process begins at ~ 500 °C [90] and may reduce the cross-sectional area of steel, which is a factor of paramount importance in case of steel fibers that have relatively reduced cross-sectional area. Although these metal related processes are well-established, the effect of temperature on the steel fibers and the fiber-matrix ITZ have not been sufficiently investigated in literature, especially regarding these metal-related processes, the microstructural changes in the fiber-matrix ITZ, and the overall bond-slip behavior [80,95–98]. The study of the changes that occur with steel fibers, the fiber-matrix ITZ, and the bond-slip behavior when embedded in cementitious matrix is required in order to improve the current scientific understanding of the effects of temperature on SFRC. Based on the discussions of this subchapter, a brief summary of changes in the physical, chemical, and mineralogical properties of SFRC with temperature is presented in Table 2.2.

Table 2.2 – Changes in the physical, chemical, and mineralogical properties of SFRC with temperature

Thermal related process	Description
Phase transformations	As temperature increases, the matrix exhibits loss of free water at about 105 °C; dihydroxylation and loss of interlayer water of Calcium Silicate Hydrate (C-S-H) over a wide range of temperatures ($T \geq 50$ °C); decomposition of calcium hydroxide at ~450 °C; reversible crystal transformation of quartz from the α -trigonal form to the β -hexagonal form at ~573 °C; and total loss of water of hydration for temperatures greater than 800 °C [85–89].
Pore structure evolution	As temperature increases, specific surface of hydration products reduces and pore structure becomes coarser [82,83]. This leads to increase in capillarity pore size and the generation of fine cracks. Also, microcracks formation is the main factor affecting permeability evolution, while changes in capillary pore size is less influent [84]. Therefore, the elevation of temperature increases porosity and pore size of the cement paste as a result of the water evaporation and the chemical changes in the hydrated products [71].
Thermo-hygro-chemo-mechanical processes	These processes are related to physical, thermal, mechanical and chemical changes due to temperature exposure. Examples of this are temperature gradients that lead to thermal related stresses, the multiphase transportation of water in the cementitious matrix, thermal spalling, and cement paste shrinkage [69].
Fiber related processes	Fiber reinforcement is affected by temperature as a function of the material properties. For example, cold drawn steel fibers recrystallize at ~450 °C, and synthetic fibers melt and ignite at much lower temperatures (e.g. polypropylene melts at 170 °C and ignites at 400-500 °C) [94].

2.2.2 Bond-slip behavior of fibers

The bond properties between the steel and the cementitious matrix are of paramount importance to the effectiveness of SFRC, especially regarding its tensile and post-cracking behavior. In fact, the behavior of SFRC is fundamentally governed by the stress transfer mechanism that results from the fiber-matrix interfacial bond. The adhesion/chemical bond between the fiber and matrix results in an additional region between the steel fiber and the cementitious matrix, which is called the interfacial transition zone (ITZ). The properties of this zone strongly influences the capacity of fibers to transfer the applied stresses [99], which also results in a significant influence to the tensile response of the SFRC [100]. Figure 2.2 illustrates the ITZ between the steel fiber and the cementitious matrix.

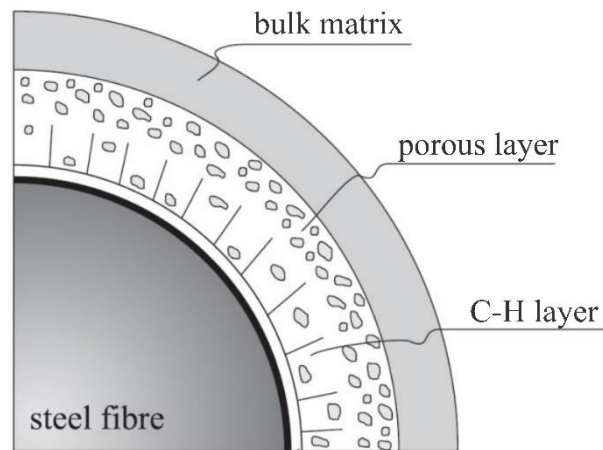


Figure 2.2 – Illustration of the ITZ between steel fiber and the cementitious matrix [101]

The effect of temperature on the bond properties of steel fibers have been studied by a limited number of authors. According to the author knowledge, Abdallah [102] was one of the pioneers in investigating the effect of temperature on the bond-slip behavior of steel fibers during his Ph.D thesis in 2017. The investigation was conducted considering a temperature range of 20-800 °C, being the variables of interest the class of concrete and fiber geometry. A few articles were extracted from the thesis and published in peer reviewed journals [95–97]. Later, Ruano et al. [80] evaluated the bond-slip behavior of straight and hooked-end steel fibers after exposure to temperatures ranging between 20-475 °C. Lastly, Zhang et al. [103] evaluated the effect of thermal shrinkage and thermal incompatibility on the bond-strength of straight and hooked-end steel fibers in concretes with variable f_c .

Based on these relevant literature results, the results were compiled and the coefficient of change in the bond properties was calculated as:

$$k_b = \frac{\tau_{b,T}}{\tau_{b,25^\circ\text{C}}} \quad (1)$$

where k_b is the coefficient of change in bond-strength (dimensionless); $\tau_{b,T}$ is the bond strength at temperature T; and $\tau_{b,25^\circ\text{C}}$ is the bond strength at room temperature. The results that correlate k_b as a function of temperature are presented in Figure 2.3, based on literature results [80,96,97,103].

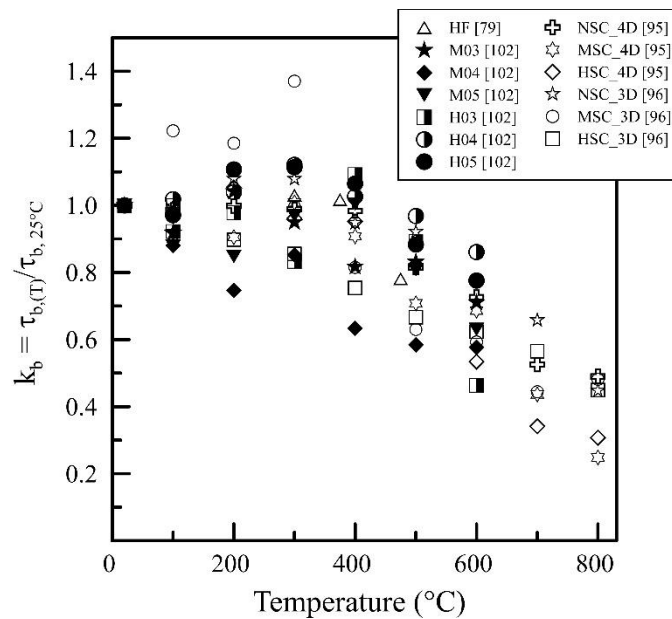


Figure 2.3 – The effect of temperature on the k_b of hooked-end steel fibers

The results in the range $25^\circ\text{C} \leq T \leq 400^\circ\text{C}$ show that k_b is between ~ 0.8 and ~ 1.2 in the majority of cases. In this initial range, some authors report that the changes in bond strength are not statistically significant, and that a significant decrease is verified only for $T \geq 600^\circ\text{C}$ [80,95–97]. These results may be related to the intrinsic variability of the pullout test methodology employed in most of these studies, which was based on a single-sided embedded test containing one single fiber. Even though this setup is widely employed in room temperature conditions, it is known for its low precision measurements and the considerable variability of results, which are expected to worsen after heat exposure. In this context, questions may arise regarding the effect of the test method on the non-significance of the bond-slip results.

Additionally, very few studies discussed the factors that contribute to the non-significance of even increase in k_b for early temperatures. Zhang et al. [103] have noticed that the shrinkage of the cement paste induces a clamping effect that enhances the fiber-matrix bond-strength for $T \leq 300$ °C. However, this is not the only factor of influence in this process. The oxidation of steel fibers and the mineralogical changes in the ITZ composition may influence the fiber-matrix bond properties are of paramount importance and have not yet been investigated. Therefore, the assessment of the bond-slip behavior of steel fibers as a function of temperature requires further study employing a more stable pull-out methodology as well as the definition of changes in the fiber-matrix ITZ. A better understanding regarding the changes in the ITZ and the bond-slip properties of steel fibers is forward step for the development of engineering procedures focused on enhancing the SFRC behavior under temperature, which may benefit the mechanical properties of the composite. In this sense, the following subsections seek to discuss the effect of temperature on the compressive and tensile parameters of SFRC.

2.2.3 Compressive parameters

The thermal-related changes in physical, chemical, and mineralogical properties of the cementitious matrix result in changes in the compressive strength and elastic modulus of the composite [25–32]. In this sense, literature results evaluating the effect of temperature on SFRC compressive strength were compiled [26,33,104–106] and the relative compressive strength (k_c) was calculated as:

$$k_c = \frac{f_{c,T}}{f_{c,25^\circ C}} \quad (2)$$

where k_c is the relative compressive strength (dimensionless); $f_{c,T}$ is the compressive strength at temperature T ; and $f_{c,25^\circ C}$ is the compressive strength at room temperature. Similarly, the changes in elastic properties were evaluated as:

$$k_{Ec} = \frac{E_{c,T}}{E_{c,25^\circ C}} \quad (3)$$

where k_{Ec} is the relative elastic modulus (dimensionless); $E_{c,T}$ is the elastic modulus at temperature T ; and $E_{c,25^\circ C}$ is the elastic modulus at room temperature. The literature results that correlate k_c and k_{Ec} as function of temperature are presented in Figure 2.4.

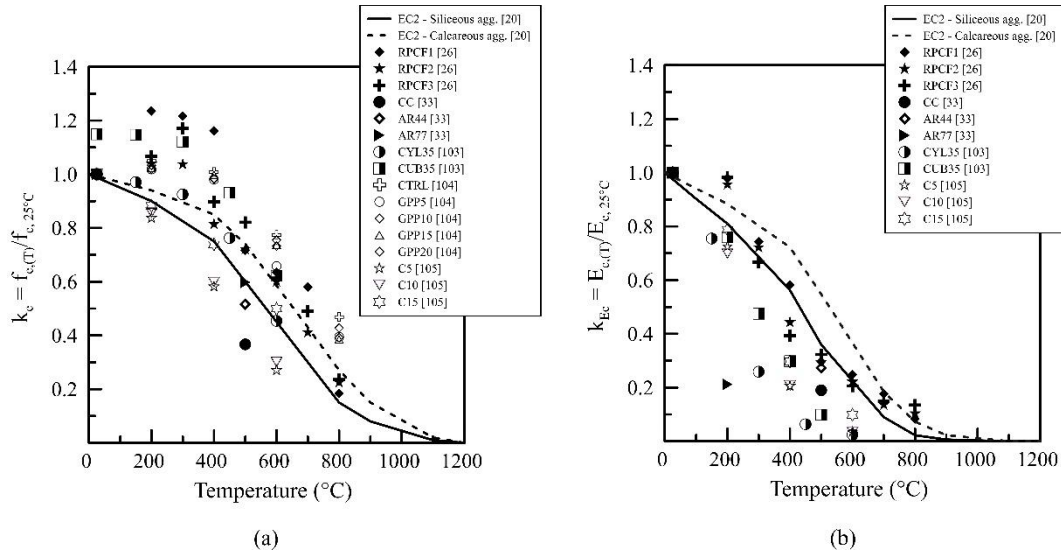


Figure 2.4 – Changes in (a) compressive and (b) elastic properties of SFRC as a function of temperature

Based on the results collected, the f_c of the SFRC is either not affected or exhibits a slight increase for temperatures up to ~ 100 °C. A reduction following a relatively linear trend can be observed for temperatures between 200 °C and 800 °C, while almost all compressive strength is lost for greater temperature values. The reductions in terms of f_c are considerably influenced by the decomposition of hydrated phases, mismatch between the expansion/shrinkage of paste and aggregates, the reversible transformation of quartz at 573 °C, and the temperature gradients that arise during heating [69]. Another important aspect is that the shape of specimens considerably influence the f_c results, since the thermal-related reductions in f_c using cylindrical specimens are greater than those obtained for cubic specimens [69,104]. This may be a result of the reduced height-diameter (h/d) ratio of cubic specimens, which reduces the sensibility to the thermal-related changes in concrete. In this sense, this may be one of the factors influencing the experimental results under the EC2 curve presented in Fig. 2.4a. Other variables of influence such as thermal stabilization period, aggregate type, moisture condition, sensibility of the test apparatus, cooling rate, and the amount of fibers used may justify the differences in literature results.

Even though a reduction trend in f_c is verified, the increase in the steel fiber content have proven to mitigate these reductions [107,108]. This mitigation effect is related to the crack bridging capacity of fibers, which benefits even the compressive strength of the composite in post-heating scenarios. The results in literature also point out to the negligible influence of fiber content on the E_c of the composite after temperature exposure [108]. Overall, the reductions in E_c are greater than those

observed for f_c , which is associated with the pronounced decomposition of hydrated phases, coarsening of pore structure, and the reduction in the total volume of solids in the paste [36,83]. In cases that employ macro-synthetic fibers as the main reinforcing mechanism, a study conducted within the research group and led by the author of this thesis have shown the absence of macro-synthetic fiber reinforcement up to ~12 cm from the surface affected by hydrocarbon fire [68]. Moreover, it is important to remind that these fibers ignite and melt at ~170 °C, resulting in voids that increase the porosity and that reduce the f_c and E_c values [36,68].

2.2.4 Tensile parameters

At room temperature, the SFRC matrix tensile strength (f_{ft}), the service limit state (SLS) post-crack tensile strength (f_{fts}), and the ultimate limit state (ULS) post-crack tensile strength (f_{ftu}) are often determined using bending tests [13]. However, bending tests tend to require relatively large specimens and specific testing apparatus that may not be readily available, limiting its applicability. In this sense, indirect tensile strength tests are developed and used for the same purpose – such as the double-punch test (DPT) [109], the Montevideo test (MVD) [110], and the double-edge wedge splitting test (DEWS) [111].

The applicability of the aforementioned test methods to the post-heat condition must be considered with caution. Studies focused on evaluating the applicability of the bending, DPT, MVD, and DEWS tests are fairly limited in literature. Although results are scarce, the bending test is the most commonly employed method to assess the effect of temperature on f_{ft} and f_{ftu} of SFRC [29,33–35]. When compared to the bending test, the double-punch test is a practical alternative – especially given its reduced specimen size, lower standard deviation, and the simpler testing apparatus required [112]. However, a recently published study shows that the use of the DPT faces a drawback associated with the puncture interaction between the piston and the deteriorated matrix during the test [36]. This puncture/frictional interaction may be confused with the bridging effect of fibers and the test results may be misinterpreted, especially for greater temperature values.

Alternatively, the split-cylinder test is successfully employed to determine the f_{ft} of brittle materials, such as mortars and plain concrete, at room temperature. However, its applicability to determine the tensile properties of SFRC is questionable

because, as crack propagates, the crushing and grinding of the specimen occurs – which dissipates energy and influences the post-crack results. Therefore, the use of the split-cylinder test is inadequate to determine the post-crack tensile properties of fiber reinforced concrete at room temperature and may worsened in post-heating conditions due to the deterioration of the composite. As a mean to overcome the drawbacks of the split-cylinder test, the DEWS test is conceived in a similar manner, however containing two triangular grooves and a notch in opposite sides of a specimen [111]. These grooves and notches have the purpose of (1) reducing the piston-specimen frictional and crushing interaction during the plastic deformation phase; and (2) stimulating the crack initiation in the tip of the notches. Although this test method is relatively new, it has shown promising results in determining the tensile properties of SFRC at room temperature [111,113] and have not been sufficiently investigated for post-heating specimens up to the publication of this thesis.

In this context, studies focused on investigating the influence of temperature on the tensile properties of SFRC by means of bending tests [26,33,34,105,106,114] and the DEWS test [108] have been identified in literature. The relevant literature results were compiled and the relative tensile strength was calculated as:

$$k_{ft} = \frac{f_{ft,T}}{f_{ft,25^{\circ}C}} \quad (4)$$

where k_{ft} is the relative matrix tensile strength (dimensionless); $f_{ft,T}$ is the matrix tensile strength at temperature T; and $f_{ft,25^{\circ}C}$ is the matrix tensile strength at room temperature. Similarly, the changes in the post-crack tensile properties at the ULS were evaluated as:

$$k_{ftu} = \frac{f_{ftu,T}}{f_{ftu,25^{\circ}C}} \quad (5)$$

where k_{ftu} is the relative ULS post-crack tensile strength (dimensionless); $f_{ftu,T}$ is the ULS post-crack tensile strength at temperature T; and $f_{ftu,25^{\circ}C}$ is the ULS post-crack tensile strength at room temperature. Figure 2.5 illustrate the relative f_{ft} and f_{ftu} results in literature compared to the Eurocode [20] and the CNR-DT 204 [22] guidelines.

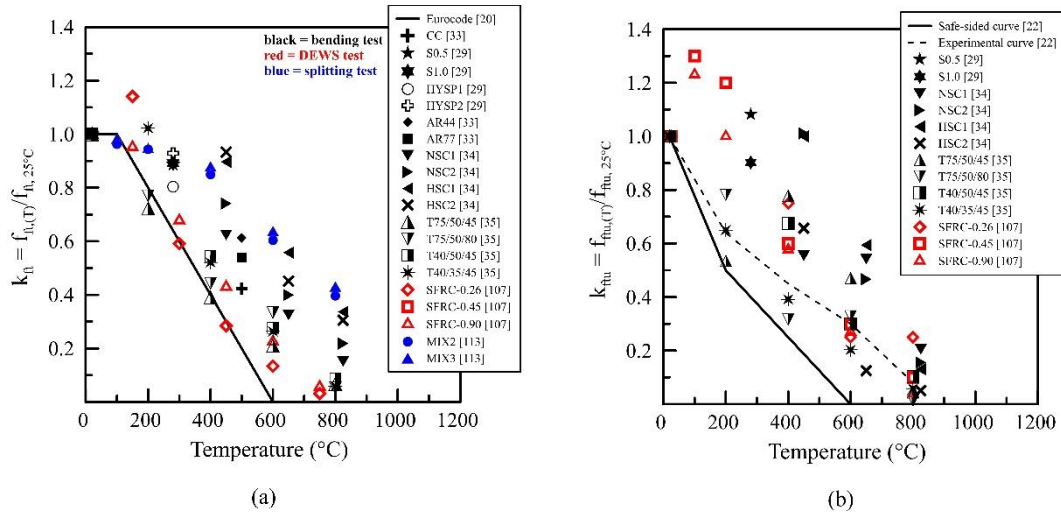


Figure 2.5 – Effect of temperature on the (a) f_{ft} and (b) f_{ftu} of SFRC

Overall, the results show that f_{ft} reduces faster than the f_c when plain concrete is exposed to elevated temperatures, which is in line with classical literature [13,69]. Moreover, the reductions in k_{ft} for SFRC seems to agree well with the analytical curve for plain concrete provided by the Eurocode (Fig. 2.5a). This confirms that reductions in f_{ft} may be considered equivalent between plain concrete and SFRC for design purposes, although recent studies show that the increase in fiber content mitigates the reductions in terms of k_{ft} [108]. The literature results employing the split-cylinder test seems to present lower reduction values than those obtained by bending and DEWS test. In average, a reduction of $\sim 60\%$ in f_{ft} is obtained by means of the split-cylinder test, while a reduction of $\sim 80\%$ is obtained by means of bending test. This may be considered an initial evidence showing the inadequacy of the split-cylinder test applied to SFRC exposed to elevated temperatures.

Regarding the reductions in k_{ftu} , the Italian guideline CNR DT 204 provides an analytical curve to describe the changes in f_{ftu} with temperature. The literature results analyzed agree well with the safe-sided analytical curve provided by the Italian guideline, however the experimental curve do not describe all the data. Regarding the f_{ftu} , the SFRC post-crack parameters are highly dependent on the mechanical properties of the fiber-matrix ITZ, as well as the properties of the reinforcing fibers [6]. In this sense, recently published results show that the steel fibers are capable of providing stability and enhanced post-crack behavior after heat exposure [28–32]. Some of the studies even show that the post-crack flexural strength of SFRC may increase up to temperatures of 400 °C [28,30,32] before significantly decreasing for higher temperatures. This behavior may be associated with the minor

or even beneficial effects of temperature on the bond-slip behavior of steel fibers up to ~450 °C [80,95–97,115].

Another relevant aspect is that alternative fibers are found in the market that may be successfully employed in plain concrete to enhance the tensile properties, such as polypropylene (PP) fibers [116]. However, the characteristics of each fiber type under temperature must be taken into account. The use of PP fibers as main reinforcement in concrete has a main concern related to the occurrence of fire events. A small-scale study conducted by the author of the thesis within the research group have shown that a uniaxial hydrocarbon fire exposure during 120 min results in the absence of flexural capacity in EN-14651 prismatic specimens reinforced with PP fibers [68]. Therefore, the use of fibers for structural purposes must take into account the accidental fire loads considering the particularities of the fiber type.

It is important to highlight that a limited amount of studies are found in literature, especially those that employ an adequate test methodology. The literature results that employed split-cylinder test to evaluate the post-crack parameters of SFRC were excluded from this analysis given that the test method was not conceived to evaluate the post-crack parameters of SFRC and have limitations for this specific purpose. In this context, this thesis is motivated to identify and evaluate the applicability of the DEWS test to SFRC exposed to elevated temperatures, given the promising setup of the test.

2.3 THE EFFECT OF FIRE ON SFRC TUNNEL LININGS

As previously discussed, the occurrence of fire causes deleterious effects in the physical, chemical and mechanical properties of the SFRC, while several variables still require more in-depth investigation. Although the previously discussed thermal-related parameters are extremely valuable, they do not account for the entirety of the variables that arise during a fire event. Complex thermal-related variables such as the differential thermal-field along the TBM tunnel, the longitudinal and lateral restraint of segments, redistribution of internal forces, the influence of joints, thermal expansion of the tunnel, and the coactions generated by soil-structure interaction are also parameters of influence [117]. In this sense, several experimental and numerical studies in literature have focused on some of these complex problems in TBM tunnels [118–120]. The next subsections seek to briefly summarize the state of the knowledge regarding the parameters of influence during a fire event in a TBM tunnel lining.

2.3.1 Fire curve and thermal field

The definition of a fire curve to be adopted for the engineering of tunnels involves the definition of a fire type and the distribution of temperatures affecting the structure in the time and space domains. The most commonly employed fire curve is the ISO 834 fire curve, which is a cellulosic fire curve conceived for surface buildings [121]. The ASTM suggests the use of the ASTM E 119 fire curve, which has a heating regime comparable to the ISO 834 fire curve [122]. In this context, it is clear that the particularities of a tunnel fire are not properly represented by these fire curves, which may be employed only in less intensive or mild tunnel fire scenarios. Therefore, fire curves with faster development of temperatures and greater temperature values have been employed to simulate fires in underground spaces, such as the hydrocarbon fire curve (HFC) and the RWS fire curve [63,123]. This is required because fire events in tunnels tend to be more severe than surface fires due to the reduced compartment dimensions, unfavorable ventilation conditions, and the amount and type of combustible materials involved [124].

The exposure of SFRC tunnels to fire events results in a non-linear distribution of temperatures – with greater temperature values closer to the intrados and lower at the extrados. This occurs because of the low thermal conductivity of concrete and results in considerable temperature gradients. Also, the thermal conductivity of the surface layers of concrete is known to reduce even further as temperature increases [70]. Figure 2.6 illustrates the thermal-field induced by a unifacial HFC on macro-synthetic fiber reinforced concrete (MSFRC) based on the work of Serafini et al. [68]. It is possible to observe that temperatures as high as ~600 °C at a distance of 3 cm from the face exposed to fire, and that temperature gradients are greater at the beginning of the fire [107].

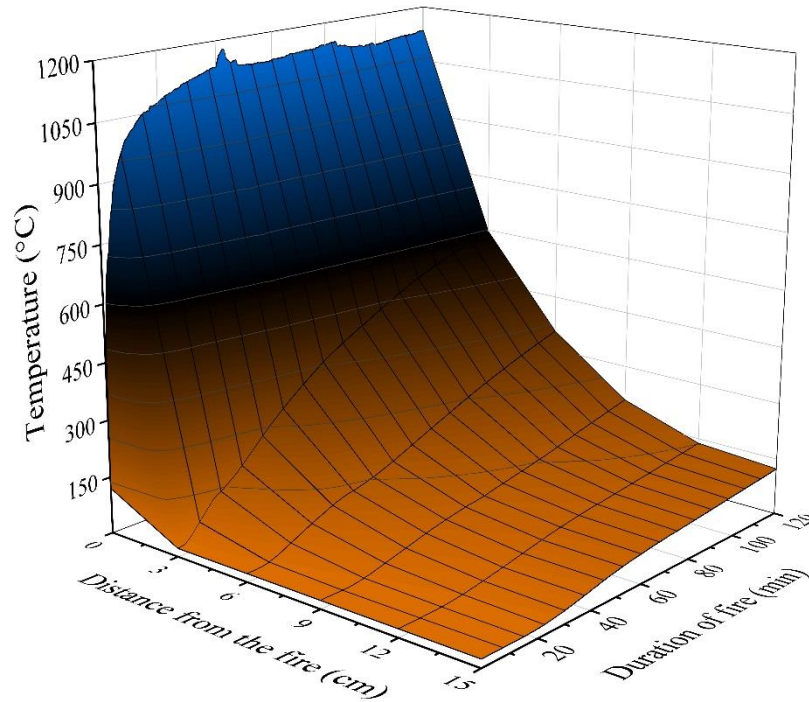


Figure 2.6 – Thermal-field in concrete elements affected by uniaxial fire [68]

In fire scenarios, explosive spalling may occur due to the generation of internal pressures caused by the steam water inside the concrete. This occurs due to the limited diffusion capacity of concrete and is further aggravated for concretes with low porosity/permeability [125]. Thermal spalling negatively affects the sectional capacity of elements and also worsen the thermal-field in the section, since deeper layers become directly exposed to the fire. To address this issue, the proper dosage of concrete using micro-synthetic fibers have shown to be capable of mitigating the occurrence of thermal spalling in laboratory scale tests. The fundamental concept is that the deterioration of micro-synthetic PP fibers leads to the formation of micro-conduits inside the composite that reduce the internal pore pressure caused by the evaporation of water [126]. For example, PP melt and ignite, respectively at ~ 170 and ~ 450 °C [94], which allows for micro-conduits to be created in the cementitious matrix. Even with this consideration, the study of micro-synthetic PP fibers is not within the scope of this thesis.

2.3.2 Thermal stresses and bearing capacity

Fire exposure induces thermal strains (ϵ_{cT}) that are non-linearly distributed along the depth of the cross-section and do not comply with the kinematic requirements of the total strain field (ϵ_c) imposed by the Navier-Bernoulli hypothesis [107]. This results in the induction of mechanical strains (ϵ_m) and, thus, thermal

stresses that arise as a countermeasure to the incompatible strains caused by the fire event [127]. These stresses can be calculated in a conservative manner by disregarding thermal creep in the strain compatibility equation, described as:

$$\varepsilon_m = \varepsilon_{cg} + \chi z - \varepsilon_{cT} \quad (6)$$

where ε_{cg} is the strain at the center of gravity; χ is the sectional curvature; and z is the position of the neutral axis. Therefore, it is possible to compute the thermal stresses based on the strain compatibility, the rotary and translation stability equations, and considering the non-linearity of the stress-strain curves of the material [107,127]. Figure 2.7 illustrates the strain field incompatibility and the consequent thermal stresses generated during an uniafacial fire exposure. These self-equilibrating thermal stresses are one of the factors responsible for the cracking of elements when exposed to fire, paired with the deterioration and dehydration processes that have been discussed in Section 2.2.1.

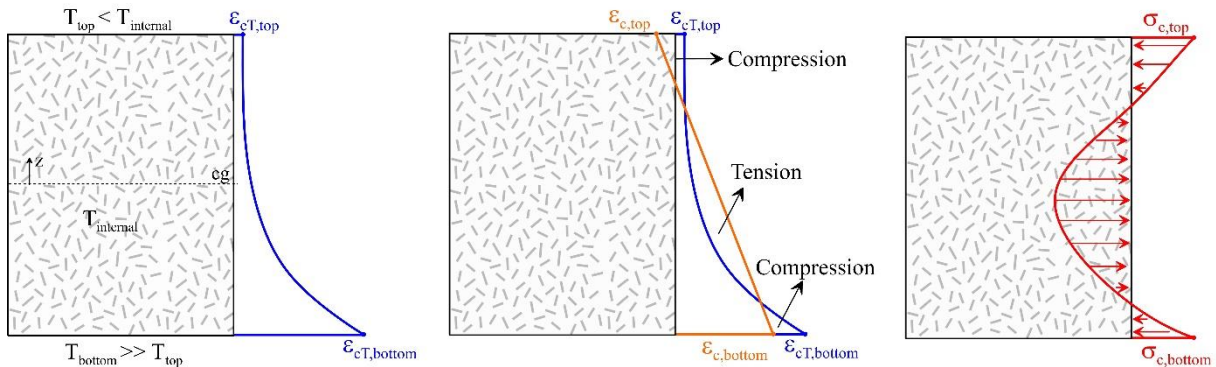


Figure 2.7 – Thermal stresses generated during an uniafacial fire exposure

More than that, the increase in internal temperatures result in the reduction of the mechanical contribution of the concrete layers to the sectional bearing capacity [38]. This, which directly affects the bearing capacity of elements. Several approaches have been developed to evaluate the changes in bearing capacity of RC sections, which may be used as basis to develop solutions applied to SFRC [107]. First, the thermal-field in the concrete section is determined. The thermal equilibrium between rebars and the surrounding concrete is achieved in most cases, which supports methods that disregard the presence of rebars during the thermal analysis. However, sections containing densely-spaced reinforcement and small concrete cover this assumption may render the analysis inadequate.

One of the simplified methods of sectional analysis is based on tabulated data presented in detail in Section 5 of the Eurocode [20]. This tabulated data is conceived based on experimental and theoretical background in literature, which means that a quick approach to the problem can be reached by the designer. However, the applicability of this method is limited to ordinary concrete and the ISO 834 fire curve. This results in the inapplicability of this method for more advanced and recent developments in civil engineering, especially applied to SFRC and tunnel linings.

Another simplified method that may be employed is the “isotherm” method. This methodology is based on the assumption that concrete layers that reach temperatures of 500 °C or above are completely damaged, providing no overall contribution to the sectional bearing capacity. Although the assumptions are reasonable, the applicability of this method to SFRC may severely punish the material’s properties, especially those related to the post-crack parameters. Also, the “isotherm” method was conceived and validated considering sections subjected to simple bending ($N = 0$) and its applicability becomes extremely conservative when used for sections subjected to excentric axial forces and for longer durations of fire [128].

The incremental-iterative method (*i.e.* “exact” method) is a method that considers the cross-section as a layered composite material, in which the thermal and mechanical properties of each layer are defined by the thermal field. The moment-axial force (M-N) interaction envelopes are computed based on the maximum temperature reached locally, the temperature-dependent stress-strain curves of the materials that compose the layers, and the rotary and translational equilibrium equations. The aforementioned process results in moment-axial force couples that define the M-N domain for a given section. This methodology yields more realistic results than the simplified “tabulated data” and “isotherm” methodologies at the cost of a rather time consuming procedure. Figure 2.8 illustrates the differences in M-N interaction envelopes computed by the “isotherm” and the “exact” method according to Bamonte and Meda [128]. The authors highlighted that the area under the M-N envelope determined using the “isotherm” method is roughly half of the area obtained by the “exact” method for greater fire durations.

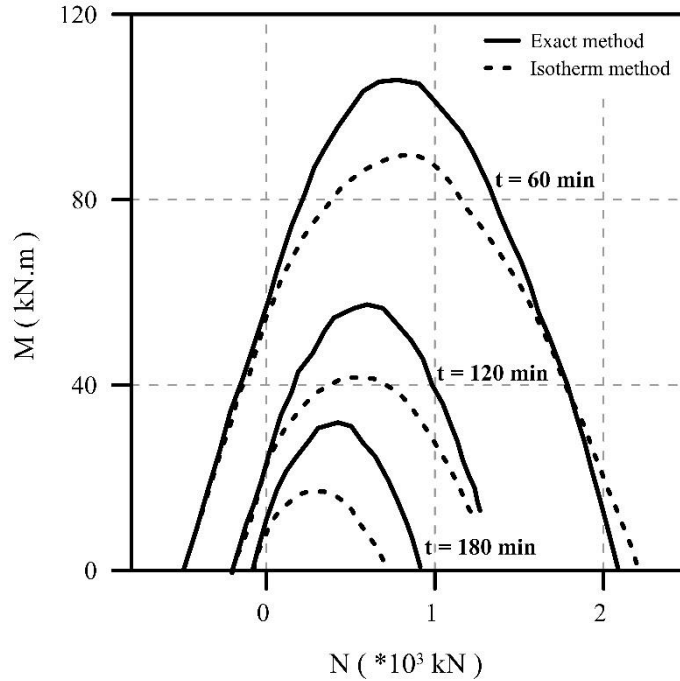


Figure 2.8 – Differences between the isotherm and exact methods (Bamonte & Meda [128]).

In this sense, a few relevant studies regarding the fire analysis of TBM tunnels can be mentioned. Lilliu and Meda [117] evaluated the effect fire events can impose in RC tunnel linings using a commercial nonlinear finite element code, called DIANA. First, the authors modelled the excavation of the tunnel to determine the soil pressure stresses and, later, imposed the fire conditions to the tunnel. The results obtained showed that a reduction of stiffness occurs due to the cracking caused by fire exposure and that the tunnel structure remained stable after $t = 120$ min. These conclusions, however, provide limited amount of informations about the influence of design parameters (*e.g.* segment thickness, position of rebars, class of concrete) on the capacity of the tunnel.

Di Carlo et al. [38] proposed a thermo-mechanical model to evaluate the effect of different fire curves and design parameters the M-N interaction envelopes of FRC sections. The thermal model was solved using the finite difference method applied to the Fourier heat transfer differential equation. The mechanical model was conceived based on the stress-block constitutive law provided by the *fib* Model Code 2010 [13] and the degradation of the mechanical properties based on the Eurocode [20] and the CNR DT-204 [22]. Results show that the compressive strength and the height of the section considerably influences the M-N interaction envelopes for FRC sections, while changes in the ULS post-crack tensile strength are not as significant for the bearing capacity.

Although some numerical studies regarding the effect of fire on RC and FRC tunnel structures are reported, a limited amount of studies focused on evaluating hybrid solutions (*i.e.* RC-FRC) is found in literature. Moreover, the effect of thermal spalling on the bending capacity of tunnels have not been investigated according to the authors knowledge. This denotes that more studies are required in order to provide parameters for the safe and reliable fire design of tunnels made with RC-FRC and FRC sections.

CHAPTER 3.

METHODOLOGY

This chapter has the objective of presenting the materials used and the methodology adopted for the investigation conducted in this thesis.

3.1 CHARACTERIZATION OF MATERIALS

The work conducted in this thesis followed the concrete mix design similar to the one used for the production of the precast segments for the tunnel linings of Subway Line 6 in São Paulo, which is described in Table 3.1. The w/cm ratio was kept constant at 0.39 and silica fume was used as supplementary cementitious material at a content of 5.5% of the cement mass. The steel fiber content was 0.45% of the total volume (35 kg/m^3) and micro-synthetic fibers were added in a content of 0.09% of the total volume (0.8 kg/m^3) to reduce the risk of explosive spalling.

Table 3.1 – The complete mix design used to produce 1 m^3 of SFRC

Materials	Dosage (kg/m^3)
Cement CEM I 52.5R	400
Silica fume Elkem 920-U	22
Tap water	165
Siliceous river sand	403
Artificial granite sand	269
Coarse granite aggregate – d_{max} : 19 mm	770
Coarse granite aggregate – d_{max} : 9.5 mm	330
Superplasticizer GCP ADVA Cast 525	3
Micro-synthetic fiber - Neomatex FireX	0.80
Hooked-end steel fiber – Dramix 80/60-BG	35

A type I Portland cement (CEM I 52.5R) was used as binder and silica fume type Elkem 920-U with 98% SiO₂ was used as pozzolanic material in this study. The particle packing was promoted by the use of river and artificial sand as fine aggregates and two coarse granite aggregates. The rheological behavior of the mix was modified by using polycarboxylate-based superplasticizer specific for precast elements, GCP ADVA Cast 525. The main concrete reinforcement used cold-drawn hooked-end steel fibers (Dramix 3D 80/60BG) since it is a commonly used fiber for structural applications. Polypropylene microfibers (Neomatex FireX) were used to mitigate the risk of explosive spalling during heat exposure of SFRC specimens. Table 3.2 shows the manufacturer data for steel fibers and micro-synthetic fibers used in this study.

Table 3.2 – Manufacturer data for steel fibers and micro-synthetic fibers

Properties	Steel fiber	Antispalling fiber
Length (mm)	60	12
Diameter (mm)	0.75	0.03
Aspect ratio (l/d)	80	400
Specific surface area (m ² /kg)	3.45	147
Specific weight (kg/m ³)	7850	910
Melting point (°C)	~1370	165
Tensile strength (MPa)	1225	Not provided
Young modulus (GPa)	210	Not provided

3.1.1 Grained materials sampling

The process of sampling the grained materials was conducted using a rotary sample divider and a manual sampler, as shown in Figure 3.1. The sampling process aims to obtain a sample of the grained materials that are representative in relation to the total amount of material (population). The process begins with the homogenization of the total mass of material, followed by sampling the population using the rotary sample divider (Fig. 3.1a). This first step had as objective to obtain a representative smaller sample of the grained materials and allow the use of a manual sampler (Fig. 3.1b). After the sampling process was conducted, the grained

materials were analyzed regarding the particle size distribution, real density, specific surface area, and mineralogical composition.



Figure 3.1 – Illustration of the (a) rotary sample divider (b) manual sampler

3.1.2 Particle size distribution

The determination of the particle size distribution, fineness modulus, and characteristic parameters followed the methodology presented in Figure 3.2. The representative samples were taken to a mechanical sieve for gradation test and particles were separated in two groups: Group A with particles sized greater than 150 μm and Group B with particles sized smaller than 150 μm .

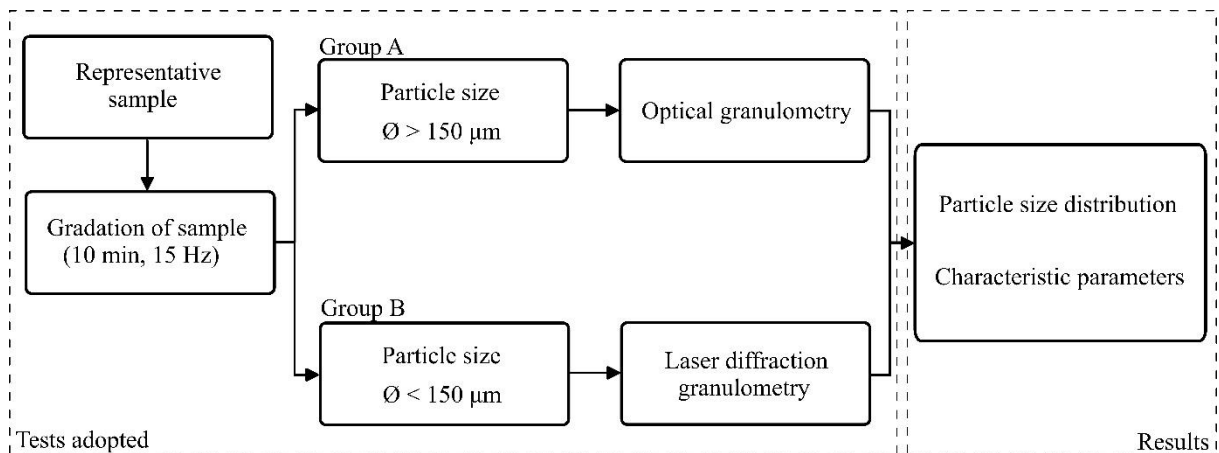


Figure 3.2 – Procedure adopted to determine the particle size distribution of grained materials

Particles with $\text{Ø} > 150 \mu\text{m}$ were taken to Optical Granulometer QICPIC – Sympatec to determine particle distribution by Dynamic Image Analysis (DIA) using M7 (range from 10 μm to 3410 μm) and M9 (range from 3410 μm to 33792 μm) lenses and dispersion by gravity. This equipment uses a pulsed light source paired

with a high resolution, high-speed camera that captures particle projections (optically frozen) with a frequency of up to 500 frames per second. Later, algorithms evaluate millions of particle images to generate statistically relevant results and data regarding particle distribution.

Particles with $\varnothing < 150 \mu\text{m}$ were analyzed by a Laser Diffraction Granulometer Helos – Sympatec with detection range from $0.1 \mu\text{m}$ to $350 \mu\text{m}$. Around 20 mg of dry powder was added to a Becker with 80 mL of water and mixed at 1000 rpm with a high-speed mixer RW20 (IKA) during 60 s. The suspension was transferred to the equipment and ultrasonic dispersion was used during 2 min before acquiring data. The principle between this equipment is based on the interaction between particles and a laser beam that results in the diffraction of the laser light. The acquisition of the intensity distribution of the diffracted light is performed with a multielement photo-detector and data is evaluated by an algorithm to determine particle size. Figure 3.3 illustrates the particle size distribution and Table 3.3 shows the characteristic values, fineness modulus (FM), and the specific surface area of the grained materials used in this doctoral thesis.

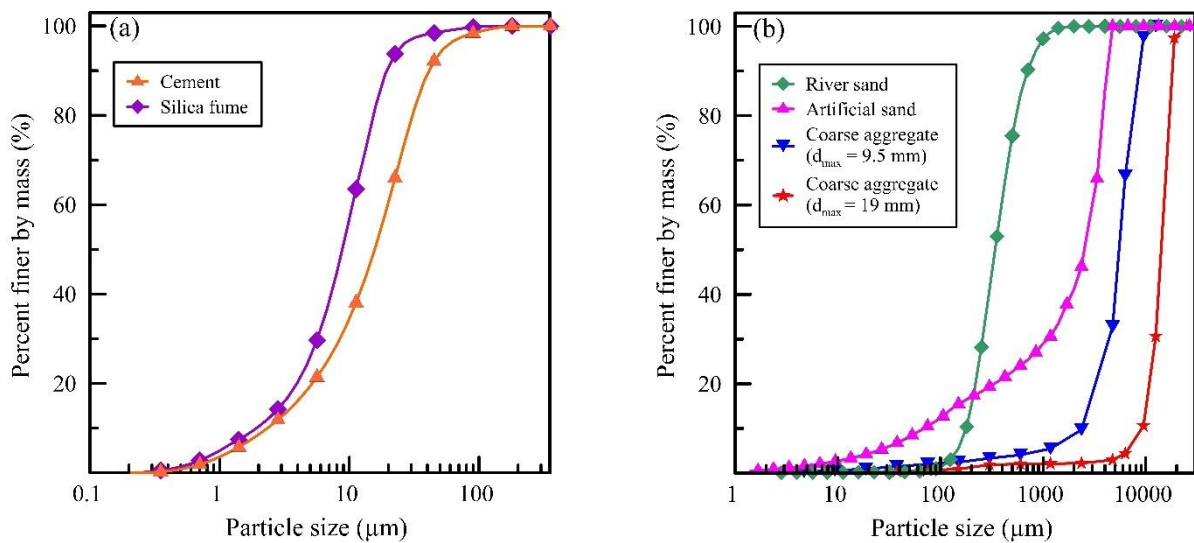


Figure 3.3 – Particle size distribution for: (a) cementitious materials, and (b) fine and coarse aggregates

Table 3.3 – Results of d_{10} , d_{50} , d_{90} , fineness modulus, and specific surface area of materials

Materials	d_{10} (μm)	d_{50} (μm)	d_{90} (μm)	FM
Cement CEM I 52.5R	2.3	15.7	41.5	-
Silica fume	1.9	8.9	19.5	-
River sand	177.8	341.1	705.7	1.2
Artificial sand	69.0	2,580	4,230	3.6
Coarse aggregate d_{max} : 9.5 mm	2390	5,540	8,720	5.5
Coarse aggregate d_{max} : 19 mm	9,210	14,390	18,280	6.8

3.1.3 Real density and specific surface area

The real density of grained materials was determined by helium picnometry using a Quantachrome MVP 5DC equipment. This equipment is able to determine the volume of solids of a sample by measuring the variation of gas pressure in relation to a calibrated volume. The real density is calculated as the ratio between the mass of the sample and the volume of solids determined by picnometry.

The specific surface area was determined by gas/vapor adsorption with application of Brunauer-Emmett-Teller (BET) method. The BET method is widely used in science and engineering to estimate the specific surface area based on the physical adsorption of gas molecules on a solid surface. Test was conducted using a Belsorp Max instrument by Nitrogen (N_2) gas/vapor adsorption. Pretreatment of the specimens were conducted at temperature of 60°C and pressure of 7×10^{-5} MPa during 24 h in a Belprep II - vac instrument. Table 3.4 shows the results of real density and specific surface area of the grained materials used in this study.

Table 3.4 – Results of real density and specific surface area of grained materials

Materials	Real density (kg/m³)	Specific surface área (m²/g)
Cement CEM I 52.5R	3084 (\pm 1.9)	1.4
Silica fume	2372 (\pm 1.8)	16.0
River sand	2667 (\pm 1.3)	Not determined
Artificial sand	2696 (\pm 1.3)	Not determined
Coarse aggregate (d_{\max} : 9.5 mm)	2670 (\pm 1.9)	Not determined
Coarse aggregate (d_{\max} : 19 mm)	2648 (\pm 1.9)	Not determined

3.1.4 Mineralogical composition

The mineralogical composition of cement powder was quantitatively determined by X-ray Diffraction (XRD) using Rietveld refinement. The XRD test was performed in a PANalytical X'Pert PRO PW 3040 00 powder diffractometer in reflection Bragg-Brentano geometry, with Ni filtered $\text{CuK}\alpha_1$ radiation ($\lambda = 1.5418 \text{ \AA}$) and a X'celerator detector (active length of 2.214°), operating at 45 kV and 40 mA.

Cylindrical sample holders with a depth of 8 mm and an internal diameter of 27 mm were used and filled with approximately 2 g of cement powder. The sample holders were spun around the vertical goniometer axis at a rate of 0.5 revolutions per second during the XRD test, which aims to improve particle statistics. The XRD patterns were obtained using an automatic divergence slit from $4^\circ 2\theta$ to $80^\circ 2\theta$, using a step width of $0.02^\circ 2\theta$ and 200 s per step. The XRD patterns were analyzed by Rietveld refinement taking as basis the structure models and the strategy for analysis proposed by Salvador et al. [129] using the software X'Pert High Score Plus. Table 3.5 shows the mineralogical composition of cement powder used in this thesis.

Table 3.5 – Mineralogical composition of the cement powder

Mineral	Quantity (%)
Alite	55.4
Belite	14.7
Ferrite	9.3
Hemihydrate	6.9
Tricalcium aluminate	5.4
Calcite	3.5
Periclase	1.7
Gypsum	1.1
Dolomite	0.9
Portlandite	0.7
Lime	0.3

3.2 MIXING, CASTING, AND PRODUCTION PROCEDURES

This section presents the mixing procedure of cement paste, mortar, and concrete employed in this thesis. All the cementitious materials produced in this thesis were based on the SFRC mix composition presented in Section 3.1. For mortar and concrete, the fine and coarse aggregates were oven dried at 100 °C for 14 h and cooled to room temperature conditions before concrete production in order to eliminate the presence of absorbed water.

3.2.1 Cement paste

The cement pastes were prepared using 200 g of cement, 11 g of silica fume, 82 g of water, and 1.4 g of superplasticizer. The materials were added all at once inside the bowl and mixed altogether at 10,000 rpm in a Makita RT0700C mixer for 120 s. The cement paste obtained was poured in amounts of 20 g each inside circular-shaped polystyrene molds with diameter of 4 cm. The molds were sealed with a plastic film and cured in a humid chamber for 72 h. After the curing period the samples were stored at room temperature at 25 ± 1 °C until the age of 150 days.

3.2.2 Mortar

The mortar mixing was conducted using a planetary mortar mixer Hobart N50 mixer with a total capacity of 5 L in a room at (25 ± 1) °C. The following procedure was adopted: microfibers were added to the bowl and dispersed with water for 90 seconds. This time period was divided into 30-30-30 seconds in, respectively low-high-low speed. Then, the fine aggregates, cement, and silica fume were added during 60 seconds with the equipment turned off and a time period of 30 seconds was given for particle wetting. At last, water and dry powder were mixed during 90 seconds, following the same 30-30-30 seconds in low-high-low speed. The aforementioned mixing procedure was adopted since it results in better homogenization of materials and microfibers in mortars [130].

The mortar produced was then cast inside dog-bone shaped molds for the pullout specimens. The pullout specimens were produced using four steel fibers instead of the usual single fiber, which was adopted as a countermeasure to the intrinsic low pullout load values of single-fiber pullout tests and the effect of temperature. Two papers of 250 g/m² were cut in a squared form and used to fix the steel fibers inside the mold. This procedure had the objective of preventing the steel fibers from moving or rotating inside the pullout specimens.

Figure 3.4 illustrates the molding procedure adopted for the pullout specimens. The mortar was poured inside one half of the mold. The embedded length was double-checked on the empty side of the mold and, after a time period of 4 h, the other half of the mold was filled with mortar. After the molding procedure, the pullout molds were sealed with a protective plastic film during 12 h until the specimens could be removed from the mold. After demolding, the pullout specimens were cured in a humid chamber for 72 h, and then stored at room temperature of (25 ± 1) °C until the age of 150 days to better simulate *in situ* humidity and curing conditions.

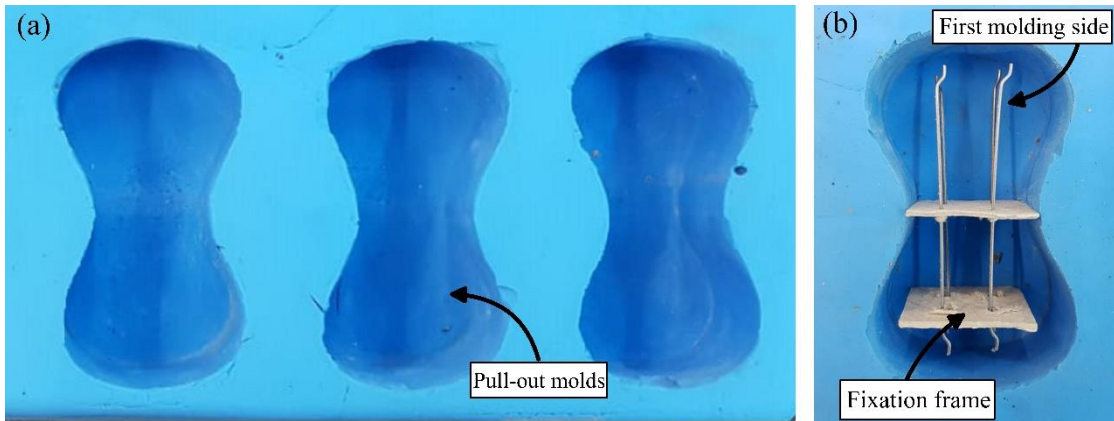


Figure 3.4 – Molding procedure: (a) pull-out molds used and (b) fixation frame and molding procedure

3.2.3 Steel fiber reinforced concrete (SFRC)

The concrete was prepared in a room at 25 ± 1 °C using a concrete mixer with total capacity of 300 L. The first step was pre-mixing the total water and superplasticizer inside an industrial polypropylene bucket. Later, the cementitious materials (cement and silica fume) were added to the concrete mixer with the coarse aggregates and a third of the total amount of the pre-mixed water and superplasticizer. The materials were homogenized for 3 min with a mixing speed of 30 rpm. Then, the total amount of fine aggregates and a third of the total amount of the pre-mixed water and superplasticizer were added and homogenized for the same time period. At last, the remaining one third of water and superplasticizer were added and macro- and micro-synthetic fibers were slowly added during 3 min of mixture. After the aforementioned procedure was finished, the mixture obtained was homogenized for a final period of 6 min. The SFRC presented a specific weight equal to 2430 ± 52 kg/m³ and a slump value of 40 ± 10 mm (average obtained from three determinations).

The concrete produced was cast in polypropylene molds with internal dimensions of 150x150x550 mm and in cylindrical steel molds measuring 100 mm in diameter and 200 mm in height. One prismatic specimen was instrumented with thermocouples during casting of SFRC in order to acquire data regarding the internal temperature distribution during a fire simulation. The thermocouples were positioned centered in the mold and in preset distances of 3, 6, 9, 12, and 15cm away from the heated surface. The positioning was stabilized during casting by a hand-made wooden tool fixed to the mold. The SFRC was consolidated using a vibrating table during 20 s

with a frequency of 60 Hz. The specimens were kept in a humid chamber for 72 h before being cured in room temperature until the age of 150 days. This procedure was adopted aiming to simulate *in situ* humidity and curing conditions. Figure 3.5 illustrates the specimens that were produced with SFRC and the wooden tool used for the fixation of thermocouples.

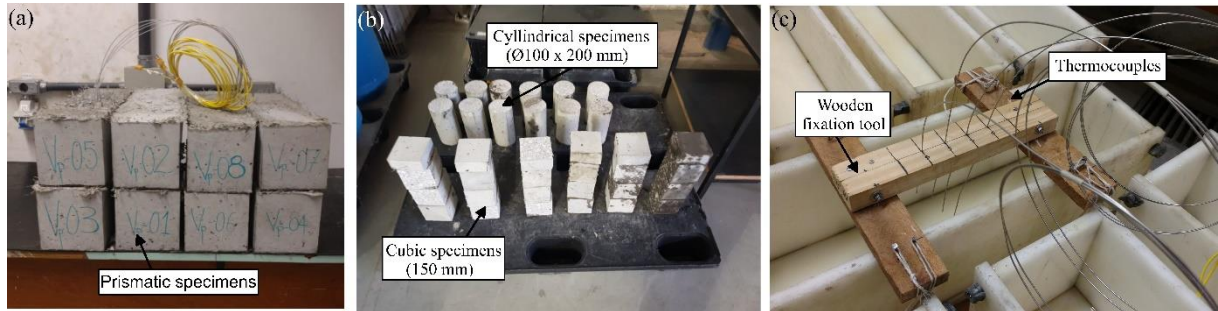


Figure 3.5 – (a) prismatic specimens, (b) cylindrical and cubic specimens, and (c) wooden tool for the fixation of thermocouples

Figure 3.6 shows the preparation of cubic specimens for the DEWS test. The prismatic specimens were cut in cubes with sides measuring 150 mm (Fig. 3.5a). Two triangular grooves with an inclination of 45° were cut along two opposite sides of the cubes in the face positioned 90° from the molding face and respecting the casting orientation. After that, two notches with a 5-mm depth and a 2-mm width were cut, starting in the groove vertices towards the center of the cubes (Fig. 3.5b). This procedure aims to induce cracks on the vertical plane of cubic specimens and was conducted before heating the specimens. Two steel plates measuring 0.9 x 15 x 150 mm (thickness x width x length) were attached to the triangular groove surfaces using body filler as glue. The steel plates had the objective of reducing the frictional interaction between the roller and the specimen during the test.

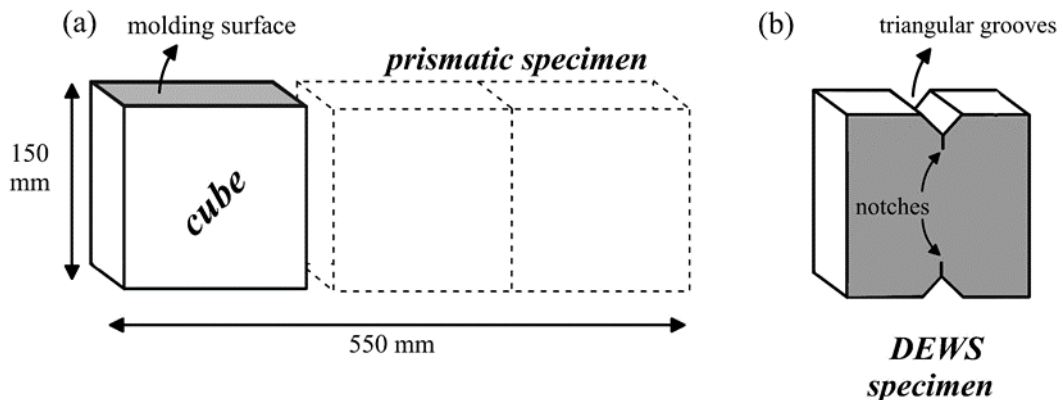


Figure 3.6 – DEWS test: (a) prismatic specimen cutting procedure, and (b) the triangular grooves and notches

3.3 HEATING OF SPECIMENS

3.3.1 Oven heating procedure

The specimens produced were exposed to elevated temperatures at the age of 150 days. The heating procedure was conducted in two different electric ovens due to the differences in the size of specimens. The smaller specimens (*i.e.* the steel fibers, pullout specimens, and the cement pastes) were heated inside an EDG FC series electric oven, model EDG10P-S with maximum temperature capacity of 1200 °C. The larger specimens (*i.e.* cylindrical and cubic specimens) were heated inside an Inforgel Genga electric oven, model GCR.SP, with maximum temperature capacity of 1000 °C. The cementitious materials were exposed to target temperatures of 150, 300, 450, 600, and 750 °C and a stabilization period adequate to ensure the thermal stability of the specimens was adopted according to the size of specimen.

3.3.2 Fire simulation procedure

The prismatic specimens were exposed to a real fire simulation with the combustion of methane gas at the age of 150 days. A masonry wall was prepared with the prismatic specimens (Fig. 3.7a) and a vertical fire simulator height of 2850 mm, width of 2850 mm, and depth of 950 mm was used to simulate the hydrocarbon fire curve (Fig 3.7b) at the Laboratory of Explosion and Fire Safety (LSFEx) at the Institute of Technological Research (IPT). The equipment uses three industrial methane gas burners on each side of the equipment to generate flames by combustion, while an exhaustion conduit is present on upper part of the equipment.

The prismatic specimens were positioned on a masonry structural wall with mortar and a high temperature resistant ceramic fabric on the perimeter (Fig. 3.7a). The ceramic fabric reduces the lateral heat flow and, therefore, favors the unifacial heating condition. The ceramic fabric was also applied on the entire surface of the wall, contributing to isolate heat at the structural masonry that could lead to lateral heating of prismatic specimens. The temperature distribution inside the SFRC was determined based on the readings of thermocouples Type K (chromel – alumel) covered with stainless steel, isolation of PVCxPVC, operating range between –200 to 1260 °C, with a precision of 0.75% and a sensibility of 41 $\mu\text{V}/^\circ\text{C}$. The thermocouples were connected to a data acquisition system and the readings were collected during the whole test in steps of 30 seconds. The prismatic specimen positioned right in the

middle of the wall was the specimen instrumented with the thermocouples, and the brick masonry wall was positioned at a distance of ~30 cm from the burning flames.



Figure 3.7 – Fire simulation: (a) positioning of prismatic specimens, and (b) the vertical fire simulator

The hydrocarbon fire curve was adopted since it is one of the curves that are recommended for the simulation of fire events in tunnel structures due to the rapid heating rate and final temperature adopted [123]. Figure 3.8 shows the experimental fire simulation compared to the hydrocarbon fire curve.

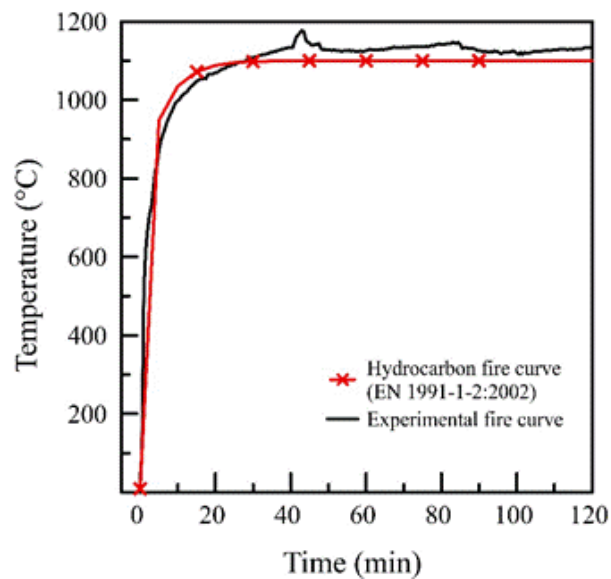


Figure 3.8 – Experimental fire simulation compared to the hydrocarbon fire curve

3.4 MICROSTRUCTURAL CHARACTERIZATIONS

3.4.1 Optical microscopy

Optical microscopy (OM) was employed in order to verify the effect of elevated temperatures on the residual cross-sectional area of steel fibers. The OM was conducted using a NIKON Epiphot 200 instrument with a NIS Element D-Live Fast software. The effective cross-sectional area was measured based on OM imagery using ImageJ image processing software. The term “effective cross-sectional area” was defined as the remaining area of steel that is capable of resisting the tensile stresses. Based on the results of effective cross-sectional area, the equivalent effective diameter was calculated considering a cross-section of circular shape. The OM analyses were conducted in steel fibers after exposure to temperatures of 100, 350, 750, and 1000 °C.

3.4.2 Scanning electron microscopy

The effect of temperature on two variables of importance were evaluated by means of scanning electron microscopy (SEM) in this thesis: 1) the changes in terms of grain-size of steel fibers; and 2) the fiber-matrix interface. The changes in terms of grain-size were evaluated by SEM using a Quanta 3D FEG instrument, accelerating voltage of 20 kV, working distance of 10 mm, using XT microscope control FEI software. The grain size of the crystalline structure of steel fiber was calculated following the procedure presented by ASTM E112 [131].

The fiber-matrix interface was evaluated by means of SEM with Energy Dispersive Spectroscopy (EDS) as a function of temperature. The pull-out specimens were sliced with a precision saw and the region around the fiber was analyzed in samples with size of 25 x 25 x 25 mm. The samples were sliced with a precision saw and the region around the fiber was analyzed in samples with size of 25 x 25 x 25 mm. The samples were embedded in resin and plane grinded using a 150 μm grained sand paper and fine grinded 9 μm grained sand paper during 10 minutes at the 1000 and 150 rpm, respectively. After grinding, the samples were dry-polished using a 2 μm diamond polishing cloth specific for metallographic purposes. Samples were then taken for SEM/EDS analysis in the Center for Metallurgical and Materials Technologies (CTMM) at the Institute for Technological Research (IPT). SEM/EDS tests were conducted using a Quanta 3D FEG instrument, equipment at the voltage

of 20 kV, working distance of 10 mm, using XT microscope control FEI software to obtain backscattered electron imagery. Lastly, the surface chemical profile was obtained by means of Line scanning EDS analysis in a radial direction perpendicular to the fiber. The linescan analysis was conducted in a radial direction for all temperatures evaluated, as show in Figure 3.9.

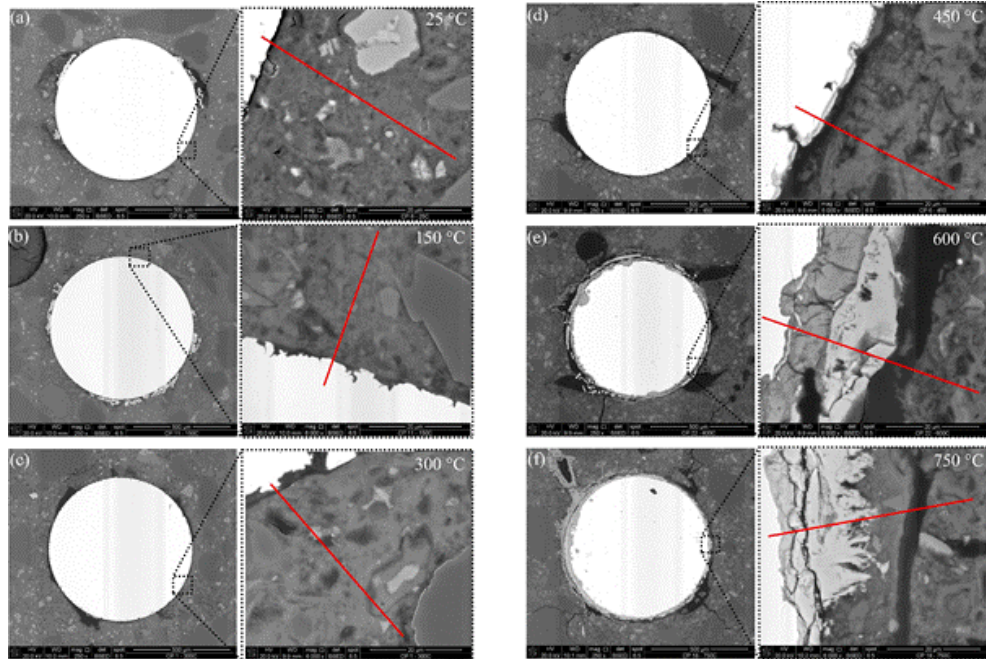


Figure 3.9 – SEM-EDS analysis for the target temperatures of (a) 25 °C, (b) 150 °C, (c) 300 °C, (d) 450 °C, (e) 600 °C, and (f) 750 °C

3.4.2 X-Ray diffraction technique

The XRD analysis conducted in this thesis was based on the evaluation of cement pastes. This procedure was adopted since, in a preliminary evaluation, the mortar samples removed from SFRC had a significant amount of quartz (around ~80%). This elevated amount of quartz negatively affect the analysis of XRD results [36] due to the reduced precision of the Rietveld methodology when applied in samples that the total mass of each hydrate in the paste is low [85]. In this context, the cement samples were crushed and ground to a maximum particle size of 90 μm and destined to XRD for mineralogical characterization.

The XRD test was performed in a PANalytical X'Pert PRO PW 3040 00 powder diffractometer in reflection Bragg-Brentano geometry, with Ni filtered $\text{CuK}\alpha_1$ radiation ($\lambda = 1.5418 \text{ \AA}$) and a X'celerator detector (active length of 2.214°), operating at 45 kV and 40 mA. Cylindrical sample holders with a depth of 8 mm and an internal diameter of 27 mm were used and filled with approximately 2 g of cement

paste. The sample holders were spun around the vertical goniometer axis at a rate of 0.5 revolutions per second during the XRD test, which aims to improve particle statistics.

X-ray patterns were obtained using an automatic divergence slit from $4^\circ 2\theta$ to $80^\circ 2\theta$, using a step width of $0.02^\circ 2\theta$ and 200 s per step. The XRD patterns were analyzed by Rietveld refinement taking as basis the structure models and the strategy for analysis proposed by Salvador et al. [129] using the software X'Pert High Score Plus. The external standard method (described in detail in [85]) was used to determine the amorphous content in samples by using alumina powder (SRM 676a, from NIST) as an external standard reference material.

3.5 MECHANICAL CHARACTERIZATIONS

3.5.1 Tensile strength of steel fibers

An electromechanical Instron Universal Testing Machine, model 5569, with loadcell of 1 kN was used to determine the tensile strength of steel fibers. The tests were conducted using a load rate control of 152 N/min which was determined based on the minimum requirements of 6 MPa/s of the Brazilian standard [132] and strain was calculated using piston displacement data. The steel fibers were directly positioned centered and perpendicular to the jaw faces of the equipment since this methodology experimentally proved to be the best option among the setups tested.

3.5.2 Pullout test

The pullout tests were conducted using an electromechanical universal testing machine in open-loop configuration, EMIC DL 10000, with a load-cell with maximum load capacity of 10 kN and precision of 1 N. The test was displacement-controlled at a rate of 0.5 mm/min. Furthermore, the pullout curves obtained from the pullout tests using four fibers were normalized to be representative of a single fiber pullout. This was achieved by dividing the pullout curves by the amount of resisting fibers in each section of the test. This normalization was required in order to make a valid comparison with literature results and because some fibers ruptured during the test after exposure to elevated temperatures.

The pullout test was interrupted before the complete pullout of the fiber from the specimen occurred. This was adopted because the ULS condition in real-life applications is achieved before the full embedded length (20 mm) is pulled out of the

matrix. Therefore, the pullout tests of this study were conducted until a conservative displacement of 10 mm was achieved, since any result obtained for greater displacement values would have no useful application from the engineering standpoint. Moreover, the analysis was conducted based on the peak load value (P_{L1}), the second peak load value (P_{L2}) and the load value at a displacement of 10 mm (P_{L3}).

3.5.3 Compressive strength and elastic modulus

Compressive strength tests were conducted in a Shimadzu Universal Testing Machine, model UH-F2000kNXR, with a computer-controlled servo-hydraulic system, operating frequency of 60 Hz, and maximum load capacity of 2000 kN. The test was load-controlled at a rate of 0.5 MPa/s and the axial strain was determined by the average readings of two displacement transducers attached around the specimen. The elastic modulus was obtained in the range of the stress-strain curves located between 0.5 MPa and $0.3f_c$. Taking into consideration that specimens were severely affected by temperature, only one loading cycle was performed in order to determine the elastic modulus. The two displacement transducers had to be removed before rupture of specimens for safety purposes, therefore the strain values were estimated by the relation between piston displacement and transducer readings in the elastic region of the test.

3.5.4 Ultrasonic propagation speed

The ultrasonic (US) propagation test was conducted using a Portable Ultrasonic Non-destructive Digital Indicating Tester (PUNDIT) equipment using 200 kHz transducers and a circular cross-section with a 20 mm diameter capable of measuring the ultrasonic P-wave propagation. The US propagation velocity was determined in the same specimens before and after temperature exposure and used to indirectly determine the changes in the elastic properties of the mortar before and after temperature exposure. The density of the material was recalculated for each target temperature based on the mass and volume of the specimens. Regarding the Poisson's ratio, results found in literature show that this property is affected by temperature – although it does not change significantly for small stress values [133]. Therefore, the Poisson's ratio was assumed to be constant at 0.2 for all target temperatures, which is taken as a simplification given the limited number of studies on this matter.

3.5.5 Three-point bending test

The three-point bending test was conducted in an INSTRON 8802 servo-hydraulic machine with maximum load capacity of 250 kN. The prismatic specimens were positioned in a manner that crushing and grinding interaction between the rollers and concrete are reduced and the fiber reinforcing mechanism is engaged in the region that was exposed to higher temperatures during the fire. Figure 3.10 illustrates the test setup adopted for the three-point bending test.



Figure 3.10 – Test setup adopted for the three-point bending test

The test was controlled by Crack Mouth Opening Displacement (CMOD) rate using a knife-edge clip-gauge with maximum length of 4 mm. During the test, CMOD opening rate was kept constant at 0.05 mm/min until CMOD = 0.1 mm, after which a constant rate of 0.2 mm/min was adopted. The flexural and the residual strengths (f_j) were calculated based on EN 14651 [134] and on the recommendations of the *fib* Model Code 2010 [43] by the following equation:

$$f_j = \frac{3F_j \cdot l}{2bh_{sp}^2} \quad (7)$$

where l is the span (in mm); b is the width of the specimen (in mm); and h_{sp} is the distance between the tip of the notch and the top of the specimen (in mm).

3.5.6 Tensile properties by means of DEWS test

Figure 3.11 shows schematic drawing and illustration of the DEWS test. The DEWS test was conducted in open-loop configuration using an electromechanical universal testing machine, EMIC DL 10000, with a load cell with maximum load capacity of 10 kN and a frame stiffness of 42 kN/mm. Tests were conducted using a

COD opening displacement rate of 0.12 mm/min. Two transducers positioned in opposite sides and in the middle height of the cubic specimens were employed to measure the average crack opening displacement (COD) during the DEWS test.

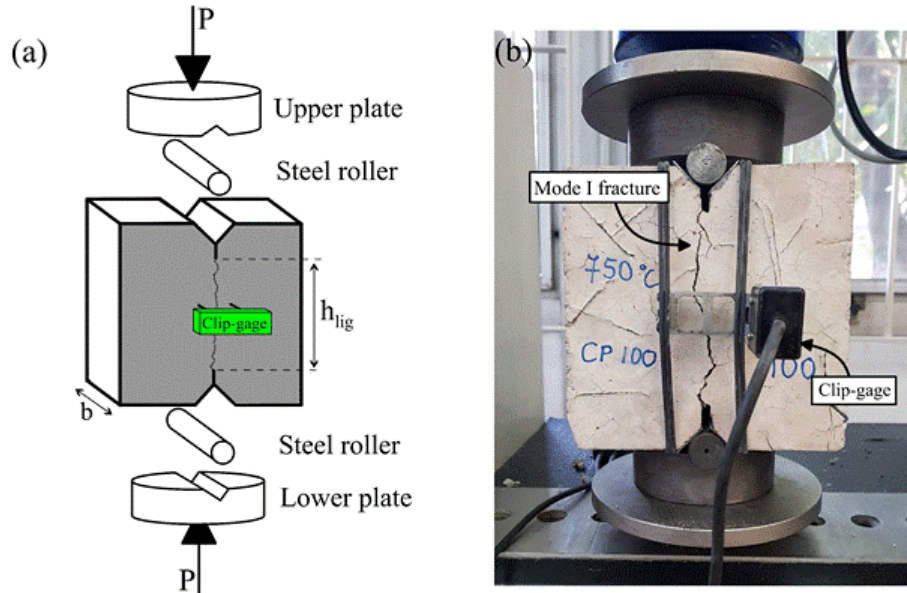


Figure 3.11 – Schematic (a) drawing and (b) illustration of the DEWS test setup

Although the displacement rate and transducer positioning are simplifications from the original methodology proposed by di Prisco et al. [111], this adaptation have proven to have no significant influence on the FRC first crack strength, to reduce the scattering of results, and have minor effects on post-crack tensile strength values [113]. Therefore, the recorded COD values presented in this paper are given by the average of two measurements taken on opposite faces of the specimen. The use of graphite to lubricate the contact surface between the steel roller and the steel plates was adopted based on the increased reliability of results due to reduced frictional interaction, as shown by di Prisco et al. [111].

Additionally, the load provided by the testing machine cannot be considered as the load in the specimen fracture surface due to the geometry of the specimens. Therefore, it is necessary to convert the load values obtained from the equipment (P) into the “splitting load” that effectively acts on the fracture surface (P_{ef}). Considering the equilibrium equations, di Prisco et al. [111] proposed the following equation to determine the actual “splitting load”:

$$P_{ef} = P \cdot \frac{(\cos\theta - \mu\sin\theta)}{(\sin\theta + \mu\cos\theta)} \quad (8)$$

where θ is the angle between the groove surface and the center line of the notch ($\theta = 45^\circ$), and μ is the coefficient of friction between two steel surfaces lubricated with graphite ($\mu = 0.06$). The tensile stress (σ) was determined based on Equation 5, proposed by di Prisco et al. [111]:

$$P_{ef} = \frac{P_{ef}}{b \cdot h_{lig}} \quad (9)$$

where b is the depth of the specimen and h_{lig} is the height of the ligament. The post-crack tensile strength values associated to the SLS and to the ULS condition were adopted as the values associated to the crack opening displacement values of COD = 0.25 mm and COD = 1.25 mm, respectively. These values of crack opening displacement were employed based on the crack mouth opening displacement recommended in EN 14651 [134] and considering the intrinsic geometrical differences in terms of test configuration between the three-point flexural test and the DEWS test.

3.5.7 Determination of DEWS sample size

The relationship between the sample size and the admissible error was determined based on inferential statistics (Bussab and Morettin 2017), by means of Eq. 10.

$$n = \frac{s^2 \cdot z_\gamma^2}{\varepsilon^2} \quad (10)$$

where n is the required sample size; s is the standard deviation obtained by the pilot sample (in MPa); z_γ is the t-distribution value; and ε is the admissible error for the test. The \bar{x} was computed from the experimental results, while $z_\gamma=2.132$ was adopted considering a confidence interval of 95% and 4 degrees of freedom.

3.6 NUMERICAL MODEL

This section presents the fundamental concepts for the development of the thermo-mechanical numerical model to assess the bearing capacity of the FRC sections with and without steel bar reinforcement under the occurrence of thermal spalling. The heat transfer model was based on common solution approach to the Fourier heat transfer equation [38,39] and applied to the FRC tunnel segments, while the mechanical model was based on the work of Di Carlo et al. [38]. The numerical

model implemented for this study is based on a staggered analysis that decouples both thermal and mechanical problems, the thermal spalling phenomenon being simulated by imposing spalling (R_{sp}) and section lost (s_L) rates. Even though the model developed simplifies the strongly dependent thermo-hygro-mechanical phenomena, it is valid and suitable for pre-design purposes.

3.6.1 Heat transfer model

The heat transfer through an isotropic solid body can be described by the Fourier heat transfer equation, as:

$$\nabla(KT) + Q = \rho C \quad (11)$$

where K is the thermal conductivity; c is the specific heat; p is the density; Q is the volumetric heat flux; T is the temperature. The heat transfer through concrete may be described as a one-dimension planar conduction with no internal heat generated when considering a concrete fully hardened. This assumption may be considered in the central zone of the segments, which represents the greatest portion of the element. However, the regions of contact between segments may be better described by a two-dimension conduction since lateral heating may influence the temperature distribution [29], which needs to be addressed in future research. Based on this assumption and the discussion provided, Eq. 11 reduces to:

$$\alpha \left(\frac{\partial^2 T}{\partial z^2} \right) = \frac{\partial T}{\partial t} \quad (12)$$

where $\alpha = \frac{K}{\rho c}$.

In this sense, a numerical model based on the finite difference method (FDM) was developed to solve the Fourier heat transfer equation, which is shown in detail in Appendix A. The space-time domain was divided in preset constant values (discrete approach) and the differential equations were approximated by FDM. The numerical model adopted a closed space-time domain \mathfrak{R} :

$$\mathfrak{R} = \{(z, t): 0 \leq z \leq L, 0 \leq t \leq t_{fire}\} \quad (13)$$

where z is the spatial variable; L is the length of the cross-section; t is the time related variable; and t_{fire} is the maximum duration of the fire event. The points within the space-time domain are equidistant and identified according to:

$$z_i = (i - 1)\Delta z, \quad i = 1, 2, \dots, n \quad (14)$$

$$t_j = (j - 1)\Delta t, \quad j = 1, 2, \dots, m \quad (15)$$

where n and m are the number of points and time instants, being $\Delta z = L/(n - 1)$ and $t_{\text{fire}}/(m - 1)$.

The computation of the second derivatives of the temperature with respect to the spatial variable at a point $z \in \mathfrak{R}$ were solved by the FDM approach, as:

$$\frac{\partial^2 T}{\partial z^2} = \frac{T(z + \Delta z, t) - 2T(z, t) + T(z - \Delta z, t)}{(\Delta z)^2} \quad (16)$$

while the first derivative of temperature related to time is computed as:

$$\frac{\partial T}{\partial t} = \frac{T(z, t + \Delta t) - T(z, t)}{\Delta t} \quad (17)$$

Substituting the Eqs. (16) and (17) into Eq. (12) it is possible to determine an equation to compute the temperature at $t = j + 1$ given that the temperature at the $t = j$ is known, described as:

$$T_{i,j+1} = (1 - 2\bar{k})T_{i,j} + \bar{k}(T_{i+1,j} + T_{i-1,j}) \quad (18)$$

where $\bar{k} = \alpha\Delta t/\Delta z^2$. The FDM results are stable if the condition $2\alpha\Delta t < \Delta z^2$ is satisfied.

3.6.2 Initial and boundary conditions

The thermal equilibrium between the cross-section and the surroundings is considered to be the initial condition for the numerical simulation. Thus, the numerical model assumes that at $t = 0$ the n layers that compose the cross-section discretization, from the intrados to the extrados, are at $T = 25$ °C. The net heat flux

(\dot{h}_{net}) transferred from the fire source to the surface of the FRC segment is the sum of the heat flux components convection (\dot{h}_c) and radiation (\dot{h}_r), according to:

$$\dot{h}_{net} = \dot{h}_c + \dot{h}_r = \alpha_c(T_f - T_s) + \sigma\varepsilon[(T_f + 273)^4 - (T_s + 273)^4] \quad (19)$$

where α_c is the convective heat transfer coefficient (in $\text{W}\cdot\text{m}^{-2}\text{K}^{-1}$); σ is the Stefan-Boltzmann constant (in $\text{W}\cdot\text{m}^{-2}\text{K}^{-4}$); ε is the dimensionless emissivity ranging from 0 (perfect reflector) to 1 (perfect absorber); T_f is the temperature of the fire source at a given t value; and T_s is the temperature at the surface of the FRC segment at given t value. Figure 3.12 illustrates the heat transfer model developed considering the heat flux transferred and the convection described by the discretized Fourier heat transfer equation.

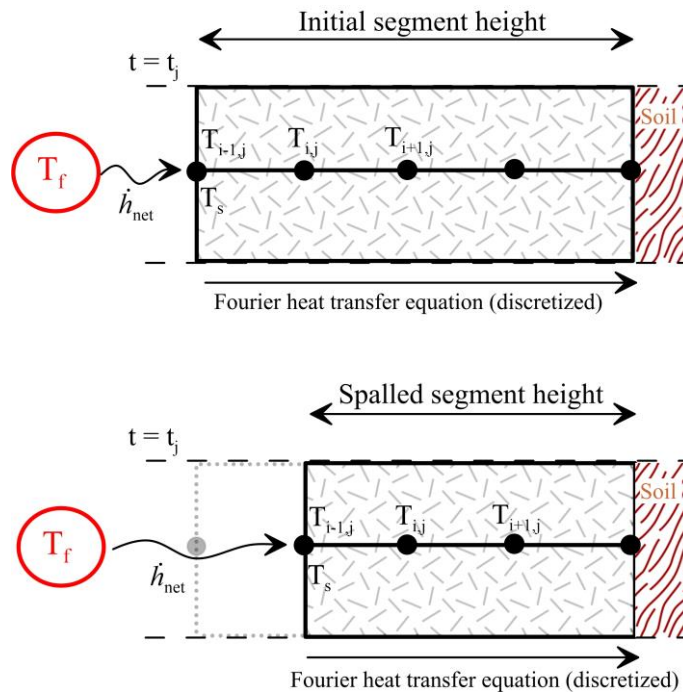


Figure 3.12 – Illustration of the heat transfer model developed

The effect of spalling is considered in the bearing capacity of FRC segments by reducing the height of the section (H) during the fire event accordingly. This reduction is implemented during the thermal simulation of the composite and results in a cross-section that varies as a function of time. The spalling rate (in mm/h) and the maximum depth of spalling (in mm) are considered the input parameter for simulating the spalling process. These parameters may be determined based on an experimental program using vertical fire simulators and a concrete mix representative

of the segment [68]. In these experimental programs, spalling initiation time versus depth diagrams are often used to determine the spalling rate [135]. The spalling rate is established to compute the time required for a concrete thickness (Δz) exposed to elevated temperature to be spalled, by applying the Eq. (20).

$$t_{sp} = \frac{3600 \cdot \Delta z}{R_{sp}} \quad (20)$$

where t_{sp} is the time required for Δz to be spalled (in seconds); and R_{sp} is the experimentally determined rate of spalling (in mm/h). Therefore, the concrete thickness measuring Δz are removed from the thermal analysis every t_{sp} seconds until the maximum depth of spalling is reached. The model takes into account that the heat transferred by the fire source, in the form of \dot{h}_c and \dot{h}_r , begins to affect an inner region of the specimen (see Fig. 1), which influences the temperature distribution in the FRC. Whenever the spalling condition is reached, the reference position containing $T_{i,j}$ moves one discretized Δz unit toward the interior of the FRC and the spalled layers are disregarded in the thermal model. This process occurs until the maximum depth of spalling accepted by the designer is reached.

3.6.3 Thermal and physical properties of FRC

The thermal conductivity (K), specific heat (c), and density (ρ) of the FRC are temperature-dependent properties. In this sense, the changes in K , c , and ρ are assumed to vary similarly to plain concrete by the equations provided by the Eurocode [20]. The specific heat of concretes produced with siliceous and calcareous aggregates vary with temperature according to the Eq. (21).

$$c(T) = \begin{cases} 900, & 20 \text{ }^\circ\text{C} \leq T \leq 100 \text{ }^\circ\text{C} \\ 900 + (T - 100), & 100 \text{ }^\circ\text{C} < T \leq 200 \text{ }^\circ\text{C} \\ 1000 + (T - 200), & 200 \text{ }^\circ\text{C} < T \leq 400 \text{ }^\circ\text{C} \\ 1100, & 400 \text{ }^\circ\text{C} < T \leq 1200 \text{ }^\circ\text{C} \end{cases} \quad (21)$$

where c is the specific heat of concrete (in $\text{J} \cdot \text{kg}^{-1} \cdot \text{K}^{-1}$); and T is the temperature (in $^\circ\text{C}$). The changes in density of concrete occurs due to the dehydration of hydrated products and consequent water loss, which may be computed by a multilinear equation as:

$$\rho(T) = \begin{cases} \rho_R, & 20\text{ }^\circ\text{C} \leq T \leq 115\text{ }^\circ\text{C} \\ \rho_R \left[1 - \frac{0.02(T - 115)}{85} \right], & 115\text{ }^\circ\text{C} < T \leq 200\text{ }^\circ\text{C} \\ \rho_R \left[0.98 - \frac{0.03(T - 200)}{200} \right], & 200\text{ }^\circ\text{C} < T \leq 400\text{ }^\circ\text{C} \\ \rho_R \left[0.95 - \frac{0.03(T - 400)}{800} \right], & 400\text{ }^\circ\text{C} < T \leq 1200\text{ }^\circ\text{C} \end{cases} \quad (22)$$

where ρ is the density of concrete as a function of temperature (in $\text{kg}\cdot\text{m}^{-3}$); ρ_R is the density of concrete at room temperature (in $\text{kg}\cdot\text{m}^{-3}$); and T is the temperature (in $^\circ\text{C}$). The concrete density at room temperature was considered to be $2430\text{ kg}/\text{m}^3$, based on the work of Serafini et al. [68]. Lastly, the thermal conductivity of normal-weight concretes exposed to temperatures between 20 and $1200\text{ }^\circ\text{C}$ can be determined by the average of lower and upper limit values given by:

$$K_U = 2 + 0.2451 \left(\frac{T}{100} \right) + 0.0107 \left(\frac{T}{100} \right)^2 \quad (23)$$

$$K_L = 1.36 + 0.136 \left(\frac{T}{100} \right) + 0.0057 \left(\frac{T}{100} \right)^2 \quad (24)$$

where K_U is the upper limit for the thermal conductivity (in $\text{W}\cdot\text{m}^{-1}\text{K}^{-1}$); K_L is the lower limit for the thermal conductivity (in $\text{W}\cdot\text{m}^{-1}\text{K}^{-1}$); and T is the temperature (in $^\circ\text{C}$).

3.6.4 FRC constitutive law

The constitutive law employed is based on a stress-block approach defined by the design compressive strength (f_{cd}) and the design post-crack tensile strength for the ultimate crack-opening (f_{ftud}), as show in Figure 3.13. The mechanical properties of the composite are influenced by the increase in temperature, which is computed by the use of coefficients of mechanical degradation as reduction factors presented in **Article C** and in design guidelines [20,22]. The mechanical model assumes an isotropic distribution of fibers in the section, which may be achieved in practice as discussed by Galobardes et al. [136]. Even with this consideration, the effect of fiber segregation in segments remain a topic of concern that must be tackled in future studies.

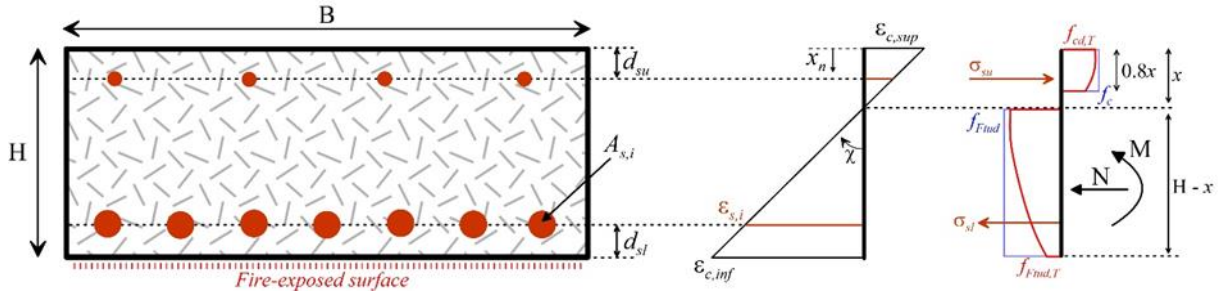


Figure 3.13 – Illustration of the mechanical model implemented

In this context, the FRC compressive strength was calculated as a function of temperature based on the cylinder compressive strength and the respective coefficient of mechanical degradation, as:

$$f_{cd,T} = K_c \frac{f_{ck}}{\gamma_F} \quad (25)$$

where $f_{cd,T}$ is the design compressive strength at a given temperature (in MPa); K_c is temperature-dependent coefficient of reduction in compressive strength; f_{ck} is the characteristic compressive strength at room temperature (in MPa); and γ_c is the partial safety factor, which is taken as $\gamma_F = 1$ in case of fire events [13]. The mechanical degradation of f_{cd} and f_{sy} are represented by K_c and K_{sy} , respectively, and defined as a function of temperature according to the values prescribed by the Eurocode [20], as shown in Figure 3.14. The K_{sy} value is based on the reductions in the yield strength of hot rolled steel.

The behavior in tension is computed based on the rigid-plastic model presented by the *fib* Model Code 2010 [13] and the tensile strength for ultimate limit state (ULS) condition may be determined by the EN 14651 three-point bending test procedure [134]. The design post-crack tensile strength of the composite can be calculated as a function of temperature, as:

$$f_{Ftud,T} = K_{Ftu} \cdot \frac{f_{R3k}}{3} \cdot \frac{1}{\gamma_F} \quad (26)$$

where $f_{Ftud,T}$ is the design post-crack tensile strength associated with the ultimate crack-opening at a given temperature (in MPa); K_{Ftu} is the coefficient of mechanical degradation for the post-crack tensile strength as a function of temperature; and f_{R3k} is the characteristic flexural tensile strength relative to the ULS at room temperature

(in MPa). The mechanical degradation of f_{Ftud} is represented by K_{Ftu} , which is defined as a function of temperature according to the experimental results obtained in **Article C** and presented in Figure 3.14.

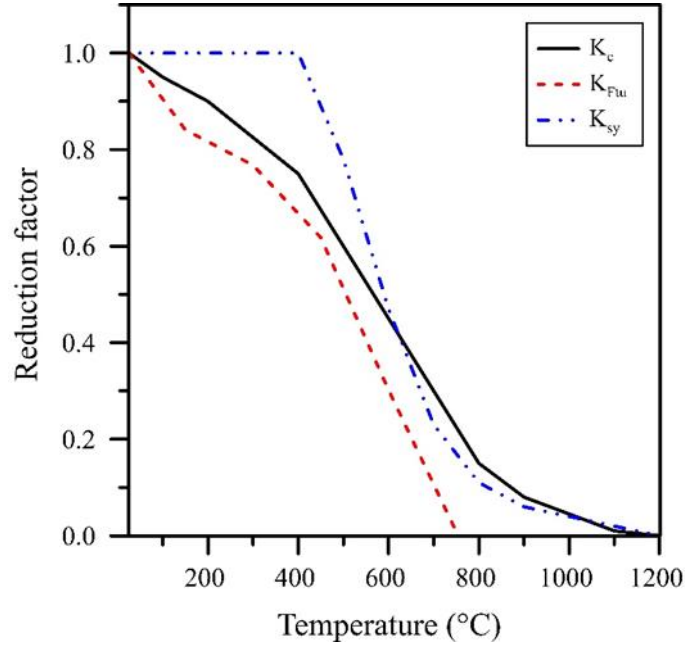


Figure 3.14 – Reduction factors employed in the numerical simulation

In cases where reinforcing steel is considered, the design yield strength of steel (f_{sd}) is reduced according to the yield strength reduction factor (K_{sy}) prescribed by the Eurocode [20], as described in Eq. (27).

$$f_{sd,T} = K_{sy} \cdot f_{syk} \cdot \frac{1}{\gamma_F} \quad (27)$$

where $f_{sd,T}$ is the design yield strength of steel (in MPa); K_{sy} is the coefficient of mechanical degradation for the yield strength of steel as a function of temperature; and f_{syk} is the characteristic steel yield strength at room temperature (in MPa).

3.6.5 Cross-sectional modelling

The procedure begins with the thermal simulation based on the thermal model developed in this thesis. After the thermal simulation is completed, the distribution of temperatures is available in the points of the cross-section for every instant of time, respecting the subdivisions adopted in Eq. 14 and Eq. 15. Once the temperature and the constitutive relationship of the FRC at that temperature are known, the

equations for the rotational and translational stability of the cross-section can be written as:

$$\begin{aligned}
 N = B \cdot & \left[\sum_{i=1}^{n_{sc}} f_{cd,(T_i)} \cdot \Delta Z + f_{cd,(T_{0.8x})} \cdot (0.8x - n_{sc} \cdot \Delta Z) - \sum_{i=1}^{n_{st}} f_{Ftud,(T_{n_s-n_{s_i}+i})} \cdot \Delta Z \right. \\
 & \left. - f_{Ftud,(T_x)} \cdot (H - x - n_{st} \cdot \Delta Z) \right] + n_{su} \cdot A_{su} \cdot f_{sd,(T_{su},\chi)} \cdot \beta_1 \\
 & - n_{sl} \cdot A_{sl} \cdot f_{sd,(T_{sl},\chi)} \cdot \beta_2
 \end{aligned} \quad (28)$$

$$\begin{aligned}
 M = B \cdot & \left[\sum_{i=1}^{n_{sc}} f_{cd,(T_i)} \cdot \Delta Z \cdot \left[\frac{H}{2} - \Delta Z \cdot \left(i - \frac{1}{2} \right) \right] \right. \\
 & + f_{cd,(T_{0.8x})} \cdot (0.8x - n_{sc} \cdot \Delta Z) \cdot \left[\frac{H}{2} - 0.8x + \frac{0.8x - n_{sc} \cdot \Delta Z}{2} \right] \\
 & + \sum_{i=1}^{n_{st}} f_{Ftud,(T_{n_s-n_{s_i}+i})} \cdot \Delta Z \cdot \left[\frac{H}{2} - \left(n_{st} - i + \frac{1}{2} \right) \cdot \Delta Z \right] \\
 & \left. + f_{Ftud,(T_x)} \cdot (H - x - n_{st} \cdot \Delta Z) \cdot \left[\frac{H}{2} - x - \frac{H - x - n_{st} \cdot \Delta Z}{2} \right] \right] \\
 & + n_{su} \cdot A_{su} \cdot f_{sd,(T_{su},\chi)} \cdot \left(\frac{H_i}{2} - d_{su} \right) \cdot \beta_1 \\
 & + n_{sl} \cdot A_{sl} \cdot f_{sd,(T_{sl},\chi)} \cdot \left(\frac{H_i}{2} - d_{sl} \right) \cdot \beta_2
 \end{aligned} \quad (29)$$

where n_s is the quantity of subsections in the cross-section; n_{sc} is the quantity of compressed subsections located within $0.8x$; n_{st} is the quantity of subsections subjected to tensile stresses; T_x is the temperature at the position of the neutral axis; $T_{0.8x}$ is the temperature at distance $0.2x$ from the neutral axis; n_{su} is the amount of rebars in the upper region of the section (extrados); n_{sl} is the amount of rebars in the lower region of the section (intrados); A_{su} is the cross-sectional area of steel (unitary) at the upper region; A_{sl} is the cross-sectional area of steel (unitary) at the lower region; H is the total height at time t ; H_i is the initial height of the segment; d_{su} is the concrete cover at the extrados; d_{sl} is the concrete cover at the intrados; and the

β_1 and the β_2 variables compute the signal for the contribution of rebars in the rotational and transitional stability according to Eq. (30) and Eq. (31), respectively. The latter is required since the failure planes are accounted by inputting a vector of neutral axes x contained between the intrados and extrados of the FRC segment, which is posteriorly necessary for assessing the M-N interaction envelopes.

$$\beta_1 = \begin{cases} \frac{d_{su} - x}{|d_{su} - x|} & \text{if } x \neq d_{su} \\ -1 & \text{if } x = d_{su} \end{cases} \quad (30)$$

$$\beta_2 = \begin{cases} \frac{(x - H + d_{sl})}{|x - H + d_{sl}|} & \text{if } x \neq (H - d_{sl}) \\ 1 & \text{if } x = (H - d_{sl}) \end{cases} \quad (31)$$

Therefore, the aforementioned thermal and mechanical models are employed to conduct a parametric study aiming to assess the effect of fire in the bearing capacity of the RC and FRC sections. The following scenarios were employed to assess the deterioration of bending capacity on RC and FRC sections exposed to fire:

- a) A conventional RC with $A_s = 792 \text{ mm}^2$ on the upper region and lower region of the section. This value was chosen since it is minimum longitudinal reinforcement ratio for compressed members according to the *fib* MC-10, which aims to ensure the ductility response in case of cracking due to transient loads related to transportation, stacking, and manipulation of the segments. The sensitivity to fire action was evaluated on a RC section with a concrete cover of $c = 30 \text{ mm}$ (RC30) based on the XC4 exposure class prescribed by the *fib* MC-10 [13], and another RC section with $c = 50 \text{ mm}$ (RC50).
- b) A FRC 45 3c composite without any steel rebar reinforcement. This solution can be used in those lining stretches along which low-moderate forces are expected and minimum amount of reinforcement is required, in which the conventional rebar reinforcement is replaceable by fibers. Likewise, local reinforcement is required to control splitting and spalling cracks due to the thrust of the jacks during excavation.
- c) A FRC 45 3c composite with the same steel reinforcement described in (1), being identified as RC30-FRC for the hybrid option with $c = 30 \text{ mm}$, and RC50-FRC for the one with $c = 50 \text{ mm}$. This hybrid reinforcement

approach could be of technical interest in those stretches along which the external forces are demanding in magnitude and/or cracking is expected due to the thrust of the TBM, resulting in the need for additional reinforcement to control cracking.

These possible configurations for the cross-section of the tunnel were analyzed in this paper as a function of the temperature-time pattern numerically obtained, based on the fire curve adopted and the axial load ratio applied. In order to ensure a conservative approach, the thermal spalling was considered to begin at $t = 0$ min for simulation purposes. Table 3.6 shows the input parameters adopted for the thermo-mechanical simulations conducted in this study.

Table 3.6 – Input parameters adopted for the thermo-mechanical simulations

Property	Input value
H (mm)	400
B (mm)	1000
f_{cd} (MPa)	45
f_{R3d} (MPa)	3.0
f_{sd} (MPa)	434
Initial temperature (°C)	25
Concrete density (kg/m ³)	2400
Specific heat (J.kg ⁻¹ .K ⁻¹)	900
Convective heat coefficient (W.m ⁻² .K ⁻¹)	25
Thermal conductivity (W.m ⁻¹ .K ⁻¹)	1.6
Emissivity	0.9

CHAPTER 4.

RESULTS AND ANALYSIS

4.1 THERMAL EFFECTS ON THE BOND-SLIP MECHANISM

The bond-slip mechanism of fibers embedded in the matrix is of paramount importance to understand and justify the tensile behavior of fiber reinforced composites. This is a topic that was not sufficiently evaluated up to the publication of this thesis, and even so, still requires attention. In this sense, this thesis evaluated the effect of temperature on the physical, mechanical, and microstructural properties of hooked-end steel fibers embedded in cementitious matrices. The **Article A** was focused on the microstructural, physical, and mechanical changes caused by temperature on the steel fibers. Based on these result, **Article B** was focused on the bond-slip behavior of steel fibers embedded in a high strength cementitious matrix.

The results showed that the steel fibers oxidise with the increase in temperature (Fig. 4.1a), resulting in the increase in mass, length, and total diameter. The oxide formed was evaluated by XRD technique and identified as a layered structure formed by wüstite, hematite, and magnetite. The mass of fibers significantly increased by 1.52% at 750 °C and 23.01% at 1000 °C. The steel fiber's length increased after temperature exposure, however no clear trend was verified. The total external diameter of fibers (*i.e.* steel + oxide) shown a statistically significant increased of 3.80% at 750 °C and 35.44% at 1000 °C, which was attributed to the expansive formation of oxides in the fiber's surface. As a result of this oxidation process, a slight reduction tendency in the fiber's effective cross-sectional area was verified up to 750 °C and an average reduction of 54.5% at 1000 °C (Fig. 4.2b).

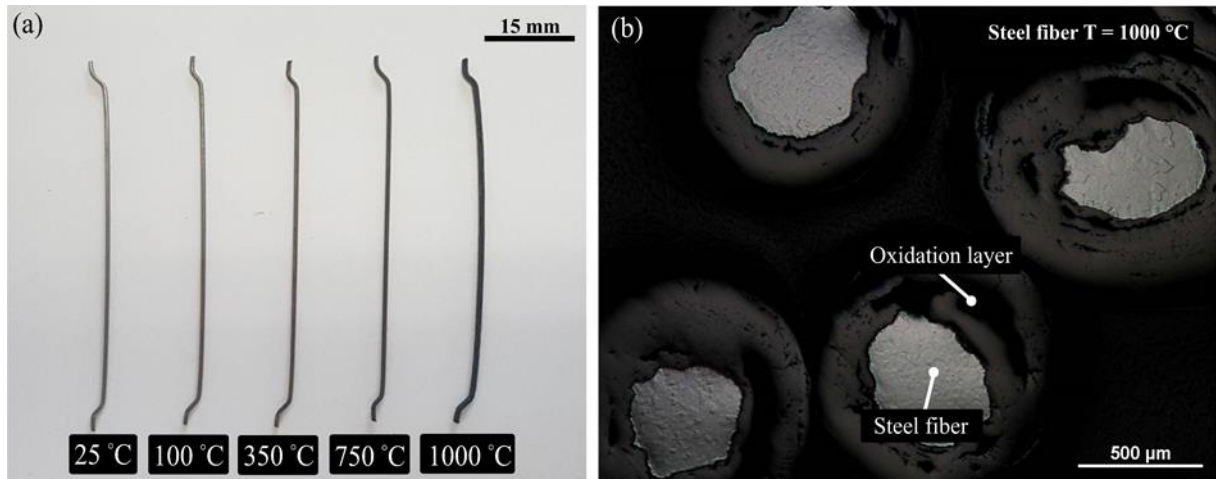


Figure 4.1 – Effect of temperature on external and effective diameters

The grain structure of the steel fibers shown an elevated degree of cold work at room temperature (Fig. 4.2a). An elevated degree of cold work was also observed for the fibers exposed to temperatures of 100 and 350 °C. However the occurrence of a recovery process by the diffusive movement and rearrangement of discordances in the microstructure was observed at 350 °C. At temperature of 750 °C, the thermal energy provided to the system was enough to favor the complete nucleation of discordances and the formation of new discordance-free grains. At 1000 °C, the recently formed grains underwent a grain growth process that consumes the previous discordances and the original grain structure. The average measured grain size was 7.03 μm at 750 °C and 16.70 μm at 1000 °C. Therefore, it is possible to observe that the formation of new grains and the grain growth process induced by temperature caused the reduction in the grain boundary density of steel fibers.

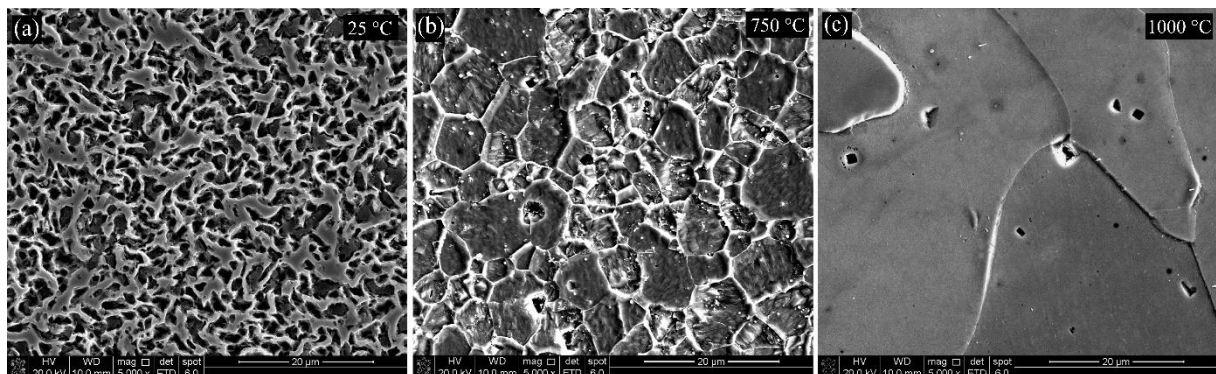


Figure 4.2 – Effect of temperature on the grain size of steel

Figure 4.3 illustrates the effect of temperature on the steel fiber's tensile strength and rupture strain. The increase in temperature resulted in a decrease in the tensile strength of steel fibers. Significant reductions of 35.9%, and 74.9% were observed for the temperatures of 350 °C and 750 °C, while the exposure to 100 °C did

not present a statistically significant difference. The reductions in steel fiber's tensile strength exposed to 350 °C resulted from the diffusive movement and rearrangement of discordances in the microstructural, with minimal influence from cross-sectional changes. At 750 °C, the tensile strength further reduces due to the formation of new sets of defect-free grains during the recrystallization process. The grain-size changes observed in SEM imagery are responsible for the tensile strength reductions observed, since the reduction in the number of grain boundaries per unit area leads to a lower amount of energy required for dislocations to cross the grain boundaries. Steel fibres exposed to 1000°C were friable and easily damaged by handling, which occurred due to coupling effects of cross-sectional area reduction and a grain size increase, which made the determination of tensile strength impossible.

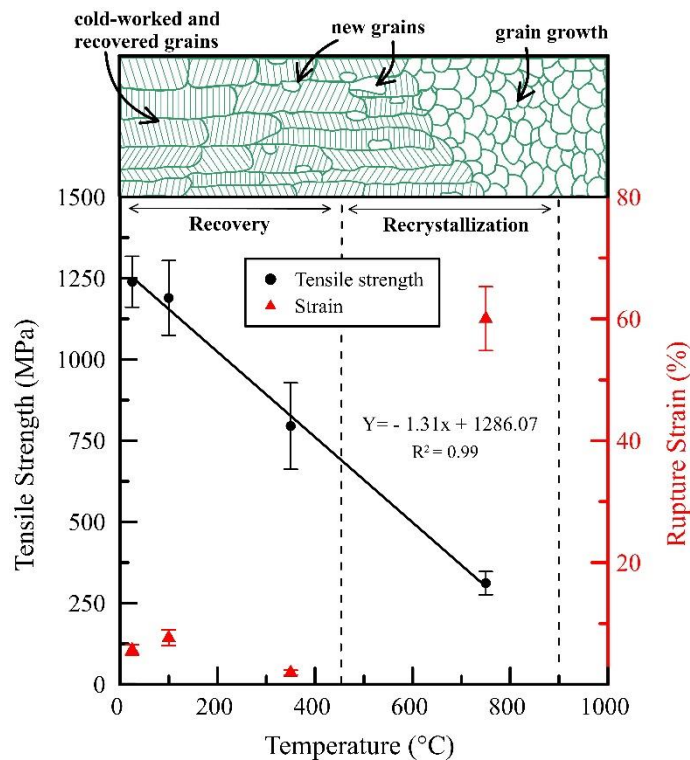


Figure 4.3 – Effect of temperature on the steel fiber's tensile strength and rupture strain

Additionally, no statistically significant difference in terms of rupture strain value was verified for temperatures equal or lower than 350 °C. However, an increase of 962% in the rupture strain values was evidenced for steel fibers exposed to a temperature of 750°C, as well as the presence of a strain yielding region before rupture. These results denote that the ductility remains unchanged for temperatures below the recrystallisation temperature, while the pre-cold-worked ductility conditions are restored for temperatures above the recrystallisation temperature.

Although understanding the effect of temperature on the physical and mechanical properties of fibers is relevant, an analysis focused solely on the fibers is not sufficient to understand the behavior of fiber reinforced concrete. In this sense, **Article B** evaluated the effect of temperature on the bond-slip properties of hooked-end steel fibers in a high strength matrix, while also focusing on the evaluation of the fiber-matrix ITZ by means of SEM-EDS. Lastly, the results obtained in **Article A** and **Article B** were employed as input parameters to a recently developed numerical model capable of representing the steel fibers in concrete in a discrete and explicit manner.

Figure 4.4 illustrates the average load-displacement curves and the maximum P_{L1} , P_{L2} , and P_{L3} values. It is important to highlight that P_{L1} accounts for the energy required to yield the hooks at two points, P_{L2} is associated with the force required to straighten the fiber, and P_{L3} evaluates the changes in the dynamic frictional interaction between fiber and matrix. Moreover, the effect of temperature on the mechanical interlocking provided by the hooked-end steel fibers may be indirectly measured by the changes in the P_{L1}/P_{L2} ratio. Considering that the microstructure of the cement paste and the ITZ is affected as a whole, the reduction of the P_{L1}/P_{L2} ratio may be attributed mainly to changes in the properties of steel fibers.

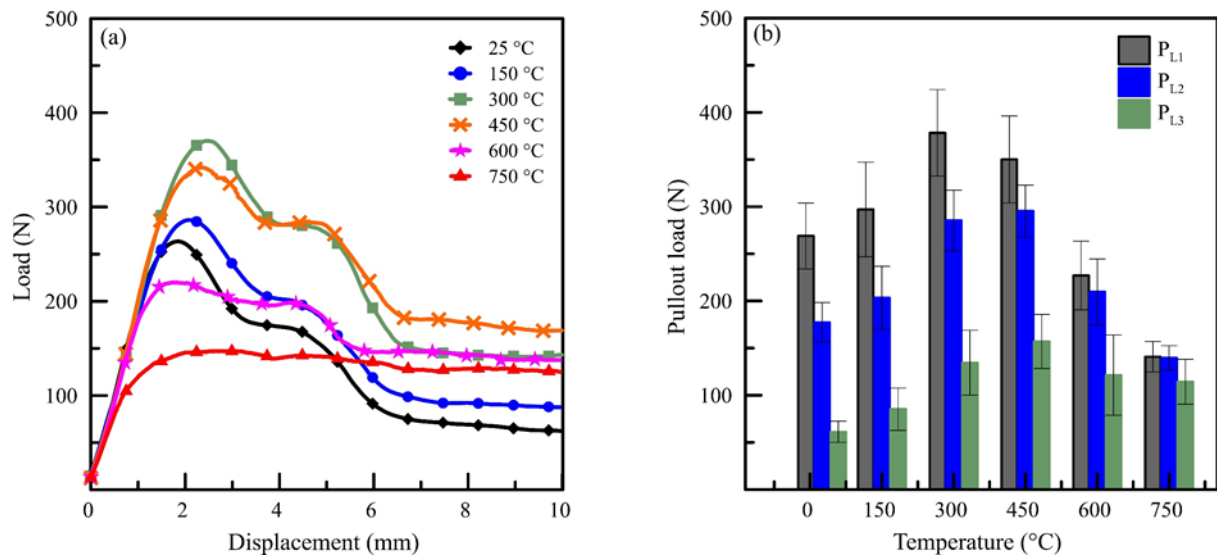


Figure 4.4 – (a) average load-displacement curves and (b) the maximum P_{L1} , P_{L2} , and P_{L3} values.

The results show that P_{L1} increases up to 30% for temperatures in the range of $150\text{ °C} \leq T \leq 450\text{ °C}$. The increase in maximum pullout load was justified by the changes in the Si/Ca ratio in the fiber-matrix ITZ, as shown in Figure 4.5. At room temperature, the Si/Ca ratio results represented systems with low concentration of C-

S-H (*i.e.* Si/Ca < 0.3 [137]). As temperature rised, the Si/Ca ratio increased to values between 0.5 and 0.8 within a distance of 7.5 mm of the fiber surface, which is in the typical range of C-S-H rich systems (*i.e.* Si/Ca > 0.3 [137]). This may be one of the first evidences that show that the fiber-matrix ITZ suffer changes that differ from the bulk matrix and may interefere with the bond-slip behavior of fibers. Two hypothesis were postulated for the microstructural changes evidenced: (1) the increase in Si/Ca ratio is related to a topochemical reaction between anhydrous cement particles and superheated water, and (2) the increase in Si/Ca ratio is justified by the consumption of C-H and SiO₂ in the ITZ for a pozzolanic reaction. These hypothesis may serve as evidence for future research on the topic, aiming to specifically study the mineralogical changes in the vicinity of the fibers. Moreover, the results show the formation of iron oxide expanding into the ITZ and changing the fracture mechanism from fiber-matrix to oxide-matrix – which affects the bond-slip mechanism.

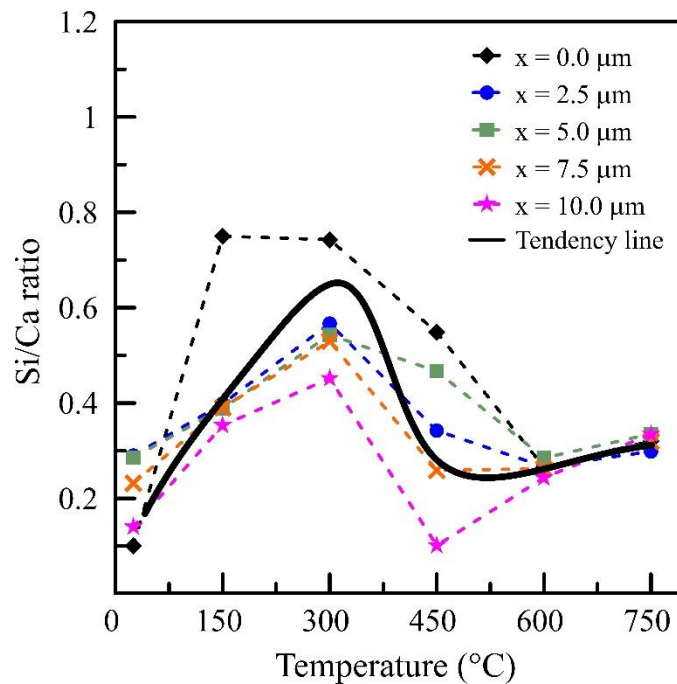


Figure 4.5 – Effect of temperature on the steel fiber’s tensile strength and rupture strain

Moreover, the P_{L1}/P_{L2} ratio reduced from 1.52 (25 °C) to 1.01 (750 °C), which serves as an indirect evidence of the reduction in the bending stiffness of the steel fibers with temperature increase. The aforementioned result suggests that the the mechanical interlock provided by the hooks of the fiber reduce with temperature increase and may be considered negligible for temperature values greater than 600 °C. The rupture of steel fibers began to occur instead of the debonding and slip of fibers

for pullout specimens exposed to temperature of 600 °C and above. These experimental results suggested that the the tensile strength of fibers is exceeded before the shear strength of the fiber–matrix interaction for $T \geq 600$ °C and is confirmed by the numerical simulation conducted, presented in Figure 4.6.

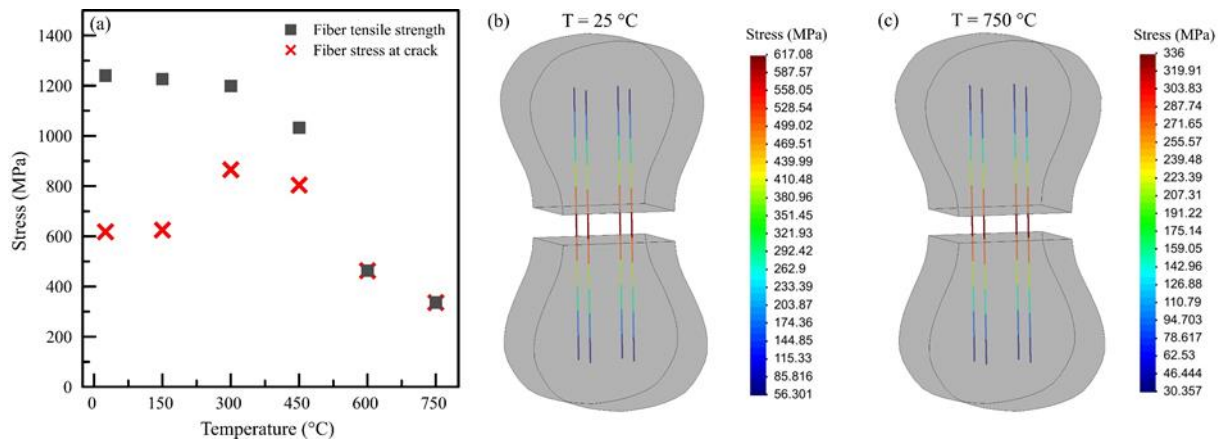


Figure 4.6 – (a) average load-displacement curves and (b) the maximum P_{L1} , P_{L2} , and P_{L3} values.

Moreover, P_{L1} reduced up to 48% for temperatures ranging between 600 °C $\leq T \leq 750$ °C. This is justified by the reduction in the bending stiffness of fibers, reduced contribution of the hooks, and the dehydration of hydrated products in the fiber-matrix ITZ. Even with those considerations, additional factors that significantly influence the behavior evidenced can be cited, such as the coarsening of the ITZ pore structure, the significant cracking caused by the thermal gradients, and the reversible transformation of quartz from α -trigonal to β -hexagonal at 573 °C.

When compared to room temperature results, the values of P_{L3} significantly increase for all the temperatures evaluated. It is also important to notice that the maximum increase of 156.6% is detected at 450 °C, which may be associated with the changes in the Si/Ca ratio in the interfacial transition zone and the initial oxidation of steel fibers. Even for temperatures of 600 °C and above a significant increase is verified in terms of P_{L3} , which may be attributed to the changes in the fracture mechanism from fiber-matrix to oxide-matrix. Another relevant aspect is that the increase in confining forces caused by the shrinkage of the cement paste may influence the bond-slip results, as pointed out in the literature [103].

Therefore, the results presented in **Article A** and **Article B** contribute to a better understanding of the effects of temperature on the bond-slip behavior that governs the SFRC. The contributions are provided by investigating the effect of temperature on the microstructural, physical, and tensile properties of the fibers, as well as their bond-slip behavior. Lastly, the results may be employed for the

parameterization of numerical models that require the characterization of the fibers – as it is the case of explicit models that were recently proposed [138,139]. Prospective research topics can arise from the results obtained, such as: 1) the quantitative investigation of the mineralogical changes in the fiber-matrix ITZ as a function of temperature; 2) the effect of surface modification of fibers on the thermal-related bond-slip properties; 3) the implementation and validation of a thermo-mechanical numerical model with discrete and explicit representation of the fibers in the matrix. Lastly, it is imperative to state that these results reflect the SFRC dosage and fiber type employed in this study. Therefore, further studies must be conducted in order to better understand the influence of these variables and other matrix conditions on the results.

4.2 THERMAL-RELATED CHANGES IN SFRC MECHANICAL PROPERTIES

The determination of the bearing capacity of a SFRC structure affected by fire depends on the thermal-related changes in materials' mechanical properties. Although the evaluation of the compressive parameters is found in literature, this is a topic that was not sufficiently evaluated, especially regarding the post-crack tensile properties of the composite. A limited amount of test methods can be successfully applied to determine the post-crack tensile strength of the composite after temperature exposure, as discussed in Section 2.2.4. In this sense, **Article C** focused on the applicability of the DEWS test to determine the tensile parameters of SFRC after exposure to elevated temperatures. The mineralogical composition and the compressive parameters of the cementitious matrix have been determined as a function of temperature in order to have the complete characterization of the SFRC evaluated in this thesis.

At room temperature, the SFRC compressive parameters obtained were $f_c = 83.9$ MPa and $E_c = 36.3$ GPa, while the tensile parameters obtained by means of the DEWS test were $f_{Ft} = 3.81$ MPa, $f_{Fts} = 2.53$ MPa, and $f_{Ftu} = 1.31$ MPa. The increase in temperature resulted in a decrease in the compressive parameters of the composite, as seen in Fig. 4.7. The f_c reduced between 6.4% (150 °C) and 97.7% (750 °C) and the E_c have shown sharper reductions between 24.6% and 99.8% (750 °C) with respect to room temperature. A severe reduction in E_c is verified between 150 °C and 450 °C, which is justified in classical literature by the extensive cracking of the

cementitious matrix and the aggregate-paste ITZ, the dehydration of hydrated products, and the deterioration of aggregates [40,69]. The K_c and K_{Ec} values obtained in this thesis are lower than the values prescribed by the Eurocode [20]. This result may be partially justified by the porosity increase caused by the degradation of micro-synthetic fibers and the differences in heat regimes employed. Another influencing factor is that the Eurocode's prescriptive curve is based on results obtained for cubic shaped specimens, while the results of this thesis are based on cylindrical specimens. The effect of specimen shape is relevant since cylindrical specimens tend to present greater reductions in K_c and K_{Ec} values than cubic specimens [104].

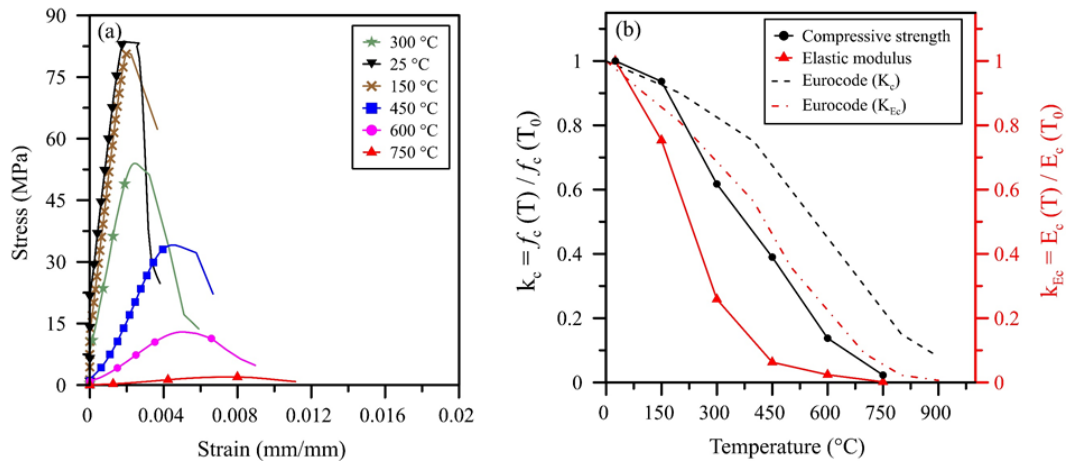


Figure 4.7 – (a) average stress-strain curve and (b) compressive strength and elastic modulus as a function of temperature

The thermal-related changes in the tensile properties of the composite are presented in Figure 4.8. The reductions in terms of tensile properties seems to follow a linear trend with the increase in temperature ($R^2 > 0.9$ in all cases). The f_{ft} of the matrix reduced between 12.3% (150 °C) and 96.8% (750 °C) with a rate of 5.4×10^{-3} MPa/°C. The f_{ftu} reduced between 15.9% (150 °C) to 99.2% (750 °C) and presented a degradation rate of 1.1×10^{-3} MPa/°C. It is worth to mention that no significant statistical reduction was observed for f_{ftu} for temperatures below 300 °C, which may be justified by the scatter of the test results in this temperature range. Moreover, the reduced or even enhanced effects of temperature on the bond-slip behavior of fibers up to ~450 °C may influence the results, as discussed in **Article B**.

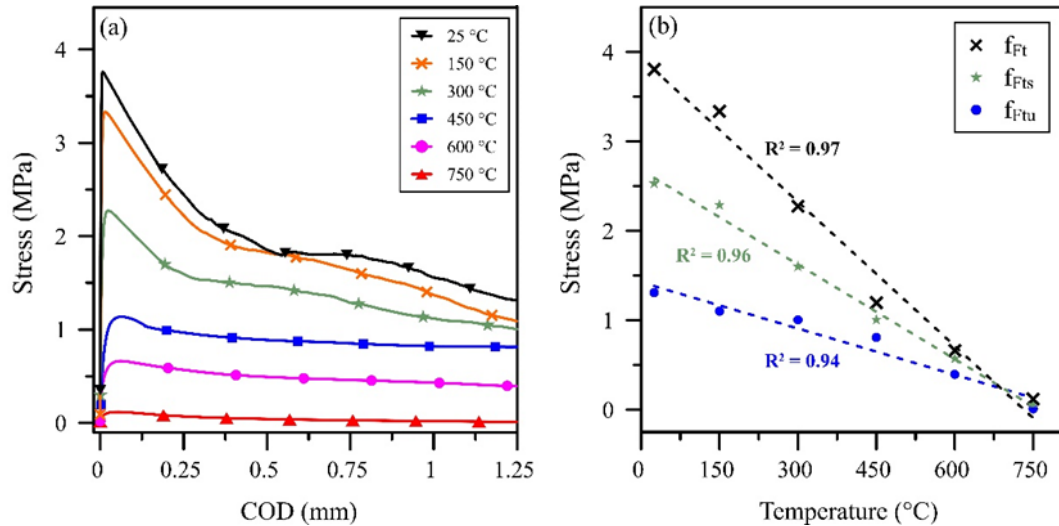


Figure 4.8 – (a) stress-COD average results and (b) tensile and post-crack tensile strength results

Moreover, the results obtained by means of the DEWS test are within the range of the prescriptive curves provided by the Eurocode [20] and the CNR DT-204 guideline for f_{ft} and for f_{ftu} , respectively, as shown in Fig. 4.9. The results are also comparable to those obtained by studies in similar methodological conditions using bending tests. Although a limited number of comparable results was found, most of the bending test's results tend to have greater K_{ftu} values than those obtained with the DEWS test. This difference may be related to the stress redistribution that occurs due to the variable gradient of tensile stresses along the cracked section during the bending test, while the stresses are mostly distributed through the entire vertical crack in the DEWS configuration. Likewise, the local curvature in bending tests may result in a second-order confinement pressure that may increase the flexural strength, especially for greater crack opening values [140].

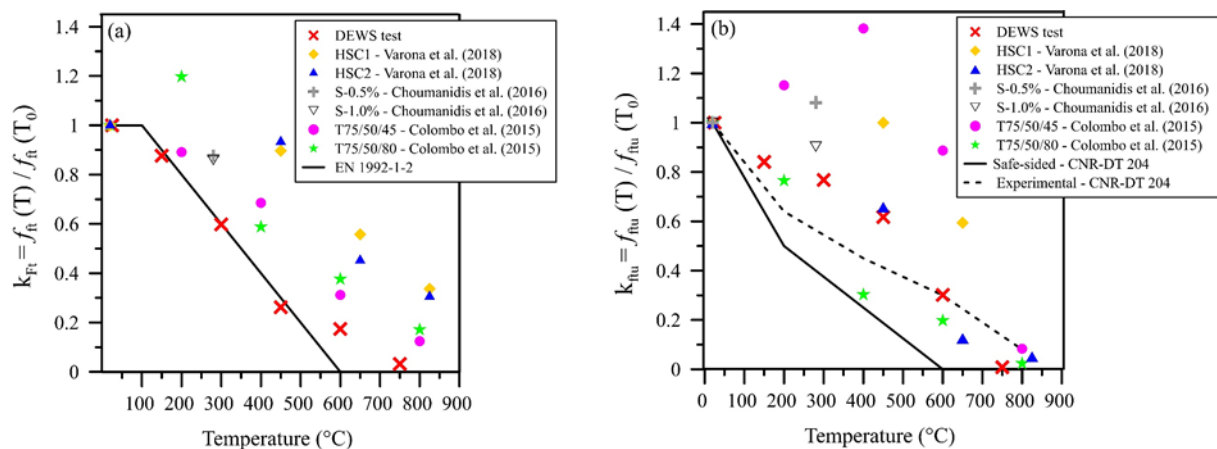


Figure 4.9 – Comparison with guidelines and literature results in terms of (a) K_{ft} and (b) K_{ftu}

Lastly, the qualitative evaluation of the DEWS test have shown the absence of deterioration in the contact between the apparatus and the specimen, avoiding any increased frictional interaction. As presented, the results obtained in terms of K_{ft} and K_{ftu} agreed well with the reduction curves prescribed by European guidelines and were comparable to those obtained by bending tests in literature. These factors combined suggest that the DEWS test is an effective indirect test method for the determination of the post-cracking behavior of SFRC. However, the variability of the post-crack tensile strength is a challenging aspect to deal with (up to 41% for f_{ftu}). Even under these considerations, average results may be used provided that a representative statistical population is considered for assessing mean values. Lastly, Figure 4.10 shows parameters regarding the determination of the sample size as a function of the admissible error for the test, which may be used to guide future studies employing the DEWS test in post-heating conditions.

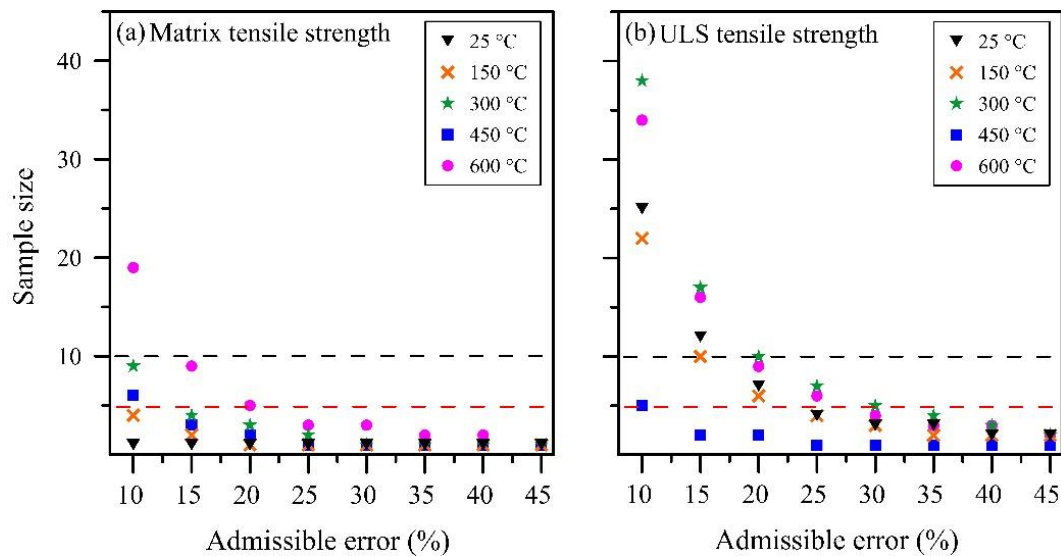


Figure 4.10 – Sample size required as a function of the admissible error for the (a) f_{ft} and (b) f_{ftu} values

4.3 EFFECT OF FIRE ON SFRC SECTIONS

The exposure of tunnels to fire induces a heat regime that may be described by a one-dimensional conduction process with greater temperature values at the intrados and lower at the extrados. This process differs considerably from the thermal regime induced in oven-heated experimental campaigns, in which the concrete specimens are evaluated for a given temperature. In this context, **Article D** is focused on an experimental campaign aiming to determine the fire-induced thermal field on SFRC prismatic specimens. After cooling, the prismatic specimens exposed to fire were tested to determine the post-crack flexural strength of the material by means of

bending and DEWS tests. Taking as basis the experimental campaigns conducted, **Article E** focused on the implementation of a numerical model capable of assessing the bending capacity of FRC, RC, and RC-FRC sections exposed to fire. The numerical model developed employed a staggered analysis that decouples the thermal problem from the mechanical one. A subroutine focused on simulating the occurrence of thermal spalling was implemented, in which the spalled layers are deleted from the analysis as the spalling occurs. The model was validated with the experimental results in terms of distribution of temperatures and the bending capacity of the SFRC prismatic specimens, presented in **Article D**. Lastly, a parametric study was conducted comparing the bending capacity reductions of RC, FRC, and RC-FRC solutions considering thermal spalling effects.

4.3.1 Results of the experimental campaign

The results in terms of thermal-field in SFRC have shown a wide range of temperatures along the section, as shown in Figure 4.11. After 120 minutes of HFC exposure, the temperatures inside the SFRC ranged between 612 °C ($z = 3$ cm) and 112 °C ($z = 15$ cm). The temperature distribution obtained in this thesis was comparable to literature results for MSFRC with comparable production and testing methodologies [68]. The aforementioned comparison may indirectly suggest that the thermal conductivity of concrete is more significantly influenced by the properties of the concrete mix than by the addition of fibers, especially considering concretes with a low fiber volume fraction. Moreover, a study conducted by Liu et al. [141] shows that an increase of 1% in the steel fiber content added to the mix increased the thermal conductivity of SFRC by ~ 0.1 W/m.K, which is close to negligible when compared to the influence of other variables, such as type of aggregate, moisture conditions, and the test methodology adopted in experiments [125,142,143]. Moreover, the numerical model implemented in this thesis was employed to estimate the distribution of temperatures in the SFRC section using parameters related to plain concrete and the thermal-field curves seems to agree well with the results obtained experimentally.

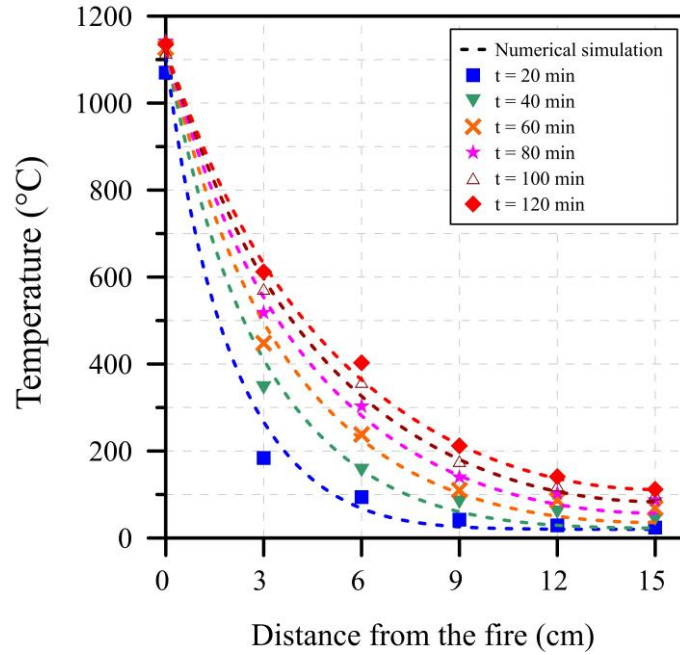


Figure 4.11 – Experimental and numerical results for the thermal field in the SFRC

Also, the distribution of K_c and K_{ftu} in the cross-section of segments was estimated comparing the experimental results with the prescriptive values in European guidelines, as shown in Figure 4.12. The comparison was made by pairing the internal temperature readings and the K_c and K_{ftu} obtained experimentally in **Article C** (solid line) and the prescriptive values given by the respective European guideline (dashed line). In terms of K_c , the experimental results yielded a more pronounced reduction in the contribution of the layers located in the range of $0 \text{ cm} \leq z \leq 12 \text{ cm}$ than the Eurocode results. Moreover, the layers closer to the fire (*i.e.* $z \leq 3 \text{ cm}$) provide virtually no contribution to the bearing capacity of the SFRC section in the experimental results. This is an indirect result of the more pronounced reduction in f_c obtained by evaluating cylindrical specimens than cubic ones, the differences in heat regime, and presence of microsynthetic fibers – as discussed in Section 4.2. The reductions in terms of K_{ftu} are similar between those obtained experimentally and the prescriptive curve presented by the CNR DT 204, being the latter slightly more conservative.

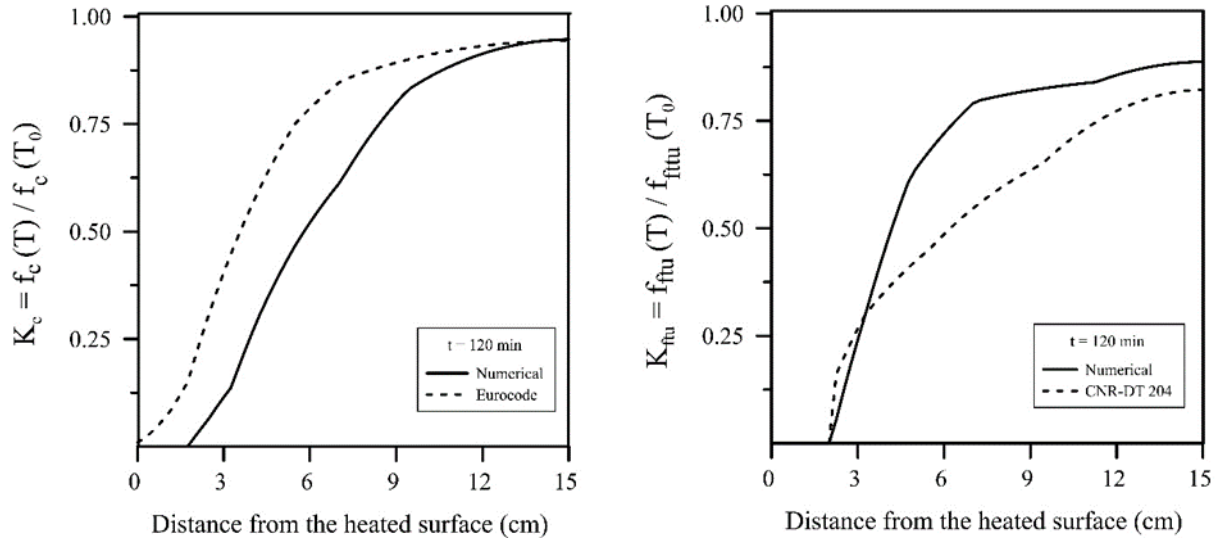


Figure 4.12 – Experimental and numerical results for the thermal field in the SFRC

After cooling, the specimens affected by fire were tested in bending and DEWS tests configurations, as shown in Figure 4.13. In the bending test configuration, the rupture peak associated with the matrix cracking is absent in specimens after fire exposure. The post-fire values of f_{LOP} and f_{R1} reduced by 88.9% and 40.1%, respectively, when compared with reference specimens. These reductions may be justified by the dehydration of hydrated products in the cement paste, the severe temperature gradients induced by fire, and the changes in the bond-slip mechanism of fibers with temperature increase. Contrarily, the f_{R3} values did not show significant differences between the pre- and post-fire values, the slight differences observed being primarily due to the scatter of the bending test itself.

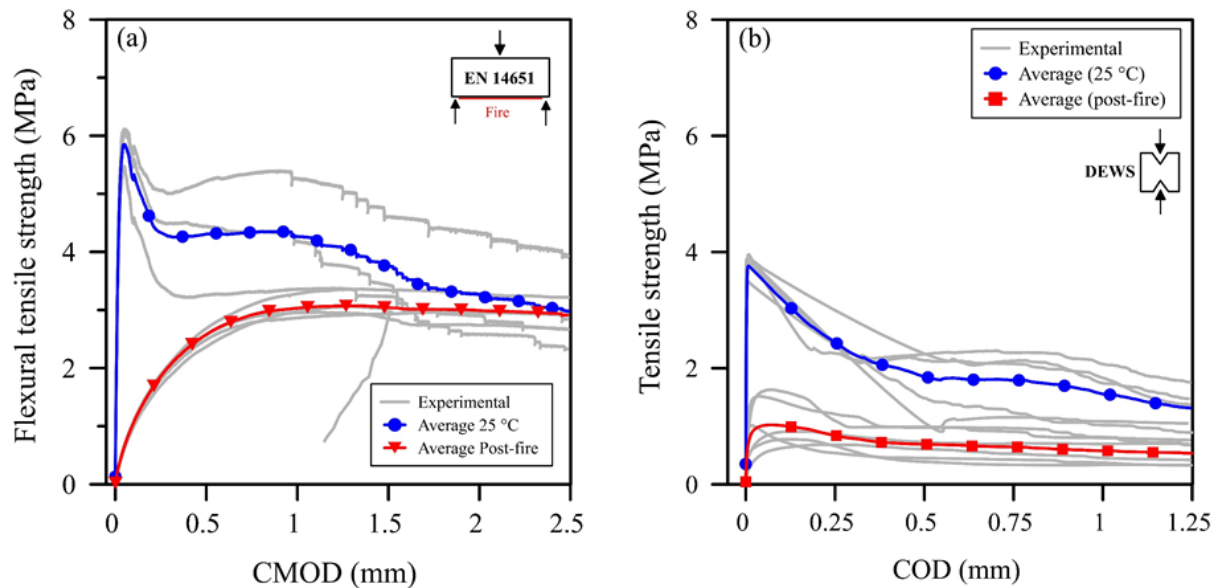


Figure 4.13 – (a) bending stress-CMOD curves and (b) DEWS stress-COD curves before and after fire

A reasonable explanation for the non-significance of results at greater crack openings was provided by conducting a sectional analysis with the numerical model developed in this thesis, shown in Figure 4.14. The numerical simulation shows that the bearing capacity of the SFRC is slightly reduced when the fire affects the flexural tensile region of the specimens (sagging bending). Contrarily, a great reduction in the bearing capacity is verified when the fire affects the compressive zone of the specimen (hogging bending). This occurs because the scalar value of f_c is greater than the scalar value of f_{ftu} , therefore the temperature-related reductions in f_c tend to affect more significantly the bearing capacity of the cross-section. Secondly, the K_c is greater than K_{Ftu} for the same internal temperature value, which results in a more rapid loss of bearing capacity when the compressive region of the beam is heated. Another intervening factor may be related to the crushing and grinding in the support-specimen contact, which may impair the translational movement and induce a restraining axial force during the test. This condition could have an increased importance when higher fiber contents are used which implies in higher levels of post-crack strength.

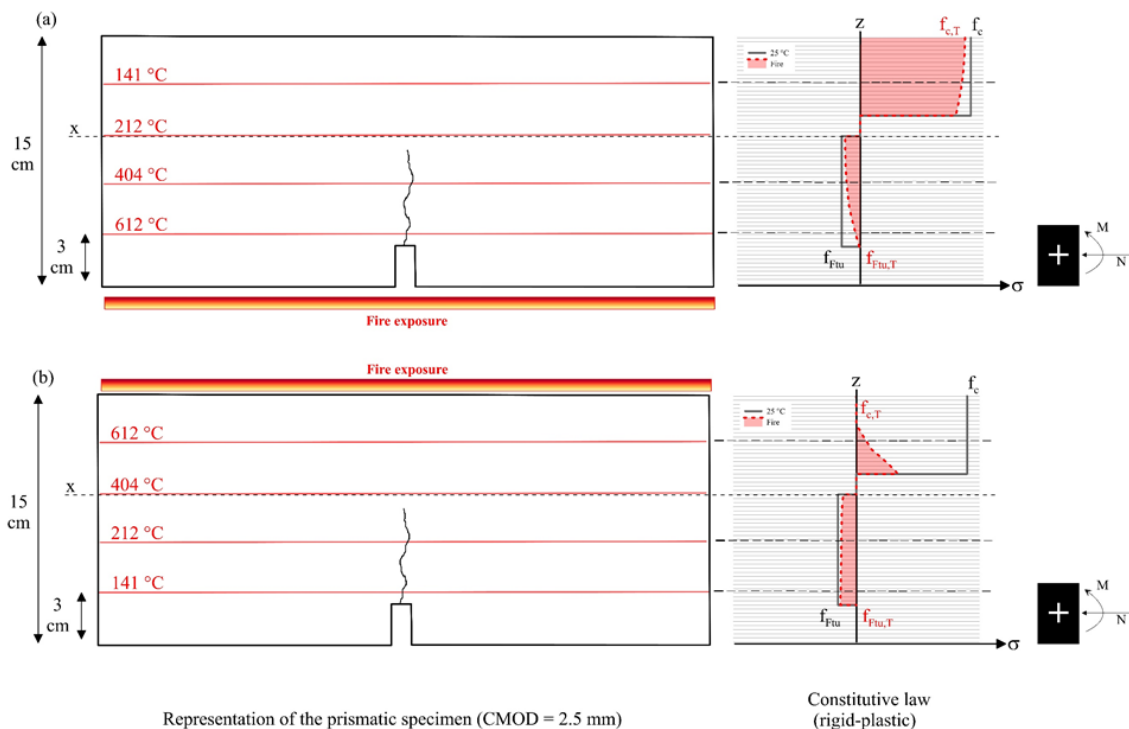


Figure 4.14 – Bending capacity with fire affecting specimens in (a) sagging bending (b) hogging bending

Regarding the DEWS test, the fire exposure resulted in reductions of 71.4% and 59.1% for the respective tensile properties of f_{ft} and f_{ftu} . The post-fire tensile properties obtained by the DEWS test may be compared to the results obtained for

oven-heated specimens, which were presented in Section 4.2. In this sense, a comparison between the post-fire stress-COD curves and the results for temperatures ranging between 150 °C and 750 °C are presented in Fig. 4.15. It is possible to observe that the post-fire f_{ftu} values tend to the average result obtained for temperatures between 450 °C and 600 °C. In this sense, the numerical simulation was employed as a tool to assess the distribution of f_{ftu} in the cross-section as a function of z (see Fig. 4.16). The results show that the post-fire f_{ftu} is null up to $z = 2$ cm and increases non-linearly up to 85.9% of the initial f_{ftu} value with the increase in z . Therefore, the average post-fire f_{ftu} value determined experimentally tends to represent the layers closer to the fire, which indicates that the DEWS test was capable of yielding more representative results than the EN 14651 bending test for the definition of f_{ftu} in post-fire conditions.

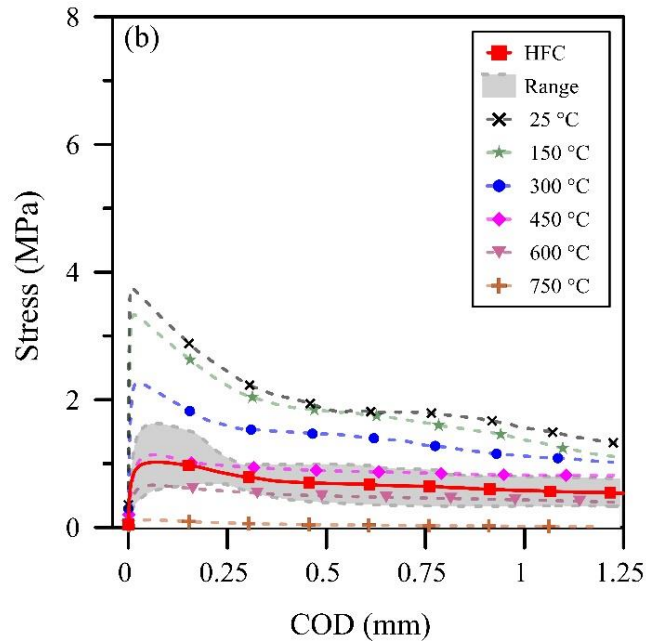


Figure 4.15 – Stress-COD results obtained after fire exposure and temperature exposure

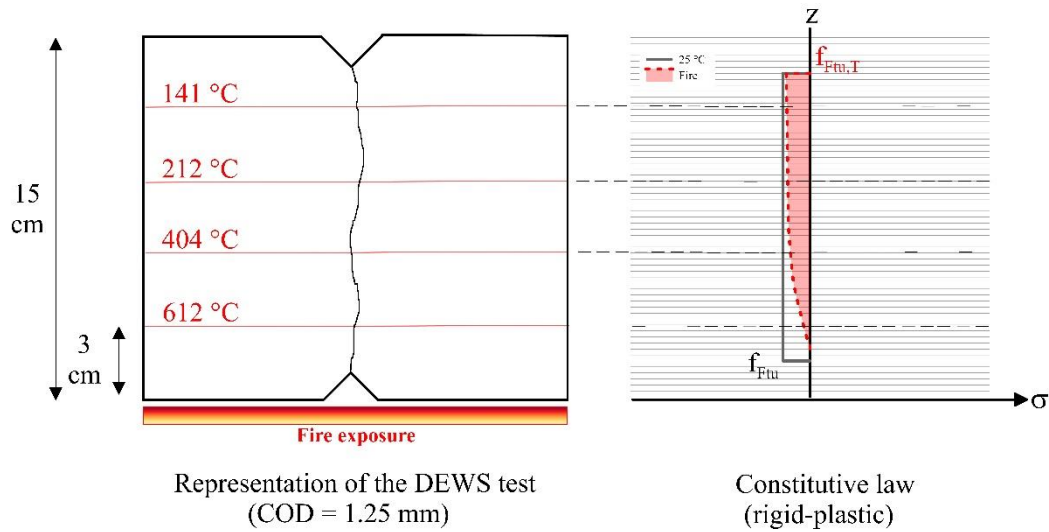


Figure 4.16 – Distribution of f_{ttu} as a function of z for the DEWS test

4.3.2 Results of the parametric study

Figure 4.17 show the effect of the ISO 834 fire curve and the HFC on the bending capacity of RC, FRC, and RC-FRC sections without considering thermal spalling. For all reinforcement types, the reductions in bending capacity were lower for the sections affected by the ISO-834 than those affected by the HFC, independently of the magnitude of the axial load. This difference is more pronounced for lower values of t , which is a reasonable considering that the ISO-834 fire curve prescribes lower heating rate and lower maximum temperature values than the HFC. The reduction in FRC bending capacity caused by the HFC was 3.5% to 5.5% greater than the reductions caused by the ISO-834, which shown to be a range valid for all values of t . Therefore, the FRC solution shows very low sensitivity to the characteristics of the fire curves evaluated in this study, which was attributed to the distributed reinforcement and the reduced contribution of the post-crack tensile properties to the sectional bearing capacity.

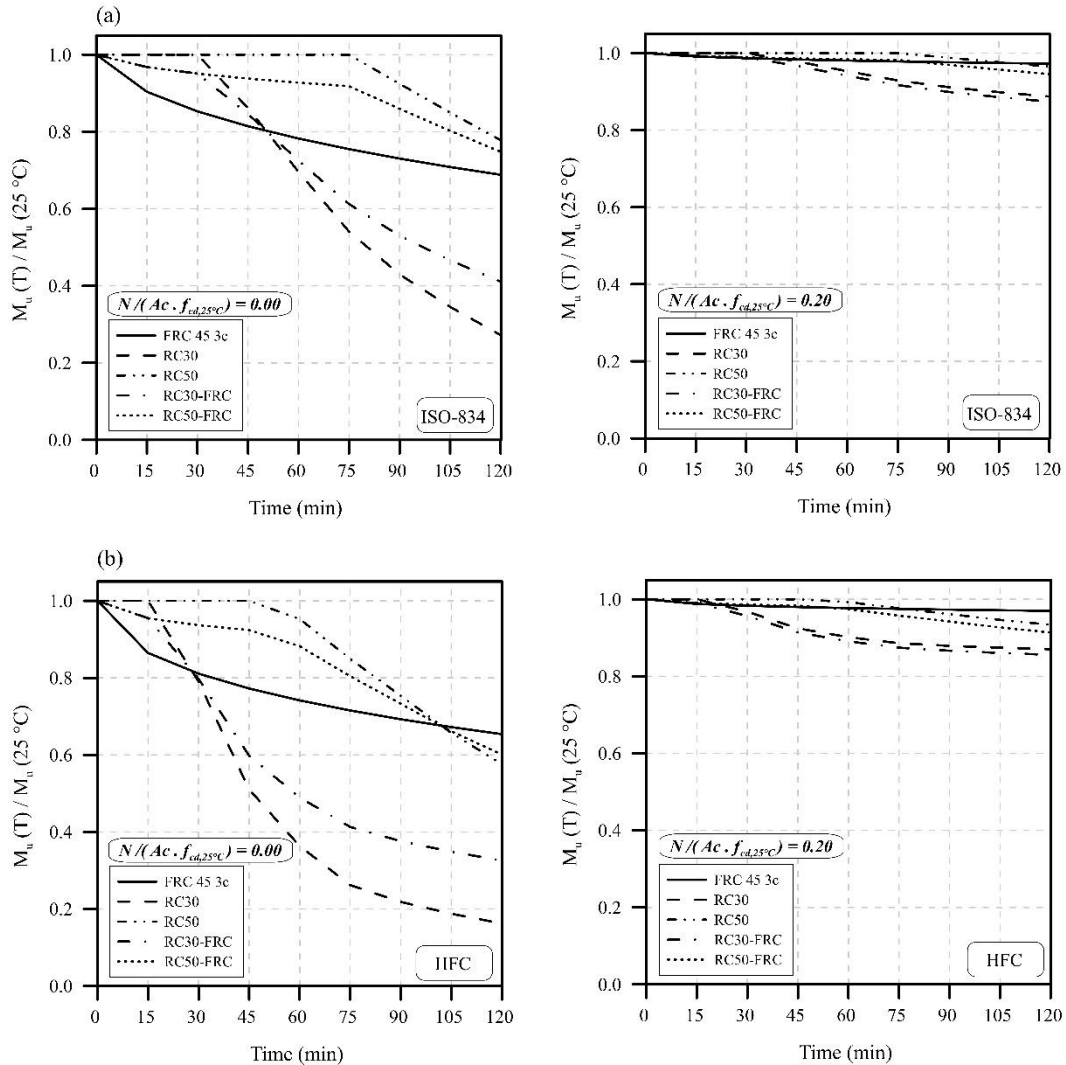


Figure 4.17 – Bending capacity of the sections exposed to (a) the ISO 834 and (b) the HFC fire curves

In cases where thermal spalling is avoided, FRC and RC-FRC solutions proved to be less sensitive to fire than conventional RC30. Moreover, the increase in concrete cover considerably reduced the effect of fire on the bending capacity of RC sections, which is directly associated with the lower temperatures developed in steel and the consequently reduced mechanical deterioration of the rebars. When the solutions are subjected to an axial load ratio of 0.20, the reductions in the bending moment capacity are considerably mitigated. This was evidenced for all reinforcement types and it occurs because a failure mode based on the crushing of the compressive layer that is not affected by fire occurs.

Moreover, the results proved that the cross-sectional ductility (represented by the curvature, χ) increases with the fire duration, as shown in Fig. 4.18. This increase was greater for RC30 and RC30-FRC alternatives, independently of the axial load ratio. Among the RC and RC-FRC solutions, the RC50 and RC50-FRC solution have shown similar ductility increments and obtained the lowest increase in ductility due

to the lower effective depth of the reinforcement. For simple bending, the FRC obtained the lowest increase in ductility after $t = 120$ min. When the section is subjected to a 0.20 axial load ratio, the RC solutions and the respective hybrid alternatives have shown similar ductility patterns and the FRC solution had the lowest increase in ductility, which occurs due to the failure being governed by concrete crushing.

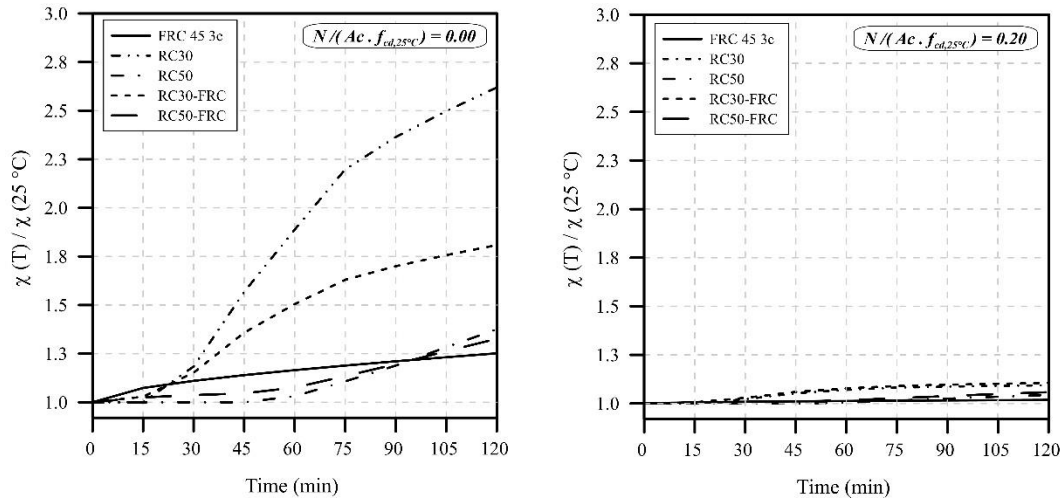


Figure 4.18 – Effect of fire on the ductility of the reinforcing solutions affected by HFC

In this sense, the effect of thermal spalling was evaluated considering the HFC since it has proven to be the worst fire scenario evaluated in this study. The reduction in bending capacity of the sections is evaluated considering two spalling parameters: the spalling rate (R_{sp}) and the percentage of section lost (s_l). Figure 4.19 illustrates the effect of spalling parameters on the bending capacity of FRC, RC30, and RC50 solutions.

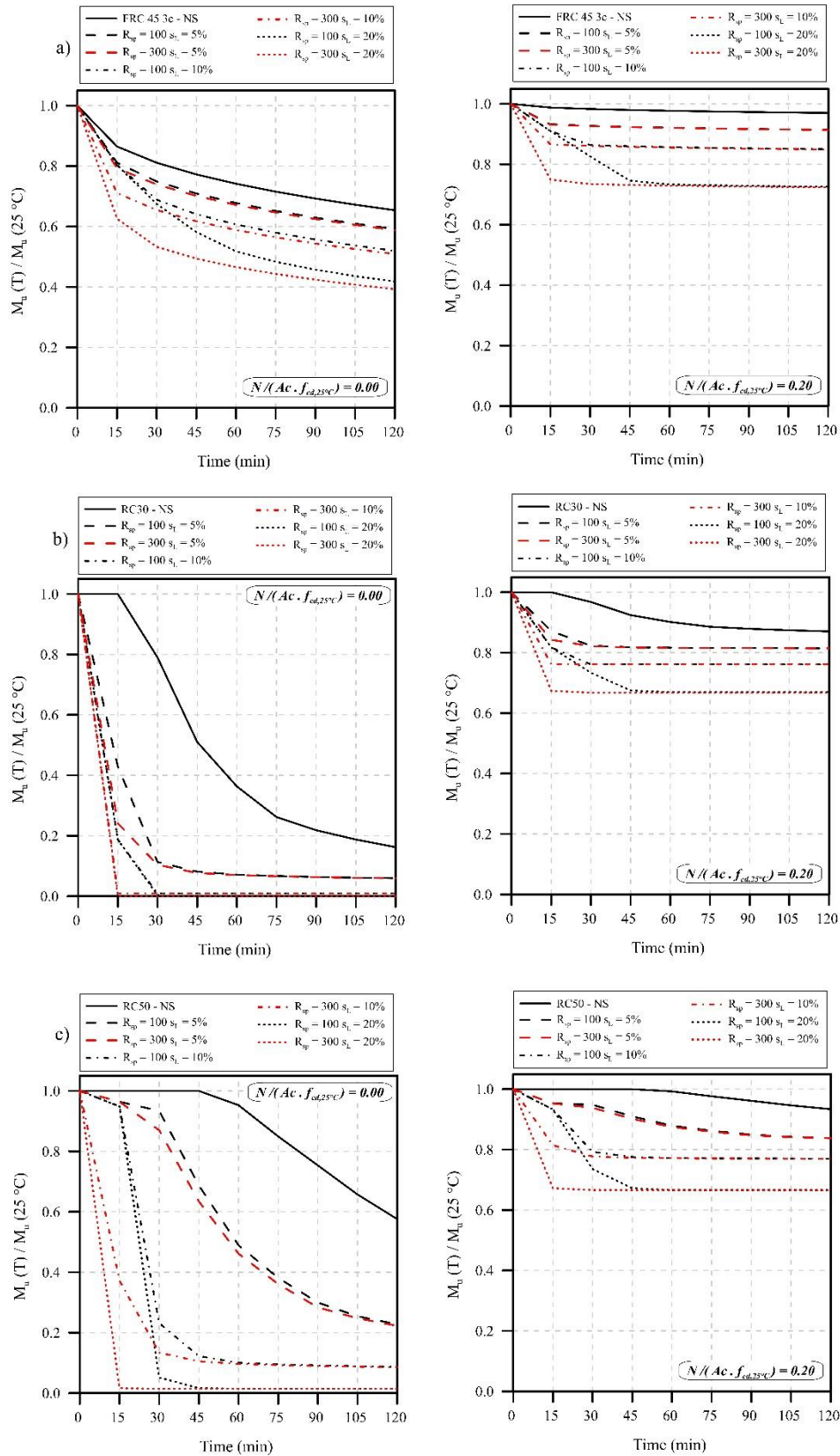


Figure 4.19 – Effect of spalling parameters on the bending capacity of (a) FRC, (b) RC30, (c) RC50 solutions

The results show that the increase in R_{sp} considerably influences the rate of reduction in the bending capacity for the initial moments of fire, while the increase in

s_L tends to predominantly influence the bending capacity for longer fire durations. A rapid reduction in bending capacity is noticed for RC sections, which arise from the rapid increase in temperature at the rebars due to the reductions in H and the aggravated thermal field induced in the section. The occurrence of thermal spalling reduces the simple bending capacity of RC30 sections by over 90% within the 30 minutes of fire with minimal influence of R_{sp} and s_L . Likewise, the increase in concrete cover had negligible influence in mitigating the reductions when moderate ($s_L = 10\%$) or severe ($s_L = 20\%$) thermal spalling occurs, which can be derived by comparing RC30 and RC50 results. However, the reductions in RC50 bending capacity was considerably lower than RC30 when mild ($s_L = 5\%$) thermal spalling occurred, especially for lower values of t . For sections with 0.20 axial load ratio, reductions of 16%, ~23%, and ~33% occurred for the respective s_L values of 5%, 10%, and after $t = 120$ min, independently of the position of the rebars.

Alternatively, the FRC solution have shown to be less sensitive to the occurrence of fire with thermal spalling than RC. The rate of reduction in bending capacity is lower for the FRC solution, which results in higher residual capacity after longer fire durations. Regarding the FRC simple bending scenario, reductions of ~40%, 49%, and ~60% occurred for the respective s_L values of 5%, 10%, and 20% after $t = 120$ min. For sections with 0.20 axial load ratio, reductions of ~9%, 15%, and 27% occurred for the respective s_L values of 5%, 10%, and 20% after $t = 120$ min.

Figure 4.20 illustrates the effect of spalling parameters on the bending capacity of RC30-FRC, and RC50-FRC hybrid solutions. The RC-FRC solutions have shown slightly lower bending reductions than the respective RC solution, which may be justified by the contribution of fibers to the bending capacity. When comparing RC30-FRC and RC50-FRC, the increase in concrete cover seems to mitigate the reductions for lower durations of fire, especially for $t \leq 15$ min and for $R_{sp} = 100$ mm/h. However, the benefits provided by the increase in concrete cover for hybrid solutions may be considered negligible for longer fire durations. Therefore, the results obtained in this parametric study are indicative that the occurrence of spalling considerably affects the bearing capacity of FRC, RC, and hybrid RC-FRC sections.

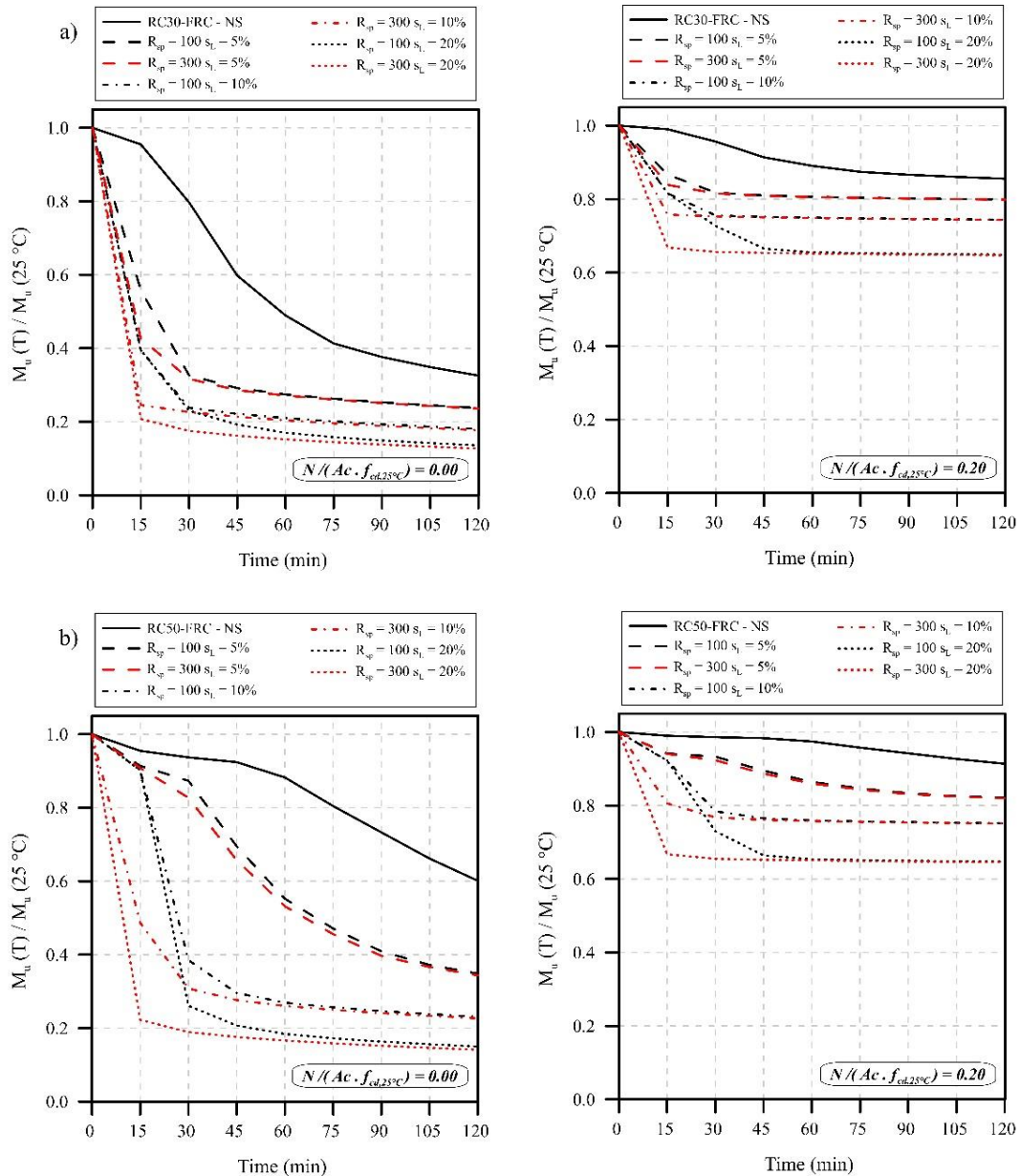


Figure 4.20 – Effect of spalling parameters on the bending capacity of (a) RC30-FRC and (b) RC50-FRC hybrid solutions

In this sense, the results presented in **Article D** provide experimental results regarding the temperature distribution in SFRC and the post-fire bending capacity of prismatic specimens made with this composite material. Also, the experimental results obtained serves as a mean to validate the numerical model developed and presented in **Article E**. Lastly, a parametric study is conducted in which FRC, RC, and RC-FRC sections are compared with varying parameters, among them the position of rebars and the thermal spalling parameters. These results represent a valuable reference for the engineering community since the procedures serves as tool for the design and rehabilitation of TBM tunnels affected by fire.

CHAPTER 5.

CONCLUSIONS

This thesis focused on evaluating the thermo-mechanical properties of steel fiber reinforced concretes. A complete mechanical characterization in terms of compressive and tensile properties was conducted as a function of temperature. Moreover, the thermal field and tensile properties of SFRC exposed to fire were experimentally determined. Based on the conducted experimental campaign, a numerical model capable of simulating the bearing capacity of RC, FRC, and RC-FRC sections was implemented and a parametric study was conducted, with a special interest in TBM tunnel linings. The results have shown that the mineralogical changes in the cement paste and the fiber-matrix ITZ can be successfully correlated to explain the meso-scale behavior of SFRC, which is a valuable information for simulation purposes. Based on the experimental results, the fire-related stability of FRC, RC, and RC-FRC tunnel sections can be calculated to determine the effect of fire on the bending capacity of tunnel structures. In this context, this thesis contributed to improve the knowledge regarding the effect of fire events on SFRC, as well as provided a design tool for the assessment of the bending capacity of tunnel sections with and without the occurrence of thermal spalling.

The reductions observed in terms of f_c and f_t were satisfactorily correlated to the mineralogical changes in the cement paste, which is also well-established in the classic literature. However, the post-crack parameters f_{ts} and f_{tu} were more considerably influenced by the properties of the fiber-matrix ITZ than the bulk matrix properties. At room temperature, the fiber-matrix ITZ had a Si/Ca ratio lower than 0.3, which is a classic indicator of a C-H rich system. Although the bulk matrix underwent dehydration process with the increase in temperature, the Si/Ca ratio in the fiber-matrix ITZ increased to values greater than 0.5 – which is characteristic of systems with C-S-H. Moreover, the maximum pull-out load values

increased up to ~30% for $T \leq 450$ °C and decreased for greater temperature values, which is another evidence that this thermal-related densification of the fiber-matrix ITZ is strongly correlated to the bond-slip behavior of the fibers. Additionally, the fiber-matrix dynamic frictional interaction increased for all temperatures evaluated, which is influenced by the densification of the fiber-matrix ITZ, the expansion of the iron oxide into the porosity of the ITZ for $T \geq 600$ °C, the consequent increased confining forces, and the change in debonding mechanism from fiber-matrix to oxide-matrix.

When embedded in cementitious matrix, the mechanical interlock provided by the hooks reduced as temperature increased, which may be related to the reduction in bending stiffness of the fibers and the deterioration of the cementitious matrix. Also, the increase in temperature reduced the tensile strength and increased the rupture strain of the steel fibers, which occurred due to the steel grain-growth and recrystallization processes. The thermal oxidation of steel resulted in a slight reduction tendency in the effective cross-sectional area of fibers for $T \leq 750$ °C, while a reduction of ~54% was evidenced for $T = 1000$ °C. Although the fibers' tensile strength reduced, the bond-slip mechanism have shown to prevail, without fiber rupture, up to ~600 °C. This means that for temperatures above ~600 °C a brittle behavior can be expected of SFRC layers in a structure, instead of the traditional pseudo-ductile behavior. The aforementioned results were evidenced in the experimental campaign and also confirmed by a numerical simulation with discrete and explicit representation of the steel fibers.

Regarding the meso-scale behavior of the composite, it is important to remark that no statistically significant change was observed in terms of f_{ftu} values for $T \leq 300$ °C. In this sense, the compilation of evidences related to the densification of the fiber-matrix ITZ, the increasing pullout load values, and the non-significant changes in terms of f_{ftu} for $T \leq 300$ °C compose the the first indicators that the post-crack mechanical properties must be interpreted in a different manner than f_c and f_t . More than that, it also suggests that mineralogical changes that occur in the bulk matrix cannot be entirely extrapolated to the fiber-matrix ITZ. Therefore, it can be concluded that the post-crack behavior of the composite is mostly governed by the thermal-related changes in (1) the steel fiber, (2) the fiber-matrix ITZ, and (3) the bond-slip behavior of the hooked-end steel fibers. These results provided an advance in the knowledge on the general behavior of the SFRC subjected to elevated temperatures. Moreover, the results indicate that the DEWS test is an adequate

methodology to determine the post-crack tensile properties of SFRC exposed to elevated temperatures.

Moreover, the use of adequate test methods to determine the bond-slip behavior of fibers and the post-crack tensile properties of the SFRC is of paramount importance, especially after temperature exposure. For the pullout test, the use of double-sided specimens containing four embedded fibers resulted in a considerable lower dispersion of results than those typically obtained for single-fiber specimens. This was verified both in room temperature conditions as well as for specimens exposed to elevated temperatures, which denoted the suitability of this methodology for both scenarios. Similarly, the use of the DEWS test to determine the post-crack tensile properties of the composite have shown diminished intervening factors related to the interaction between the testing apparatus and the degraded specimen.

Although the aforementioned procedures are relevant to discretize the effect of temperature on the mechanical properties of SFRC, they are not sufficient to fully describe the behavior of the composite under a real fire event. This occurs because the bearing capacity of SFRC sections exposed to fire depends on the distribution of temperatures and the consequent thermo-mechanical properties of the internal layers of concrete. After exposure to a hydrocarbon fire simulation, the distribution of temperatures in SFRC is comparable to those obtained by plain concrete and MSFRC results in literature. Moreover, the thermal model employed in this thesis was developed considering well-established thermal parameters for plain concrete, being capable of representing the distribution of temperatures inside the SFRC with errors below 11% for a fire duration of 120 min. The sum of these factors indicate that the distribution of temperatures in plain concrete and SFRC may be assumed equivalent for design purposes, especially for the fiber content employed in this thesis (35 kg/m³ or 0.45% in volume).

The validated thermal model was employed to determine the distribution of temperatures in segments for TBM tunnel linings exposed to the ISO 834 fire and the HFC. The coupled thermo-mechanical model was employed to determine the M-N interaction envelopes for a FRC section with $f_{ck} = 45$ MPa and $f_{R1k} = f_{R3k} = 3$ MPa (*i.e.* FRC 45 3c), two RC sections with $c = 30$ mm (RC30) and $c = 50$ mm (RC50), and the hybrid RC-FRC solutions. The fire simulation resulted that the reductions in bearing capacity caused by the ISO 834 fire curve are significantly lower than those caused by the HFC for all sections evaluated, which is reasonable considering the aggressive heating rate and higher maximum temperature of the HFC. For the FRC

sections, a comparable bearing capacity is reached when the $t_{\text{ISO}} = 2t_{\text{HFC}}$ condition is satisfied. Moreover, the reductions in bearing capacity of all the sections are lower when the fire affects the flexural-tensile region (*i.e.* sagging moment) than when it affects the flexural-compressive region (*i.e.* hogging moment) of the segments. These reductions in bearing capacity are even greater for axially loaded sections, meaning that the critical are those axially loaded and with fire affecting a hogging section.

When thermal spalling is not considered, both the FRC and the RC-FRC solutions are less sensitive to fire than the RC30 solution. This occurs because the reinforcement in RC30 solution is considerably close to the fire source, resulting in a rapid increase in temperature of steel, and a rapid drop in the mechanical contribution of the rebars. Nevertheless, the increase in concrete cover in RC50 solution have shown to considerably mitigate the reductions in terms of bending capacity due to the increased concrete cover protection. However, the increase in concrete cover has negligible influence on mitigating the reductions caused by mild or severe thermal spalling. In this sense, the use of FRC and RC-FRC sections resulted in lower reductions in bending capacity due to the diffuse reinforcing capacity of fibers in the cross-section. Among the solutions tested, the FRC section have shown the lowest reductions in terms of bending capacity when thermal spalling occurs. Lastly, the results show that the R_{sp} defines mostly the rate of reduction in bending capacity at the initial moments of the fire, while the total s_{L} influences the bending capacity at intermediate-final stages of the fire.

5.1 PROSPECTIVE RESEARCH TOPICS

In light of the studies produced in this thesis, a few prospective investigations can be suggested for future studies. These future studies may engage in investigations related to the following topics:

1. *Investigation on the bond-slip behavior of hooked-end steel fibers containing SiO_2 surface treatment after temperature exposure;*
2. *Experimentally assess the porosity and permeability changes in the fiber-matrix ITZ as a function of temperature, correlating to the bond-slip behavior of fibers;*
3. *Evaluate the applicability of indirect tensile strength methodologies to determine the post-crack tensile parameters of SFRC exposed to elevated temperatures;*

4. *Investigate the applicability of the rigid-plastic conversion factor proposed in fib MC-10 to determine the post-crack tensile properties of SFRC exposed to elevated temperatures;*
5. *Experimental analysis of the behavior of a full-scale tunnel ring exposed to fire considering sagging and hogging bending moments;*
6. *Development a thermo-hygro-mechanical model capable of computing the effect of thermal spalling on the bearing capacity of FRC sections;*
7. *Evaluate the influence of temperature on the tension stiffening effect in RC-FRC sections for the development of M-curvature diagrams;*
8. *Experimental and numerical analysis of tunnels built with sprayed fiber reinforced concrete exposed to fire events;*
9. *Evaluate the bond-slip behavior and the fiber-matrix ITZ of sprayed fiber reinforced concrete exposed to elevated temperatures;*
10. *Development of a thermo-mechanical model considering the discrete and explicit representation of fibers in concrete.*

REFERENCES

- [1] F.-L. Peng, Y.-K. Qiao, S. Sabri, B. Atazadeh, A. Rajabifard, A collaborative approach for urban underground space development toward sustainable development goals: Critical dimensions and future directions, *Front. Struct. Civ. Eng.* 15 (2021) 20–45. <https://doi.org/10.1007/s11709-021-0716-x>.
- [2] M.L. Tender, J.P. Couto, L. Bragança, The role of underground construction for the mobility, quality of life and economic and social sustainability of urban regions, *REM - Int. Eng. J.* 70 (2017) 265–271. <https://doi.org/10.1590/0370-44672016700151>.
- [3] I. Josa, A. Aguado, Infrastructure, innovation and industry as solutions for breaking inequality vicious cycles, *IOP Conf. Ser. Earth Environ. Sci.* 297 (2019) 012016. <https://doi.org/10.1088/1755-1315/297/1/012016>.
- [4] D. Klenert, L. Mattauch, O. Edenhofer, K. Lessmann, Infrastructure and inequality: insights from incorporating key economic facts about household heterogeneity, *Macroecon. Dyn.* 22 (2018) 864–895. <https://doi.org/10.1017/S1365100516000432>.
- [5] International Tunneling and Underground Space Tecnology, About tunneling: why go underground, (n.d.). <https://tunnel.ita-aites.org/en/why-go-underground>.
- [6] A.D. de Figueiredo, *Concreto reforçado com fibras.*, Universidade de São Paulo, 2012. <https://doi.org/10.11606/T.3.2012.tde-18052012-112833>.
- [7] A.B. Alvarez, *Characterization and modelling of SFRC elements*, Universitat Politècnica de Catalunya, 2013.
- [8] R. Monte, *Caracterização e controle do comportamento mecânico do concreto reforçado com fibras para tubos.*, Universidade de São Paulo, 2016. <https://doi.org/10.11606/T.3.2016.tde-18022016-124850>.
- [9] M. Di Prisco, G. Toniolo, Structural applications of steel fibre reinforced concrete, in: *Proc. Int. Work., CTE Publ., Milan (Italy)*, 2000. <http://hdl.handle.net/11311/248435>.
- [10] M. di Prisco, G. Plizzari, L. Vandewalle, Fiber Reinforced Concrete in the New fib Model Code, in: *3rd Fib Int. Congr. Inc. PCI Annu. Conv. Bridg. Conf. 2010*, Precast prestressed concrete institute, Chicago, IL, USA, 2010.
- [11] A. de la Fuente, P. Pujadas, A. Blanco, A. Aguado, Experiences in Barcelona with the use of fibres in segmental linings, *Tunn. Undergr. Sp. Technol.* (2012). <https://doi.org/10.1016/j.tust.2011.07.001>.
- [12] A. de la Fuente, A. Blanco, J. Armengou, A. Aguado, Sustainability based-approach to determine the concrete type and reinforcement configuration of TBM tunnels linings. Case study: Extension line to Barcelona Airport T1, *Tunn. Undergr. Sp.*

- Technol. 61 (2017) 179–188. <https://doi.org/10.1016/j.tust.2016.10.008>.
- [13] Federation Internationale du Beton, Model Code for Concrete Structures 2010, in: Ernst & Sohn, Germany, 2013: p. 434.
- [14] J.-L. Granju, S. Ullah Balouch, Corrosion of steel fibre reinforced concrete from the cracks, *Cem. Concr. Res.* 35 (2005) 572–577. <https://doi.org/10.1016/j.cemconres.2004.06.032>.
- [15] G.A. Plizzari, G. Tiberti, Steel fibers as reinforcement for precast tunnel segments, *Tunn. Undergr. Sp. Technol.* 21 (2006) 438–439. <https://doi.org/10.1016/j.tust.2005.12.079>.
- [16] G. Plizzari, C. Blom, J. Walraven, G. Tiberti, Concrete tunnel segments with combined traditional and fiber reinforcement, in: *Taylor Made Concr. Struct.*, CRC Press, 2008: pp. 66–66. <https://doi.org/10.1201/9781439828410.ch37>.
- [17] A. Caratelli, A. Meda, Z. Rinaldi, P. Romualdi, Structural behaviour of precast tunnel segments in fiber reinforced concrete, *Tunn. Undergr. Sp. Technol.* 26 (2011) 284–291. <https://doi.org/10.1016/j.tust.2010.10.003>.
- [18] F. Dehn, A. Herrmann, Concreto reforçado com fibra de aço (SFRC) em situação de incêndio – requisitos normativos, pré-normativos e código-modelo, *CONCRETO&Construções*. (2017) 108–112.
- [19] American Concrete Institute, Report on the Physical Properties and Durability of Fiber-Reinforced Concrete, Michigan, USA, 2010.
- [20] BS EN 1992-1-2, Eurocode 2 Design of concrete structures - Part 1-2: General rules-Structural fire design, *Des. Concr. Struct. - Part 1-2 Gen. Rules-Structural Fire Des.* (2004).
- [21] French Association of Civil Engineering, Ultra high-performance fibre-reinforced concretes: recommendations, France, 2013. <https://www.afgc.asso.fr/app/uploads/2007/10/Recommandations-BFUP-Juin-2013.pdf>.
- [22] CNR-DT 204, Guide for the Design and Construction of Fibre-Reinforced Concrete Structures, *Ital. Natl. Res. Counc. (CNR)*, Rome, Italy. (2007). <https://doi.org/10.14359/10516>.
- [23] Brazilian National Standards Organization (ABNT), NBR 15200: Fire design of concrete structures, Rio de Janeiro, RJ, 2012.
- [24] International Tunnelling and Underground Space Association, ITAtech Report n°7 - Design guidance for precast fibre reinforced concrete segments, 2016.
- [25] C.S. Poon, Z.H. Shui, L. Lam, Compressive behavior of fiber reinforced high-performance concrete subjected to elevated temperatures, *Cem. Concr. Res.* 34 (2004) 2215–2222. <https://doi.org/10.1016/j.cemconres.2004.02.011>.
- [26] Y.-S. Tai, H.-H. Pan, Y.-N. Kung, Mechanical properties of steel fiber reinforced reactive powder concrete following exposure to high temperature reaching 800°C, *Nucl.*

- Eng. Des. 241 (2011) 2416–2424. <https://doi.org/10.1016/j.nucengdes.2011.04.008>.
- [27] D. Choumanidis, E. Badogiannis, P. Nomikos, A. Sofianos, Barcelona test for the evaluation of the mechanical properties of single and hybrid FRC, exposed to elevated temperature, *Constr. Build. Mater.* 138 (2017) 296–305. <https://doi.org/10.1016/j.conbuildmat.2017.01.115>.
- [28] P. Pliya, A.L. Beaucour, A. Noumowé., Contribution of cocktail of polypropylene and steel fibres in improving the behaviour of high strength concrete subjected to high temperature, *Constr. Build. Mater.* (2011). <https://doi.org/10.1016/j.conbuildmat.2010.11.064>.
- [29] D. Choumanidis, E. Badogiannis, P. Nomikos, A. Sofianos, The effect of different fibres on the flexural behaviour of concrete exposed to normal and elevated temperatures, *Constr. Build. Mater.* 129 (2016) 266–277. <https://doi.org/10.1016/j.conbuildmat.2016.10.089>.
- [30] A. Jameran, I.S. Ibrahim, S.H.S. Yazan, S.N.A.A. Rahim, Mechanical properties of steel-polypropylene fibre reinforced concrete under elevated temperature, in: *Procedia Eng.*, 2015. <https://doi.org/10.1016/j.proeng.2015.11.146>.
- [31] J. Xiao, H. Falkner, On residual strength of high-performance concrete with and without polypropylene fibres at elevated temperatures, *Fire Saf. J.* (2006). <https://doi.org/10.1016/j.firesaf.2005.11.004>.
- [32] P. Sukontasukkul, W. Pomchiengpin, S. Songpiriyakij, Post-crack (or post-peak) flexural response and toughness of fiber reinforced concrete after exposure to high temperature, *Constr. Build. Mater.* 24 (2010) 1967–1974. <https://doi.org/10.1016/j.conbuildmat.2010.04.003>.
- [33] A.C.S. Bezerra, P.S. Maciel, E.C.S. Corrêa, P.R.R. Soares Junior, M.T.P. Aguilar, P.R. Cetlin, Effect of High Temperature on the Mechanical Properties of Steel Fiber-Reinforced Concrete, *Fibers*. 7 (2019) 100. <https://doi.org/10.3390/fib7120100>.
- [34] F.B. Varona, F.J. Baeza, D. Bru, S. Ivorra, Influence of high temperature on the mechanical properties of hybrid fibre reinforced normal and high strength concrete, *Constr. Build. Mater.* 159 (2018) 73–82. <https://doi.org/10.1016/j.conbuildmat.2017.10.129>.
- [35] M. Colombo, M. di Prisco, R. Felicetti, SFRC exposed to high temperature: Hot vs. residual characterization for thin walled elements, *Cem. Concr. Compos.* 58 (2015) 81–94. <https://doi.org/10.1016/j.cemconcomp.2015.01.002>.
- [36] D.A.S. Rambo, A. Blanco, A.D. de Figueiredo, E.R.F. dos Santos, R.D. Toledo, O. da F.M. Gomes, Study of temperature effect on macro-synthetic fiber reinforced concretes by means of Barcelona tests: An approach focused on tunnels assessment, *Constr. Build. Mater.* 158 (2018) 443–453. <https://doi.org/10.1016/j.conbuildmat.2017.10.046>.
- [37] R. Serafini, R.R. Agra, R. Monte, A.D. Figueiredo, The effect of elevated temperatures on the tensile properties of steel fiber reinforced concrete by means of double edge

- wedge splitting (DEWS) test: Preliminary results, in: G. Pijaudier-Cabo, P. Grassl, C. La Borderie (Eds.), Proc. 10th Int. Conf. Fract. Mech. Concr. Concr. Struct., IA-FraMCoS, Bayonne, France, 2019: p. 6. <https://doi.org/10.21012/FC10.240385>.
- [38] F. Di Carlo, A. Meda, Z. Rinaldi, Evaluation of the bearing capacity of fiber reinforced concrete sections under fire exposure, *Mater. Struct.* 51 (2018) 154. <https://doi.org/10.1617/s11527-018-1280-2>.
- [39] J.M. Carpio, R. Serafini, D. Rambo, A. de la Fuente, A.D. De Figueiredo, Assessment of the bearing capacity reduction of FRC elements subjected to fire, in: Proc. Fib Symp. 2019 Concr. - Innov. Mater. Des. Struct., Kraków, Poland, 2019: pp. 1378–1386.
- [40] P.K. Mehta, P.J. Monteiro, *Concrete: Microstructure, Properties, and Materials*, McGraw-Hill Education, 2014.
- [41] J.K. Wight, J.G. MacGregor, *Reinforced Concrete: Mechanics and Design*, Prentice Hall, 2011.
- [42] N. Banthia, *Fiber Reinforced Concrete*, ACI SP-142ACI, Detroit, MI. (1994). <https://doi.org/10.4188/transjtmsj1965a.24.P621>.
- [43] L. Liao, A. de la Fuente, S. Cavalaro, A. Aguado, Design procedure and experimental study on fibre reinforced concrete segmental rings for vertical shafts, *Mater. Des.* 92 (2016) 590–601. <https://doi.org/10.1016/j.matdes.2015.12.061>.
- [44] L. Liao, A. de la Fuente, S. Cavalaro, A. Aguado, Design of FRC tunnel segments considering the ductility requirements of the Model Code 2010, *Tunn. Undergr. Sp. Technol.* 47 (2015) 200–210. <https://doi.org/10.1016/j.tust.2015.01.006>.
- [45] A. Conforti, G. Tiberti, G.A. Plizzari, Splitting and crushing failure in FRC elements subjected to a high concentrated load, *Compos. Part B Eng.* 105 (2016) 82–92. <https://doi.org/10.1016/j.compositesb.2016.08.032>.
- [46] D.-Y. Yoo, N. Banthia, Impact resistance of fiber-reinforced concrete – A review, *Cem. Concr. Compos.* 104 (2019) 103389. <https://doi.org/10.1016/j.cemconcomp.2019.103389>.
- [47] V. Afroughsabet, L. Biolzi, T. Ozbakkaloglu, High-performance fiber-reinforced concrete: a review, *J. Mater. Sci.* 51 (2016) 6517–6551. <https://doi.org/10.1007/s10853-016-9917-4>.
- [48] A.E. Naaman, Fiber reinforced concrete: five decades of progress, in: Proc. 4th Brazilian Conf. Compos. Mater., Pontificia Universidade Católica do Rio de Janeiro, 2018: pp. 35–56. <https://doi.org/10.21452/bccm4.2018.02.01>.
- [49] Fédération Internationale du Béton, Bulletin 83 - Precast Tunnel Segments in Fibre-Reinforced Concrete, Switzerland, 2017.
- [50] M. Jamshidi Avanaki, Effects of hybrid steel fiber reinforced composites on structural performance of segmental linings subjected to TBM jacks, *Struct. Concr.* (2019). <https://doi.org/10.1002/suco.201800322>.
- [51] A. de la Fuente, A. Aguado, C. Molins, J. Armengou, Numerical model for the analysis

- up to failure of precast concrete sections, *Comput. Struct.* (2012). <https://doi.org/10.1016/j.compstruc.2012.04.007>.
- [52] R. Burgers, J. Walraven, G.A. Plizzari, G. Tiberti, Structural behavior of SFRC tunnel segments during TBM operations, in: *Undergr. Sp. – 4th Dimens. Metropolises*, Taylor & Francis, London, 2007: pp. 1461–1467.
- [53] L. Liao, A. de la Fuente, S. Cavalaro, A. Aguado, G. Carbonari, Experimental and analytical study of concrete blocks subjected to concentrated loads with an application to TBM-constructed tunnels, *Tunn. Undergr. Sp. Technol.* (2015). <https://doi.org/10.1016/j.tust.2015.04.020>.
- [54] A. Fernandes, Utilização de fibras de aço para reforço de concreto em anéis pré-moldados segmentados para revestimento de túneis, Universidade Estadual de Campinas, 2005.
- [55] A. Bentur, S. Mindess, *Fibre reinforced cementitious composites*, 2nd ed., Taylor & Francis, New York, 2007.
- [56] H. Toutanji, Z. Bayasi, Effects of manufacturing techniques on the flexural behavior of steel fiber-reinforced concrete, *Cem. Concr. Res.* (1998). [https://doi.org/10.1016/S0008-8846\(97\)00213-5](https://doi.org/10.1016/S0008-8846(97)00213-5).
- [57] S.T. Kang, B.Y. Lee, J.K. Kim, Y.Y. Kim, The effect of fibre distribution characteristics on the flexural strength of steel fibre-reinforced ultra high strength concrete, *Constr. Build. Mater.* (2011). <https://doi.org/10.1016/j.conbuildmat.2010.11.057>.
- [58] M. di Prisco, G. Plizzari, L. Vandewalle, Fibre reinforced concrete: new design perspectives, *Mater. Struct.* 42 (2009) 1261–1281. <https://doi.org/10.1617/s11527-009-9529-4>.
- [59] D. Schütz, Fire protection in tunnels: Focus on road & train tunnels, (2014) 1–12. https://www.scor.com/sites/default/files/pc_nl_tunnels.pdf.
- [60] D. Lacroix, The Mont Blanc tunnel fire. What happened and what has been learned, in: *Proc. Fourth Int. Conf. Saf. Road Rail Tunnels*, Madrid, Spain, 2001: pp. 3–15.
- [61] P. Capella, 35 die, 1 Briton missing in Mont Blanc tunnel fire, *Guard.* (1999). <https://www.theguardian.com/world/1999/mar/27/6>.
- [62] W.H. Hong, The progress and controlling situation of Daegu subway fire disaster., in: *Proc. 6th Asia—Oceania Symp. Fire Sci. Technol.*, Daegu, 2004.
- [63] B. Yun, Operation Systems in Underground Engineering, in: *Undergr. Eng.*, Elsevier, 2019: pp. 239–259. <https://doi.org/10.1016/B978-0-12-812702-5.00006-2>.
- [64] A. Lau, M. Anson, Effect of high temperatures on high performance steel fibre reinforced concrete, *Cem. Concr. Res.* 36 (2006) 1698–1707. <https://doi.org/10.1016/j.cemconres.2006.03.024>.
- [65] Brazilian National Standards Organization (ABNT), NBR 16938: Fiber reinforced concrete - Quality control, Rio de Janeiro, RJ, 2021.

- [66] Brazilian National Standards Organization (ABNT), NBR 16939: Fiber reinforced concrete - Determination of tensile strength using double punch test (cracking and residuals strength) - Test method, Rio de Janeiro, RJ, 2021.
- [67] Brazilian National Standards Organization (ABNT), NBR 16940: Fibre reinforced concrete - Determination of the flexural tensile strengths (limit of proportionality and residual strengths) - Test Method, 2021.
- [68] R. Serafini, S.R.A. Dantas, R.P. Salvador, R.R. Agra, D.A.S. Rambo, A.F. Berto, A.D. de Figueiredo, Influence of fire on temperature gradient and physical-mechanical properties of macro-synthetic fiber reinforced concrete for tunnel linings, *Constr. Build. Mater.* 214 (2019) 254–268. <https://doi.org/10.1016/j.conbuildmat.2019.04.133>.
- [69] Z.P. Bažant, M.F. Kaplan, *Concrete at high temperatures: material properties and mathematical models*, Longman, 1996.
- [70] T.T. Lie, V.K.R. Kodur, Thermal and mechanical properties of steel-fibre-reinforced concrete at elevated temperatures, *Can. J. Civ. Eng.* 23 (1996) 511–517. <https://doi.org/10.1139/196-055>.
- [71] Q. Ma, R. Guo, Z. Zhao, Z. Lin, K. He, Mechanical properties of concrete at high temperature—A review, *Constr. Build. Mater.* 93 (2015) 371–383. <https://doi.org/10.1016/j.conbuildmat.2015.05.131>.
- [72] J. Xiao, Q. Xie, W. Xie, Study on high-performance concrete at high temperatures in China (2004–2016) - An updated overview, *Fire Saf. J.* (2018). <https://doi.org/10.1016/j.firesaf.2017.10.007>.
- [73] R. Philleo, Some Physical Properties of Concrete at High Temperatures, *J. Am. Concr. Inst.* 54 (1958) 857–864.
- [74] T. Harada, J. Takeda, S. Yamane, F. Furumura, Strength, elasticity and thermal properties of concrete subjected to elevated temperatures, in: *International Semin. Concr. Nucl. React. ACI Spec. Publ. No.34, Vol.1, 1972: pp. 377–406*.
- [75] C.R. Cruz, M. Gillen, Thermal expansion of Portland cement paste, mortar and concrete at high temperatures, *Fire Mater.* 4 (1980) 66–70. <https://doi.org/10.1002/fam.810040203>.
- [76] M.S. Crowley, Initial thermal expansion characteristics of insulating refractory concretes, *Bull. Am. Ceram. Soc.* 35 (1956) 465–468.
- [77] R.F. Feldman, V.S. Ramachandran, Differentiation of interlayer and adsorbed water in hydrated portland cement by thermal analysis, *Cem. Concr. Res.* 1 (1971) 607–620. [https://doi.org/10.1016/0008-8846\(71\)90016-0](https://doi.org/10.1016/0008-8846(71)90016-0).
- [78] H.F.W. Taylor, *Cement chemistry*. 2nd ed., Acad. Press. (1997). [https://doi.org/10.1016/S0958-9465\(98\)00023-7](https://doi.org/10.1016/S0958-9465(98)00023-7).
- [79] M.H. Maciel, G.S. Soares, R.C. de O. Romano, M.A. Cincotto, Monitoring of Portland cement chemical reaction and quantification of the hydrated products by XRD and TG in function of the stoppage hydration technique, *J. Therm. Anal. Calorim.* (2018).

- <https://doi.org/10.1007/s10973-018-7734-5>.
- [80] G. Ruano, F. Isla, B. Luccioni, R. Zerbino, G. Giaccio, Steel fibers pull-out after exposure to high temperatures and its contribution to the residual mechanical behavior of high strength concrete, *Constr. Build. Mater.* 163 (2018) 571–585. <https://doi.org/10.1016/j.conbuildmat.2017.12.129>.
- [81] V. Kocaba, Development and evaluation of methods to follow microstructural development of cementitious systems including slags, *École Polytechnique Fédérale de Lausanne*, 2009. <https://doi.org/10.5075/epfl-thesis-4523>.
- [82] R. Felicetti, P.G. Gambarova, Effects of high temperature on the residual compressive strength of high-strength siliceous concretes, *ACI Mater. J.* 95 (1998) 395–406.
- [83] V. Vydra, F. Vodák, O. Kapičková, Š. Hošková, Effect of temperature on porosity of concrete for nuclear-safety structures, *Cem. Concr. Res.* 31 (2001) 1023–1026. [https://doi.org/10.1016/S0008-8846\(01\)00516-6](https://doi.org/10.1016/S0008-8846(01)00516-6).
- [84] C. Gallé, Permeability and pore structure evolution of silico-calcareous and hematite high-strength concretes submitted to high temperatures, *Mater. Struct.* 34 (2001) 619–628. <https://doi.org/10.1617/13695>.
- [85] K. Scrivener, R. Snellings, B. Lothenbach, *A Practical Guide to Microstructural Analysis of Cementitious Materials*, CRC Press, 2017.
- [86] R.J. Myers, E. L'Hôpital, J.L. Provis, B. Lothenbach, Effect of temperature and aluminium on calcium (alumino)silicate hydrate chemistry under equilibrium conditions, *Cem. Concr. Res.* (2015). <https://doi.org/10.1016/j.cemconres.2014.10.015>.
- [87] H.F. Mitsuda, T.; Taylor, Normal and anomalous tobermorites, *Mineral. Mag.* (1978) 229–235.
- [88] D.J. Naus, *The Effect of Elevated Temperature on Concrete Materials and Structures — A Literature Review*, 2005.
- [89] G.A. Khoury, Effect of fire on concrete and concrete structures, *Prog. Struct. Eng. Mater.* 2 (2000) 429–447. <https://doi.org/10.1002/pse.51>.
- [90] R.Y. Chen, W.Y.D. Yuen, Review of the high-temperature oxidation of iron and carbon steels in air or oxygen, *Oxid. Met.* (2003). <https://doi.org/10.1023/A:1023685905159>.
- [91] W. Callister, D. Rethwisch, *Materials science and engineering: an introduction*, 7th ed., John Wiley, New York, USA, 2007.
- [92] H. Abuluwefa, The effect of oxygen concentration on the oxidation of low-carbon steel in the temperature range 1000 to 1250°C, *Oxid. Met.* (1996). <https://doi.org/10.1007/BF01048639>.
- [93] J.S. Sheasby, W.E. Boggs, E.T. Turkdogan, Scale growth on steels at 1200°C: rationale of rate and morphology, *Met. Sci.* (1984). <https://doi.org/10.1179/msc.1984.18.3.127>.
- [94] S. James, W. Alexander, *Materials Science and Engineering Handbook*, 2001.

- <https://doi.org/10.1126/science.232.4757.1485>.
- [95] S. Abdallah, M. Fan, K.A. Cashell, Pull-out behaviour of straight and hooked-end steel fibres under elevated temperatures, *Cem. Concr. Res.* 95 (2017) 132–140. <https://doi.org/10.1016/j.cemconres.2017.02.010>.
- [96] S. Abdallah, M. Fan, D.W.A. Rees, Effect of elevated temperature on pull-out behaviour of 4DH/5DH hooked end steel fibres, *Compos. Struct.* 165 (2017) 180–191. <https://doi.org/https://doi.org/10.1016/j.compstruct.2017.01.005>.
- [97] S. Abdallah, M. Fan, K.A. Cashell, Bond-slip behaviour of steel fibres in concrete after exposure to elevated temperatures, *Constr. Build. Mater.* 140 (2017) 542–551. <https://doi.org/10.1016/j.conbuildmat.2017.02.148>.
- [98] L.M.S. Mendes, R. Serafini, A.D. Figueiredo, The effect of high temperature on the mechanical properties of steel fibers and polymeric macrofibers, in: *Proc. 9th Int. Conf. Concr. Under Sev. Cond. - Environ. Load., MENVIA, Porto Alegre, Brazil, 2019*. <https://doi.org/10.31808/5ca6e03b5ca4f0d406ac888a>.
- [99] A. Bentur, S. Wu, N. Banthia, R. Baggott, W. Hansen, A. Katz, C. Leung, B.M. V Li, A. Naaman, R. Robertson, P. Soroushian, H. Stang, L. Taerwe, Fiber-Matrix Interfaces, in: *Pre-Proceedings 2nd Int. Work. "High Perform. Fiber Reinf. Cem. Compos. (HPF-RCC-95)"*, Michigan, USA, 1995: pp. 139–182.
- [100] R.J. Gray, C.D. Johnston, The influence of fibre-matrix interfacial bond strength on the mechanical properties of steel fibre reinforced mortars, *Int. J. Cem. Compos. Light. Concr.* (1987). [https://doi.org/10.1016/0262-5075\(87\)90036-4](https://doi.org/10.1016/0262-5075(87)90036-4).
- [101] V.M.C.F. Cunha, Steel fibre reinforced self-compacting concrete (from micromechanics to composite behavior), University of Minho, 2010. <http://hdl.handle.net/1822/10667>.
- [102] S.M. Abdallah, *Bonding Mechanisms and Strength of Hooked-end Steel Fibre Reinforced Cementitious Composites*, Brunel University London, 2017.
- [103] Y. Zhang, J.W. Ju, Q. Chen, Z. Yan, H. Zhu, Z. Jiang, Characterizing and analyzing the residual interfacial behavior of steel fibers embedded into cement-based matrices after exposure to high temperatures, *Compos. Part B Eng.* 191 (2020) 107933. <https://doi.org/10.1016/j.compositesb.2020.107933>.
- [104] R. Serafini, F.P. Santos, R.R. Agra, A. De la Fuente, A.D. de Figueiredo, Effect of specimen shape on the compressive parameters of steel fiber reinforced concrete after temperature exposure, *J. Urban Technol. Sustain.* 1 (2018) 10–20. <https://doi.org/10.47842/juts.v1i1.7>.
- [105] M. Karatas, M. Dener, A. Benli, M. Mohabbi, High temperature effect on the mechanical behavior of steel fiber reinforced self-compacting concrete containing ground pumice powder, *Struct. Concr.* 20 (2019) 1734–1749. <https://doi.org/10.1002/suco.201900067>.
- [106] G.M. Chen, Y.H. He, H. Yang, J.F. Chen, Y.C. Guo, Compressive behavior of steel fiber reinforced recycled aggregate concrete after exposure to elevated temperatures,

- Constr. Build. Mater. 71 (2014) 1–15.
<https://doi.org/10.1016/j.conbuildmat.2014.08.012>.
- [107] Fédération Internationale du Béton, Bulletin 46 - Fire design of concrete structures - structural behaviour and assessment, Switzerland, 2008.
- [108] R.R. Agra, Influence of steel fiber content on the behavior of concrete exposed to elevated temperatures (in Portuguese), Universidade de São Paulo, 2020.
<https://doi.org/10.11606/D.3.2020.tde-04032021-110133>.
- [109] W.F. Chen, R.L. Yuan, Tensile Strength of Concrete: Double-Punch Test, *J. Struct. Div.* 106 (1980) 1673–1693. <https://doi.org/10.1061/JSDEAG.0005493>.
- [110] L. Segura-Castillo, R. Monte, A.D. de Figueiredo, Characterisation of the tensile constitutive behaviour of fibre-reinforced concrete: A new configuration for the Wedge Splitting Test, *Constr. Build. Mater.* 192 (2018) 731–741.
<https://doi.org/10.1016/j.conbuildmat.2018.10.101>.
- [111] M. di Prisco, L. Ferrara, M.G.L. Lamperti, Double edge wedge splitting (DEWS): an indirect tension test to identify post-cracking behaviour of fibre reinforced cementitious composites, *Mater. Struct.* 46 (2013) 1893–1918. <https://doi.org/10.1617/s11527-013-0028-2>.
- [112] C. Molins, A. Aguado, S. Saludes, Double punch test to control the energy dissipation in tension of FRC (Barcelona test), *Mater. Struct. Constr.* (2009).
<https://doi.org/10.1617/s11527-008-9391-9>.
- [113] L.A.C. Borges, R. Monte, D.A.S. Rambo, A.D. de Figueiredo, Evaluation of post-cracking behavior of fiber reinforced concrete using indirect tension test, *Constr. Build. Mater.* 204 (2019) 510–519. <https://doi.org/10.1016/j.conbuildmat.2019.01.158>.
- [114] O. Adel Qasim, A. Sinan Ahmed, High Temperature Effect on Shear Transfer Strength of Steel Fiber Reinforced Self-Compacted Concrete, *J. Eng. Appl. Sci.* 14 (2019) 3158–3174. <https://doi.org/10.36478/jeasci.2019.3158.3174>.
- [115] R. Serafini, S.R.A. Dantas, D.A.S. Rambo, A.D. de Figueiredo, Pull-out response of steel fiber reinforced concretes exposed to elevated temperatures, in: *Proc. Seventh Int. Colloq. Performance, Prot. Strength. Struct. under Extrem. Load. Events*, The University of British Columbia, Whistler, Canada, 2019: pp. 614–621.
- [116] A. Conforti, G. Tiberti, G.A. Plizzari, A. Caratelli, A. Meda, Precast tunnel segments reinforced by macro-synthetic fibers, *Tunn. Undergr. Sp. Technol.* 63 (2017) 1–11.
<https://doi.org/10.1016/j.tust.2016.12.005>.
- [117] G. Lilliu, A. Meda, Nonlinear Phased Analysis of Reinforced Concrete Tunnels Under Fire Exposure, *J. Struct. Fire Eng.* 4 (2013) 131–142. <https://doi.org/10.1260/2040-2317.4.3.131>.
- [118] C. Feist, M. Aschaber, G. Hofstetter, Numerical simulation of the load-carrying behavior of RC tunnel structures exposed to fire, *Finite Elem. Anal. Des.* 45 (2009) 958–965. <https://doi.org/10.1016/j.finel.2009.09.010>.

- [119] Z. Yan, H. Zhu, J. Woody Ju, W. Ding, Full-scale fire tests of RC metro shield TBM tunnel linings, *Constr. Build. Mater.* 36 (2012) 484–494. <https://doi.org/10.1016/j.conbuildmat.2012.06.006>.
- [120] C. Pichler, R. Lackner, H.A. Mang, Safety Assessment of Concrete Tunnel Linings under Fire Load, *J. Struct. Eng.* 132 (2006) 961–969. [https://doi.org/10.1061/\(ASCE\)0733-9445\(2006\)132:6\(961\)](https://doi.org/10.1061/(ASCE)0733-9445(2006)132:6(961)).
- [121] International Organization for Standardization, Fire-resistance tests — Elements of building construction — Part 1: General requirements, 1999.
- [122] A. Wolfenden, T. Harmathy, M. Sultan, J. MacLaurin, Comparison of Severity of Exposure in ASTM E 119 and ISO 834 Fire Resistance Tests, *J. Test. Eval.* 15 (1987) 371. <https://doi.org/10.1520/JTE11036J>.
- [123] C.N. Costa, Dimensionamento de elementos de concreto armado em situação de incêndio., Universidade de São Paulo, 2008. <https://doi.org/10.11606/T.3.2008.tde-04092008-155911>.
- [124] A. Lönnemark, On the Characteristics of Fires in Tunnels, Lund University, 2005.
- [125] L. Phan, Fire Performance of High-Strength Concrete: A Report of the State-of-the-Art, *Fire Res.* (1996).
- [126] G.F. Peng, W.W. Yang, J. Zhao, Y.F. Liu, S.H. Bian, L.H. Zhao, Explosive spalling and residual mechanical properties of fiber-toughened high-performance concrete subjected to high temperatures, *Cem. Concr. Res.* (2006). <https://doi.org/10.1016/j.cemconres.2005.12.014>.
- [127] J.M. Carpio, Numerical model for the thermo-hygro-mechanical analysis of concrete elements from early ages, Universitat Politècnica de Catalunya, 2019.
- [128] P. Bamonte, A. Meda, On fire behavior of R/C sections subjected to an eccentric axial force, in: *Fire Des. Concr. Struct. Now? What Next?*, 2004; pp. 133–146.
- [129] R.P. Salvador, S.H.P. Cavalaro, I. Segura, A.D. Figueiredo, J. Pérez, Early age hydration of cement pastes with alkaline and alkali-free accelerators for sprayed concrete, *Constr. Build. Mater.* 111 (2016) 386–398. <https://doi.org/10.1016/j.conbuildmat.2016.02.101>.
- [130] S.R.A. Dantas, R. Serafini, R.C. de O. Romano, F. Vittorino, K. Loh, Influence of polypropylene microfibers (PPMF) dispersion procedure on fresh and hardened rendering mortar properties, *Ambient. Construído.* 20 (2020) 7–23. <https://doi.org/10.1590/s1678-86212020000200384>.
- [131] American Society for Testing and Materials, E112-13:Standard Test Methods for Determining Average Grain Size, *ASTM Int.* (2013). <https://doi.org/10.1520/E0112-13>.
- [132] Associação brasileira de normas técnicas (ABNT), ABNT NBR ISO 6892-2002 Materiais metálicos - Ensaio de tração à temperatura ambiente, Rio de Janeiro, RJ, 2002.

- [133] U. Schneider, Concrete at high temperatures - A general review, *Fire Saf. J.* (1988). [https://doi.org/10.1016/0379-7112\(88\)90033-1](https://doi.org/10.1016/0379-7112(88)90033-1).
- [134] EN 14651, Test method for metallic fibred concrete — Measuring the flexural tensile strength (limit of proportionality (LOP), residual), United Kingdom, 2007.
- [135] W. Kusterle, W. Lindbauer, G. Hampejs, A. Heel, P.F. Donauer, M. Zeiml, W. Brunnsteiner, R. Dietze, W. Hermann, H. Viechtbauer, M. Schreiner, Technical Report 544: Fire resistance of fibre-reinforced, reinforced and prestressed concrete, Vienna: Bundesministerium für Verkehr, Innovation und Technologie [in German], 2004.
- [136] I. Galobardes, A. de la Fuente, A.D. de Figueiredo, M.A. Peixoto, Characterization of tunnel lining segments produced with fibre reinforced concrete, in: *57 Congr. Bras. Do Concreto*, 2015: p. 16.
- [137] A. Nonat, The structure and stoichiometry of C-S-H, *Cem. Concr. Res.* (2004). <https://doi.org/10.1016/j.cemconres.2004.04.035>.
- [138] L.A.G. Bitencourt, Y.T. Trindade, T.N. Bittencourt, O.L. Manzoli, E.A. Rodrigues, Multiscale modeling of steel fiber reinforced concrete based on the use of coupling finite elements and mesh fragmentation technique, in: *Comput. Model. Concr. Struct.*, CRC Press, 2018: pp. 877–888. <https://doi.org/10.1201/9781315182964-102>.
- [139] L. A. G. Bitencourt, O.L. Manzoli, T.N. Bittencourt, F.J. Vecchio, Numerical modeling of steel fiber reinforced concrete with a discrete and explicit representation of steel fibers, *Int. J. Solids Struct.* 159 (2019) 171–190. <https://doi.org/10.1016/j.ijsolstr.2018.09.028>.
- [140] C. Soranakom, B. Mobasher, Correlation of tensile and flexural responses of strain softening and strain hardening cement composites, *Cem. Concr. Compos.* 30 (2008) 465–477. <https://doi.org/10.1016/j.cemconcomp.2008.01.007>.
- [141] K. Liu, L. Lu, F. Wang, W. Liang, Theoretical and experimental study on multi-phase model of thermal conductivity for fiber reinforced concrete, *Constr. Build. Mater.* 148 (2017) 465–475. <https://doi.org/10.1016/j.conbuildmat.2017.05.043>.
- [142] K.Y. Shin, S.B. Kim, J.H. Kim, M. Chung, P.S. Jung, Thermo-physical properties and transient heat transfer of concrete at elevated temperatures, *Nucl. Eng. Des.* (2002). [https://doi.org/10.1016/S0029-5493\(01\)00487-3](https://doi.org/10.1016/S0029-5493(01)00487-3).
- [143] V.K.R. Kodur, M.A. Sultan, Effect of temperature on thermal properties of high-strength concrete, *J. Mater. Civ. Eng.* (2003). [https://doi.org/10.1061/\(ASCE\)0899-1561\(2003\)15:2\(101\)](https://doi.org/10.1061/(ASCE)0899-1561(2003)15:2(101)).

ATTACHMENTS

ARTICLE A

Title: The effect of elevated temperatures on the physical, mechanical, and microstructural properties of cold-drawn hooked-end steel fibers.

Submit to: Magazine of Concrete Research

Publication date: 17/02/2020.

Status: Published (doi: 10.1680/jmacr.19.00498)

THE EFFECT OF ELEVATED TEMPERATURES ON THE PROPERTIES OF COLD-DRAWN STEEL FIBERS

Ramoel Serafini^{1*}, Livia Mourão Mendes², Renan Pícolo Salvador³, Antonio
Domingues de Figueiredo⁴

¹ PhD candidate, Bachelor of Engineering, University of São Paulo, ORCID 0000-0002-7698-649X

² Bachelor of Engineering, University of São Paulo, ORCID 0000-0001-8612-9208

³ Professor, PhD, University São Judas Tadeu, ORCID 0000-0002-1590-231X

⁴ Professor, PhD, University of São Paulo, ORCID 0000-0003-4658-3355

*corresponding author: rserafini@usp.br. Department of Civil Construction Engineering, Polytechnic
School of University of São Paulo | Avenida Professor Almeida Prado, Travessa 2, 83, 05424-970, São
Paulo, Brazil.

Date last revised: January 21, 2020.

Number of words count in the main text: 4180. Number of tables: 03. Number of figures: 07

ABSTRACT

This study aims to evaluate the effect of elevated temperatures on the physical, mechanical, and microstructural properties of a hooked-end steel fiber for temperatures of 100, 350, 750, and 1000 °C. Results show that an oxidation layer is formed on the surface of the fibers exposed to temperatures of 750 °C and above, which leads to an increase in external diameter and mass. Reductions in tensile strength are directly proportional to the temperature increase, while rupture strain values significantly increase for temperatures above the recrystallization temperature of steel. The present study contributes to the understanding of the contribution of steel fibers to the overall behavior of the composite after temperature exposure and serve as input for recently developed numerical models.

Keywords: tensile properties; temperature-related & thermal effects; fibre-reinforced concrete.

1 Introduction

The vast majority of applications of steel fiber reinforced concrete (SFRC) are related to infrastructure elements, such as pavements, tunnels, and sanitary pipes [1–3]. The SFRC is successfully used in civil engineering as a total or partial replacement to conventionally reinforced concrete [4,5]. In this context, the evaluation of the post-crack behavior of fiber reinforced concrete is essential to ensure the safety of structures built with this composite, especially after fire events.

During a fire event a wide range of temperatures is generated in the composite, which results in changes in three main aspects: the physical and mechanical properties of the cementitious matrix [6–9], the reinforcing fibers [10], and the fiber-matrix interface [11–13]. The fibers play an important role to bridge micro- and macro-cracks in order to prevent unstable crack growth and delay crack opening [14], therefore the characterization of their properties after heat exposure is of paramount importance. The physical-mechanical properties of steel are affected by temperature since the steel oxidize, the microstructure recrystallization process occurs, and the steel grain size changes [15–17].

The high temperature oxidation of steel is driven by the reaction between the metal and the atmospheric oxygen at elevated temperatures. This corrosive process occurs especially for temperatures from 700 to 1250 °C and forms a friable three-layered scale structure [17]. The formation of this scale structure may significantly affect the cross-sectional area of steel fibers and reduce their tensile strength. The recrystallization process is the formation of a new set of strain-free grains that reduces the strength and hardness of steel, while increasing ductility [16]. After these new grains are formed, they begin to grow in size and the reduction in grain boundary density results in tensile strength reductions. Although all these metal related processes are well defined in literature [15], the outcome of these processes have not yet been quantified for steel fibers.

Considering the above, the objective of the present study is to evaluate the physical and mechanical properties of cold-drawn hooked-end steel fibers after exposure to elevated temperatures. Changes in terms of external diameter, mass, and length were evaluated as function of temperature and the tensile strength of steel fibers was determined based on direct tensile strength tests. The effective cross-sectional area of

steel fibers was determined by optical microscopy (OM), and the steel grain size was determined by scanning electron microscopy (SEM). Additionally, the mineralogical composition of the oxide layer formed was characterized by X-ray diffraction (XRD). This research paper serve as valuable data to explain the behavior of SFRC after exposure to elevated temperatures and provide results that are of great value for the parameterization of numerical modeling where the characteristics of the fibers are relevant in their implementation [18]. Therefore, the assessment of the residual capacity of SFRC structures can be performed by designers using numerical simulation based, in part, on the conclusions of this paper.

2 Experimental methodology

2.1 Hooked-end steel fibers

A low-carbon, cold drawn, hooked-end steel fiber, Dramix RC-80/60-BG, was employed in this study. This fiber type was selected since hooked-end steel fibers are commonly employed in structural applications of fiber reinforced concrete due to enhanced bond strength with concrete matrix [19]. Table 1 shows the properties and characteristics of steel fibers according to the data provided by manufacturer.

Table 1 – Properties and characteristics of steel fibers (provided by manufacturer)

Characteristics	Hooked-end steel fiber
Length (mm)	60
Diameter (mm)	0.75
Aspect ratio (l/d)	80
Specific weight (kg/m ³)	7450
Melting point (°C)	~ 1370 °C
Tensile strength (MPa)	1225
Young modulus (GPa)	210

2.2 Fiber characterization

2.2.1 Mineralogical composition

X-ray diffraction (XRD) was performed to qualitatively analyze the mineralogical composition of the oxide formed in the steel fibers. The oxide sample was removed from steel fibers that were exposed to the target temperature of 1000 °C by grinding two fibers inside a plastic bag. The oxide removed was mechanically crushed and ground to a maximum particle diameter of 53 μm and taken for XRD analysis.

The XRD test was performed in a PANalytical X'Pert PRO PW 3040 00 powder diffractometer with Ni filtered $\text{CuK}\alpha_1$ radiation ($\lambda = 1.5418 \text{ \AA}$) and a X'celerator detector (active length of $2.214^\circ 2\theta$). The test was performed in reflection Bragg-Brentano geometry operating at 45 kV and 40 mA. Cylindrical sample holders were filled with approximately 3 g of the oxide and had an internal diameter of 27 mm and a depth of 8 mm. In order to improve particle statistics, the sample holders were spun around the vertical goniometer axis at a rate of 0.5 revolutions per second during the XRD test. X-ray patterns were obtained using an automatic divergence slit from $10^\circ 2\theta$ to $70^\circ 2\theta$, using a step width of $0.02^\circ 2\theta$ and 200 s per step, according to [20,21]. X-ray patterns were analyzed qualitatively using the software X'Pert High Score Plus.

2.2.2 Optical and scanning electron microscopies

Microscopy analyses were conducted in steel fibers after exposure to temperatures of 100, 350, 750, and 1000 °C. Optical microscopy was employed in order to verify the effect of elevated temperatures on the residual cross-sectional area of steel fibers, while the changes in terms of grain-size of steel were assessed by scanning electron microscopy. Fibers kept at room temperature were analyzed for comparative purposes.

Optical microscopy (OM) was conducted using a NIKON Epiphot 200 instrument with a NIS Element D-Live Fast software. The effective cross-sectional area was measured based on OM imagery using ImageJ image processing software. The term “effective cross-sectional area” was used in this paper and is defined as the remaining area of steel that is capable of resisting the tensile stresses. Based on the results of effective cross-sectional area, the equivalent effective diameter was calculated considering a cross-section of circular shape. Scanning electron microscopy (SEM) was conducted using a Quanta 3D FEG instrument, accelerating voltage of 20 kV, working distance of 10 mm, using XT microscope control FEI software. The grain size of the crystalline structure of steel fiber was calculated following the procedure presented by ASTM E112 [22].

2.2.3 Direct tensile strength test

Direct tensile strength tests were conducted in order to assess the changes in terms of tensile strength of steel fibers as a function of temperature. Tests were performed in an Instron Universal Testing Machine, model 5569, using a loadcell with maximum

capacity of 1000 N and Instron mechanical wedge action grips (catalog #2716-020). Steel fibers were positioned centered and perpendicular to the grip faces since this methodology was experimentally proved to be the best option among the setups evaluated. A load application rate of 152 N/min was used, following the minimum value recommended for metallic materials according to Brazilian standards [23]. Engineering tensile strength was calculated using the initial cross-sectional area of steel fibers (at 25 °C), while the true tensile strength was calculated using the residual diameter measured by optical microscopy.

The elastic modulus of steel fibers was not determined due to limitations in the measurement mechanisms (piston displacement) and the small displacement values of the cross-head during the test. However, it is well established in literature that elastic modulus values are influenced by the inter-atomic distance of metallic ions [15]. As the inter-atomic distance is significantly increased at elevated temperatures, the elastic modulus of steel reduces considerably in hot conditions due to the lower energy required to separate the ions in the microstructural level. After cooling, however, metallic ions return to the initial interatomic distance and elastic modulus is not significantly affected at environmental temperature [15,16]. This scenario is valid for evaluations in environmental temperature conditions only, since in hot conditions elastic modulus is significantly affected by temperature.

2.3 Heating procedure

Figure 1 shows the heating procedure adopted for the steel fibers. The hooked-end steel fibers were heated in an industrial EDG FC series electric oven, model EDG10P-S, with maximum temperature capacity of 1200 °C. Before heating, steel fibers were positioned inside refractory vessels to avoid sample contamination, and then exposed to target temperatures of 100, 350, 750, and 1000 °C (see Fig. 2). These target temperatures were chosen based on the internal temperature readings after a fire simulation conducted previously [10] and on the recrystallization temperature of steel, since close to this temperature, mechanical and microstructural properties of steel significantly change.

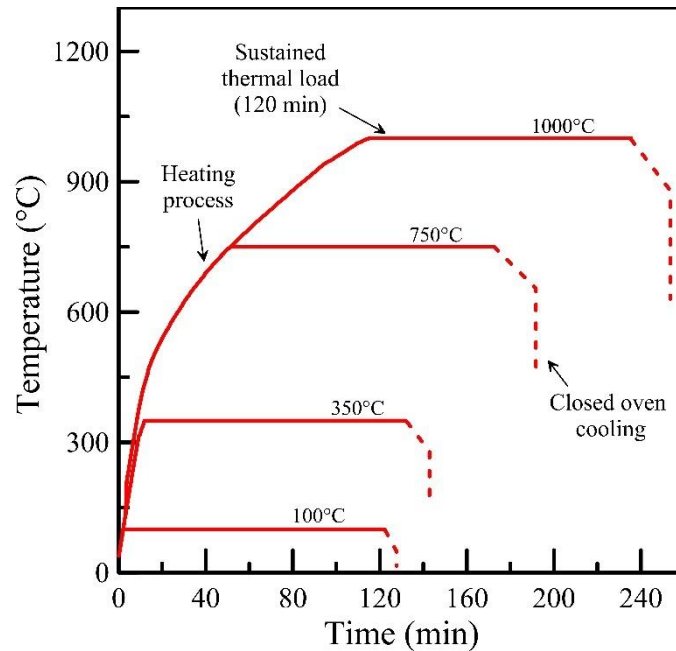


Figure 1 – Heating procedure adopted for steel fibers

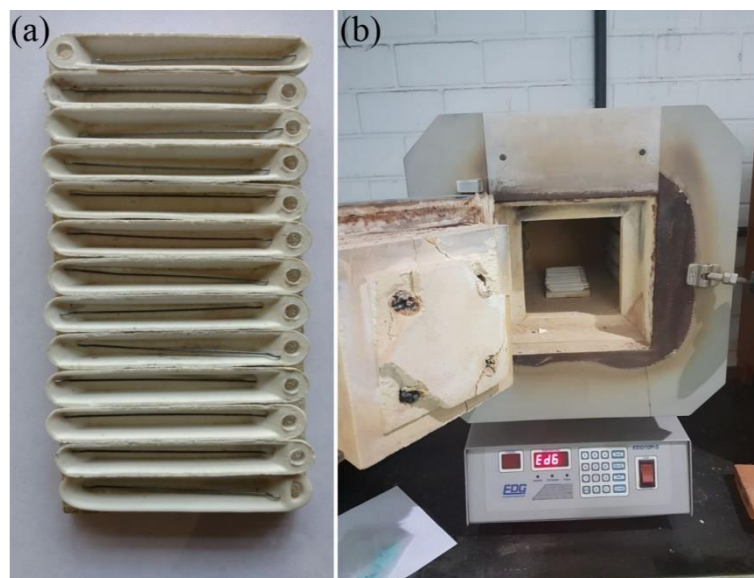


Figure 2 – (a) steel fibers positioned inside refractory vessels (b) electric oven employed in this study

Steel fibers were kept at the target temperature for 120 min because that is the duration of the hydrocarbon fire curve, which is one of the most severe fire curves found in literature [24]. After the heating regime, the electric oven was turned off and kept closed to allow fibers to cool until room temperature (cooling rate was not controlled). Steel fibers were then stored in sealed plastic bags and kept in a vacuum desiccator containing silica gel in order to avoid the contact of the fiber with air and humidity. A total of 13 steel fibers was evaluated for each target temperature in terms of physical and mechanical changes.

3 Results and discussion

3.1 Visual and physical evaluation

Figure 3 depicts steel fibers subjected to different temperatures. In Figure 3a, it is possible to observe the changes that occurred due to the exposure of steel fibers to elevated temperatures. As temperature increases, steel fibers undergo a temperature related oxidation process that visually changes the surface of the fiber due to the formation of a dark oxide layer. This iron oxide layer may be observed in Figure 3c and is more representative for fibers exposed to 750 and 1000 °C.

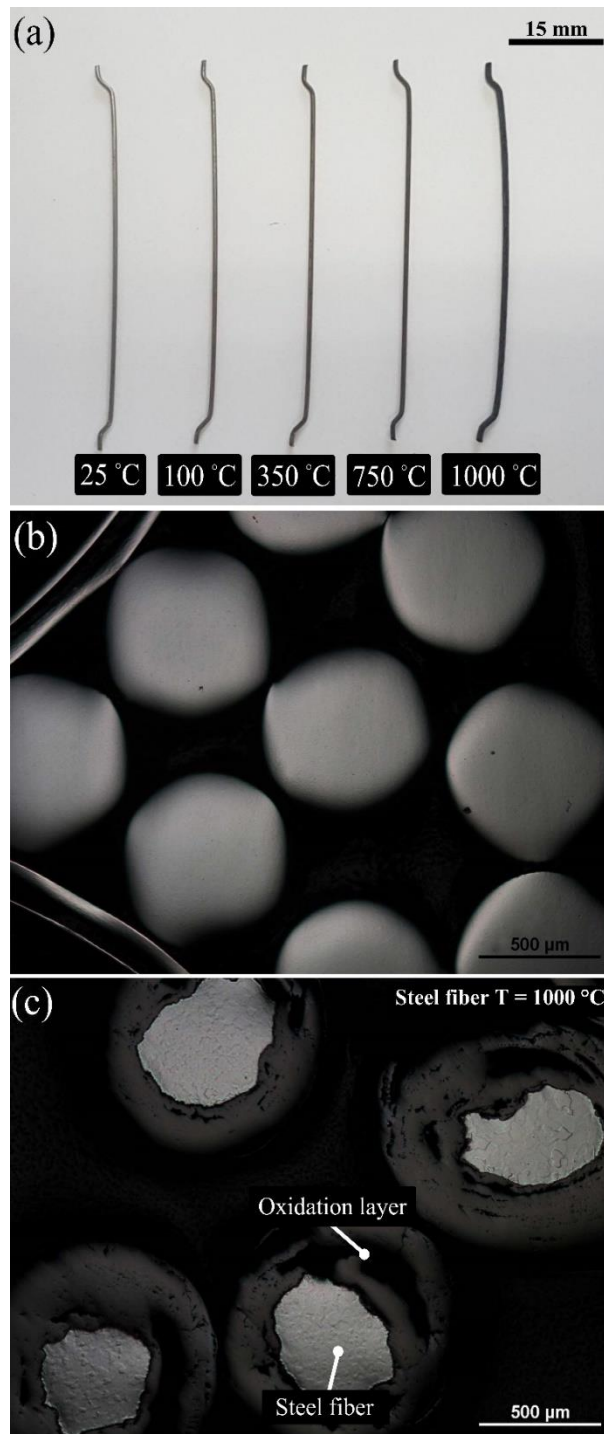


Figure 3 – Steel fibers: (a) after temperature exposure, (b) steel fiber at environmental condition, and (c) oxide layer formed in the surface of the fiber exposed to 1000 °C

Table 2 shows the average results obtained in terms of length, mass, external diameter, effective cross-sectional area, and effective diameter of steel fibers after elevated temperature exposure. Results obtained show that fiber length increases by 0.29% and 0.50% for the target temperatures evaluated. In this sense, no clear tendency between the steel fiber length and temperature has been evidenced. In terms of fiber mass, no significant increase has been noticed for target temperatures of 100 and 350 °C, while an increase of 1.5% and 23.0% was verified for the respective temperatures of 750 and 1000 °C. Changes in external diameter were not significant for target temperatures of 100 and 350 °C, while a significant increase of 3.8% and 35.4% was noticed for fibers exposed to 750 and 1000 °C, respectively. This increase in terms of external diameter may even be observed by the naked eye (see Fig. 3a).

Table 2– Summary of the physical properties of steel fibers after elevated temperature exposure

Properties	Temperature (°C)				
	25	100	350	750	1000
Length (mm)	61.76 (± 0.09)	62.06 (± 0.08)	62.06 (± 0.08)	61.94 (± 0.07)	62.05 (± 0.13)
Mass (g)	0.22 (± 0.01)	0.22 (± 0.01)	0.22 (± 0.01)	0.22 (± 0.01)	0.27 (± 0.01)
External diameter (mm)	0.76 (± 0.01)	0.76 (± 0.01)	0.75 (± 0.01)	0.79 (± 0.02)	1.03 (± 0.04)
Effective cross- sectional area (mm ²)	0.48 (± 0.01)	0.47 (± 0.05)	0.47 (± 0.01)	0.46 (± 0.01)	0.18 (± 0.03)
Effective diameter (mm)	0.78 (± 0.01)	0.77 (± 0.01)	0.77 (± 0.01)	0.77 (± 0.01)	0.48 (± 0.05)

The increase in terms of length, external diameter and total mass of steel fibers is directly associated with the process of high-temperature oxidation of steel. This process occurs because the oxidizing nature of the atmosphere favors the combination between oxygen and iron present in steel fibers to form an addition product (the oxide). This reaction forms an oxide with a friable three-layered scale structure that does not contribute to mechanical properties [17], and presents higher mass, but lower density than the original steel structure. As a consequence of this additive and expansive process of oxidation, mass, length, and external diameter of the steel fibers have shown a significant increase after exposure to elevated temperatures.

Although the total external diameter of fibers increase, a slight reduction tendency in the effective cross-sectional area of steel fibers can be noticed from 25 to 750 °C. However, this reduction lies in the same range of its standard deviation, which results

in the non-significance of results from the statistical standpoint. Associating this observation with the fact that the concrete surrounding the fiber in SFRC may act as a barrier to oxygen access, it is safe to assume that the oxidation process does not account for significant changes in the cross-sectional area of the steel fibers in temperatures equal or lower than 750 °C. For steel fibers after exposure to the target temperature of 1000 °C, a statistically significant reduction of 54.5% in terms of cross-sectional area was noticed, which is directly associated with the increased degree of oxidation that occurs in steel when temperature is higher than 800 °C [17].

The aforementioned conclusions are limited to the steel fiber evaluated in this study and for the similar testing conditions, since variables such as heating rate, cooling rate, and duration of the exposure may affect the oxidation process. Another important aspect is that steel fibers inside SFRC are passively protected by the concrete – which is exposed to an O₂ rich atmosphere. Therefore, the concrete that surrounds steel fibers may act as a barrier to oxygen access which means that the oxidation process inside concrete may not be as severe as in the experimental results hereby presented. In this way, the dynamics discussed in this paper can undergo some alteration when the fiber is embedded in concrete, which should be evaluated in the future. Even with this limitation, the main objective of this paper was not compromised and the results obtained are in favor of safety.

3.2 Mineralogical composition of the oxide

Figure 4 presents the XRD pattern obtained from the analysis of the oxide found in steel fibers. The results show that wüstite (FeO), hematite (Fe₂O₃), and magnetite (Fe₃O₄) are the main phases formed in high temperature oxidation of steel fibers. The high-temperature oxidation of carbon-steel follows a parabolic law in the temperature range of 800 to 1250 °C with the formation of a friable three-layered scale structure [17]. Thermodynamically, iron oxidizes to wüstite (FeO) as the initial oxide, while magnetite (Fe₃O₄) and hematite (Fe₂O₃) are formed at the expense of this lower oxide [25].

Also, oxide phases are composed of a thin outermost hematite layer, a thin intermediate magnetite layer, and a thick wüstite layer due to differences in the diffusive capacity of the oxide layers [17]. For temperatures lower than 800 °C, literature results show that the degree of oxidation is drastically reduced and is significantly affected by sample preparation methodology [17], which is also affected by the differences in terms of diffusion coefficient of each oxide phase [26–28].

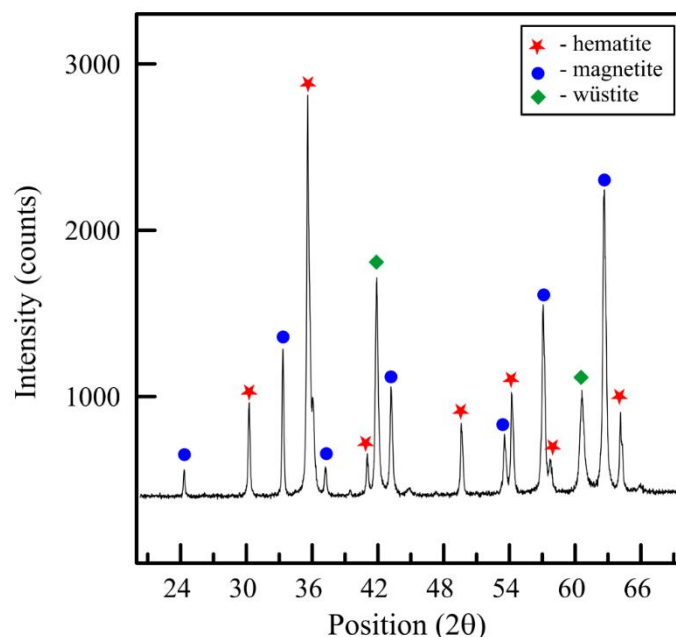


Figure 4 – XRD pattern of the oxide found in steel fibers

3.3 Grain size changes

Figure 5 shows the microstructural grain structure for target temperatures of 25, 350, 750, and 1000 °C. Steel fibers present an elevated degree of cold-work due to the characteristic orientation of the grain structure for temperatures of 25, 100, and 350 °C. This degree of cold-work results in difficulties to measure grain size, since the accumulation of discordances result in grain boundaries with poor definition.

At the temperature of 350 °C, it is possible to observe the occurrence of a recovery process by the diffusive movement and re-arranging of discordances in the microstructure. The grain size was measured for temperatures of 750 and 1000 °C and results are, respectively, 7.03 μm and 16.70 μm . This denotes an increase of almost 130% in grain-size from 750 to 1000 °C. At the temperature of 750 °C, the energy provided to the system is enough to favor the complete nucleation of discordances to form new sets of discordance-free grains. At the temperature of 1000 °C, it is possible to observe that the recently formed grains undergo a grain growth process that consumes previous discordances and the original grain structure.

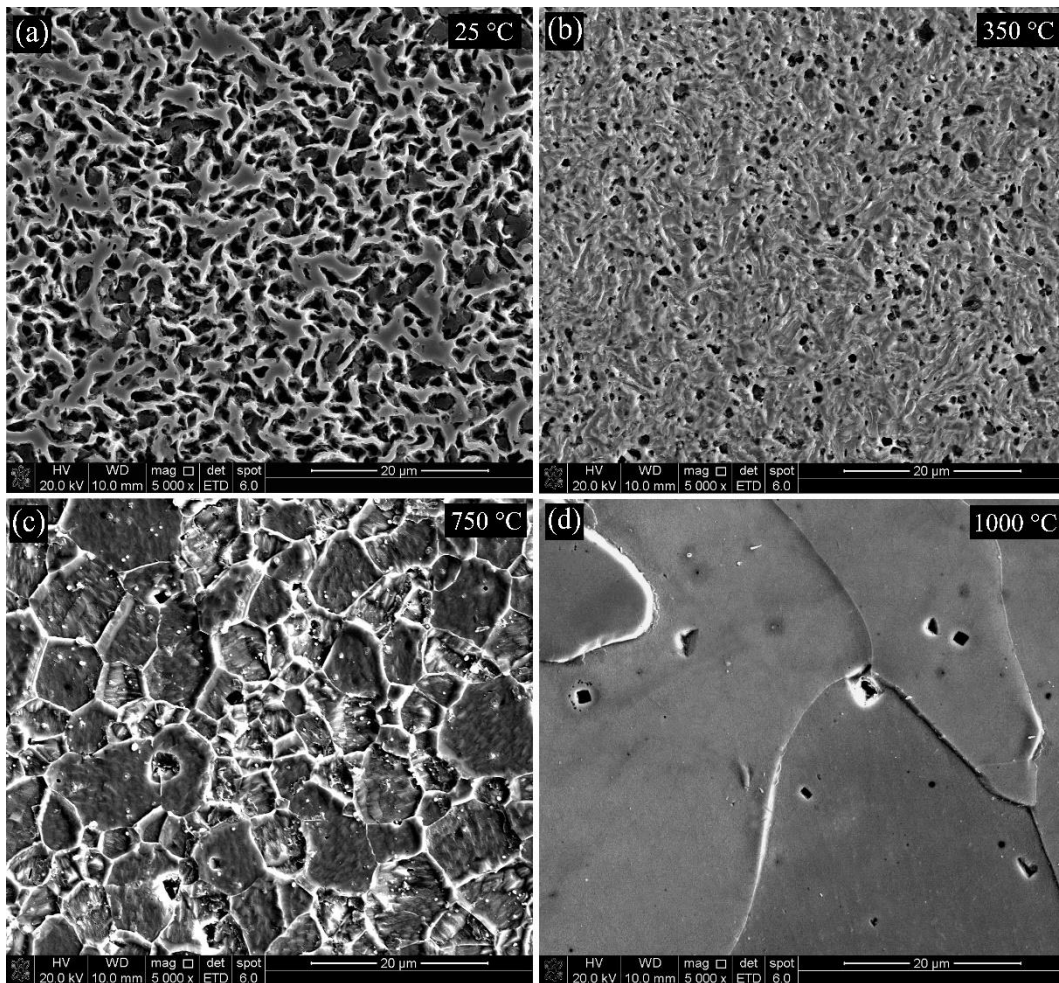


Figure 5 –Grain structure for target temperatures of (a) 25, (b) 350, (c) 750, and (d) 1000 °C

The formation of new grains and the grain growth process are responsible for the reduction in terms of grain boundary density values for the steel fibers. This reduction in grain boundary density affects the mechanical properties of the metal because a smaller amount of grain boundaries per unit area leads to a reduction in total energy required for dislocations to cross grain boundaries. Therefore, coarse-grained metals present, in general, lower tensile strength when compared to fine-grained ones [16,29,30].

3.4 Tensile strength of steel fibers

Figure 6 shows the stress-strain curves as a function of temperature for steel fibers. Table 3 presents the results of tensile strength and rupture strain of steel fibers as a function of temperature. All results obtained from the mechanical characterization were analyzed statistically through analysis of variances (ANOVA) and Tukey tests.

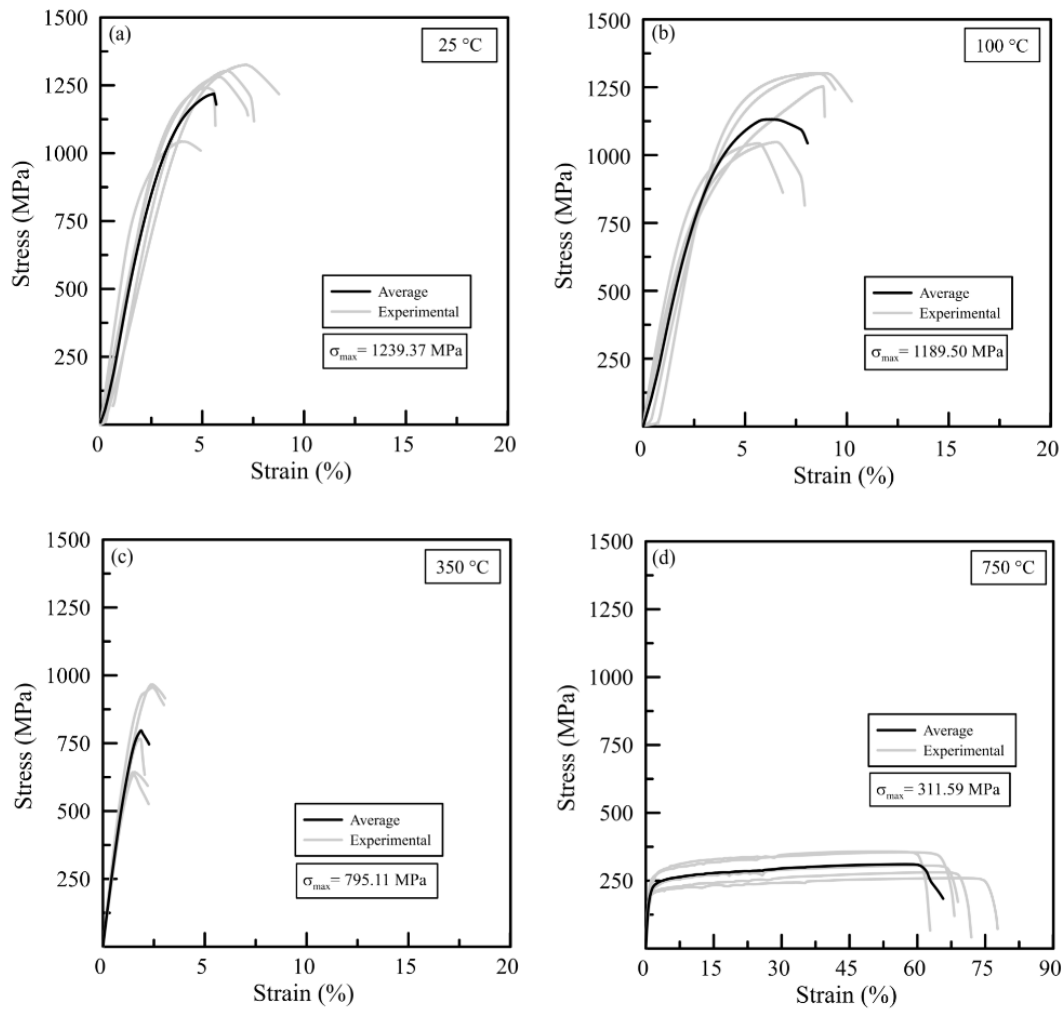


Figure 6 – Stress-strain curves of steel fibers exposed to (a) 25 °C, (b) 100 °C, (c) 350 °C, and (d) 750 °C

Table 3 – Tensile strength and rupture strain of steel fibers exposed to different temperatures

Property	25 °C	100 °C	350 °C	750 °C
Tensile strength (MPa)	1,239.37 (± 78.36)	1,189.50 (± 115.01)	795.11 (± 132.96)	311.59 (± 35.52)
Rupture strain (%)	5.66 (± 0.86)	7.67 (± 1.29)	1.94 (± 0.40)	60.04 (± 5.24)

The confining torque applied on steel fibers during the test resulted in fiber rupture on the jaw edge of the equipment instead of mid-span rupture. This was especially true for fibers exposed to temperatures of 25, 100 and 350 °C. This occurrence is related to the reduction on fiber cross-sectional area by the jaws and results in reduced values of tensile strength. Even with this limitation, the test allows to

evaluate the tensile strength of the fiber as a function of temperature, which is one of the key objectives of this study. Mid-span rupture was observed in steel fibers exposed to 750 °C. Steel fibers exposed to 1000 °C were friable and easily damaged while handling, which made the determination of tensile strength impossible.

Tensile strength of steel fibers exposed to 100 °C reduces when compared to fibers kept at room temperature. However, the difference observed is not statistically significant since it lies in the same range of its standard deviation. Steel fibers exposed to 100, 350, and 750 °C presented a reduction in tensile strength equal to 4.2%, 35.9%, and 74.9%, respectively, when compared to fibers not subjected to elevated temperatures. These reductions may be attributed to the microstructural changes since the cross-section of these fibers are not influenced at these temperatures. Reductions in tensile strength of fibers exposed to 350 °C are a result of the diffusive movement and re-arranging of discordances in the microstructure. The formation of new sets of defect-free grains and reduction in grain boundary surface area during the recrystallization process are the factors behind the tensile reduction in fibers exposed to 750 °C.

In terms of ductility, rupture strain values for temperatures of 100 °C and 350 °C remain statistically the same as reference. For the temperature of 750 °C, an increase of 962% in terms of rupture strain was evidenced as well as the presence of a strain yielding region before the descending branch associated with rupture (see Fig. 6). These results denote that no significant change in terms of ductility is evidenced for temperatures below the recrystallization temperature, while for temperatures above the recrystallization temperature the pre-cold-worked ductility conditions are restored. This behavior is in accordance with classical literature [15,16] and with the microstructural analysis presented in Section 3.2.

Figure 7 shows the average tensile strength and rupture strain as function of temperature for steel fibers. Grain structure during recovery, recrystallization, and grain growth stages are presented schematically according to the microstructural analysis conducted in this study.

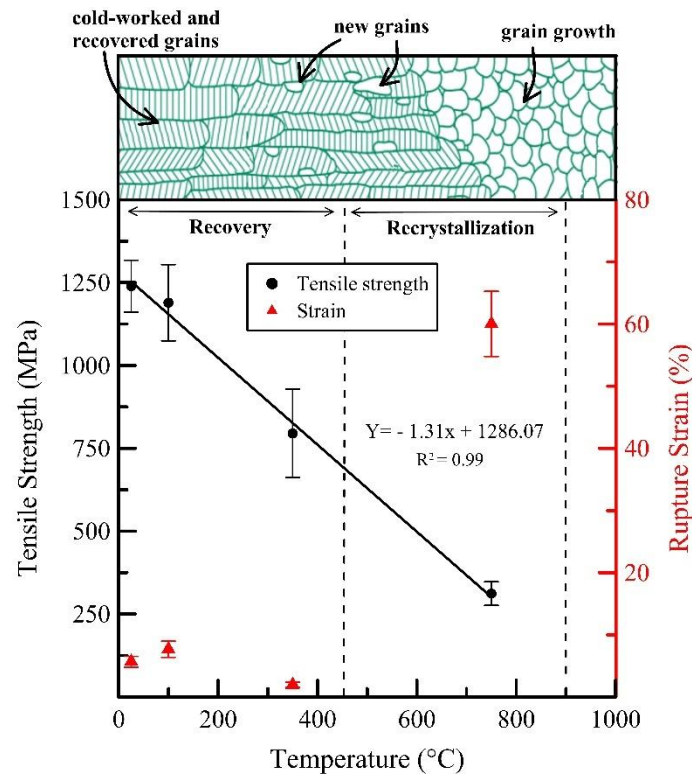


Figure 7 – Average tensile strength and rupture strain of steel fibers as functions of temperature

The residual tensile strength of steel fibers decreases linearly as temperature increases ($R^2 = 0.99$), even after the recrystallization temperature. Steel fibers exposed to 1000 °C were friable and easily damaged because of coupling effects of cross-sectional area reduction and a significant increase in the grain size of steel, as previously discussed from Sections 3.1 to 3.3. Considering that the friability evidenced for steel fibers exposed to 1000 °C is a result of both reduced cross-sectional area and the coarsening of steel fiber grain structure, the tensile strength results for temperatures above 750 °C may not follow the linear behavior evidenced in this study. Therefore, the linear relationship evidenced may not be valid for higher temperature values. Another relevant aspect to be mentioned is that concrete at temperatures of ~1000 °C have undergone severe physical, mechanical, and microstructural deterioration [10,31], which renders the applicability of the SFRC and the steel fiber itself in this temperature range.

In this context, the tensile properties of the steel fibers determined in this paper may be employed by designers using numerical models capable of a discrete and explicit representation of steel fibers inside the structural elements. Even with that statement, the effects of elevated temperature on the mechanical and microstructural properties of steel fibers account for part of the reinforcing mechanism of SFRC. The fundamental principle of SFRC is based on the fiber-matrix interaction and the capacity of the steel fibers to bridge the formation of cracks. Therefore, the behavior

of the SFRC is intrinsically bound not only to the mechanical properties of the fiber, but also to the bond properties between the fiber and the cementitious matrix [32], which is known to influence the post-crack behavior of the composite significantly [14,33], and the creep behavior at temperature, factors that need to be deeply investigated in the future.

4 Conclusions

The following conclusions may be drawn from the present study:

- Steel fibers oxidize with temperature forming a dark oxide layer composed of wüstite (FeO), hematite (Fe_2O_3), and magnetite (Fe_3O_4) on the surface of steel fibers. This oxidation process is more pronounced for steel fibers after exposure to temperatures of 750 °C and above. The mass of steel fibers increased by 1.52% and 23.01% for the respective temperatures of 750 and 1000 °C. A considerable increase in steel fiber length was noticed after temperature exposure, however no clear tendency has been evidenced.
- Although the total external diameter of fibers increased by 3.80% and 35.44% for the respective temperatures of 750 and 1000 °C, the effective cross-sectional area of steel fibers presented a slight reduction tendency for temperatures up to 750 °C and an average reduction of 54.5% for the temperature of 1000 °C.
- The grain structure was differently affected according to each target temperature. The hooked-end steel fibers present an elevated degree of cold-work for temperatures of 25, 100, and 350 °C. For samples exposed to 750 °C, the formation of a new sets of defect-free grains was evidenced and at target temperature of 1000 °C, the recently formed grains go through the grain growth process.
- The residual tensile strength of steel fibers decreases linearly as temperature increases up to 750 °C. The tensile strength reductions for temperatures of 100, 350, and 750 °C were of 4.2%, 35.9%, and 74.9%, respectively. In terms of ductility, rupture strain values for temperatures of 100 °C and 350 °C remain statistically the same as reference, while the restoration of the pre-cold worked conditions was evidenced for steel fibers exposed to temperature of 750 °C. Additionally, steel fibers exposed to 1000 °C were friable and easily damaged because of coupling effects of cross-sectional area reduction and a significant increase in the grain size of steel.

This study provides a better understanding of the behavior of the steel fibers subjected to high temperatures in terms of physical, microstructural, and tensile behavior. In addition to that, results presented in this study may be of great value for

the parameterization of numerical models where the characteristics of the fibers are relevant in their implementation, which can later be employed to simulate structural elements.

Acknowledgements

The authors would like to thank the Institute for Technological Research (IPT) and its foundation (FIPT) for their financial and institutional support through the New Talents Program N.01/2017. Renan Pícolo Salvador would like to thank FAPESP (process 2017/00125-9) for the scholarship granted. The authors would like to thank the CAPES (Coordenação de Aperfeiçoamento de Pessoal de Nível Superior). Authors would like to thank Dra. Ana Paola Villalva Braga (IPT) for the valuable contribution regarding the SEM analysis conducted.

References

- [1] A.D. de Figueiredo, *Concreto reforçado com fibras.*, Universidade de São Paulo, 2012. <https://doi.org/10.11606/T.3.2012.tde-18052012-112833>.
- [2] L.A.C. Borges, R. Monte, D.A.S. Rambo, A.D. de Figueiredo, Evaluation of post-cracking behavior of fiber reinforced concrete using indirect tension test, *Constr. Build. Mater.* 204 (2019) 510–519. <https://doi.org/10.1016/j.conbuildmat.2019.01.158>.
- [3] A. de la Fuente, P. Pujadas, A. Blanco, A. Aguado, Experiences in Barcelona with the use of fibres in segmental linings, *Tunn. Undergr. Sp. Technol.* (2012). <https://doi.org/10.1016/j.tust.2011.07.001>.
- [4] Federation Internationale du Beton, *Model Code for Concrete Structures 2010*, in: Ernst & Sohn, Germany, 2013: p. 434.
- [5] M. di Prisco, G. Plizzari, L. Vandewalle, *Fiber Reinforced Concrete in the New fib Model Code*, in: 3rd Fib Int. Congr. Inc. PCI Annu. Conv. Bridg. Conf. 2010, Precast prestressed concrete institute, Chicago, IL, USA, 2010.
- [6] Y.-S. Tai, H.-H. Pan, Y.-N. Kung, Mechanical properties of steel fiber reinforced reactive powder concrete following exposure to high temperature reaching 800°C, *Nucl. Eng. Des.* 241 (2011) 2416–2424. <https://doi.org/10.1016/j.nucengdes.2011.04.008>.
- [7] G.M. Chen, Y.H. He, H. Yang, J.F. Chen, Y.C. Guo, Compressive behavior of steel fiber reinforced recycled aggregate concrete after exposure to elevated temperatures, *Constr. Build. Mater.* 71 (2014) 1–15. <https://doi.org/10.1016/j.conbuildmat.2014.08.012>.

- [8] O. Düğenci, T. Haktanir, F. Altun, Experimental research for the effect of high temperature on the mechanical properties of steel fiber-reinforced concrete, *Constr. Build. Mater.* (2015). <https://doi.org/10.1016/j.conbuildmat.2014.11.005>.
- [9] W. Zheng, H. Li, Y. Wang, Compressive stress–strain relationship of steel fiber-reinforced reactive powder concrete after exposure to elevated temperatures, *Constr. Build. Mater.* 35 (2012) 931–940. <https://doi.org/10.1016/j.conbuildmat.2012.05.031>.
- [10] R. Serafini, S.R.A. Dantas, R.P. Salvador, R.R. Agra, D.A.S. Rambo, A.F. Berto, A.D. de Figueiredo, Influence of fire on temperature gradient and physical-mechanical properties of macro-synthetic fiber reinforced concrete for tunnel linings, *Constr. Build. Mater.* 214 (2019) 254–268. <https://doi.org/10.1016/j.conbuildmat.2019.04.133>.
- [11] S. Abdallah, M. Fan, K.A. Cashell, Bond-slip behaviour of steel fibres in concrete after exposure to elevated temperatures, *Constr. Build. Mater.* 140 (2017) 542–551. <https://doi.org/10.1016/j.conbuildmat.2017.02.148>.
- [12] G. Ruano, F. Isla, B. Luccioni, R. Zerbino, G. Giaccio, Steel fibers pull-out after exposure to high temperatures and its contribution to the residual mechanical behavior of high strength concrete, *Constr. Build. Mater.* 163 (2018) 571–585. <https://doi.org/10.1016/j.conbuildmat.2017.12.129>.
- [13] S. Abdallah, M. Fan, D.W.A. Rees, Effect of elevated temperature on pull-out behaviour of 4DH/5DH hooked end steel fibres, *Compos. Struct.* 165 (2017) 180–191. <https://doi.org/https://doi.org/10.1016/j.compstruct.2017.01.005>.
- [14] N. Banthia, *Fiber Reinforced Concrete*, ACI SP-142ACI, Detroit, MI. (1994). <https://doi.org/10.4188/transjtmsj1965a.24.P621>.
- [15] S. James, W. Alexander, *Materials Science and Engineering Handbook*, 2001. <https://doi.org/10.1126/science.232.4757.1485>.
- [16] W. Callister, D. Rethwisch, *Materials science and engineering: an introduction*, 7th ed., John Wiley, New York, USA, 2007.
- [17] R.Y. Chen, W.Y.D. Yuen, Review of the high-temperature oxidation of iron and carbon steels in air or oxygen, *Oxid. Met.* (2003). <https://doi.org/10.1023/A:1023685905159>.
- [18] L. A. G. Bitencourt, O.L. Manzoli, T.N. Bittencourt, F.J. Vecchio, Numerical modeling of steel fiber reinforced concrete with a discrete and explicit representation of steel fibers, *Int. J. Solids Struct.* 159 (2019) 171–190. <https://doi.org/10.1016/j.ijsolstr.2018.09.028>.

- [19] T. Abu-Lebdeh, S. Hamoush, W. Heard, B. Zornig, Effect of matrix strength on pullout behavior of steel fiber reinforced very-high strength concrete composites, *Constr. Build. Mater.* (2011). <https://doi.org/10.1016/j.conbuildmat.2010.06.059>.
- [20] R.P. Salvador, S.H.P. Cavalaro, R. Monte, A.D. d. Figueiredo, Relation between chemical processes and mechanical properties of sprayed cementitious matrices containing accelerators, *Cem. Concr. Compos.* (2017). <https://doi.org/10.1016/j.cemconcomp.2017.02.002>.
- [21] R.P. Salvador, D.A.S. Rambo, R.M. Bueno, K.T. Silva, A.D. de Figueiredo, On the use of blast-furnace slag in sprayed concrete applications, *Constr. Build. Mater.* (2019). <https://doi.org/10.1016/j.conbuildmat.2019.05.132>.
- [22] American Society for Testing and Materials, E112-13:Standard Test Methods for Determining Average Grain Size, *ASTM Int.* (2013). <https://doi.org/10.1520/E0112-13>.
- [23] Associação brasileira de normas técnicas (ABNT), ABNT NBR ISO 6892-2002 Materiais metálicos - Ensaio de tração à temperatura ambiente, Rio de Janeiro, RJ, 2002.
- [24] BS EN 1992-1-2, Eurocode 2 Design of concrete structures - Part 1-2: General rules-Structural fire design, *Des. Concr. Struct. - Part 1-2 Gen. Rules-Structural Fire Des.* (2004).
- [25] H. Abuluwefa, The effect of oxygen concentration on the oxidation of low-carbon steel in the temperature range 1000 to 1250°C, *Oxid. Met.* (1996). <https://doi.org/10.1007/BF01048639>.
- [26] W.W. Smeltzer, D.J. Young, Oxidation properties of transition metals, *Prog. Solid State Chem.* (1975). [https://doi.org/10.1016/0079-6786\(75\)90003-5](https://doi.org/10.1016/0079-6786(75)90003-5).
- [27] J.S. Sheasby, W.E. Boggs, E.T. Turkdogan, Scale growth on steels at 1200°C: rationale of rate and morphology, *Met. Sci.* (1984). <https://doi.org/10.1179/msc.1984.18.3.127>.
- [28] B. Gleeson, S.M.M. Hadavi, D.J. Young, Isothermal transformation behavior of thermally-grown wustite, *Mater. High Temp.* (2000). <https://doi.org/10.1179/mht.2000.17.2.020>.
- [29] C. Yue, L. Zhang, S. Liao, H. Gao, Kinetic analysis of the austenite grain growth in GCr15 steel, *J. Mater. Eng. Perform.* (2010). <https://doi.org/10.1007/s11665-009-9413-y>.
- [30] M. Militzer, H. EB, Analysis of the austenite grain size distribution in plain carbon steels, *ISIJ Int.* 39 (1999) 271–280.

- [31] Z.P. Bažant, M.F. Kaplan, Concrete at high temperatures: material properties and mathematical models, Longman, 1996.
- [32] B. Luccioni, G. Ruano, F. Isla, R. Zerbino, G. Giaccio, A simple approach to model SFRC, *Constr. Build. Mater.* (2012).
<https://doi.org/10.1016/j.conbuildmat.2012.07.027>.
- [33] A. Bentur, S. Mindess, Fibre reinforced cementitious composites, 2nd ed., Taylor & Francis, New York, 2007.

ARTICLE B

Title: Bond-slip response of steel fibers after exposure to elevated temperatures: experimental program and design-oriented constitutive equation

Submit to: Composite Structures

Publication date: 01/01/2021.

Status: Published (doi: [10.1016/j.compstruct.2020.112916](https://doi.org/10.1016/j.compstruct.2020.112916))

**BOND-SLIP RESPONSE OF STEEL FIBERS AFTER EXPOSURE TO
ELEVATED TEMPERATURES: EXPERIMENTAL PROGRAM AND DESIGN-
ORIENTED CONSTITUTIVE EQUATION**

Ramoel Serafini^{1,2*}, Ronney Rodrigues Agra^{1,2}, Luís A. G. Bitencourt Jr.³, Albert de la
Fuente⁴, Antonio D. de Figueiredo¹

¹Department of Civil Construction Engineering, Polytechnic School at the University of São Paulo |
Avenida Professor Almeida Prado, Travessa do Biênio, 83, 05424-970, São Paulo, Brazil.

² Institute of Technological Research | Avenida Professor Almeida Prado, 532, 05508-901, São Paulo,
Brazil

³ Department of Structural and Geotechnical Engineering, Polytechnic School at the University of São
Paulo | Avenida Professor Almeida Prado, Travessa do Biênio, 83, 05424-970, São Paulo, Brazil.

⁴ Department of Construction Engineering, Polytechnic University of Catalonia | Jordi Girona, 1-3,
08034, Barcelona, Spain

*corresponding author: rserafini@usp.br

Keywords: pullout; bond-slip response; hooked-end steel fibers; elevated temperatures; numerical
simulation

ABSTRACT

This study aimed to evaluate the effect of elevated temperatures on the bond-slip behavior of hooked-end steel fibers. A total of 180 pullout specimens were tested in post-cooling conditions using a double-sided pullout test with multiple embedded fibers for target temperatures between 25 and 750 °C. Results proved that the bond strength significantly increases for temperatures up to 450 °C, and drastically decreases for temperatures of 600 and 750 °C. The contribution of hooks reduced with

temperature and is negligible for temperatures higher than 600 °C, while the fiber-matrix frictional interaction seems to improve for all temperatures evaluated. A temperature-sensitive constitutive equation that allows simulating the bond-slip behavior of hooked-end steel fibers is proposed and its suitability confirmed through a numerical model.

1 Introduction

The fundamental principle of steel fiber reinforced concrete (SFRC) is based on the interaction between fibers and the cementitious matrix to provide plain concrete a pseudo-ductile behavior and enhance post-crack mechanical properties. The steel fibers bridge the cracks through the matrix and enhance the post-crack tensile strength of the composite, which is a key feature for structural applications [1,2]. Three main components that must be characterized to analyze these composites after temperature exposure are the cementitious matrix, the fibers, and the fiber-matrix interface. In this regard, the bond-slip response between the fiber and the cementitious matrix is a key parameter to model the SFRC mechanical behavior [3] and is known to strongly influence the post-crack behavior of the composite [4,5]. The bond-slip response of hooked-end steel fibers in the cementitious matrix can be parameterized by pullout test results and can be divided into five main stages [6], which are schematically shown in Figure 1.

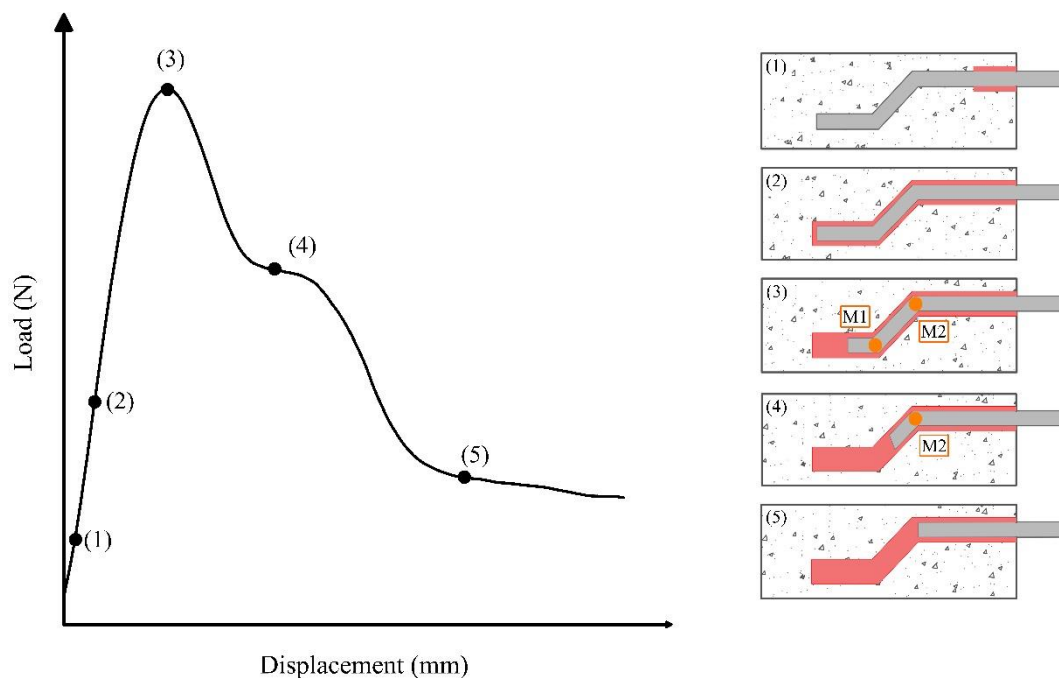


Figure 1 – Schematic diagram of the pullout mechanism for hooked-end steel fibers

Stage 1 and 2 are defined as the partial and full debonding between fiber and matrix, respectively. Once the full debonding takes place, the dynamic frictional interaction

between fiber and matrix begins. At this stage, the fibers must undergo a considerable plastic deformation due to the straightening of the hooks before the dynamic frictional interaction occurs [6], which defines Stages 3 and 4. The mechanical interlocking caused by the plastic deformation of the hooks at M1 and M2 increases the maximum pullout load value at Stage 3.

As soon as the tip of the fiber goes beyond M1, the pullout load substantially decreases and the mechanical interlocking is caused only by the plastic deformation of the hook at M2. It is important to remind that the matrix cracks as the pullout occurs [5] and that the energy required to yield the hooks is intrinsically bound to the bending stiffness and the hook geometry of the steel fiber, as well as the interfacial bond properties [7,8]. After the hook is completely straightened, the dynamic frictional interaction between fiber and matrix takes place in Stage 5. This last phase results in a rapid drop in the pullout load values and prevails until the whole fiber is removed from the matrix pathway [6].

Pullout tests are conducted in a wide variety of setups in the literature. The difference between methodologies adopted is usually related to the number of fibers embedded (single or multiple fibers) and the method of applying the tensile force (single- or double-sided). The pullout tests are commonly performed employing single-sided tests on a single fiber, owing to the simplicity of the methodology during the preparation of specimens and during the test [6]. However, a major drawback of this methodology is that the test setup needs to be capable of precision measurements due to the intrinsically low pullout forces. More than that, difficulties encountered in single-sided tests are mainly associated with the interaction between the grip and the fiber. Also, high variability is common in single-sided tests on a single fiber, which requires a considerable number of specimens to guarantee the reliability of the results [9].

The drawbacks of using single-sided tests with a single fiber are further aggravated for pullout specimens that are exposed to elevated temperatures. This occurs because the pullout forces are expected to reduce and the steel fiber mechanical properties to be negatively affected after high-temperature exposure. Several studies have investigated the bond-slip properties of hooked-end steel fibers at room temperature conditions in the last decades [9–12]. However, the studies regarding the bond-slip behavior of steel fibers after elevated temperatures are very scarce in the literature. In this sense, there is a need for identifying constitutive equations and analytical

formulations to the designers' community so that the effect of fire on SFRC structures can be properly assessed.

Results obtained by recent studies show that the pullout load values were comparable up to ~ 400 °C and significantly reduced for higher temperatures [13–16]. However, the non-significant effect of temperature up to 400 °C may be a side effect of the intrinsic dispersion of single-sided tests with a single fiber, since the standard deviation values were omitted. Moreover, numerical models focusing on the explicit and discrete representation of the steel fibers in SFRC have been developed recently and require an accurate description of the steel fiber bond-slip behavior as input [17,18]. So far, the results published in the literature have not provided a microstructural based explanation for the changes in the bond-slip behavior or proposed a constitutive equation for design purposes, which denotes that the topic still needs to be deeply investigated.

The present study aims to evaluate the bond-slip behavior of hooked-end steel fibers after exposure to elevated temperatures employing a double-sided pullout test using multiple fibers. This test methodology aims at increasing the stability of the test and avoiding the drawbacks associated with single-sided and single fiber pullout tests. The interfacial transition zone of the steel fibers was characterized to assess the effect of temperature on the vicinity of the fiber and relate the microstructural results with the mechanical behavior. Additionally, an analytical model was proposed and the pullout tests were validated through numerical simulations using a discrete and explicit representation of steel fibers inside the pullout specimens.

2 Materials and methods

Figure 2 shows a schematic drawing of the experimental program conducted in this study. The investigation herein conducted took place within the framework of a Ph.D. research project regarding the study of the effect of temperature on the properties of fiber-reinforced composites. In this sense, all the characterizations were conducted using a mortar that followed the SFRC mix design based on the work of Serafini et al. [19] and a detailed description and characterization of the materials employed can be found in the referenced study. Even with those considerations, a brief description is presented in this section.

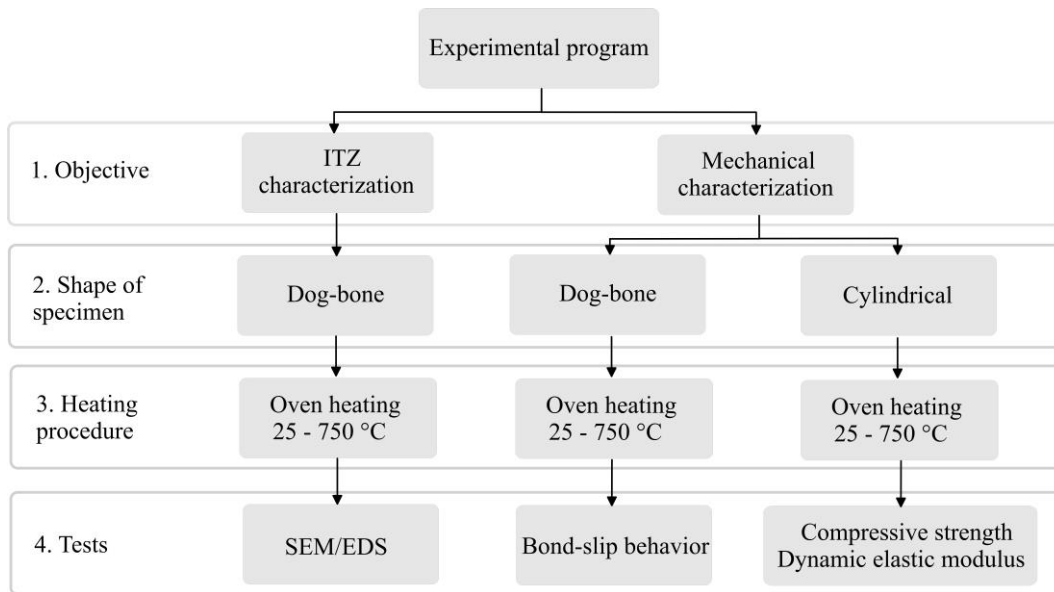


Figure 2 – Scheme adopted for the experimental program of this study

The bond-slip response of the hooked-end steel fibers was evaluated after exposure to high temperatures. Based on the experimental results, an analytical equation that computes the effect of temperature on the bond-slip behavior of steel fibers is proposed. This equation is used as input for a refined numerical model that is capable of representing the steel fibers discretely and explicitly inside the plain concrete [18]. As supplementary investigations, the characterization of the interfacial transition zone (ITZ) is performed and aims to verify the effect of temperature on the vicinity of the fiber, which can be correlated with the bond-slip response. Additionally, the effect of temperature on the compressive strength and dynamic elastic modulus of the mortar were evaluated and serve as input for the numerical simulation conducted in this study.

2.1 Materials

The cementitious materials used in this study were a Type I Portland cement (CEM I 52.5R) and silica fume type Elkem 920-U. The particle packing was increased by using river and artificial sand as fine aggregates and two coarse granite aggregates. A polycarboxylate-based superplasticizer, GCP ADVA Cast 525, was used to provide consistency to the mix. A cold-drawn, hooked-end steel fiber, Dramix 3D 80/60-BG, was employed. This steel fiber was chosen since it is commonly used in structural applications. The explosive spalling phenomenon was mitigated by the addition of Neomatex FireX polypropylene microfibers. Table 1 shows fiber manufacturer data for both fiber types.

Table 1 – Fiber manufacturer data for both fiber types

Characteristics	Hooked-end steel fiber	Micro-synthetic fiber
Length (mm)	60	12
Diameter (mm)	0.75	0.03
Aspect ratio (l/d)	80	400
Specific weight (kg/m ³)	7850	910
Specific surface area (m ² /kg)	3.45	147
Melting point (°C)	~1370	165
Tensile strength (MPa)	1225	Not provided
Young modulus (GPa)	210	Not provided

2.2 Composition and preparation of mortar

The composition of the mortar was based on the mix design of the precast segments used in tunnel linings of Subway Line 6 of São Paulo [19], which is described in Table 2. Silica fume was used as supplementary cementitious material at a content of 5.5% of the cement mass, and the w/cm ratio was kept constant at 0.39. All aggregates were oven-dried at 100 °C for 14 h before mortar production. Synthetic micro-fibers were added in a content of 0.15% of the total volume, or 1.4 kg/m³, according to project specifications, to avoid damage of the mortar due to explosive spalling.

Table 2 – Dosage of materials to produce 1 m³ of mortar

Materials	Dosage (kg/m ³)
Portland cement	700
Silica fume	39
Water	289
Siliceous river sand	705
Artificial granite sand	471
Superplasticizer	5.25
Synthetic micro-fiber	1.4

The mortar mixing was conducted by using a planetary Hobart N50 mixer with a total capacity of 5 L in a room at (25 ± 1) °C. The following procedure was adopted: microfibers were added to the bowl and dispersed with water for 90 seconds. This period was divided into 30-30-30 seconds in, respectively, low-high-low speed. Then, the fine aggregates, cement, and silica fume were added during 60 seconds with the equipment turned off and 30 seconds were given for particle wetting. At last, water and dry powder were mixed for 90 seconds, following the same 30-30-30 seconds in low-high-low speed. The aforementioned mixing procedure was adopted since it

results in better homogenization of materials and microfibers according to Dantas et al. [20]. A total of 30 cylindrical specimens with a diameter of 50 mm and a height of 100 mm were produced to assess the compressive strength and the dynamic elastic modulus of the material.

Pullout specimens in the shape of dog-bones were produced to assess the bond-slip behavior of the hooked-end steel fibers. Figure 3 shows the dimensions of the pullout specimens produced. The pullout specimens were manufactured using four steel fibers instead of the usual single fiber, which had as objective to increase the stability of the test. This was adopted by the authors as a countermeasure to the intrinsic low pullout load values of single-fiber pullout tests, which are made even more severe by the exposure to elevated temperatures [13,14,16]. A total of 180 pullout specimens were produced and tested in this study.

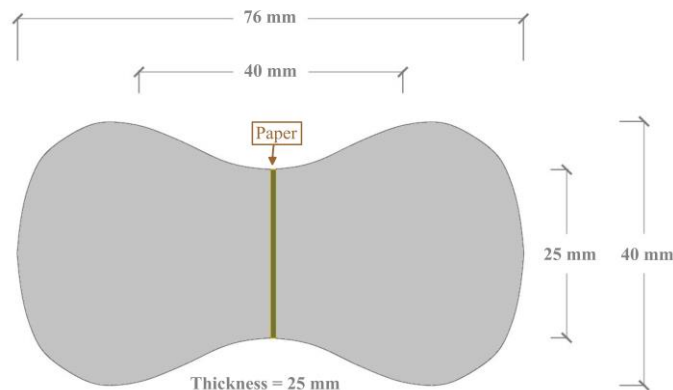


Figure 3 – Dimensions of the pullout specimen produced

Figure 4 illustrates the molding procedure, the fixation frame, and the pullout specimen produced. The four steel fibers were positioned in the middle of the molds with a measured embedded length of 30 mm at each side and separated by a distance of 10 mm between the fibers. Since the embedded lengths are the same on both sides, the pullout may occur from either side without any detrimental effect on the results. In cases where different embedded lengths are adopted, the methodology must ensure that the four fibers are pulled out from the same side of the specimen to ensure the reliability of the results.

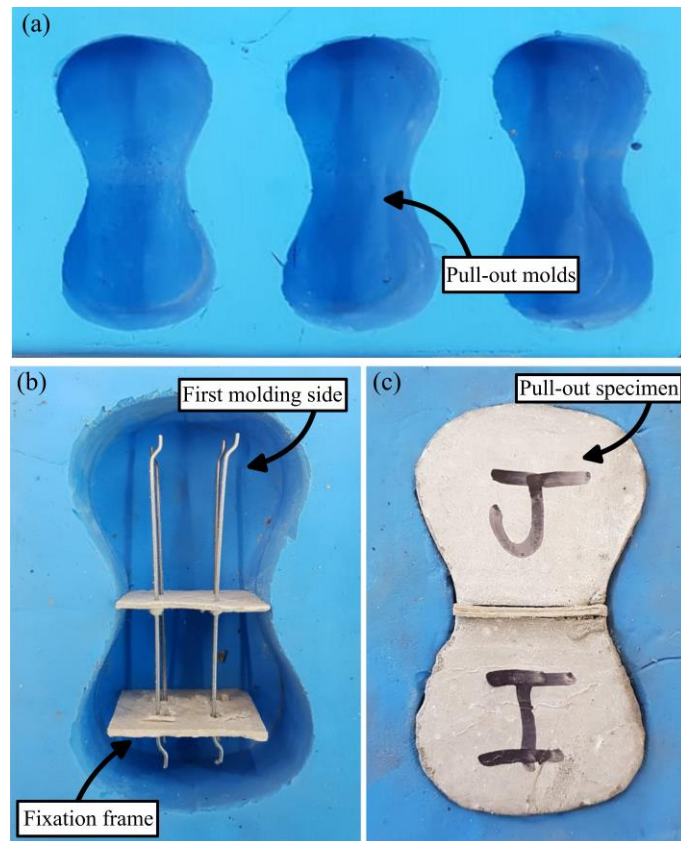


Figure 4 – Molding procedure: (a) the pullout molds (b) fixation frame (c) pullout specimen

Two papers of 250 g/m^2 were used to fix the steel fibers inside the mold. This procedure had the objective of preventing the steel fibers from moving or rotating inside the pullout specimens. After that, the mortar was poured inside one half of the mold. The embedded length was double-checked on the empty side of the mold and, after 4 hours, the fixation frame was removed, and the other half of the mold was filled with mortar. After the molding procedure, the pullout molds were sealed with a protective plastic film during 12 h until the specimens could be removed from the mold. After demolding, the pullout specimens were cured in a humid chamber for 72 h and then stored at room temperature of $(25 \pm 1) \text{ }^\circ\text{C}$ until the age of 150 days to better simulate *in situ* humidity and curing conditions.

2.3 Heating procedure

The cylindrical and pullout specimens were heated using an EDG FC series electric oven, model EDG10P-S, at a heating rate of $(20 \pm 3) \text{ }^\circ\text{C}/\text{min}$ at the age of 150 days. The period at target temperature adopted was determined by numerical simulation to ensure the thermal stability of the specimens based on the work of Carpio et al. [21]. Therefore, the pullout specimens were kept at target temperatures during 10, 8, 6, 4, and 4 h for the respective temperatures of 150, 300, 450, 600, and $750 \text{ }^\circ\text{C}$. After the heat exposure was over, the chamber was kept closed and cooling until the room temperature was achieved for 24 h. The cooling rate was not controlled. After

cooling, both the cylindrical and pullout specimens were taken for mechanical testing. Figure 5 shows the heating procedure adopted for the cylindrical and pullout specimens.

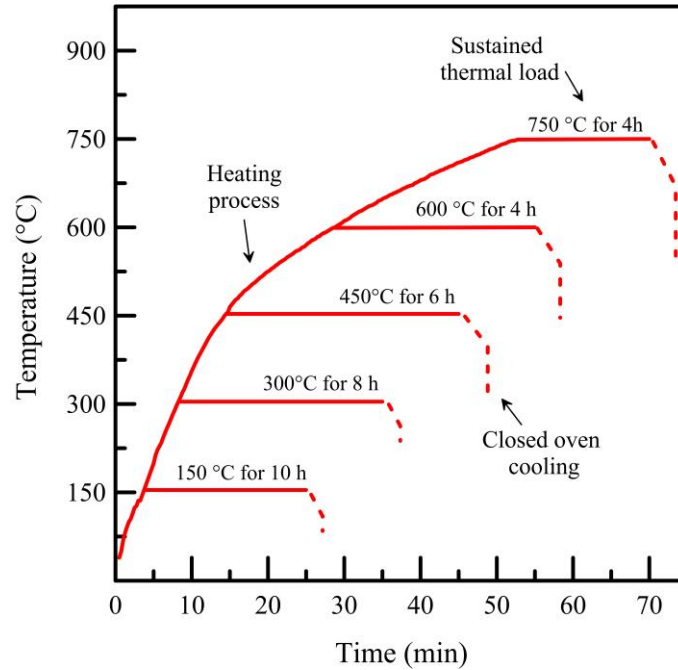


Figure 5 – Heating procedure adopted for cylindrical and pullout specimens

2.4 Test method

2.4.1 Compressive strength test

The compressive strength tests were conducted on a Shimadzu Universal Testing Machine, model UH-F1000kN, with a computer-controlled hydraulic servo system, and a maximum load capacity of 1,000 kN. The test was load-controlled at a rate of 0.5 MPa/s and piston displacement data was used to calculate the strain values during the test. A total of 30 specimens were tested, 5 for each target temperature: 25, 150, 300, 450, 600, and 750 °C.

2.4.2 Ultrasonic pulse velocity test

The ultrasonic (US) propagation test was conducted by using a Portable Ultrasonic Non-destructive Digital Indicating Tester (PUNDIT) equipment using 200 kHz transducers and a circular cross-section with a 20 mm diameter. The US propagation velocity was determined in the same specimens before and after temperature exposure and used to determine the dynamic elastic modulus (E_c) of the mortar before and after temperature exposure, calculated as:

$$E_c = \frac{\rho \cdot V^2 \cdot (1 + \nu) \cdot (1 - 2\nu)}{1 - \nu} \quad (1)$$

where ρ is the density of the mortar (in kg/m^3); V is the propagation pulse velocity (in km/s); ν is the Poisson's ratio). The density of the material was recalculated for each target temperature based on the mass and volume of the specimens. Although data about the effect of temperature on Poisson's ratio are relatively scarce and tend to be inconsistent, the results found in the literature show that this property does not change significantly for small stress values [22]. Therefore, the Poisson's ratio was assumed to be constant at 0.2 for all target temperatures.

2.4.3 Fiber-matrix interface

The effect of elevated temperatures on the fiber-matrix interface was evaluated through Scanning Electron Microscopy (SEM) with Energy Dispersive Spectroscopy (EDS) for a more in-depth analysis of the results. Line scanning EDS analyses were conducted to obtain the surface chemical profile concerning the radial distance from the fiber, represented by the red line in the example presented in Figure 6.

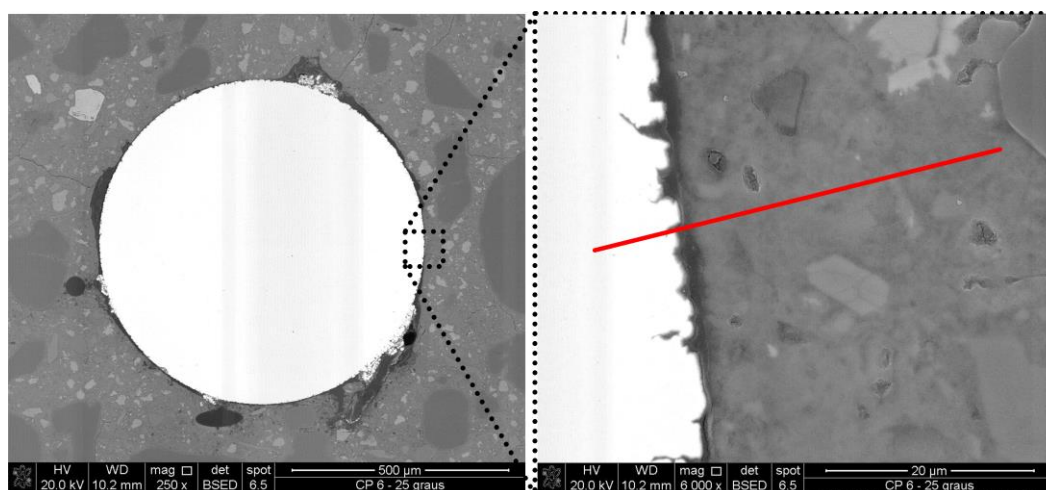


Figure 6 – EDS analysis conducted to obtain the surface chemical profile in the vicinity of the fiber

Samples were prepared by using the dog-bone shaped pullout specimens after the heat procedure and mechanical testing was conducted. The pullout specimens were sliced with a precision saw and the region around the fiber was analyzed in samples measuring 25 x 25 x 25 mm. The samples were embedded in resin and plane ground employing 150 μm grained sandpaper and fine ground employing 9 μm grained sandpaper for 10 minutes at the 1000 and 150 rpm, respectively. After grinding, the samples were dry-polished using a 2 μm diamond polishing cloth specific for metallographic purposes. Samples were then taken for SEM/EDS analysis in the Center for Metallurgical and Materials Technologies (CTMM) at the Institute for Technological Research (IPT). SEM/EDS tests were conducted using a Quanta 3D FEG instrument, equipment at the voltage of 20 kV, working distance of 10 mm, using XT microscope control FEI software to obtain backscattered electron imagery.

The calcium (Ca) and silicon (Si) contents were determined by EDS and can be used as an indirect method to assess the composition of the cementitious matrix utilizing the Si/Ca ratio [23]. Additionally, the contents of iron (Fe), oxygen (O), and carbon (C) were determined and served as a means to assess the changes in steel and the location of fracture surfaces.

2.4.4 Pullout test

Figure 7 illustrates the pullout test setup conducted in this study. The pullout tests were conducted using an electromechanical universal testing machine in an open-loop configuration, EMIC DL 10000, with a load-cell with a maximum load capacity of 10 kN and precision of 1 N. The test was displacement-controlled at a rate of 0.5 mm/min. The load cell was placed on the top of the machine crosshead to read the fiber pullout force while the slip between the fiber and matrix was determined by piston displacement readings. The initial accommodation was minimized by slowly applying the load to the specimens until some load was recorded by the load cell before initiating the test.



Figure 7 – Pullout test setup conducted in this study

The pullout test was stopped before the complete pullout of the fiber from the specimen occurred. This was adopted because the failure criteria established into the design guidelines (i.e. maximum crack width of 2.5 mm according to the *fib* Model Code 2010 [24]) is achieved before the full embedded length (30 mm) is pulled out of the matrix. Therefore, the pullout tests of this study were conducted until a displacement of 10 mm was achieved, since any result obtained for greater displacement values would have no useful application from the engineering standpoint. In this sense, 30 pullout tests were performed for each target temperature of 25, 150, 300, 450, 600, and 750 °C, representing a total of 180 specimens.

Furthermore, the pullout curves obtained from the pullout tests were normalized to be representative of a single fiber pullout. This was achieved by dividing the pullout curves by the amount of resisting fibers in each section of the test. This normalization was required to make a valid comparison with the literature results. Additionally, the rupture of some fibers occurred in specimens exposed to elevated temperatures, thus, this normalization was strictly necessary to guarantee the validity of the comparison.

2.4.5 Statistical analysis

The compressive strength and dynamic elastic modulus of the mortar, as well as the results of bond-slip results obtained in this study, were statistically analyzed through analysis of variances (ANOVA) and Tukey tests [25]. The relationship between the sample size and the admissible error was determined only for the variables associated with the bond-slip response of the hooked-end steel fibers since this topic is the main contribution of this study. In this sense, the relationship between the sample size and the admissible error was determined based on concepts of inferential statistics [26], as follows:

$$n = \frac{s^2 \cdot z_\gamma^2}{\varepsilon^2} \quad (2)$$

where n is the required sample size; s is the standard deviation obtained by the pilot sample (in MPa); z_γ is the Student's t-distribution value; ε is the admissible error for the test. The average and standard deviation values were determined based on the experimental campaign conducted, while a t-distribution value was adopted considering a confidence interval of 95% and $(n - 1)$ degrees of freedom.

3 Results and discussion

3.1 Compressive strength and elastic modulus

Figure 8 illustrates the density values and pulse velocity changes as a function of temperature. Table 3 shows the average results for the density and pulse velocity of mortar before and after temperature exposure.

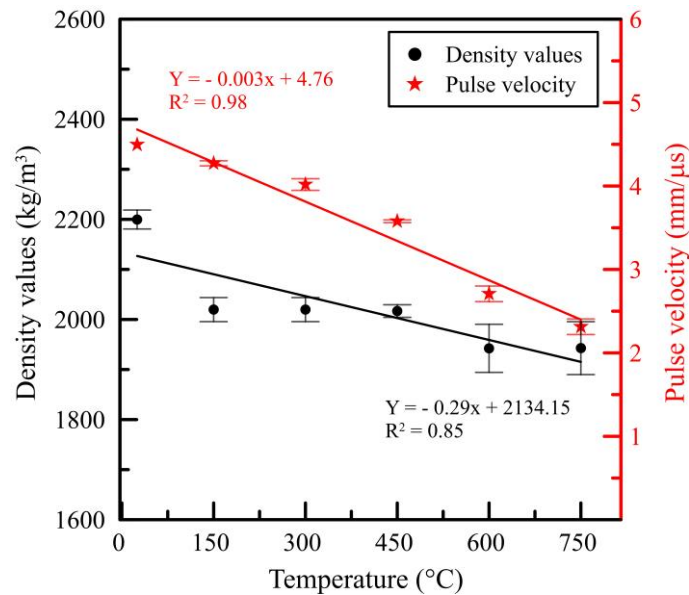


Figure 8 – Average density values and pulse velocity changes as a function of temperature

Table 3 – Average results for the density and US propagation velocity of the mortar

Temperature (°C)	Before temperature exposure		After temperature exposure	
	Density (kg/m ³)	Pulse velocity (mm/μs)	Density (kg/m ³)	Pulse velocity (mm/μs)
25	2200 (± 19)	4.50 (± 0.06)	Not applicable	Not applicable
150	2186 (± 23)	4.52 (± 0.04)	2020 (± 24)	4.27 (± 0.03)
300	2192 (± 16)	4.52 (± 0.06)	2020 (± 24)	4.02 (± 0.07)
450	2212 (± 9)	4.52 (± 0.11)	2017 (± 13)	3.58 (± 0.02)
600	2202 (± 25)	4.53 (± 0.08)	1942 (± 48)	2.71 (± 0.09)
750	2186 (± 23)	4.50 (± 0.11)	1943 (± 53)	2.31 (± 0.09)

The reductions in density values were of 7.6%, 7.9%, 8.8%, 11.8%, and 11.1% for the respective temperatures of 150, 300, 450, 600, and 750 °C. Reductions were also observed in terms of the ultrasonic pulse velocity, which were 5.4%, 11.1%, 20.9%, 40.3%, and 48.5% for the same respective temperatures. As temperature increases, the release of free water and the dehydration of hydrated products of the cement paste occurs [19,27]. This dehydration is responsible for the reduction in the specific surface area of the hydrates and the coarsening of the pore structure, which increases the porosity of the cement paste [27,28], the increase in capillarity pore size, and the

generation of cracks [29]. The aforementioned changes significantly contribute to the reductions in terms of density values and ultrasonic pulse velocity evidenced in this study.

Figure 9 shows the stress-strain curves and the residual values of compressive strength (f_c) and dynamic elastic modulus (E_c) as a function of temperature for the mortar used in this study. The average results can be found in Table 4. Specimens tested at room temperature presented an average compressive strength of 89.3 MPa and an average elastic modulus of 40.0 GPa.

Table 4 – Average results in terms of mechanical properties for each target temperature

Target temperature (°C)	f_c (MPa)	E_c (GPa)
25	89.3 (\pm 6.4)	40.0 (\pm 1.3)
150	85.5 (\pm 3.2)	34.2 (\pm 0.5)
300	72.3 (\pm 5.3)	29.4 (\pm 1.3)
450	57.6 (\pm 3.4)	23.2 (\pm 0.3)
600	42.3 (\pm 5.0)	12.8 (\pm 1.1)
750	26.0 (\pm 3.4)	9.4 (\pm 0.6)

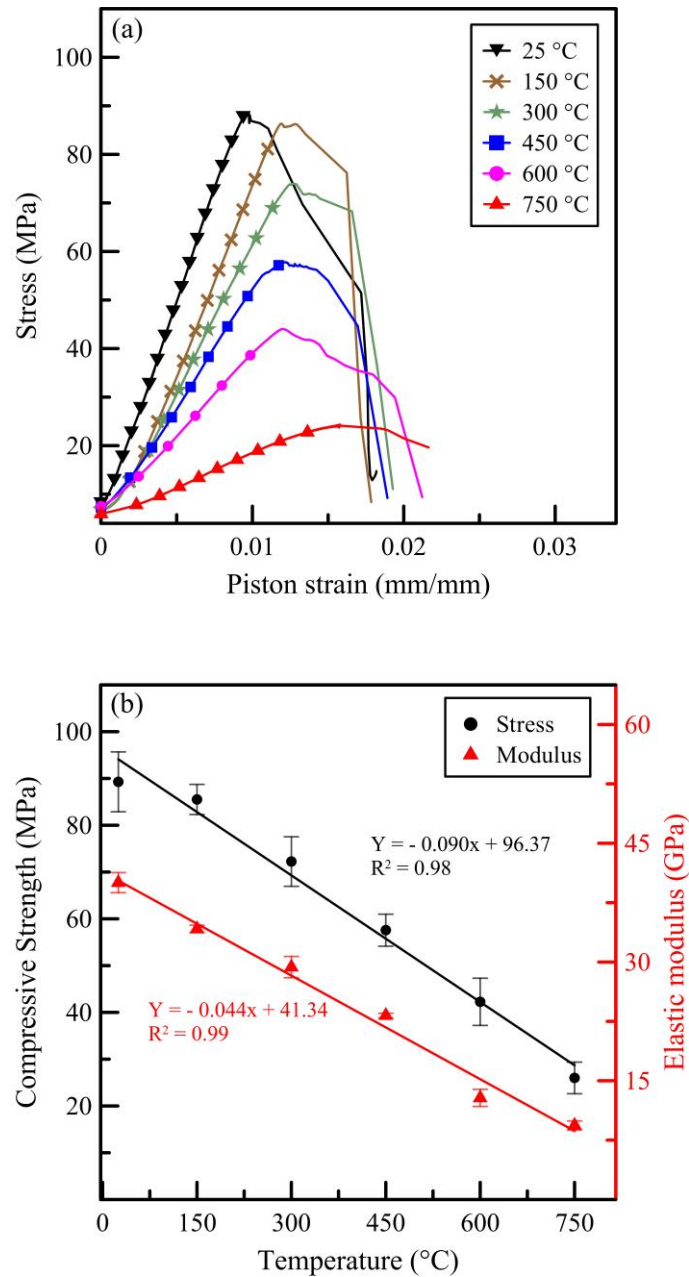


Figure 9 – (a) Stress-strain curves and (b) residual values of compressive strength and dynamic elastic modulus as a function of temperature

The residual compressive strength values after temperature exposure of 150, 300, 450, 600, and 750 °C were, respectively, 4.2%, 19.1%, 35.5%, 52.7%, and 70.9% lower than the value reached at room temperature (89.3 MPa). The changes in terms of elastic modulus may be qualitatively observed by analyzing the slope of the stress-strain curves shown in Fig. 9a. The dynamic elastic modulus results denote a reduction trend of 14.9%, 27.1%, 43.0%, 68.5%, and 76.5% for the respective target temperatures of 150, 300, 450, 600, and 750 °C when compared to room temperature (40 GPa). It is possible to observe that the properties of compressive strength and elastic modulus linearly reduce with temperature increase. The elastic properties of the composite are significantly affected by the changes in the cement paste pore

structure caused by the dehydration of hydrated products [19]. The reduction trend observed for the compressive strength and elastic modulus of the mortar is in line with the results found in the literature conducted in comparable conditions [30,31].

3.2 Interfacial transition zone properties

Figure 10 shows the fiber-matrix interface obtained by SEM analysis as a function of temperature. The region analyzed with EDS is indicated by the red line. Figure 11 illustrates the line scanning EDS results in the fiber-matrix interface as a function of temperature.

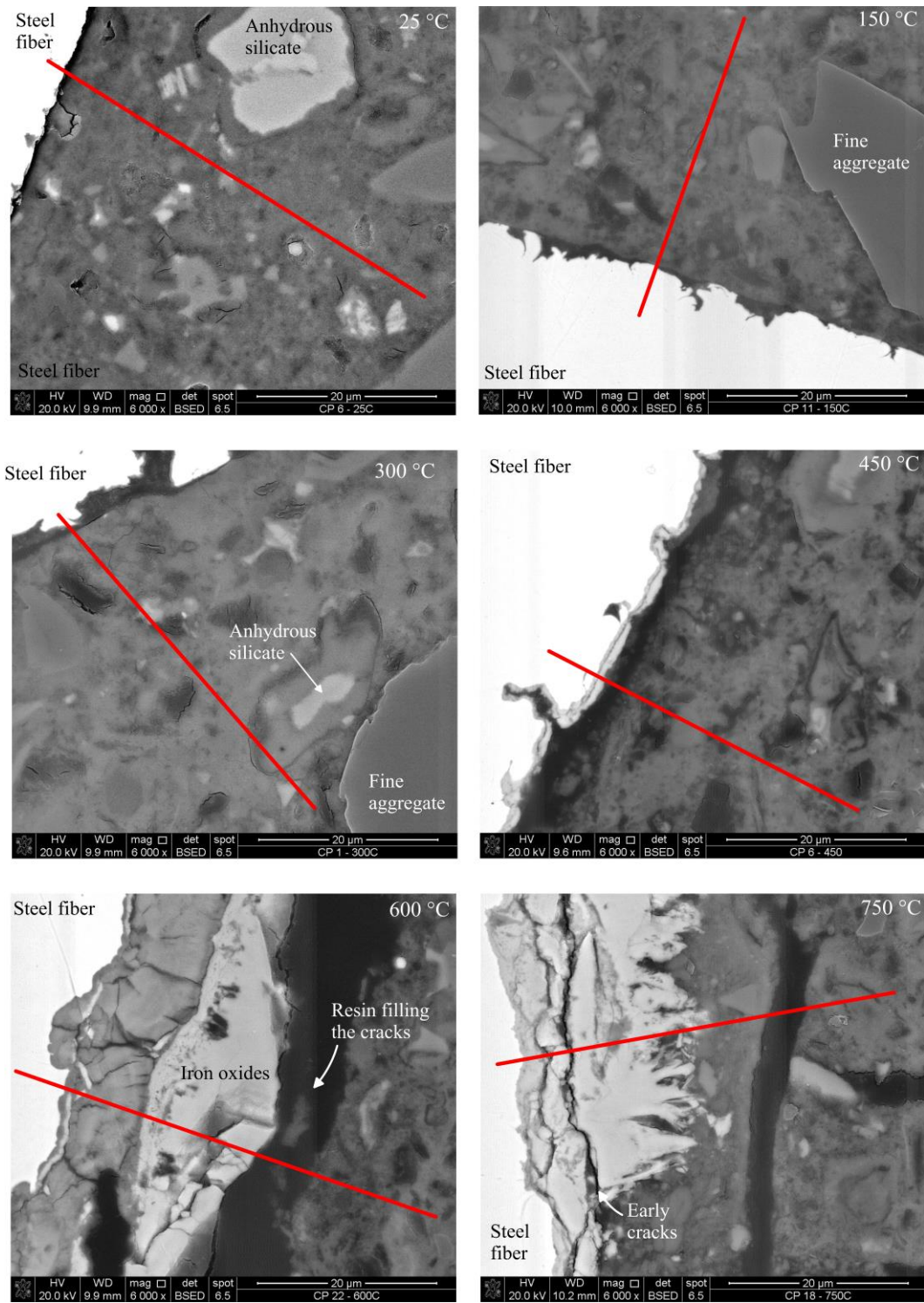


Figure 10 – Fiber-matrix interface obtained by SEM analysis as a function of temperature

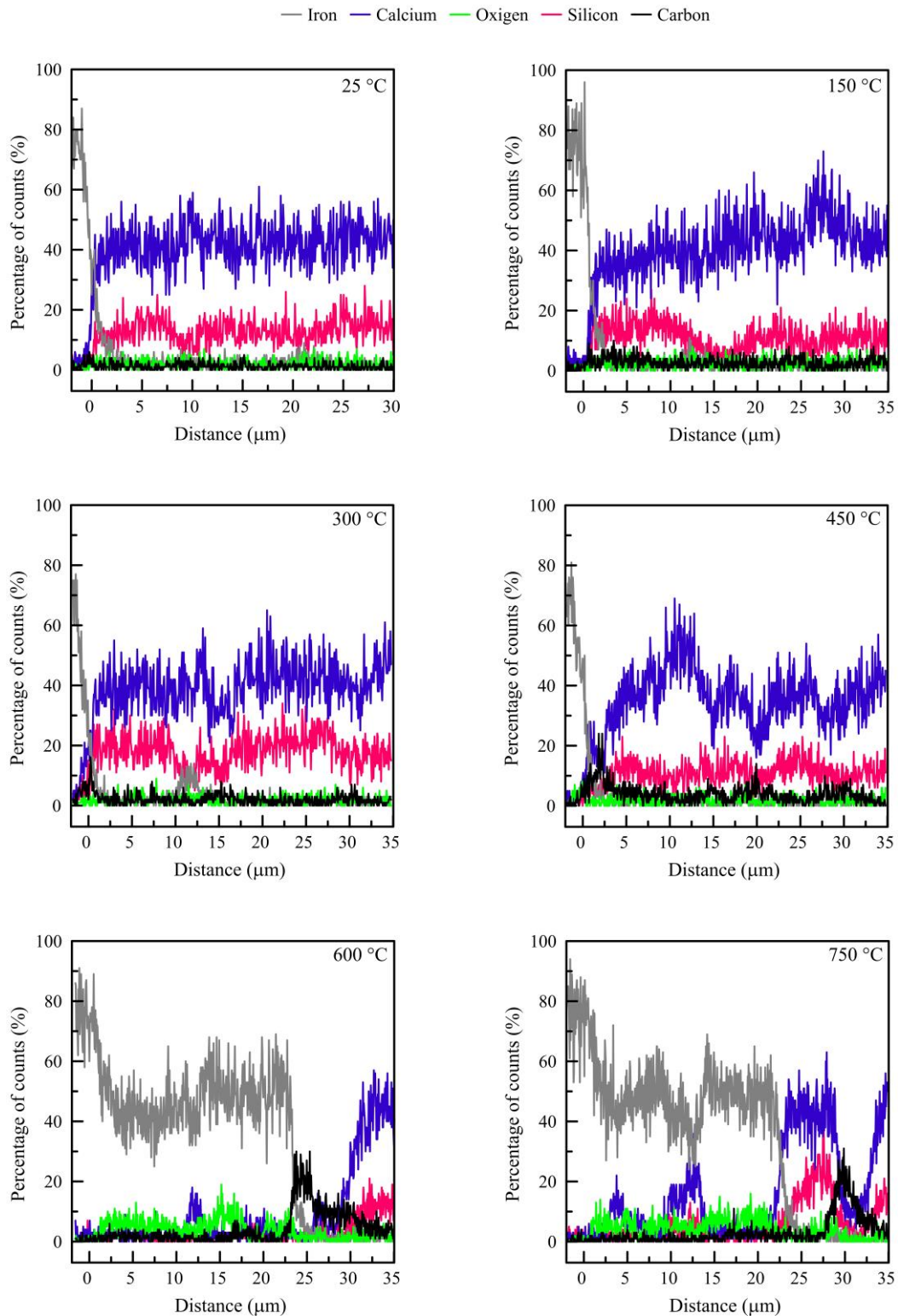


Figure 11 – Line scanning EDS results in the fiber-matrix interface as a function of maximum temperature

The qualitative evaluation of SEM images provided in Fig. 10 shows that the oxidation of the steel fibers begins at ~ 450 °C and increases significantly for temperatures of 600 and 750 °C. Literature results show that this oxide phase is a three-layered scaled structure composed of wüstite (FeO), hematite (Fe_2O_3), and magnetite (Fe_3O_4) and that this oxide product has higher mass and lower density

than the original steel structure, which results in the significant increase in terms of the external diameter of the steel fibers. Results in the literature point out to an increase of 3.8% in total diameter (steel + oxide) after exposure to 750 °C [32]. Also, the iron oxide may expand into the interfacial transition zone porosity for temperatures of 600 °C and above, which is denoted by the overlap of Si, Ca, Fe, and O peaks in the EDS results (see Fig. 11).

Cracks were formed in the vicinity of the fiber can be verified by analyzing the cracks filled with resin (see Fig. 10), as well as by the peak of carbon determined by EDS (see Fig. 11). This crack formation can be attributed to the detachment of fibers from the cementitious matrix and the passive thrust generated by the expansive oxidation process suffered by steel fibers. The debonding of fibers during the pullout test seems to occur in the region between the steel fiber and the interfacial transition zone for temperatures up to 450 °C. For temperatures of 600 °C and above the debonding of fibers seems to occur in the interface between the iron oxide formed and the interfacial transition zone. This rupture pattern change may result in changes in the fracture energy associated with the debonding of steel fibers and the energy dissipated during the slip portion of the test since the oxide formation increases the total diameter of the fiber [33,34].

It is worth highlighting that the cracks filled with resin are the only cracks that may be evaluated in SEM imagery since they were generated before the resin was applied. A few “early cracks” that are not filled with resin can be also noticed in Fig. 11, however, those must not be interpreted as a result of the pullout test or temperature exposure since they are likely to be generated by the vacuum applied during preparation and testing of samples, or even due to the influence of the beam of electrons during the SEM test.

Figure 12 shows the Si/Ca ratio as a function of temperature and distance from the fractured surface. For room temperature conditions, values of Si/Ca ratio lower than 0.3 represent systems with a high content of portlandite crystals and reduced amount of C-S-H, while Si/Ca ratios greater than 0.3 indicate systems rich in C-S-H [35]. Some studies conducted also show that systems formed mainly by C-S-H show a Si/Ca ratio of 0.5 or more in the form of α -C-S-H ($1 \leq \text{Si/Ca} < 1.5$), β -C-S-H ($0.66 < \text{Si/Ca} < 1$), and γ -C-S-H ($0.5 < \text{Si/Ca} < 0.66$) [36]. The results obtained for specimens tested at room temperature (25 °C) present a Si/Ca ratio between 0.1 and 0.3 for the first 10 μm from the fracture surface, which denotes that portlandite tends

to precipitate around the steel fiber and a low amount of C-S-H is present in this interface, which is in agreement with classical literature [5].

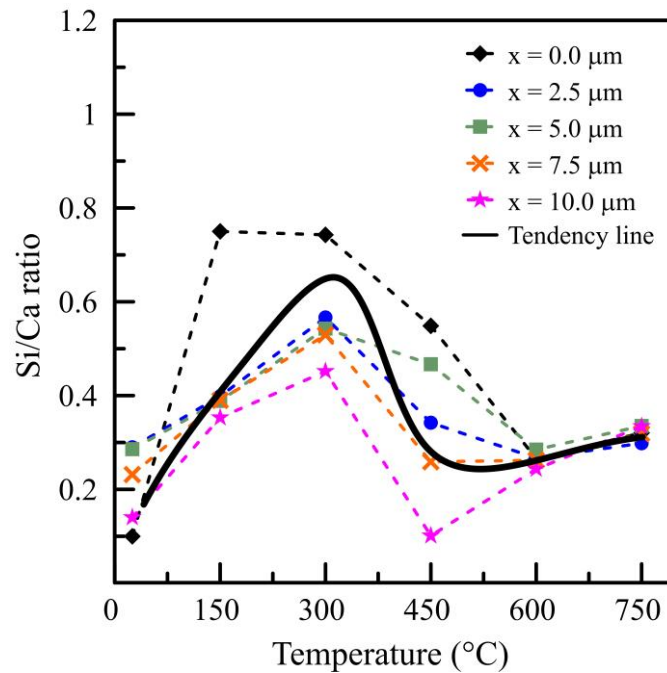


Figure 12 – Si/Ca ratio as a function of temperature and distance from fractured surface

At the temperature range between 150 and 300 °C, the Si/Ca ratio exhibits an increasing tendency. Considering that very limited data is available in the literature regarding the effect of temperature on the Si/Ca ratio of hydrated products, the origin of this behavior cannot be precisely determined based on SEM/EDS results alone. This investigation requires specific studies that aim to investigate the chemical and mineralogical changes in the vicinity of the fiber, which is a methodological challenge given the significantly reduced size of this region. Even though this specific experimental investigation is out of the scope of this paper, a few possible scenarios may be discussed.

The first hypothesis is that the thermal energy provided may work as a catalyst for the topochemical reaction of anhydrous silicates (i.e. C_3S and C_2S) that are deposited on the interfacial transition zone. This reaction may occur with silicates that are either partially hydrated or non-hydrated, which have been found in the interfacial transition zone in SEM imagery (see Fig. 11). Additionally, recently published studies pointed out that the temperature range between 100 and 400 °C is favorable for the formation of new hydration products capable of filling the pores of concrete [37,38]. This hypothetical hydration process could lead to the densification of the interfacial transition zone due to the formation of hydrated products and affect the bond-slip behavior of the hooked-end steel fibers.

The second hypothesis is based on the fact that the vicinity of the fiber has a considerable amount of portlandite in room temperature conditions (see Fig. 12). In this sense, the increase in temperature acts as a catalyst to the pozzolanic reaction between the $\text{Ca}(\text{OH})_2$ rich interfacial transition zone and the SiO_2 present in the concrete mix. Literature results show that the increase in temperature has been responsible for the significant increase in the compressive strength for lime-pozzolan mortars [39,40], which may be another factor that indicates the plausibility of the hypothesis proposed. According to recent studies, the presence of SiO_2 in the ITZ is so significant that the coating of steel and carbon fibers with nano-silica significantly reduced the ITZ porosity around the fiber matrix and improved the interfacial adhesion [41,42].

What is particularly concerning about the two hypotheses proposed is that both require water for the chemical reaction to occur. In this sense, the steam generated by the evaporation of free, adsorbed, and interlayer water results in the increase of the internal pressure in the mortar and induces an internal autoclaving condition [43]. Therefore, the water required could be trapped inside the specimen in the form of steam and superheated water, associated with the gas-liquid-solid triple point of a substance. Superheated water occurs between the usual boiling temperature ($\sim 100^\circ\text{C}$ at 1 atm) and the critical temperature of 374°C in pressured environments. This pressured environment could be provided by the low porosity and limited permeability of the mortar used in this study, which has a compressive strength of ~ 90 MPa (see Section 3.1).

In this context, the fiber-matrix interface is composed of three main phases at room temperature: the steel fiber, an interfacial transition zone (mostly portlandite), and the cementitious matrix. The increase in temperature within the range between 25 and 450°C leads to changes in the Si/Ca ratio of the interfacial transition zone and the debonding of fibers seems to occur between the steel fiber and the interfacial transition zone. For temperatures equal or higher than 450°C the oxidation process of steel fibers becomes relevant, which means that a new phase is present in the fiber-matrix interface. Therefore, the fiber-matrix interface can be described as having four phases: the steel fiber, the oxide layered structure, the interfacial transition zone, and the cementitious matrix. This oxide formation leads to an increase in the confinement forces applied in the steel fiber and change the location where the fracture occurs from fiber-matrix to oxide-matrix, which are both factors that affect the bond-slip mechanism.

3.3 Bond-slip behavior

Figure 13 shows both the individual and averaged load-displacement curves obtained experimentally for each target temperature. The maximum pullout load (P_{L1}) accounts for the energy required to yield the hooks at two points, while the lower peak (P_{L2}) is associated with the force required to straighten the fiber. The load values at a displacement of 10 mm (P_{L3}) were used to evaluate the changes in the dynamic frictional interaction between fiber and matrix. Table 5 shows the load values of P_{L1} , P_{L2} , P_{L3} , and the observations made during the pullout tests, as well as the standard deviation values. The results presented show that the temperature exposure tends to increase the dispersion of the experimental curves even in a double-sided pullout test using multiple fibers; however, this dispersion increase is not as significant as in single-fiber pullout tests found in the literature [16].

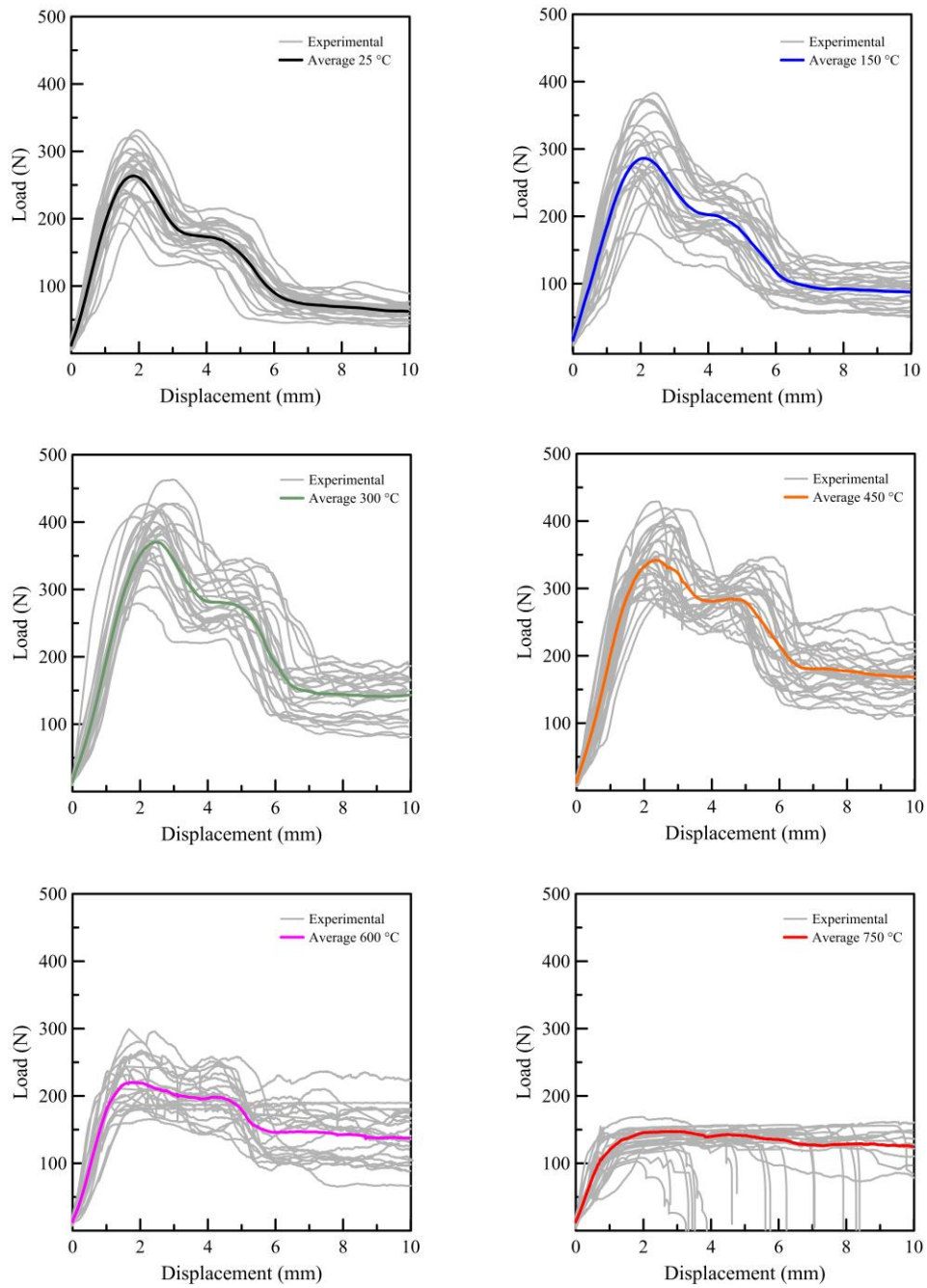


Figure 13 – Experimental and average load-displacement curves obtained for each target temperature

Table 5 – Load values of P_{L1} , P_{L2} , P_{L3} and the observations that were made during the pullout tests

Temperature (°C)	P_{L1} (N)	P_{L2} (N)	P_{L3} (N)	P_{L1}/P_{L2}	Observation
25	269.0 (± 34.9)	177.3 (± 21.0)	61.2 (± 11.3)	1.52	NFR in 30 specimens
150	297.1 (± 50.2)	203.4 (± 33.5)	85.3 (± 22.4)	1.46	NFR in 30 specimens
300	378.3 (± 45.9)	285.4 (± 32.0)	134.5 (± 34.5)	1.33	NFR in 30 specimens
450	350.1 (± 46.1)	295.5 (± 27.3)	157.0 (± 28.7)	1.18	NFR in 30 specimens
600	227.1 (± 36.3)	209.6 (± 34.9)	121.3 (± 42.7)	1.08	3 FR in 03 specimens 2 FR in 04 specimens 1 FR in 08 specimens NFR: 15 specimens
750	140.8 (± 16.1)	139.6 (± 12.9)	114.3 (± 23.9)	1.01	4 FR in 15 specimens 3 FR in 05 specimens 2 FR in 03 specimens NFR: 07 specimens

NFR – no fiber rupture; FR – fiber rupture

For specimens exposed to temperatures of 600 °C, it is possible to observe the occurrence of pullout and rupture of steel fibers (see Table 5). This suggests that for temperatures of 600 °C and above the tensile strength of fibers is exceeded before the shear strength of the fiber-matrix interaction. Considering that the peaks P_{L1} and P_{L2} are directly associated with the yielding of the hooks, the changes in the P_{L1}/P_{L2} ratio can be used as a qualitative indirect method to verify the tendency changes in the mechanical interlocking caused by the fibers. Since elevated temperatures affect the microstructure of the cement paste and the ITZ as a whole, the reduction of the P_{L1}/P_{L2} ratio may be attributed mainly to changes in the properties of steel fibers.

Results obtained are presented in Table 5, confirming that the P_{L1}/P_{L2} values significantly reduce as temperature increases. This reduction may be evidence that the bending stiffness of the steel fibers substantially reduces after temperature exposure, and could suggest that the mechanical interlock provided by the hooks is negligible for temperatures of 600 °C and above. This would also confirm that the dynamic frictional interaction between fiber and matrix is the preponderant factor in this temperature range. Furthermore, the reduction in bending stiffness is associated

with the effects of elevated temperatures on the physical, mechanical, and microstructural properties of hooked-end steel fibers, mainly due to the oxidation and recrystallization processes. These temperature-related processes have shown to significantly increase the grain-size structure of the fiber for temperatures of 600 °C and above [32].

Figure 14 illustrates the effect of temperature on the average load-displacement curves and the maximum values of P_{L1} , P_{L2} , and P_{L3} . The maximum pullout load (P_{L1}) values have shown an increasing trend up to 450 °C. In this sense, the P_{L1} values increased by 10.5%, 40.6%, 30.2% for the respective target temperatures of 150, 300, and 450 °C when compared to room temperature results. This increasing tendency may be associated with the Si/Ca ratio changes that may occur in the interfacial transition zone (see Section 3.2), which may result in increased interfacial chemical adhesion and enhances the dynamic frictional interaction between fiber and matrix due to the densification of the ITZ. Since the bond-slip response is sensitive to normal stresses, the changes in the Poisson's ratio of the materials [5] and the shrinkage behavior of the cementitious matrix up to ~300 °C [29] may influence the results obtained.

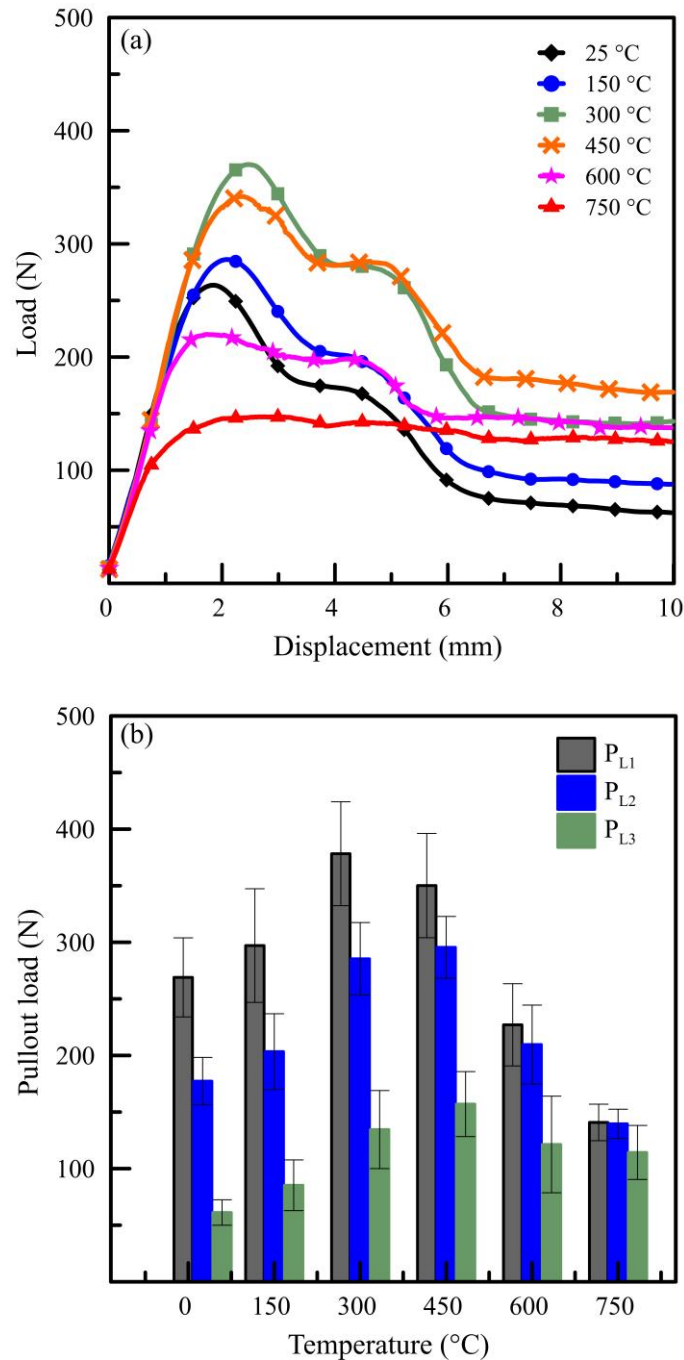


Figure 14 – Effect of temperature on (a) the average load-displacement curves and (b) the maximum values of P_{L1} , P_{L2} , and P_{L3}

Although an increasing trend is verified in this study, literature results show that the values of P_{L1} remain relatively constant up to ~ 400 °C [13–16]. This negligible effects of temperature on P_{L1} values may be associated with two main factors. The first factor is that literature results were obtained using less stable test methods than the one proposed in this study, which increases the dispersion and may result in the non-significance of results. The second is that the ITZ remains relatively unchanged when compared to the cement paste up to the dehydration temperature of portlandite (~ 450 °C [44]) since the region in the vicinity of the fiber contains a considerable volume of CaOH_2 crystals (see Section 3.2).

After exposure to temperatures of 600 and 750 °C, a reduction trend was observed in the P_{L1} values with the respective reductions of 15.6% and 47.6% when compared to room temperature results. This reduction is mainly associated with the drastic reductions in the bending stiffness of steel fibers, as previously determined by the analysis of the P_{L1}/P_{L2} ratio, and the dehydration of hydrated products in the ITZ. Even with those considerations, additional factors that significantly influence the evidenced behavior can be cited, such as the coarsening of the ITZ pore structure, the significant cracking caused by the thermal gradients, and the reversible transformation of quartz from α -trigonal to β -hexagonal at 573 °C [29].

The values of P_{L3} significantly increase by 39.4%, 119.8%, 156.6%, 98.2%, and 86.7% for the respective temperatures of 150, 300, 450, 600, and 750 °C when compared to room temperature results. It is also important to notice that the maximum increase is detected at 450 °C, which may be associated with the changes in the Si/Ca ratio in the interfacial transition zone and the initial oxidation of steel fibers. Even for temperatures of 600 °C and above a significant increase is verified in terms of P_{L3} when compared to room temperature results. This increase may be attributed to the increase in the confining forces and the changes in the fracture mechanism from fiber-matrix to oxide-matrix, discussed in Section 3.2. Another relevant aspect is that the increase in the confining forces may be associated with the shrinkage suffered by the cement paste for temperatures above 300 °C, which can easily overcome 1.6% [29,45].

3.4 Admissible error and sample size determination

Figure 15 shows the sample size required as a function of the admissible error for the peak load values P_{L1} , P_{L2} , and P_{L3} . The analysis conducted using inferential statistics and a 95% confidence interval shows that the sample size increases with the reduction of the admissible error for the pullout test. This increase in sample size is particularly greater for the P_{L3} values both in room conditions and after exposure to elevated temperatures, which can be justified by the reduced stability during the dynamic portion of the test and the consequent increase in the variability of results.

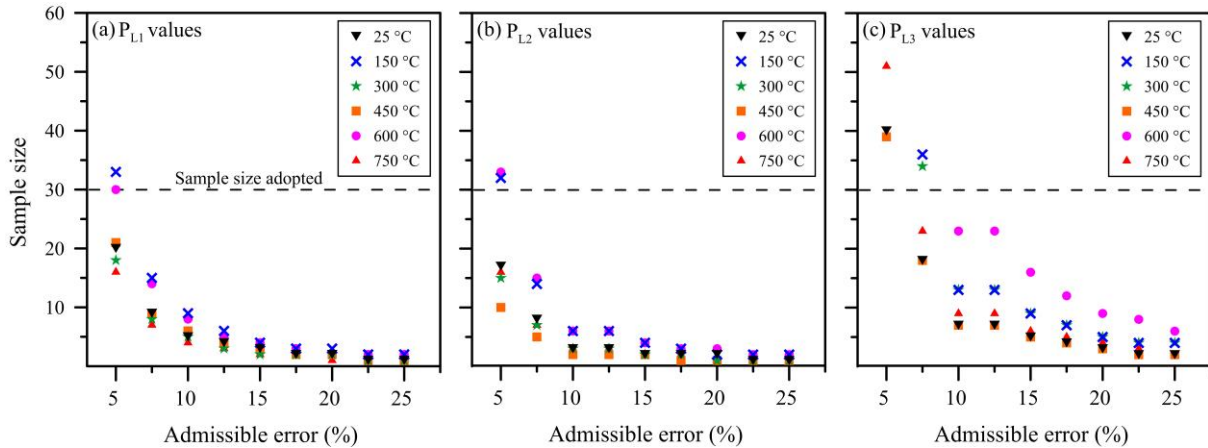


Figure 15 – Sample size required as a function of the admissible error for the (a) P_{L1} values, (b) P_{L2} values, and (c) P_{L3} values

It is possible to observe that the sample size of 30 pullout specimens adopted in this study was enough to ensure an admissible error of $\sim 11\%$. Moreover, a total of 16 pullout specimens ensure a maximum admissible error of $\sim 15\%$ and 9 pullout specimens a maximum admissible error of $\sim 20\%$ for all the peak loads evaluated. In this sense, the results obtained using double-sided and with multiple fibers have shown an acceptable error for the purpose. This suggests that the adoption of a double-sided pullout test using multiple fibers may be a stable and adequate test method to improve the reliability of the pullout results obtained, both in room conditions and after exposure to elevated temperatures.

Even with those considerations, the results regarding the admissible error of the pullout test proposed in this paper (double-sided, multiple fibers) could not be compared with the tests found in current literature (single-sided, single fiber). The comparison was not possible because the standard deviation values are not provided in studies found in the literature [13–16]. Therefore, the experimental data reported in this work serves as a reference for comparison for future works that aim to study the effect of temperature on the bond-slip of steel fibers.

4. Numerical simulation

In this section, the numerical approach proposed by Bitencourt et al. [18] for modeling steel fiber reinforced concrete (SFRC) is employed. This was found to be an appropriate approach for the numerical simulation of pullout tests since the model allows representing the fiber/matrix interaction separately.

Figure 16 illustrates the 3D model constructed for the numerical simulations of the pullout tests. As it can be seen in this figure, the fibers are represented discretely and explicitly and a crack is predefined at the central part of the specimen, as considered

in the laboratory tests. Therefore, the interaction between the top and bottom parts is given by the fiber/matrix interface. The bottom part of the specimen is fixed, while a vertical displacement of 10 mm with a displacement rate of 0.5 mm/min is imposed at the top part, as depicted in the Figure 16a.

Initially, fibers and mortar matrix are discretized in finite elements in a totally independent way (non-conforming meshes) using two-noded truss finite elements and four-noded tetrahedral finite elements, respectively. Then, five-noded tetrahedral coupling finite elements (CFEs) are inserted (see light blue elements in Figure 16b) to describe the fiber-matrix interaction [46].

In this work, the mechanical response of the fibers is described by a one-dimensional elastoplastic material model, while the mortar matrix is simulated with a linear elastic behavior. The fiber/matrix interaction is described by the non-rigid version of the CFEs, and a continuum damage model, by adjusting the parameters obtained in the laboratory tests. Details about the fiber/matrix interaction and a comparison with an analytical model can be found in Bitencourt et al. [18].

It is important to mention that the effect of the hooks is distributed along the length of a straight fiber in the numerical model. This simplification has proven to be a feasible manner to represent hooked-end steel fibers in the model since the effect of the hooked-end is considered in the bond-slip law adopted. Recently, this numerical strategy was successfully employed for modeling three-point bending tests (3-PBT) to predict the post-cracking parameters of SFRC [47] and the behavior of beams with combined reinforcement of steel fibers and rebars [48].

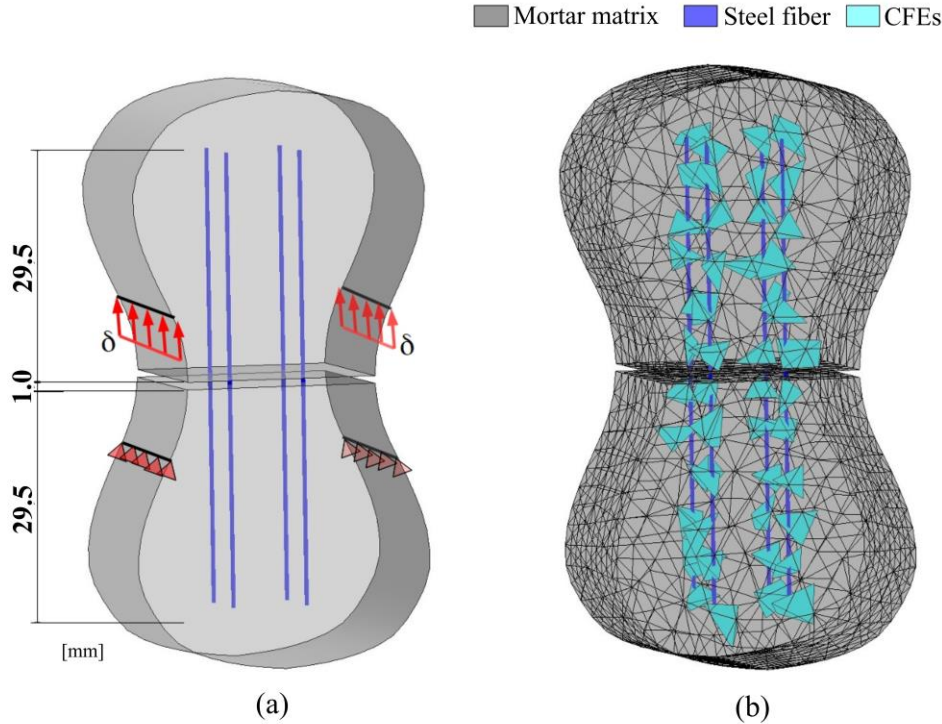


Figure 16 –3D model for the numerical simulation of the pullout tests: (a) geometry of the specimen, boundary conditions and imposed displacement, and (b) discretization in finite elements

In the numerical analyses performed, the mortar matrix was discretized by 8,165 four-noded tetrahedral finite elements, whereas 11 two-noded truss finite elements were used for each steel fiber. To couple the initially independent meshes of the mortar matrix and steel fibers, 48 five-noded tetrahedral CFEs were added.

The behavior of the CFEs, given by a continuum damage model is adjusted to describe the response of the pullout test at room temperature. Therefore, a bond-slip model defined by the relationship between the shear stress (adherence stress) and relative sliding is initially constructed for the temperature of 25° according to the response presented in Fig. 14a. An appropriate damage coefficient is introduced in the constitutive equation based on the experimental responses to capture the responses for other temperatures. In the following sections, the definition of the damage coefficient, and the bond-slip model are presented as the main constitutive parameters for the definition of the fiber-matrix interaction.

4.1 Fiber-matrix interaction

4.1.1 Damage coefficient

In this section, the damage coefficient (K_i) and the factors of change (k_{Ln}) that are applied in the constitutive model as the effect of temperature on the bond-slip behavior of the hooked-end steel fibers are presented. Figure 17 illustrates the analytical model for the damage coefficient as a function of temperature. One damage

coefficient (K_i) is generated for each major peak of the bond-slip model, therefore K_1 , K_2 and K_3 for the respective peak loads of P_{L1} , P_{L2} , and P_{L3} .

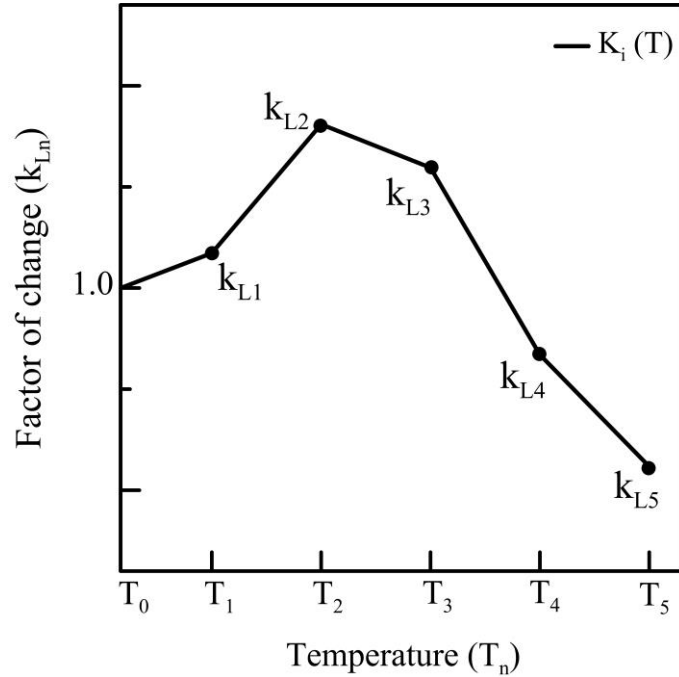


Figure 17 – The analytical model for the damage coefficient as a function of temperature

The factors of change (k_{Ln}) are determined based on the value of one of the peak loads (P_{Li}) after exposure to a given temperature (T_n) related to room temperature (T_0) results, which is calculated as:

$$k_{Ln} = \frac{P_{Li}(T_n)}{P_{Li}(T_0)} \quad (3)$$

The damage coefficient (K_i) is a multilinear equation that interpolates the factor of change for other temperatures than the temperatures evaluated. Therefore, the analytical equation for K_i can be defined as a function of temperature, as follows:

$$K_i = \begin{cases} 1 + (k_{L1} - 1) \frac{(T - T_0)}{(T_1 - T_0)} & \text{if } T_0 \leq T \leq T_1 \\ k_{L1} + (k_{L2} - k_{L1}) \frac{(T - T_1)}{(T_2 - T_1)} & \text{if } T_1 \leq T \leq T_2 \\ \vdots & \\ k_{L(n-1)} + (k_{Ln} - k_{L(n-1)}) \frac{(T - T_{(n-1)})}{(T_n - T_{(n-1)})} & \text{if } T_{(n-1)} \leq T \leq T_n \end{cases} \quad (4)$$

4.1.2 Bond-slip

A constitutive model for the bond-slip behavior of hooked-end steel fibers after exposure to elevated temperatures is proposed. The shear stresses associated with P_{L1} , P_{L2} , and P_{L3} used as input in the model may be calculated by the simplified

assumption that the shear stress is constant, and the effect of the hook is distributed along the length of the fiber, as follows:

$$\tau_{bn} = \frac{P_{Ln}}{\pi * d * l_e} \quad (5)$$

where τ_{bn} is the average shear stress for a given peak load; P_{Ln} is the respective load value for P_{L1} , P_{L2} , or P_{L3} ; d is the diameter of the steel fiber; l_e is the embedded length of the fiber in the cementitious matrix. In this sense, the bond stresses (τ_b) between the substrate and the hooked-end steel fiber for pullout and splitting failure are given as a function of the slip (s) along the axis of the fiber, as follows:

$$\tau_b(s) = \begin{cases} K_1 \cdot \tau_{b1} \left(\frac{s}{s_1}\right)^a & \text{if } 0 \leq s \leq s_1 \\ K_1 \cdot \tau_{b1} - (K_1 \cdot \tau_{b1} - K_2 \cdot \tau_{b2}) \left(\frac{s - s_1}{s_2 - s_1}\right) & \text{if } s_1 \leq s \leq s_2 \\ K_2 \cdot \tau_{b2} & \text{if } s_2 \leq s \leq s_3 \\ K_2 \cdot \tau_{b2} - (K_2 \cdot \tau_{b2} - K_3 \cdot \tau_{b3}) \left(\frac{s - s_3}{s_4 - s_3}\right) & \text{if } s_3 \leq s \leq s_4 \\ K_3 \cdot \tau_{b3} & \text{if } s \geq s_4 \end{cases} \quad (6)$$

where K_1 , K_2 , and K_3 are the analytical equations that relate the factors of change for the peaks of P_{L1} , P_{L2} , and P_{L3} , respectively. The shear stresses τ_{b1} , τ_{b2} , and τ_{b3} account respectively for the shear generated by P_{L1} , P_{L2} , and P_{L3} for the steel fibers at room temperature (see Eq. 5), while the variable s is the slip of fibers in the cementitious matrix. Figure 18 shows the curve defined by the Eq. 6.

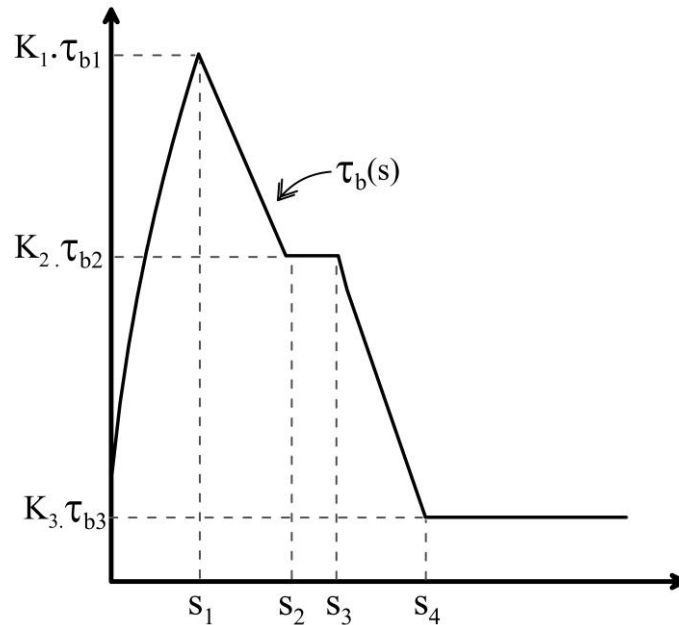


Figure 18 – Bond-slip constitutive model for the hooked-end steel fibers after elevated temperatures

By assuming that the function $q(r)$ represents the hardening/softening law of the continuum damage model assumed to describe the fiber-matrix interaction, the Eq. 6

can be rewritten in terms of these stress (q) and strain (r) like internal variables by considering the relationship $q(r) = \tau_b \left(\frac{r}{k}\right)$, as follows:

$$q(r) = \begin{cases} K_1 \cdot \tau_{b1} \left(\frac{r/k}{s_1}\right)^a & \text{if } 0 \leq r/k \leq s_1 \\ K_1 \cdot \tau_{b1} - (K_1 \cdot \tau_{b1} - K_2 \cdot \tau_{b2}) \left(\frac{r/k - s_1}{s_2 - s_1}\right) & \text{if } s_1 \leq r/k \leq s_2 \\ K_2 \cdot \tau_{b2} & \text{if } s_2 \leq r/k \leq s_3 \\ K_2 \cdot \tau_{b2} - (K_2 \cdot \tau_{b2} - K_3 \cdot \tau_{b3}) \left(\frac{r/k - s_3}{s_4 - s_3}\right) & \text{if } s_3 \leq r/k \leq s_4 \\ K_3 \cdot \tau_{b3} & \text{if } r/k \geq s_4 \end{cases} \quad (7)$$

where k is the coupling parameter in the direction normal to the fiber, varying from 10^6 to 10^9 (MPa/mm) according to the recommendation of Bitencourt et al. [46]. More details about the numerical model for SFRC may be found in the work of Bitencourt et al. [18].

The mortar matrix is assumed as a linear elastic material with Poisson's ratio of $\nu = 0.2$ and the elastic modulus (E_c) determined based on the experimental characterization conducted for each target temperature. The behavior of the steel fibers is given by an elastic perfectly plastic model, with an elastic modulus of $E_f = 210$ GPa for all target temperatures, since the initial interatomic distance of the metallic ions is not changed after the steel fibers are exposed to the heat-cooling process [49,50]. The yield stress (σ_y) of the steel fibers as a function of temperature was estimated based on the rate of change obtained in the experimental work conducted by Abdallah et al [13] applied to the tensile strength of the steel fiber used in this study. The damage coefficient values were calculated based on the peak load values (P_{L1} , P_{L2} , and P_{L3}) presented in Table 5 of Section 3.3. Table 6 shows a summary of the parameters adopted in the numerical simulations.

Table 6 – Summary of the parameters adopted in the numerical simulations

Target temperature (°C)	Bond-slip parameters								Mortar properties			Steel fiber properties			
	τ_{b1} (MPa)	τ_{b2} (MPa)	τ_{b3} (MPa)	s_1 (mm)	s_2 (mm)	s_3 (mm)	s_4 (mm)	a	K_1	K_2	K_3	f_c (MPa)	E_c (GPa)	σ_y (MPa)	E_f (GPa)
25	3.9	2.6	0.9	0.9	2.3	3.5	5.6	0.7	1.0	1.0	1.0	89.3	40.0	1240	210
150	3.9	2.6	0.9	1.0	2.7	3.5	5.6	0.6	1.1	1.1	1.3	85.5	34.2	1226	210
300	3.9	2.6	0.9	1.2	2.7	3.9	5.7	0.7	1.4	1.6	2.0	72.3	29.4	1199	210
450	3.9	2.6	0.9	1.2	2.7	4.0	5.6	0.6	1.3	1.6	2.3	57.6	23.2	1032	210
600	3.9	2.6	0.9	0.8	2.3	3.5	4.8	0.6	0.8	1.1	2.0	42.3	12.8	463	210
750	3.9	2.6	0.9	0.8	2.3	3.5	4.8	0.6	0.6	0.8	1.7	26.0	9.4	336	210

4.2. Numerical results

Figure 19 shows the average experimental curves compared to the numerical simulation conducted in this study. It is confirmed that the numerical curves are capable of describing the bond-slip behavior of fibers as a function of temperature. In this sense, a good agreement between the experimental and numerical results is observed.

The value adopted for the slip parameter s_1 in the numerical simulation is the half of that obtained in the experimental results. Moreover, the other slip parameters (i.e. s_2 , s_3 , and s_4) are defined as the experimental slip value subtracted by the half of the slip parameter s_1 . The difference in terms of slip values can be explained by the slip mechanism that occurs in double-sided pullout specimens.

For slip values up to the peak load P_{L1} , both sides of the pullout specimen are experiencing the mechanical anchorage of the hooks and fiber slipping. In general lines, half of the total slip can be attributed to each side of the pullout specimen. Once the hook is straightened in one of the sides, the slip mechanism is similar to the single-sided pullout tests. Therefore, the difference between experimental and numerical values of slip occurs since the Eq. 5 was developed considering the pullout test of a single fiber embedded on one side, while the fibers are embedded on both sides in the pullout tests performed in this research. This difference in terms of slip values was also reported by other researchers in the literature. According to Lee et al. [51], the slip s_1 for fiber embedded on both sides is about twice that obtained with fiber embedded on one side and this difference between responses decreases as smaller is the fiber embedded length.

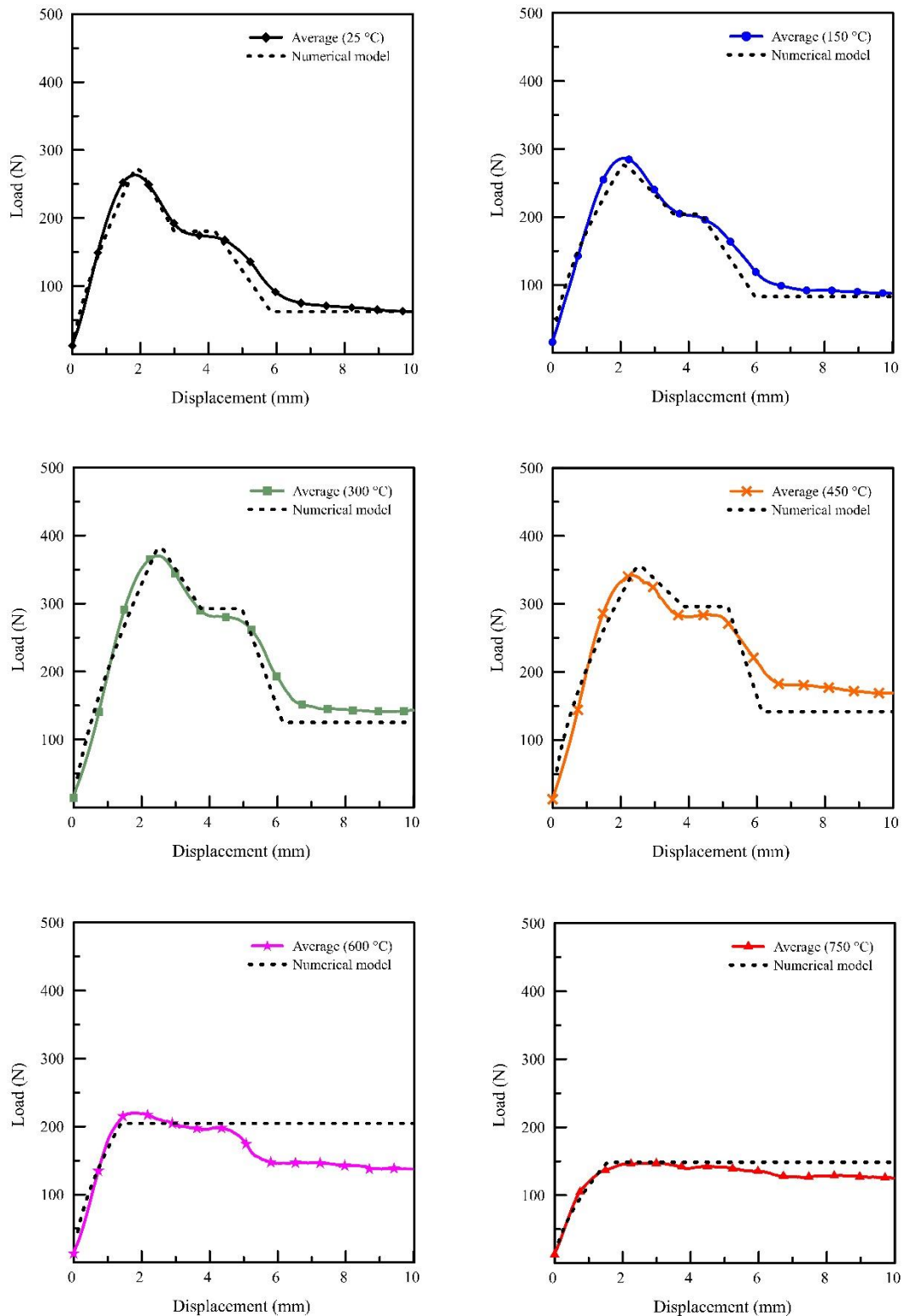


Figure 19 – Average experimental load curves compared to the numerical simulation

Figure 20 shows the fiber stress at the crack compared to the tensile strength of steel fibers, and the stress distribution for temperatures of 25 and 750 °C. Comparing the results, it can be observed that in the temperature range of 25 and 450 °C the governing mechanism can be attributed to the shear interaction between the steel

fibers and the cementitious matrix since the tensile stresses generated on the steel fibers are not sufficient to cause fiber rupture. For specimens exposed to temperatures of 600 and 750 °C, the tensile strength of the steel fibers is reached, therefore fiber rupture occurs. This can also be noticed in the numerical simulations in Fig. 19. Additionally, the difference between the experimental and numerical results for $T = 600$ °C may be attributed to the fact that the numerical model does not account for partial yielding of the steel fibers as occurred for the experimental results (see Table 5, column “Observations”), and instead considers that all steel fibers reach the yield strength at the same time.

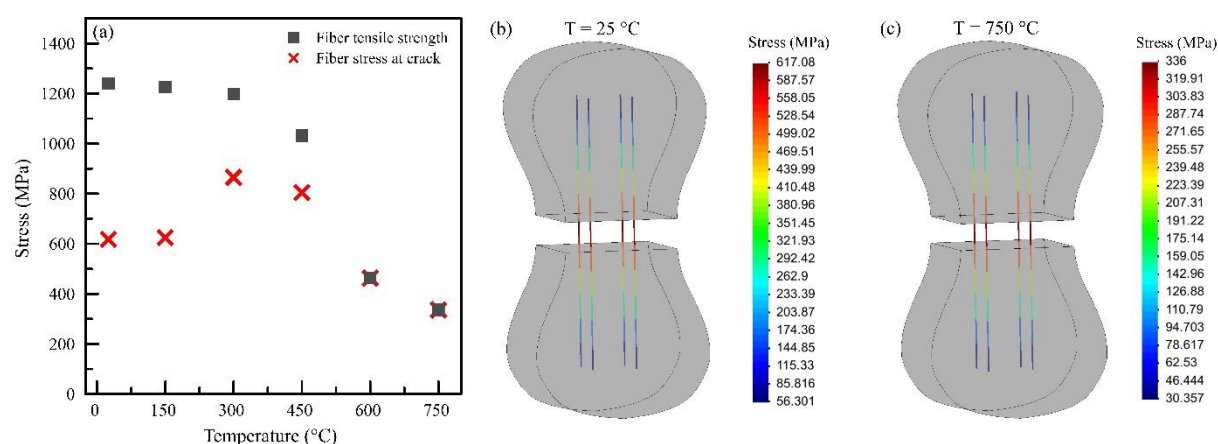


Figure 20 – Effect of temperature on (a) the fiber stress at the crack, and the stress distribution for (b) $T = 25$ °C and (c) $T = 750$ °C

This suggests that for temperatures of 600 °C and above the tensile strength of fibers is exceeded before the shear strength of the fiber-matrix interaction (see Fig. 20a). This behavior is in line with the experimental results presented in Table 5 and Figure 14 of this study. The significant reduction of the tensile strength of steel fibers can be attributed to the reduction of grain boundary surface due to the grain-growth process induced by temperature [32]. In summary, the governing mechanism changes from bond-slip behavior to the tensile strength capacity of fibers for temperatures of 600 °C and above.

5 Conclusions

The following conclusions can be drawn from the present study:

- The compressive strength and elastic properties of the mortar reduced linearly with temperature increase. The compressive strength was reduced by 4.2% (150 °C) to 70.9% (750 °C) and the dynamic elastic modulus was reduced by

14.9% (150 °C) to 76.5% (750 °C), both related to room temperature results. These changes were attributed to the severe dehydration of hydrated products and were comparable with the results found in the literature.

- The iron oxide began to form ~450 °C and expanded into the ITZ porosity for temperatures of 600 °C and above. This process resulted in changes in the rupture pattern and the debonding of fibers, which occurred in the interface between the oxide and the matrix. Additionally, the Si/Ca ratio in the region surrounding the steel fibers increased considerably up to 300 °C, denoting changes in the mineralogical properties in the vicinity of the fiber.
- The maximum pullout load values increased up to ~30% in the range of $150\text{ °C} \leq T \leq 450\text{ °C}$ and decreased up to ~48% for $600\text{ °C} \leq T \leq 750\text{ °C}$. Additionally, the dynamic frictional interaction between fiber and matrix increases for all temperatures evaluated. These changes were attributed to the changes in the Si/Ca ratio in the vicinity of the fiber, the oxide formation, and the increase in the confining forces applied to the fibers. Additionally, the bending stiffness of the steel fibers reduced with the increase in temperature and reached a negligible contribution at ~600 °C.
- The numerical model can describe the bond-slip behavior of fibers as a function of temperature with a good agreement between the experimental and numerical results. For $25\text{ °C} \leq T \leq 450\text{ °C}$, the governing mechanism is the shear interaction between the fibers and the cementitious matrix. For $T \geq 600\text{ °C}$, the tensile strength of steel fibers is achieved before the bond-slip can take place. The aforementioned governing mechanisms were confirmed by experimental results and the numerical simulation conducted.

Finally, it must be highlighted that the experimental campaign conducted, and the numerical model developed in this study may serve as a reference for the simulation of mesoscale tests and assessing the behavior of structural elements built with steel fiber reinforced concrete under high temperatures.

Acknowledgments

The authors would like to thank the Institute for Technological Research (IPT) and its foundation (FIPT) for their financial and institutional support through the New Talents Program N.01/2017. The authors would also like to thank the researchers Ph.D. Renata Monte (USP), MSc Priscila Rodrigues Melo Leal (IPT), and Eng.

Tiago Haddad Marum (USP) for the technical contributions that improved the quality of this work.

Data availability: The raw/processed data required to reproduce these findings cannot be shared at this time as the data also forms part of an ongoing study. The raw/processed data may be provided by the corresponding author upon request.

References

- [1] M. di Prisco, G. Plizzari, L. Vandewalle, Fibre reinforced concrete: New design perspectives, *Mater. Struct.* 42 (2009) 1261–1281.
- [2] R.P. Manfredi, F. de Andrade Silva, Test Methods for the Characterization of Polypropylene Fiber Reinforced Concrete: A Comparative Analysis, *KSCE J. Civ. Eng.* 24 (2020) 856–866. doi:10.1007/s12205-020-0741-7.
- [3] B. Luccioni, G. Ruano, F. Isla, R. Zerbino, G. Giaccio, A simple approach to model SFRC, *Constr. Build. Mater.* (2012). doi:10.1016/j.conbuildmat.2012.07.027.
- [4] N. Banthia, Fiber Reinforced Concrete, ACI SP-142ACI, Detroit, MI. (1994). doi:10.4188/transjtmsj1965a.24.P621.
- [5] A. Bentur, S. Mindess, Fibre reinforced cementitious composites, 2nd ed., Taylor & Francis, New York, 2007.
- [6] S. Abdallah, M. Fan, D.W.A. Rees, Bonding Mechanisms and Strength of Steel Fiber-Reinforced Cementitious Composites: Overview, *J. Mater. Civ. Eng.* (2018). doi:10.1061/(asce)mt.1943-5533.0002154.
- [7] F.L. de Oliveira, Design-oriented constitutive model for steel fiber reinforced concrete, Universitat Politècnica de Catalunya, 2010.
- [8] Victor M. C. F. Cunha, Steel fibre reinforced self-compacting concrete (from micromechanics to composite behavior), 2010. <http://hdl.handle.net/1822/10667>.
- [9] Y.W. Chan, S.H. Chu, Effect of silica fume on steel fiber bond characteristics in reactive powder concrete, *Cem. Concr. Res.* (2004). doi:10.1016/j.cemconres.2003.12.023.
- [10] F. Laranjeira, C. Molins, A. Aguado, Predicting the pullout response of inclined hooked steel fibers, *Cem. Concr. Res.* (2010). doi:10.1016/j.cemconres.2010.05.005.
- [11] Y. Lee, S.T. Kang, J.K. Kim, Pullout behavior of inclined steel fiber in an

- ultra-high strength cementitious matrix, *Constr. Build. Mater.* (2010). doi:10.1016/j.conbuildmat.2010.03.009.
- [12] M.J. Shannag, R. Brincker, W. Hansen, Pullout behavior of steel fibers from cement-based composites, *Cem. Concr. Res.* (1997). doi:10.1016/S0008-8846(97)00061-6.
- [13] S. Abdallah, M. Fan, K.A. Cashell, Bond-slip behaviour of steel fibres in concrete after exposure to elevated temperatures, *Constr. Build. Mater.* 140 (2017) 542–551. doi:10.1016/j.conbuildmat.2017.02.148.
- [14] S. Abdallah, M. Fan, D.W.A. Rees, Effect of elevated temperature on pull-out behaviour of 4DH/5DH hooked end steel fibres, *Compos. Struct.* 165 (2017) 180–191. doi:https://doi.org/10.1016/j.compstruct.2017.01.005.
- [15] S. Abdallah, M. Fan, K.A. Cashell, Pull-out behaviour of straight and hooked-end steel fibres under elevated temperatures, *Cem. Concr. Res.* 95 (2017) 132–140. doi:10.1016/j.cemconres.2017.02.010.
- [16] G. Ruano, F. Isla, B. Luccioni, R. Zerbino, G. Giaccio, Steel fibers pull-out after exposure to high temperatures and its contribution to the residual mechanical behavior of high strength concrete, *Constr. Build. Mater.* (2018). doi:10.1016/j.conbuildmat.2017.12.129.
- [17] A. Caggiano, E. Martinelli, A unified formulation for simulating the bond behaviour of fibres in cementitious materials, *Mater. Des.* 42 (2012) 204–213. doi:10.1016/j.matdes.2012.05.003.
- [18] L. A. G. Bitencourt, O.L. Manzoli, T.N. Bittencourt, F.J. Vecchio, Numerical modeling of steel fiber reinforced concrete with a discrete and explicit representation of steel fibers, *Int. J. Solids Struct.* 159 (2019) 171–190. doi:10.1016/j.ijsolstr.2018.09.028.
- [19] R. Serafini, S.R.A. Dantas, R.P. Salvador, R.R. Agra, D.A.S. Rambo, A.F. Berto, A.D. de Figueiredo, Influence of fire on temperature gradient and physical-mechanical properties of macro-synthetic fiber reinforced concrete for tunnel linings, *Constr. Build. Mater.* 214 (2019) 254–268. doi:10.1016/j.conbuildmat.2019.04.133.
- [20] S.R.A. Dantas, R. Serafini, R.C. de O. Romano, F. Vittorino, K. Loh, Influence of polypropylene microfibers (PPMF) dispersion procedure on fresh and hardened rendering mortar properties, *Ambient. Construído.* 20 (2020) 7–23. doi:10.1590/s1678-86212020000200384.
- [21] J.M. Carpio, R. Serafini, D. Rambo, A. de la Fuente, A.D. De Figueiredo,

- Assessment of the bearing capacity reduction of FRC elements subjected to fire, in: Proc. Fib Symp. 2019 Concr. - Innov. Mater. Des. Struct., Kraków, Poland, 2019: pp. 1378–1386.
- [22] U. Schneider, Concrete at high temperatures - A general review, *Fire Saf. J.* (1988). doi:10.1016/0379-7112(88)90033-1.
- [23] T. Materne, F. de Buyl, G.L. Witucki, *Organosilane Technology in Coating Applications: Review and Perspectives*, Dow Corning. (2012). doi:10.1017/CBO9781107415324.004.
- [24] Federation Internationale du Beton, *Model Code for Concrete Structures 2010*, in: Ernst & Sohn, Germany, 2013: p. 434.
- [25] C.M. Judd, G.H. McClelland, C.S. Ryan, *Data Analysis: A Model Comparison Approach to Regression, ANOVA, and Beyond*, 2009.
- [26] W. de O. Bussab, P.A. Morettin, *Estatística básica*, Saraivauni, São Paulo, 2017.
- [27] V. Vydra, F. Vodák, O. Kapičková, Š. Hošková, Effect of temperature on porosity of concrete for nuclear-safety structures, *Cem. Concr. Res.* 31 (2001) 1023–1026. doi:10.1016/S0008-8846(01)00516-6.
- [28] E. Gallucci, X. Zhang, K.L. Scrivener, Effect of temperature on the microstructure of calcium silicate hydrate (C-S-H), *Cem. Concr. Res.* 53 (2013) 185–195. doi:10.1016/j.cemconres.2013.06.008.
- [29] Z.P. Bažant, M.F. Kaplan, *Concrete at high temperatures: material properties and mathematical models*, Longman, 1996.
- [30] M.S. Culfik, T. Özturan, Effect of elevated temperatures on the residual mechanical properties of high-performance mortar, *Cem. Concr. Res.* (2002). doi:10.1016/S0008-8846(02)00709-3.
- [31] E. Horszczaruk, P. Sikora, K. Cendrowski, E. Mijowska, The effect of elevated temperature on the properties of cement mortars containing nanosilica and heavyweight aggregates, *Constr. Build. Mater.* (2017). doi:10.1016/j.conbuildmat.2017.02.003.
- [32] R. Serafini, R.R. Agra, R. Monte, A.D. Figueiredo, The effect of elevated temperatures on the tensile properties of steel fiber reinforced concrete by means of double edge wedge splitting (DEWS) test: Preliminary results, in: G. Pijaudier-Cabo, P. Grassl, C. La Borderie (Eds.), *Proc. 10th Int. Conf. Fract. Mech. Concr. Concr. Struct.*, IA-FraMCoS, Bayonne, France, 2019: p. 6. doi:10.21012/FC10.240385.

- [33] R. Serafini, L.M. Mendes, R.P. Salvador, A.D. de Figueiredo, The effect of elevated temperatures on the properties of cold-drawn steel fibers, *Mag. Concr. Res.* (2020) 1–28. doi:10.1680/jmacr.19.00498.
- [34] L.M.S. Mendes, R. Serafini, A.D. de Figueiredo, The effect of high temperature on the mechanical properties of steel fibers and polymeric macrofibers, in: *Proc. 9th Int. Conf. Concr. Under Sev. Cond. - Environ. Load.*, Menvia, Porto Alegre, Brazil, 2019. doi:10.31808/5ca6e03b5ca4f0d406ac888a.
- [35] R.P. Salvador, S.H.P. Cavalaro, I. Segura, A.D. Figueiredo, J. Pérez, Early age hydration of cement pastes with alkaline and alkali-free accelerators for sprayed concrete, *Constr. Build. Mater.* 111 (2016) 386–398. doi:10.1016/j.conbuildmat.2016.02.101.
- [36] A. Nonat, The structure and stoichiometry of C-S-H, *Cem. Concr. Res.* (2004). doi:10.1016/j.cemconres.2004.04.035.
- [37] K.Y. Kim, T.S. Yun, K.P. Park, Evaluation of pore structures and cracking in cement paste exposed to elevated temperatures by X-ray computed tomography, *Cem. Concr. Res.* (2013). doi:10.1016/j.cemconres.2013.03.020.
- [38] M.C.R. Farage, J. Sercombe, C. Gallé, Rehydration and microstructure of cement paste after heating at temperatures up to 300 °C, *Cem. Concr. Res.* (2003). doi:10.1016/S0008-8846(03)00005-X.
- [39] V. Pachta, S. Triantafyllaki, M. Stefanidou, Performance of lime-based mortars at elevated temperatures, *Constr. Build. Mater.* 189 (2018) 576–584. doi:10.1016/j.conbuildmat.2018.09.027.
- [40] R.K. Ibrahim, R. Hamid, M.R. Taha, Fire resistance of high-volume fly ash mortars with nanosilica addition, *Constr. Build. Mater.* 36 (2012) 779–786. doi:10.1016/j.conbuildmat.2012.05.028.
- [41] Z. Pi, H. Xiao, J. Du, M. Liu, H. Li, Interfacial microstructure and bond strength of nano-SiO₂-coated steel fibers in cement matrix, *Cem. Concr. Compos.* 103 (2019) 1–10. doi:10.1016/j.cemconcomp.2019.04.025.
- [42] M. Lu, H. Xiao, M. Liu, X. Li, H. Li, L. Sun, Improved interfacial strength of SiO₂ coated carbon fiber in cement matrix, *Cem. Concr. Compos.* 91 (2018) 21–28. doi:10.1016/j.cemconcomp.2018.04.007.
- [43] H. El-Didamony, E.A. El-Rahman, R.M. Osman, Fire resistance of fired clay bricks-fly ash composite cement pastes, *Ceram. Int.* (2012). doi:10.1016/j.ceramint.2011.06.050.
- [44] H.F.W. Taylor, *Cement chemistry*. 2nd ed., Acad. Press. (1997).

- doi:10.1016/S0958-9465(98)00023-7.
- [45] C.R. Cruz, M. Gillen, Thermal expansion of Portland cement paste, mortar and concrete at high temperatures, *Fire Mater.* 4 (1980) 66–70. doi:10.1002/fam.810040203.
- [46] L.A.G. Bitencourt, O.L. Manzoli, P.G.C. Prazeres, E.A. Rodrigues, T.N. Bittencourt, A coupling technique for non-matching finite element meshes, *Comput. Methods Appl. Mech. Eng.* 290 (2015) 19–44. doi:10.1016/j.cma.2015.02.025.
- [47] Y.T. Trindade, L.A.G. Bitencourt Jr., R. Monte, A.D. de Figueiredo, O.L. Manzoli, Design of SFRC members aided by a multiscale model: Part I – Predicting the post-cracking parameters, *Compos. Struct.* 241 (2020) 112078. doi:10.1016/j.compstruct.2020.112078.
- [48] Y.T. Trindade, L.A.G. Bitencourt Jr., O.L. Manzoli, Design of SFRC members aided by a multiscale model: Part II – Predicting the behavior of RC-SFRC beams, *Compos. Struct.* 241 (2020) 112079. doi:10.1016/j.compstruct.2020.112079.
- [49] S. James, W. Alexander, *Materials Science and Engineering Handbook*, 2001. doi:10.1126/science.232.4757.1485.
- [50] W. Callister, D. Rethwisch, *Materials science and engineering: an introduction*, 7th ed., John Wiley, New York, USA, 2007.
- [51] S.C. Lee, J.Y. Cho, F.J. Vecchio, Diverse embedment model for steel fiber-reinforced concrete in tension: Model development, *ACI Mater. J.* (2011). doi:10.14359/51683262.

ARTICLE C

Title: Double Edge Wedge Splitting test to characterize the design post-cracking parameters of fiber reinforced concrete subjected to high temperatures

Submit to: Magazine of Concrete Research

Publication date: 01/05/2021.

Status: Published (doi: 10.1061/(ASCE)MT.1943-5533.0003701)

DOUBLE EDGE WEDGE SPLITTING TEST TO CHARACTERIZE THE
DESIGN POST-CRACKING PARAMETERS OF FIBER REINFORCED
CONCRETE SUBJECTED TO HIGH TEMPERATURES

Ramoel Serafini¹, Ronney R. Agra², Renan P. Salvador³, Albert de la
Fuente⁴, Antonio D. de Figueiredo⁵

¹Ph.D. candidate, Department of Civil Construction Engineering, Polytechnic School of the University
of São Paulo | Avenida Professor Almeida Prado, Travessa 2, 83, 05424-970, São Paulo, Brazil.

rserafini@usp.br

² Master graduate, Department of Civil Construction Engineering, Polytechnic School of the
University of São Paulo | Avenida Professor Almeida Prado, Travessa 2, 83, 05424-970, São Paulo,
Brazil. ronney.agra@usp.br

³ Professor, Department of Civil Engineering, São Judas Tadeu University | Rua Taquari, 546, 03166-
000, São Paulo, Brazil. renan.salvador@usp.br

⁴ Professor, Department of Construction Engineering, Polytechnic University of Catalonia | Jordi
Girona, 1-3, 08034, Barcelona, Spain. albert.de.la.fuente@upc.edu

⁵ Professor, Department of Civil Construction Engineering, Polytechnic School of the University of São
Paulo | Avenida Professor Almeida Prado, Travessa 2, 83, 05424-970, São Paulo, Brazil.

antonio.figueiredo@usp.br

ABSTRACT

The determination of the post-crack tensile properties of steel fiber reinforced concrete (SFRC) after exposure to elevated temperatures is a current methodological

challenge. The objective of this research is to evaluate the applicability of the Double Edge Wedge Splitting (DEWS) test to characterize the post-crack tensile properties of SFRC after exposure to elevated temperatures. Results show that the DEWS test has reduced scatter and facilitates the interpretation of results with diminished frictional interaction between the apparatus and the specimen. The results in terms of coefficient of mechanical degradation were comparable to those obtained by bending tests in literature, which highlights the suitability of the DEWS test to be adopted in future researches and guidelines. The post-crack tensile properties were not significantly affected up to ~ 300 °C and a linear reduction ratio was verified with the increase in temperature. Additionally, the constitutive model proposed may reproduce the effect of temperature on the tensile stress-strain behavior of the SFRC and is a valuable input for hygro-thermo-mechanical numerical models oriented to simulate the mechanical behavior of structures made with SFRC.

Keywords: steel fiber reinforced concrete; double edge wedge splitting test; elevated temperature; post-crack behavior; tensile strength

1 Introduction

Steel fiber reinforced concrete (SFRC) is a composite material that has been used to replace steel rebars either partially or totally in reinforced concrete [1–3]. Due to this reason, the post-crack tensile properties of SFRC when exposed to elevated temperatures are of paramount importance for buildings and tunnels, in which fire must be considered as an accidental load. In these cases, SFRC may undergo dehydration of hydrated phases, extensive cracking, and coarsening of the pore structure, resulting in a deteriorated matrix and reduction of the tensile strength [4–6]. These factors are detrimental for the proper characterization of the tensile properties of the SFRC by means of mechanical tests.

In this sense, Rambo et al. [7] evaluated the applicability of the double punch test (DPT) for the determination of the tensile properties of SFRC after exposure to elevated temperatures. Results showed an increased frictional interaction between the steel punch and the deteriorated specimen, which led to an incorrect interpretation of the results. This highlighted that an inaccurate test methodology may significantly affect the post-crack tensile strength results and lead to unsafe design assumptions.

The determination of the design-oriented constitutive equations for SFRC subjected to high temperatures is well-established when bending tests are performed [8,9]. In bending tests, the friction between the supports and the specimen when the matrix is deteriorated by the high temperature may be altered, raising doubts about the effect of this condition on the post-crack response of the composite. Since bending tests require prismatic specimens, its execution is more complex and results present a higher scatter than DPT [10]. In addition, the bending response of the composite may be significantly different from its tensile behavior, requiring the use of conversion factors for structural design that might be unrepresentative for some load levels [11] and induce to incorrect assumptions during the design stages [12,13].

In this sense, the Double Edge Wedge Splitting (DEWS) test may be a proper procedure to evaluate SFRC exposed to elevated temperatures [14]. A fracture mode I is induced in the specimen, minimizing the occurrence of compressive stresses that could alter results and their interpretation. Furthermore, this test requires small cubic specimens, which may be easily extracted from the structure affected by fire for the evaluation of the tensile properties. The DEWS test provides a simpler yet more reliable test method to assess the post-heat tensile properties of SFRC for structural applications, which highlights the practical significance of the work. Moreover, the DEWS test is a suitable candidate to be implemented in future guidelines related to the evaluation of SFRC structures affected by fire. Even though the methodology is promising, this is the first work evaluating the suitability of the DEWS test applied to SFRC after high temperatures according to the authors knowledge.

Therefore, the objective of this study is to evaluate the applicability of the DEWS test to characterize the post-crack tensile properties of SFRC subjected to elevated temperatures. This study contributes to the limited literature regarding the application of a proper methodology to evaluate the post-cracking behavior of SFRC subjected to high temperatures. Moreover, a design-oriented model that relates the tensile pre- and post-cracking properties with temperature was proposed.

2 Experimental methodology

Figure 1 shows the scheme adopted for the experimental program conducted in this study. Mechanical tests were performed on SFRC to characterize the matrix properties and the post-crack behavior. The mineralogical characterization was

conducted in cement pastes to avoid the dilution of the cement matrix phases by the aggregates [7]. Therefore, phases present in amounts lower than 2% could be quantified [15].

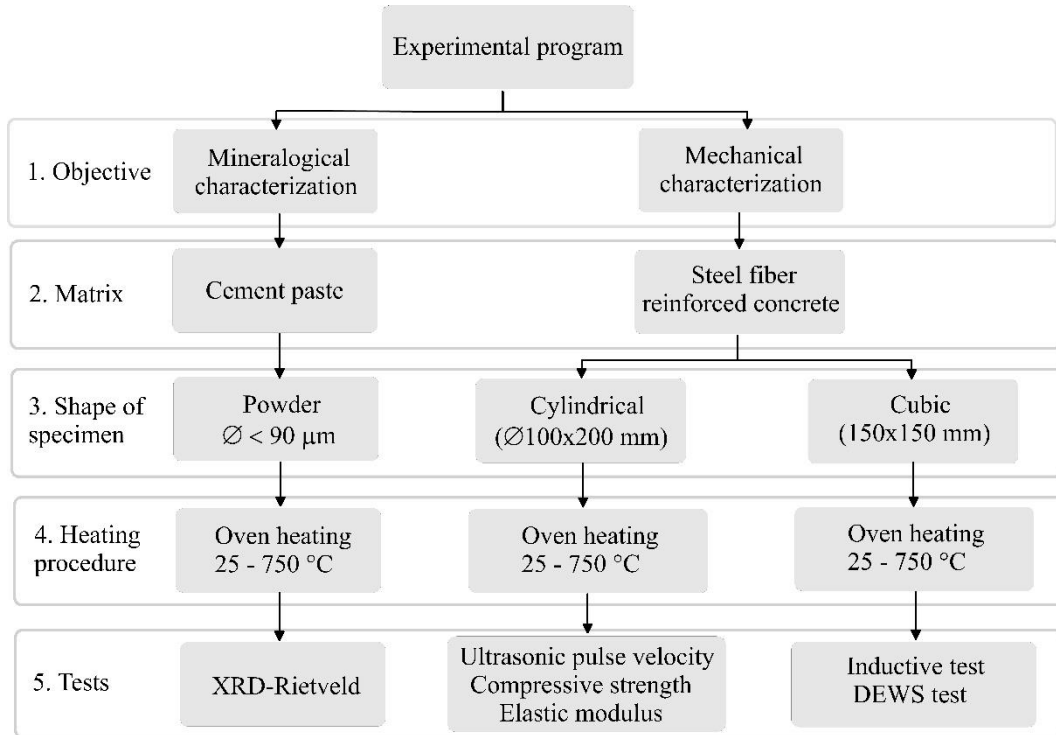


Figure 1 – Scheme adopted for the experimental program of this study

The research conducted is framed within a larger project regarding the study of the effect of temperature on the properties of fiber reinforced composites [16]. Information related with production and characterization of materials is partially presented to avoid repetition.

2.1 Materials

A Portland cement CEM I 52.5R and silica fume type Elkem 920-U with 98% SiO₂ were used as cementing materials. Aggregates were composed by dry river and artificial sand and two coarse granite aggregates ($\varnothing_{\max} = 19$ mm and $\varnothing_{\max} = 9.5$ mm). The complete characterization of these materials is described in Serafini et al. [16]. A polycarboxylate-based superplasticizer, GCP ADVA Cast 525, was employed to provide adequate workability to the fresh mix.

Cold-drawn hooked-end steel fibers were used as reinforcement and play an important role at improving the post-crack mechanical properties of plain concrete. Polypropylene microfibers were used to reduce the risk of explosive spalling during

heating. Table 1 shows the physical and mechanical properties of the steel and micro-synthetic fibers provided by their manufacturers.

Table 1 – Physical and mechanical properties of the steel and micro-synthetic fibers

Property	Hooked-end steel fiber	Micro-synthetic fiber
Length (mm)	60	12
Diameter (mm)	0.75	0.03
Aspect ratio (l/d)	80	400
Specific surface area (m ² /kg)	3.45	147
Specific weight (kg/m ³)	7850	910
Melting point (°C)	~1370	165
Tensile strength (MPa)	1225	Not provided
Young modulus (GPa)	210	Not provided

2.2 Mineralogical characterization

The phase composition of cement pastes was evaluated as a function of temperature. This complementary characterization is discussed in detail in Appendix A.

2.3 Composition and preparation of SFRC

The concrete mix design is described in Table 2. It was based on the mix design of precast segments produced for the construction of the Line 6 tunnel of São Paulo public subway system [16]. The steel fiber content was 0.45% in volume (35 kg/m³) and micro-synthetic fibers were added at 0.09% in volume (0.8 kg/m³). The steel fiber content adopted in this study is lower than the critical fiber volume fraction that grants concrete a strain-hardening behavior. The use of fiber volumes lower than the critical fiber volume fraction is commonly adopted in some structural applications worldwide [17,18].

Table 2 – Dosage of materials to produce 1 m³ of SFRC

Materials	Dosage (kg/m ³)
Portland cement	400
Silica fume	22
Water	165
Siliceous river sand	403
Artificial granite sand	269
Coarse granite aggregate - d _{max} :19 mm	770
Coarse granite aggregate - d _{max} :9.5 mm	330
Superplasticizer	3
Micro-synthetic fiber	0.80
Hooked-end steel fiber	35

Concrete was prepared in a laboratory with temperature of (25 ± 1) °C using a 300 L-concrete mixer, following the procedure presented by Serafini et al. [16]. The fresh concrete presented a slump value equal to (40 ± 10) mm and a specific weight equal to (2430 ± 52) kg/m³. Once concrete production was finished, 12 prismatic specimens measuring 150x150x550 mm (width x height x length) and 30 cylindrical specimens measuring 100 mm in diameter and 200 mm in height were molded. Specimens were consolidated using a vibrating table during 20 s with a frequency of 60 Hz and kept in a humid chamber for 72 h before being cured at room temperature for 150 days. This procedure was used to simulate the curing conditions adopted for the precast elements employed in the São Paulo subway line.

A total of 30 cubic specimens with 150 mm-edges employed in the DEWS test were prepared by sawing prismatic specimens, according to Borges et al. [13]. Two triangular grooves with an inclination of 45° were cut along two opposite sides of the cubes in the face positioned 90° from the molding face and respecting the casting orientation. After that, two notches with a 5-mm depth and a 2-mm width were sawn, starting in the groove vertices towards the center of the cubes (see Fig. 2).

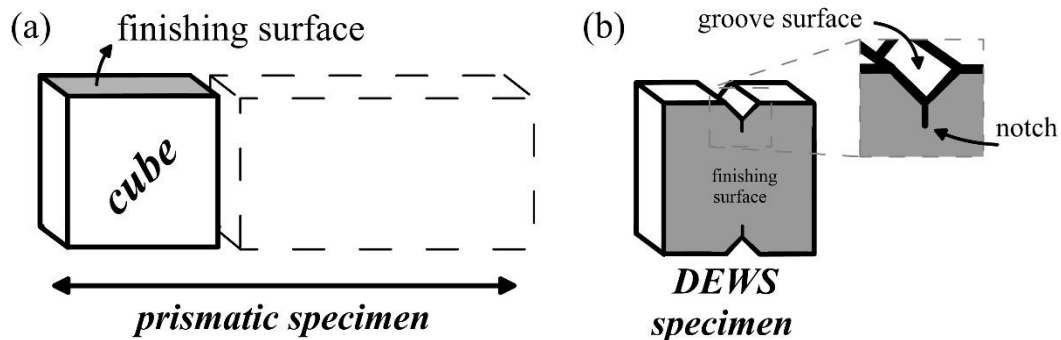


Figure 2 – Preparation of cubic specimens for the DEWS test

Two steel sheets measuring 0.9x15x150 mm were attached onto the groove surfaces using polyester putty as glue. These steel sheets were used to reduce the frictional interaction between the roller and the specimen during the test. For specimens that were exposed to high temperatures, the steel sheets were glued after the heating and cooling procedures were conducted.

2.4 Heating procedure

An INFORGEL GENGA electric oven, model GCR.SP, with maximum temperature capacity of 1000 °C was employed to heat cubic and cylindrical specimens. The heating rate adopted was (12 ± 2) °C/min, which was the maximum heating rate possible in the equipment used. Specimens were heated at the temperatures of 150, 300, 450, 600, and 750 °C and kept at each temperature during 10, 8, 6, 4, and 4 h, respectively. The duration of the sustained thermal load was determined by numerical simulation based on the work of Carpio et al. [19] and had the objective to ensure uniform temperature of the specimens. After the heat exposure, the chamber was kept closed and cooling occurred during 24 h. Specimens that were not subjected to heating were used for comparative purposes.

2.5 Test methods

2.5.1. Compressive strength and elastic modulus

Cylindrical specimens were used for the characterization of compressive strength (f_c) and elastic modulus (E_c) of the SRFC. Tests were conducted in a Shimadzu Universal Testing Machine, model UH-F2000kNXR, with a computer-controlled servo-hydraulic system, operating frequency of 60 Hz, and maximum load capacity of 2000 kN. Tests were conducted following the procedure adopted by Serafini et al [16]. 5 specimens were tested for each target temperature and the results obtained were analyzed statistically by analysis of variances (ANOVA) and Tukey tests.

2.5.2. Double edge wedge splitting test

The DEWS test was conducted in an open-loop electromechanical universal test machine EMIC DL 10000, with a load cell with maximum load capacity of 10 kN, and frame stiffness of 42 kN/mm. The tensile strength and post-crack tensile strength were obtained following the simplified procedure presented by Borges et al. [13].

Figure 3 shows a schematic drawing of the DEWS test setup adopted in this study. A total of 5 specimens were tested for each target temperature.

Two 50 mm length transducers were positioned in opposite sides and in the middle height of the cubic specimens to measure the average crack opening displacement (COD). A COD rate of 0.12 mm/min was employed. Although the displacement rate and transducer positioning are simplifications from the original methodology proposed by di Prisco et al. [14], this adaptation does not present any significant influence on the first crack strength. In addition, it reduces the scattering of results and causes minor effects on post-crack tensile strength values [13]. COD values provided are the average of the two measurements obtained.

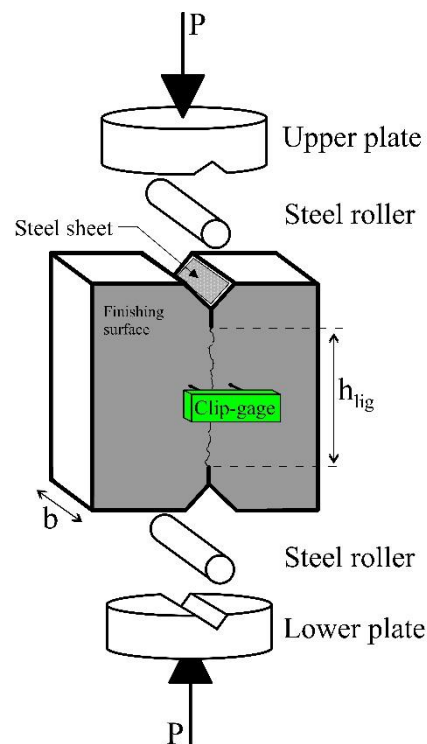


Figure 3 – Schematic drawing of the DEWS test setup adopted in this study

Graphite was used to lubricate the contact between the rollers and the steel sheets, minimizing the scatter of the results caused by frictional phenomena [14]. Also, these steel sheets prevent a large plastic deformation in the contact area of the steel roller and the groove surface of the specimen due to the concentration of stress, especially when the matrix is deteriorated by high temperatures. This contact deformations may generate distortions in the results when using flexural tests due to the increased friction between the contact of the supports and the prismatic specimens.

Consequently, the DEWS test has less influence of extrinsic deformations in the contact area of the specimen and the test apparatus, providing more accurate results.

The post-cracking tensile strength values associated to serviceability (f_{Fts}) and to the ultimate limit state (f_{Ftu}) conditions were adopted as the values associated to the COD equal to 0.25 mm and 1.25 mm, respectively. These values were assumed based on the crack mouth opening displacement recommended in EN 14651 [9] and considering the intrinsic geometrical differences in terms of test configuration between the three-point flexural test and the DEWS test.

2.6. Admissible error and sample size determination

The relationship between the sample size and the admissible error was determined based on inferential statistics [20], by means of Eq. 1.

$$n = \frac{s^2 \cdot z_\gamma^2}{\varepsilon^2} \quad (1)$$

where n is the required sample size; s is the standard deviation obtained by the pilot sample (in MPa); z_γ is the t -distribution value; and ε is the admissible error for the test. The \bar{x} was computed from the experimental results, while $z_\gamma = 2.132$ was adopted considering a confidence interval of 95% and 4 degrees of freedom.

3 Results and discussion

3.1 Compressive strength and elastic modulus

Figure 4 shows the average stress-strain curves and both f_c and E_c for each temperature. The average f_c of specimens at room temperature was 83.9 MPa and the average E_c was equal to 36.3 GPa. It is important to highlight that no explosive spalling occurred during heating of the specimens. Also, the qualitative visual inspection conducted have shown that the micro-synthetic fibers melted for specimens exposed to $T \geq 150$ °C, which is in line with literature results [7,16,21]. Additionally, a dark oxide layer was verified on the surface of the steel fibers for specimens exposed to $T \geq 600$ °C. This oxide phase is a three-layered scaled structure composed of wüstite (FeO), hematite (Fe₂O₃), and magnetite (Fe₃O₄) that is known to slightly reduce the effective cross-sectional area of fibers up to ~750 °C [22].

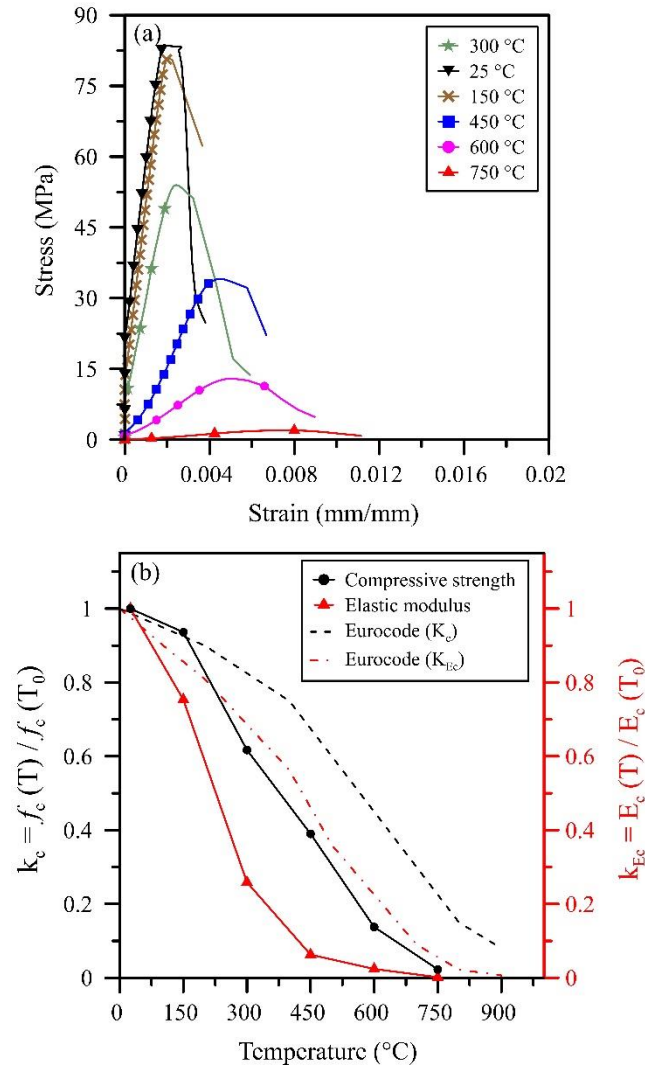


Figure 4 – (a) average stress-strain curves and (b) compressive strength and elastic modulus as a function of temperature

The f_c was reduced by 6.4% (150 °C) to 97.7% (750 °C) with respect to the f_c at room temperature. These reductions are in line with SFRC and plain concrete results found in literature [23–26], which suggests that low contents of steel fiber do not affect the post-heat compressive strength of concrete. Nonetheless, it is worth noticing that the strength reduction obtained in this experimental program resulted to be more drastic than that suggested by Eurocode [27] as may be seen in Fig. 4b. This difference may be attributed to the porosity increased by the ignition of the micro-synthetic fibers and to differences in the heat regimes employed.

On the other hand, the reduction of E_c due to high temperature ranged from 24.6% (150 °C) to 99.8% (750 °C). A severe reduction in E_c between the temperatures of 150 and 450 °C may be observed in Fig. 4b due to the thermal expansion mismatch between aggregates and paste, the consequent formation of micro-cracks in the

interfacial transition zone, and the considerable dehydration of hydrated products [26]. The dehydration process results in the coarsening of the cement paste pore structure and combined with the degradation of the synthetic fibers and changes in the porosity of aggregates affect the compressive strength and elastic properties of the composite. These reductions are in line with the literature [7,23,25].

3.2 Tensile strength and post-crack tensile strength

Figure 5 relates the average stress-COD and the tensile and post-crack tensile strengths of the composite. Results depicted in Figure 5 allow to state that both pre- and post-cracking tensile strengths are negatively affected by temperature. The reductions follow a linear decreasing relationship ($R^2 > 0.94$ in cases).

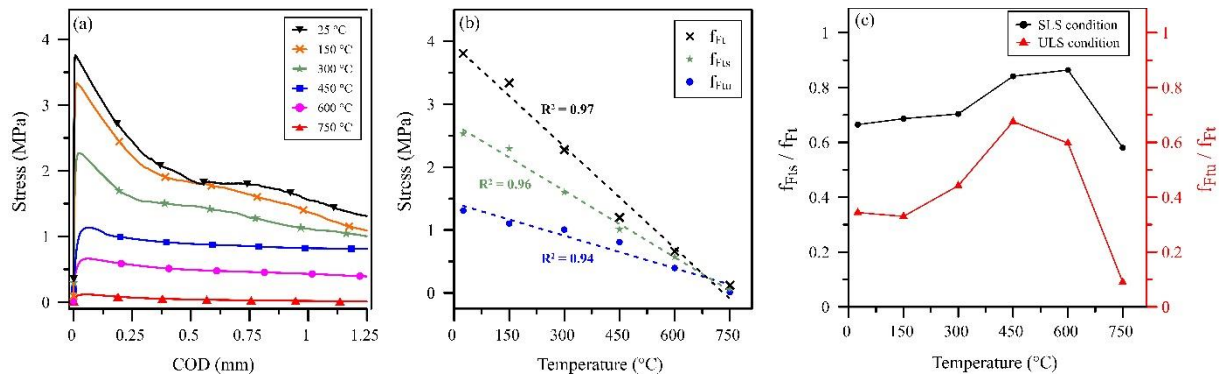


Figure 5 – (a) stress-COD average results, (b) tensile and post-crack tensile strength results, and (c) ductility parameters

It can be remarked that the tensile strength (f_{Ft}) was the property most affected by temperature, with a degradation rate of $5.4 \cdot 10^{-3}$ MPa/°C, and reductions from 12.3% (150 °C) to 96.8% (750 °C) with respect to the reference. This reduction is associated with changes of the mineralogical and microstructural properties of the cement paste and is further aggravated by the sudden increase in the volume of quartz that may induce cracking of the composite and weaken aggregates [16]. This increase in volume is associated with the reversible crystal transformation of quartz at the temperature of 573 °C, from α -trigonal to the β -hexagonal form. The relation between f_{Ft} and temperature is in line with the classical literature [26] and also with recent results obtained with a similar class of concrete tested in comparable conditions [28]. Nevertheless, other studies found no significant reduction in f_{Ft} for temperatures below 300 °C [24,29], which may be a result of the differences in the duration of the temperature stabilization phase of specimens.

The f_{Fts} and f_{Ftu} presented degradation rates of $2.7 \cdot 10^{-3}$ and $1.1 \cdot 10^{-3}$ MPa/°C, respectively. These reductions ranged from 9.5% (150 °C) to 99.2% (750 °C) for f_{Fts} and 15.9% (150 °C) to 99.2% (750 °C) for f_{Ftu} . It is worth to mention that no significant statistical reduction was observed for f_{Ftu} in temperatures below 300 °C, justified by the negligible influence of this temperature range on the bond-slip behavior [30–33]. Therefore, the increase in temperature reduces the tensile capacity of SFRC with respect to f_{Ft} , f_{Fts} , f_{Ftu} at different rates, which also results in a significant increase in terms of ductility, especially for temperatures up to ~ 600 °C (see Fig. 5c). It is important to remark that the ductility gain occurs in terms of approximating the behavior of the material to the perfect elastoplastic behavior and not in terms of the energy absorption during the rupture process.

In view of the results, it is evident that elevated temperatures alter the pre- and post-cracking response of the SFRC and must be considered for structural purposes according to the fib MC-2010 [34].

3.3 Coefficient of mechanical degradation

Figure 6 shows a specimen after the DEWS test. It is clear that no visible damage, such as crushing, was caused by the interaction between the roller and the specimen subjected to the temperature of 750 °C. In addition, the crack opening was remarkably similar at the two faces of the specimen. This behavior may be considered typical for the entire experimental plan and allows to state that DEWS test is not subjected to the influence of crushing in compressed regions such as in bending [16] and DPT tests [7,35]. Moreover, it is important to emphasize that the results of the stress-COD curves (see Fig. 5a) were remarkably more stable and coherent in relation to the results previously obtained by the DPT method [7].

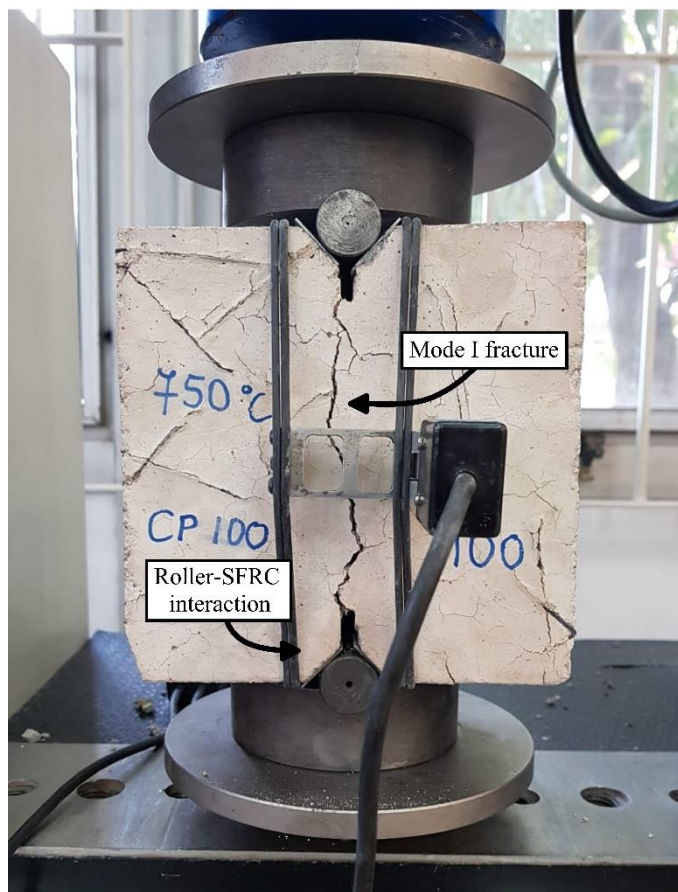


Figure 6 – Interaction between roller and DEWS specimen and the mode I fracture after the test

European guidelines for the design of SFRC structures present the concept of a coefficient of mechanical degradation for the tensile strength of the matrix (k_{Fi}), serviceability (k_{Fts}), and ultimate limit state (k_{Ftu}) to be used for the post-fire assessment of structures by means of cross-sectional analysis [27,36]. This coefficient may be calculated based on experimental results and applied as a reduction factor for the bearing capacity of the layers of SFRC in a structure. Figure 7 shows the coefficients of mechanical degradation for this study compared to literature results and European standards.

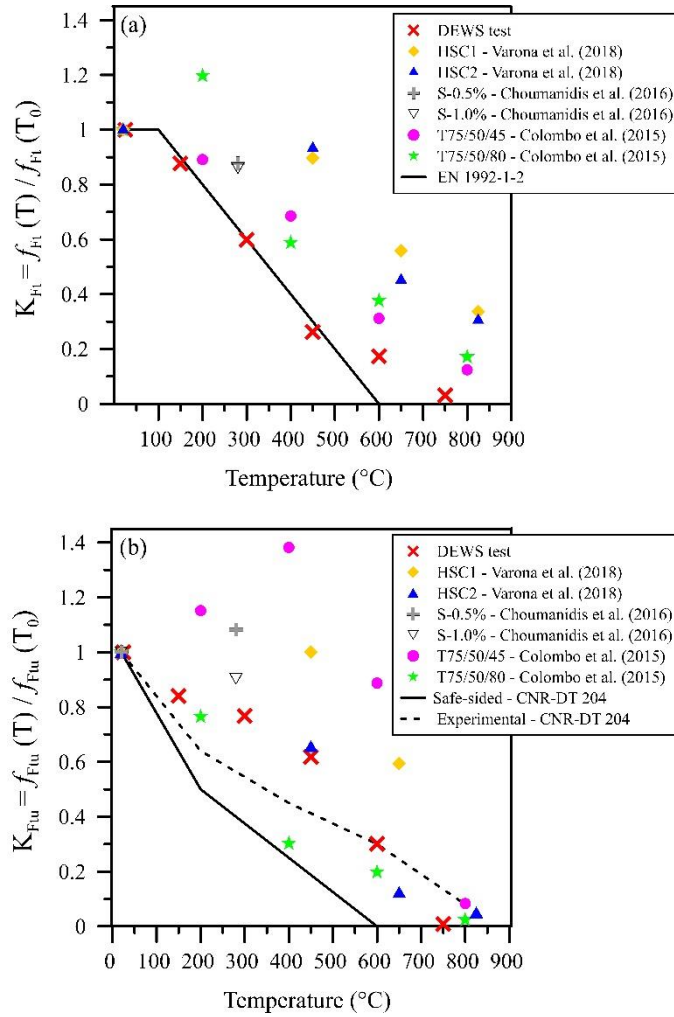


Figure 7 – Coefficients of mechanical degradation compared to literature results and European standards

In Fig. 7b, the dashed line represents the qualitative pattern for experimental results while the continuous lines represent the pattern assumed to be on the safe side, according to CNR DT 204 [36]. Bending test results found in literature were selected based on a similar class of concrete [37–39] and the post-crack tensile strength values were determined using $\text{CMOD} = 2.5 \text{ mm}$ for the ultimate limit state (ULS) condition, based on EN 14651 [9] and on *fib* MC-2010 [34].

Although a limited number of comparable results was found in the literature, most of the bending test's results tend to have greater k_{F_t} values (matrix and ULS) than those obtained with the DEWS test. This difference may be related to the stress redistribution that occurs due to the variable gradient of tensile stresses along the cracked section during the bending test, while the stresses are distributed through the entire vertical crack in the DEWS configuration (except at the vicinity of the edges). Likewise, the local curvature in bending tests may result in a second-order

confinement pressure that may increase the flexural strength, especially for greater crack opening values [40].

In any case, results presented in Figure 7 paired with the qualitative visual inspection of the test shown in Figure 6 suggest that the DEWS test may be suitable to determine the tensile properties of SFRC after exposure to elevated temperatures. Moreover, results in terms of coefficient of degradation for the tensile properties are found to be within the same range of results obtained by bending tests and are comparable to the patterns presented by European standards.

3.4 Sample size determination

Figure 8 shows the sample size required as a function of the admissible error for the tensile properties of the composite. Given that the tensile properties of the composite after 750 °C are almost null, the sample size analysis for this target temperature may not be consistent and was excluded of the discussions provided.

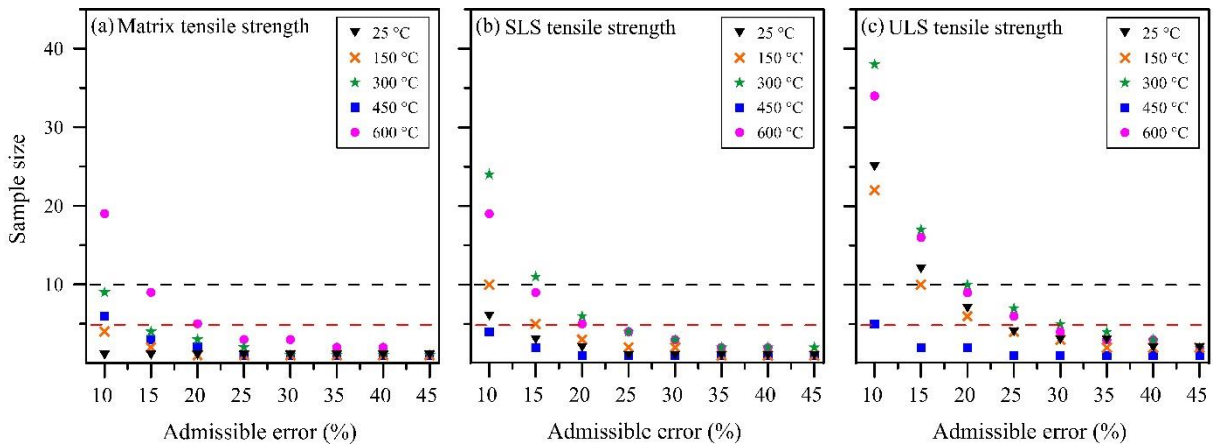


Figure 8 – Sample size required as a function of the admissible error for the (a) f_{Ft} , (b) f_{Fts} , and (c) f_{Ftu} values

In this sense, the analysis conducted using inferential statistics and a 95% confidence interval show that the sample size increases with the reduction of the admissible error for the DEWS test. This increase in sample size is particularly greater for the post-crack tensile properties and for specimens after exposure to elevated temperatures, which may be attributed to the intrinsic bound variability of the material and the reduction of the tensile properties after heating. In addition, results show that the use of 10 cubic specimens ensure a maximum admissible error of ~20%, while 5 cubic specimens are required for a maximum admissible error of ~28%, which is the case of this study.

4. Constitutive model

In this section, the damage coefficient (K_{Ftik}) and a constitutive model to be used in cross-sectional analyses are presented as an approach to deal with the design of SFRC after exposure to elevated temperatures. Characteristic post-cracking tensile strength values were considered to develop the approach in order to be aligned with the safety format established in the fib MC-2010 [34].

4.1 Damage coefficient

The damage coefficient (K_{Ftik}) is formulated considering the auxiliary parameter $k_{Fti,n}$, which is based on the “coefficient of mechanical degradation” presented by the Italian guideline for the Design and Construction of Fiber-Reinforced Concrete Structures [36], calculated as:

$$k_{Fti,n} = \frac{f_{Ftik}(T_n)}{f_{Ftik}(T_0)} \quad (2)$$

where f_{Ftik} is the characteristic tensile strength properties (f_{Ftk} , f_{Ftsk} , and f_{Ftuk}) for a given temperature (T_n) and to room temperature (T_0). Therefore, the K_{Ftik} is a multilinear equation that interpolates $k_{Fti,n}$ for different values of T other than those tested experimentally, which may be computed for K_{Ftk} , K_{Ftsk} , and K_{Ftuk} as:

$$K_{Ftik} = \begin{cases} 1 + (k_{Fti,1} - 1) \frac{(T - T_0)}{(T_1 - T_0)} & \text{if } T_0 \leq T \leq T_1 \\ k_{Fti,1} + (k_{Fti,2} - k_{Fti,1}) \frac{(T - T_1)}{(T_2 - T_1)} & \text{if } T_1 \leq T \leq T_2 \\ \vdots \\ k_{Fti,(n-1)} + (k_{Fti,n} - k_{Fti,(n-1)}) \frac{(T - T_{(n-1)})}{(T_n - T_{(n-1)})} & \text{if } T_{(n-1)} \leq T \leq T_n \end{cases} \quad (3)$$

where $k_{Fti,n}$ is the auxiliary parameter, T_n is the temperatures experimentally assessed, and T is the temperature in which the damage coefficient is to be determined. Figure 9 illustrates the analytical model for the damage coefficient as a function of temperature.

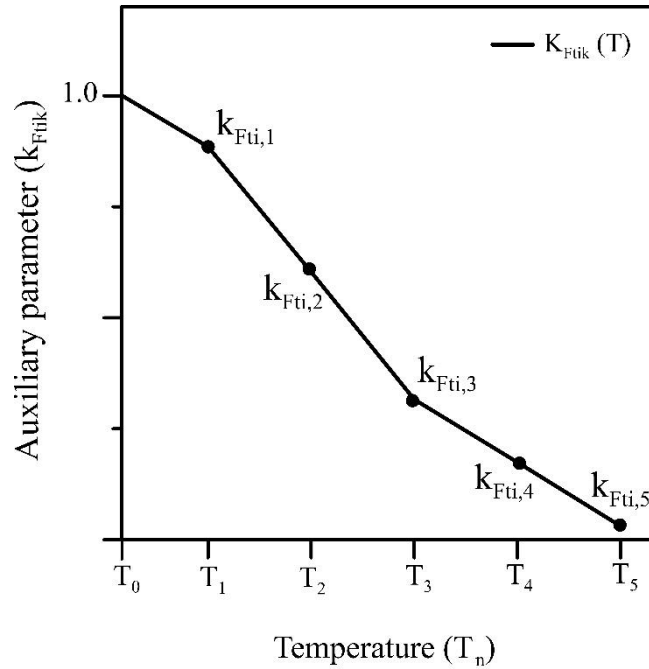


Figure 9 – The analytical model for the damage coefficient as a function of temperature

4.2 Stress-strain model

The $\sigma_t - \varepsilon$ model was developed taking as basis the linear model proposed by *fib* MC 2010 [34], and is mathematically described as:

$$\sigma_t(\varepsilon) = \begin{cases} K_{Ftk} \cdot f_{Ftk} \left(\frac{\varepsilon}{\varepsilon_{Ft}} \right) & \text{if } 0 \leq \varepsilon \leq \varepsilon_{Ft} \\ K_{Ftk} \cdot f_{Ftk} - (K_{Ftk} \cdot f_{Ftk} - K_{Ftsk} \cdot f_{Ftsk}) \left(\frac{\varepsilon - \varepsilon_{Ft}}{\varepsilon_{Fts} - \varepsilon_{Ft}} \right) & \text{if } \varepsilon_{Ft} \leq \varepsilon \leq \varepsilon_{Fts} \\ K_{Ftsk} \cdot f_{Ftsk} - (K_{Ftsk} \cdot f_{Ftsk} - K_{Ftuk} \cdot f_{Ftuk}) \left(\frac{\varepsilon - \varepsilon_{Fts}}{\varepsilon_{Ftu} - \varepsilon_{Fts}} \right) & \text{if } \varepsilon_{Fts} \leq \varepsilon \leq \varepsilon_{Ftu} \end{cases} \quad (4)$$

where K_{Ftk} is the damage coefficient for f_{Ftk} ; K_{Ftsk} is the damage coefficient for f_{Ftsk} ; K_{Ftuk} is the damage coefficient for f_{Ftuk} ; ε_{Ft} is the strain related to f_{Ftk} ; ε_{Fts} is the strain related to f_{Ftsk} ; and ε_{Ftu} is the strain related to f_{Ftuk} . Figure 10 illustrates the stress-strain constitutive model as a function of temperature.

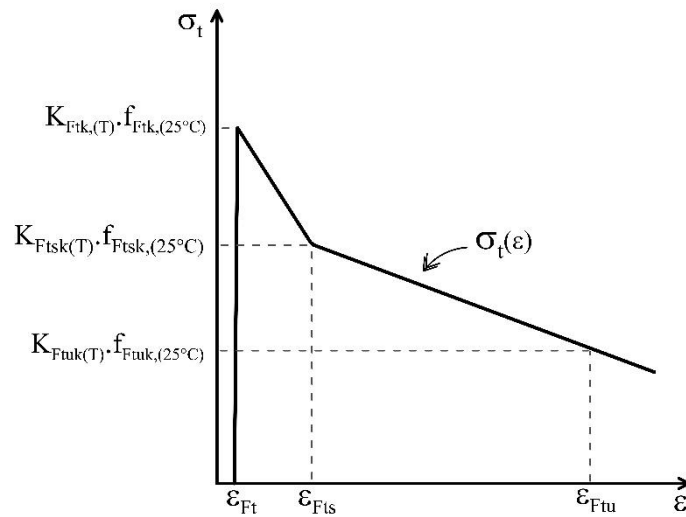


Figure 10 – Stress-strain constitutive model as a function of temperature.

For comparison purposes, Figure 11 shows the experimental average curves and those derived from the application of the model proposed herein considering average and characteristic values. The characteristic values were based on a gaussian distribution and the simplified estimation presented in the fib MC-2010 [34], and a summary of the parameters adopted can be seen in Table 3.

Table 3 – Summary of the parameters adopted to generate the analytical model for each target temperature

Target temperature (°C)	Parameters adopted		
	ε_{Ft}	ε_{Fts}	ε_{Ftu}
25	$8.2 \cdot 10^{-5}$	$2.2 \cdot 10^{-3}$	$1.1 \cdot 10^{-2}$
150	$1.4 \cdot 10^{-4}$	$2.2 \cdot 10^{-3}$	$1.1 \cdot 10^{-2}$
300	$1.9 \cdot 10^{-4}$	$2.2 \cdot 10^{-3}$	$1.1 \cdot 10^{-2}$
450	$5.2 \cdot 10^{-4}$	$2.2 \cdot 10^{-3}$	$1.1 \cdot 10^{-2}$
600	$5.6 \cdot 10^{-4}$	$2.2 \cdot 10^{-3}$	$1.1 \cdot 10^{-2}$
750	$5.2 \cdot 10^{-4}$	$2.4 \cdot 10^{-3}$	$1.2 \cdot 10^{-2}$

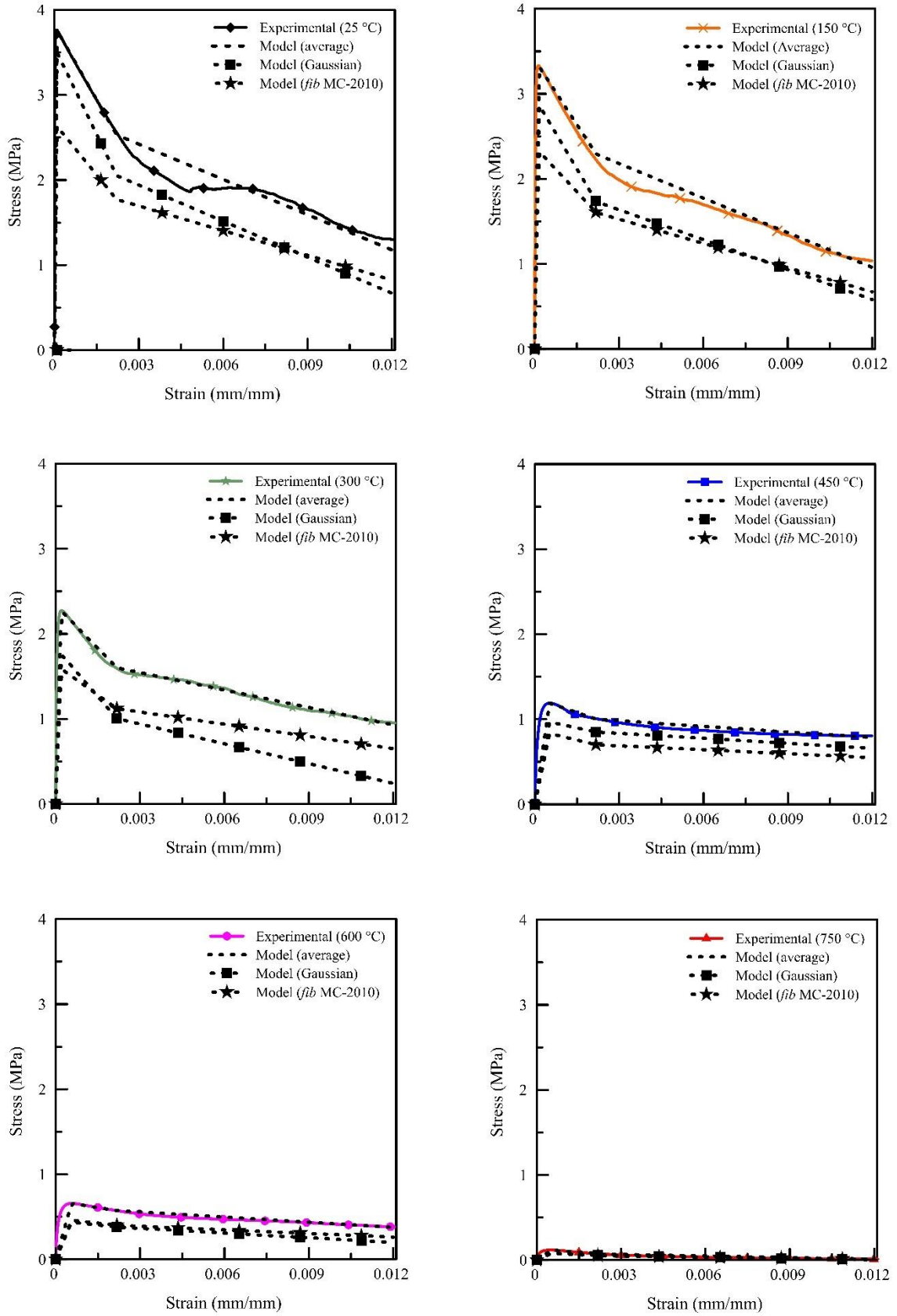


Figure 11 – The experimental results compared to the curves generated by the constitutive stress-strain equation

The analytical curves based on characteristic values are remarkably similar in this case. Although the gaussian approach is widely accepted, its use is not recommended for this purpose since the standard deviation of f_{Ft} for each target temperature might be different and this could lead to inconsistent results. An example may be verified by the lower value of f_{Ftuk} for $T = 300$ °C than for temperatures of 450 °C (see Fig. 11). In contrast, the lower bound values approach, described in the fib MC-2010 [34], overcomes this drawback.

In summary, it may be assumed that the analytical model proposed herein may reproduce the experimental results. In addition, the “safe-sided” curve provided by the CNR DT 204 [36] may be used to define K_{Ftik} since it has shown to be in favor of safety (see Fig. 7). Therefore, this analytical model may be used as an input for recently developed hygro-thermo-mechanical numerical models [19,41] aimed at modelling the mechanical response of SFRC subjected to fire.

5 Conclusions

Based on the results obtained from the mechanical characterization of SFRC subjected to elevated temperatures, the main considerations of this study are:

- The DEWS test proved to be an effective method for the determination of the post-cracking behavior of SFRC. The test showed no deterioration in the contact between the apparatus and the specimen, avoiding any frictional interaction that may influence on the results. The k_{Ft} and k_{Ftu} values are comparable to those obtained by bending tests in literature. Also, the crack opening pattern was similar at both faces of the specimens, reducing scatter and facilitating the results interpretation. In this sense, the DEWS test is a suitable candidate to be implemented in future guidelines related to the evaluation of SFRC structures affected by fire.
- The f_c and f_{Ft} linearly decreased as temperature increases, while E_c shows sharper reductions for temperatures up to 450 °C. The reductions in terms of f_c , f_{Ft} , and E_c were associated with the severe decomposition of cement phases and the consequent changes in the pore structure of the paste after heating.
- The reductions of f_c and E_c due to elevated temperatures are higher than that predicted by European standards due to the presence of micro-synthetic fibers and to differences in heat regimes adopted. Likewise, the reductions observed for f_{Ft} , f_{Fts}

and f_{Ftu} are aligned with those presented in European standards and results found in literature.

- Elevated temperatures led to a decrease in the post-cracking capacity of SFRC since f_{Fts} and f_{Ftu} reduced linearly with a rate of $2.7 \cdot 10^{-3}$ and $1.1 \cdot 10^{-3}$ MPa/°C, respectively. Nonetheless, a slight increase of the ductility was observed.
- The constitutive model proposed may reproduce the effect of temperature on the tensile stress-strain behavior of the SFRC. The model is proposed as a valuable input for hygro-thermo-mechanical numerical models oriented to simulate the behavior of structures made with SFRC, such as those presented by Di Carlo et al. [41] and Carpio et al. [19].

Although the DEWS test may be applied, the variability of the residual strength results (up to 41% for f_{Ftu}) is a challenging aspect to be dealt with, particularly for SFRC that exhibits strain-softening behavior at pre- and/or post-fire conditions. Even under these considerations, average results may be used for comparison purposes (e.g. post-cracking performance of mixes with different amount of fibers) provided a representative statistical population is considered for assessing mean values. Likewise, characteristic magnitudes may also be derived from the characterization results and considered with designing purposes within the context of the limit states safety format. The authors consider that there is still necessity of research on this topic from both the material characterization and structural design perspectives.

Data Availability Statement:

All data, models, and code generated or used during the study appear in the published article.

Acknowledgments

The first and second authors would like to thank the Institute for Technological Research (IPT) and its foundation (FIPT) for their financial and institutional support through the New Talents Program N.01/2017 and N.01/2018, respectively. This work was partially supported by the Fundação de Amparo à Pesquisa do Estado de São Paulo (FAPESP) [Grant # 2017/00125-9 (Renan P. Salvador)] and the Conselho Nacional de Desenvolvimento Científico e Tecnológico (CNPq) [Grant # 305055/2019-4 (Antonio Domingues de Figueiredo)]. Authors would also like to thank

the support of their colleague Dr. Renata Monte for her valuable technical contribution to this work.

Appendix A

Composition and preparation:

Cement paste was produced with CEM I 52.5, silica fume (5.5% by cement weight) and a fixed water/cementitious material (w/cm) ratio equal to 0.39. Pastes were prepared using 200 g of cement, 11 g of silica fume, 82 g of water, and 1.4 g of superplasticizer. All the materials were added to a mixing recipient and homogenized at 10,000 rpm for 120 s using a Makita RT0700C mixer. The cement paste obtained was cast in cylindrical polyethylene molds with diameters of 4 cm. A total of 9 samples were produced, containing around 20 g of paste each. Molds were sealed with a plastic film and cured in a humid chamber for 72 h. After the curing period, samples were stored at room temperature at (25 ± 1) °C for 150 days, which was based to maintain the same curing period adopted for the SFRC.

Heating procedure:

At the age of 150 days, cement paste samples were heated inside an EDG FC series electric oven, model EDG10P-S, at a heating rate of (20 ± 3) °C/min. Samples were exposed to the temperatures of 25, 150, 300, 450, 600, and 750 °C and kept at target temperature for 2 h. The cooling phase was conducted with closed oven during 24h for all specimens. After the heating and cooling procedures were completed, all samples were kept in a desiccator to reduce the possibility of cement paste rehydration and carbonation.

Test method:

Samples were crushed and ground to a maximum particle size of 90 μm before being tested. XRD was performed in a PANalytical X'Pert PRO PW 3040 00 powder diffractometer with Ni filtered $\text{CuK}\alpha_1$ radiation ($\lambda = 1.5418$ Å) and a X'celerator detector (active length of 2.214°). The test was performed in reflection Bragg-Brentano geometry operating at 45 kV and 40 mA. Cylindrical sample holders were filled with approximately 2 g of cement paste and had an internal diameter of 27 mm and a depth of 8 mm. To improve particle statistics, sample holders were spun around the vertical goniometer axis at a rate of 0.5 revolutions per second during the measurement.

X-ray patterns were obtained using an automatic divergence slit from $4^{\circ}2\theta$ to $80^{\circ}2\theta$, using a step width of $0.02^{\circ}2\theta$ and 200 s per step. The XRD patterns were analyzed by Rietveld refinement taking as basis the structure models and the strategy for analysis proposed by Salvador et al. [42] using the software X'Pert High Score Plus. The external standard method was used to determine the amorphous content in samples by using alumina powder (SRM 676a, from NIST) as an external standard reference material and is described in detail in [15].

Discussion of the results:

Figure 12 shows XRD results for cement pastes exposed to target temperatures evaluated in this study. Ettringite crystals dehydrate in the temperature range from 25 to 150°C , resulting in a slight increase of the amorphous content ($\sim 4.5\%$). The dehydration process occurs with the reduction of the water content per formula unit from $32 \text{ H}_2\text{O}$ to $18 \text{ H}_2\text{O}$ or less [16]. This reduction results in the microscopical cracking of ettringite crystals, reducing their crystallinity degree [43–45].

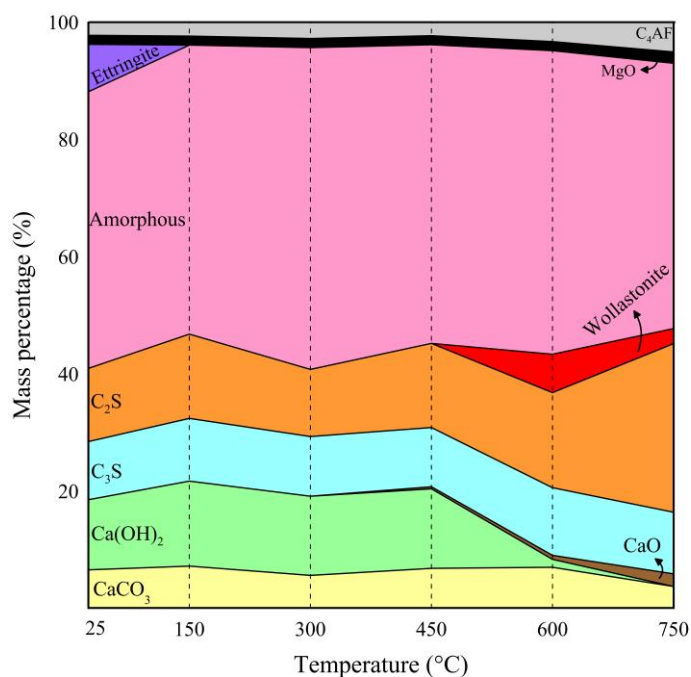


Figure A.1. Mineralogical composition of cement pastes exposed to elevated temperatures

For temperatures between 150 and 300°C the formation of belite may be verified. This formation is a result of the dehydration of the amorphous C-S-H gel, which

results in the formation of a new nesosilicate phase with similar structure to belite. The crystallographic properties and the profile of the XRD peaks in diffractograms suggest that the belite formed after heat exposure is significantly different from those found in anhydrous cement powder, which is also verified in literature [6,16,32]. This inherent crystal structure difference may result in changes in terms of hydraulic activity of this nesosilicate, which is a consequence of the variable Ca-Ca bond length [32], therefore affecting rehydration kinetics

In the temperature range of 300 to 450 °C, the dehydration of portlandite begins, increasing the lime content. In addition, the dehydration of C-S-H gel results in the formation of wollastonite (CaSiO_3), which is associated with the dehydration of jennite and tobermorite [46,47]. Since jennite silicate chains lose interlayer water and Ca-OH and Si-OH groups with the increase in temperature, a depolymerized amorphous jennite phase can be found for temperatures up to 600 °C. Additionally, tobermorite remains stable for temperatures above 600 °C and the elevation of temperature makes the silicate chains cross-link and the interlayer water of Si-OH groups to be lost.

For temperatures between 450 and 750 °C the dehydration of portlandite and the decomposition of calcite contribute to the increase in lime content in the samples. The presence of calcite in samples exposed to target temperature of 750 °C may be a result of a carbonation process that may have occurred during the preparation and storage of samples. This brief exposure of samples to environment may lead to the rapid formation of calcium carbonates, as shown in literature [15]. This formation, however, does not compromise the results of this study.

A small amount of portlandite was found in cement paste samples after exposure to temperatures of 600 °C. The presence of portlandite was not expected because literature results point out that portlandite dehydrates at temperatures around 450 °C [4]. This residual amount may be a result of the specimen size and low porosity, which favors the presence of internally trapped water. Even with that, the absence of portlandite is verified in samples exposed to 750 °C, which may indicate that the residual amount of portlandite was not formed during the preparation or storage of samples.

Between 600 and 750 °C, C-S-H gel continues to decompose, producing nesosilicates in the form of belite and wollastonite. It is possible to observe in Fig. 4 that the total

belite content sharply increases in this temperature range. This significant increase was also verified in recent studies found in literature [16] and was related to the sintering process of belite, which begins only at temperatures of 700 °C in cement production [4].

Additionally, the ferrite (C_4AF) content and the magnesium oxide (MgO) content are not significantly affected by the increase in temperature. These observations may be justified by the fact that these products are formed at temperatures higher than those evaluated in this study during cement production, which results in increased physical and chemical stability [4,16,48]. The decomposition of C-S-H into nesosilicates in the form of alite (C_3S) was not verified in the samples evaluated in this study. This may be reasoned by the fact that the sintering process of alite occurs for temperatures of ~1250 °C [4].

References

- [1] M. Di Prisco, G. Toniolo, Structural applications of steel fibre reinforced concrete, in: Proc. Int. Work., CTE Publ., Milan (Italy), 2000. <http://hdl.handle.net/11311/248435>.
- [2] M. di Prisco, G. Plizzari, L. Vandewalle, Fibre reinforced concrete: new design perspectives, *Mater. Struct.* 42 (2009) 1261–1281. <https://doi.org/10.1617/s11527-009-9529-4>.
- [3] A. de la Fuente, A. Aguado, C. Molins, J. Armengou, Innovations on components and testing for precast panels to be used in reinforced earth retaining walls, *Constr. Build. Mater.* 25 (2011) 2198–2205. <https://doi.org/10.1016/j.conbuildmat.2010.11.003>.
- [4] H.F.W. Taylor, *Cement chemistry*. 2nd ed., Acad. Press. (1997). [https://doi.org/10.1016/S0958-9465\(98\)00023-7](https://doi.org/10.1016/S0958-9465(98)00023-7).
- [5] V. Vydra, F. Vodák, O. Kapičková, Š. Hošková, Effect of temperature on porosity of concrete for nuclear-safety structures, *Cem. Concr. Res.* 31 (2001) 1023–1026. [https://doi.org/10.1016/S0008-8846\(01\)00516-6](https://doi.org/10.1016/S0008-8846(01)00516-6).
- [6] C. Alonso, L. Fernandez, Dehydration and rehydration processes of cement paste exposed to high temperature environments, *J. Mater. Sci.* 39 (2004) 3015–3024. <https://doi.org/10.1023/B:JMISC.0000025827.65956.18>.
- [7] D.A.S. Rambo, A. Blanco, A.D. de Figueiredo, E.R.F. dos Santos, R.D. Toledo, O. da F.M. Gomes, Study of temperature effect on macro-synthetic fiber reinforced concretes by means of Barcelona tests: An approach focused on

- tunnels assessment, *Constr. Build. Mater.* 158 (2018) 443–453. <https://doi.org/10.1016/j.conbuildmat.2017.10.046>.
- [8] ASTM C 1609, Standard Test Method for Flexural Performance of Fiber-Reinforced Concrete (Using Beam With Third-Point Loading), ASTM Stand. (2012). <https://doi.org/10.1038/nmat3099>.
- [9] EN 14651, Test method for metallic fibred concrete — Measuring the flexural tensile strength (limit of proportionality (LOP), residual), United Kingdom, 2007.
- [10] E. Galeote, A. Blanco, S.H.P. Cavalaro, A. de la Fuente, Correlation between the Barcelona test and the bending test in fibre reinforced concrete, *Constr. Build. Mater.* 152 (2017) 529–538. <https://doi.org/10.1016/j.conbuildmat.2017.07.028>.
- [11] E.S. Bernard, Predicting crack widths in FRC/reinforced concrete members using small deformation post-crack parameters, *Struct. Concr.* 20 (2019) 2138–2149. <https://doi.org/10.1002/suco.201900083>.
- [12] M. di Prisco, G. Plizzari, L. Vandewalle, Fiber Reinforced Concrete in the New fib Model Code, in: 3rd Fib Int. Congr. Inc. PCI Annu. Conv. Bridg. Conf. 2010, Precast prestressed concrete institute, Chicago, IL, USA, 2010.
- [13] L.A.C. Borges, R. Monte, D.A.S. Rambo, A.D. de Figueiredo, Evaluation of post-cracking behavior of fiber reinforced concrete using indirect tension test, *Constr. Build. Mater.* 204 (2019) 510–519. <https://doi.org/10.1016/j.conbuildmat.2019.01.158>.
- [14] M. di Prisco, L. Ferrara, M.G.L. Lamperti, Double edge wedge splitting (DEWS): an indirect tension test to identify post-cracking behaviour of fibre reinforced cementitious composites, *Mater. Struct.* 46 (2013) 1893–1918. <https://doi.org/10.1617/s11527-013-0028-2>.
- [15] K. Scrivener, R. Snellings, B. Lothenbach, *A Practical Guide to Microstructural Analysis of Cementitious Materials*, CRC Press, 2017.
- [16] R. Serafini, S.R.A. Dantas, R.P. Salvador, R.R. Agra, D.A.S. Rambo, A.F. Berto, A.D. de Figueiredo, Influence of fire on temperature gradient and physical-mechanical properties of macro-synthetic fiber reinforced concrete for tunnel linings, *Constr. Build. Mater.* 214 (2019) 254–268. <https://doi.org/10.1016/j.conbuildmat.2019.04.133>.
- [17] T.S. Ng, T.N.S. Htut, Structural application of steel fibres reinforced concrete with and without conventional reinforcement, in: *New Zeal. Concr. Ind.*, 2017.

- [18] A. de la Fuente, P. Pujadas, A. Blanco, A. Aguado, Experiences in Barcelona with the use of fibres in segmental linings, *Tunn. Undergr. Sp. Technol.* (2012). <https://doi.org/10.1016/j.tust.2011.07.001>.
- [19] J.M. Carpio, R. Serafini, D. Rambo, A. de la Fuente, A.D. De Figueiredo, Assessment of the bearing capacity reduction of FRC elements subjected to fire, in: *Proc. Fib Symp. 2019 Concr. - Innov. Mater. Des. Struct.*, Kraków, Poland, 2019: pp. 1378–1386.
- [20] W. de O. Bussab, P.A. Morettin, *Estatística básica*, Saraivauni, São Paulo, 2017.
- [21] L.T. Phan, Pore pressure and explosive spalling in concrete, *Mater. Struct.* 41 (2008) 1623–1632. <https://doi.org/10.1617/s11527-008-9353-2>.
- [22] R. Serafini, L.M. Mendes, R.P. Salvador, A.D. de Figueiredo, The effect of elevated temperatures on the properties of cold-drawn steel fibers, *Mag. Concr. Res.* (2020) 1–28. <https://doi.org/10.1680/jmacr.19.00498>.
- [23] A. Lau, M. Anson, Effect of high temperatures on high performance steel fibre reinforced concrete, *Cem. Concr. Res.* 36 (2006) 1698–1707. <https://doi.org/10.1016/j.cemconres.2006.03.024>.
- [24] B. Chen, J. Liu, Residual strength of hybrid-fiber-reinforced high-strength concrete after exposure to high temperatures, *Cem. Concr. Res.* 34 (2004) 1065–1069. <https://doi.org/10.1016/j.cemconres.2003.11.010>.
- [25] W. Zheng, H. Li, Y. Wang, Compressive stress–strain relationship of steel fiber-reinforced reactive powder concrete after exposure to elevated temperatures, *Constr. Build. Mater.* 35 (2012) 931–940. <https://doi.org/10.1016/j.conbuildmat.2012.05.031>.
- [26] Z.P. Bažant, M.F. Kaplan, *Concrete at high temperatures: material properties and mathematical models*, Longman, 1996.
- [27] BS EN 1992-1-2, Eurocode 2 Design of concrete structures - Part 1-2: General rules-Structural fire design, *Des. Concr. Struct. - Part 1-2 Gen. Rules-Structural Fire Des.* (2004).
- [28] S.L. Suhaendi, T. Horiguchi, Effect of short fibers on residual permeability and mechanical properties of hybrid fibre reinforced high strength concrete after heat exposition, *Cem. Concr. Res.* 36 (2006) 1672–1678. <https://doi.org/10.1016/j.cemconres.2006.05.006>.
- [29] M. Colombo, M. di Prisco, R. Felicetti, Mechanical properties of steel fibre reinforced concrete exposed at high temperatures, *Mater. Struct.* 43 (2010)

- 475–491. <https://doi.org/10.1617/s11527-009-9504-0>.
- [30] S. Abdallah, M. Fan, D.W.A. Rees, Effect of elevated temperature on pull-out behaviour of 4DH/5DH hooked end steel fibres, *Compos. Struct.* 165 (2017) 180–191. <https://doi.org/https://doi.org/10.1016/j.compstruct.2017.01.005>.
- [31] S. Abdallah, M. Fan, K.A. Cashell, Pull-out behaviour of straight and hooked-end steel fibres under elevated temperatures, *Cem. Concr. Res.* 95 (2017) 132–140. <https://doi.org/10.1016/j.cemconres.2017.02.010>.
- [32] G. Ruano, F. Isla, B. Luccioni, R. Zerbino, G. Giaccio, Steel fibers pull-out after exposure to high temperatures and its contribution to the residual mechanical behavior of high strength concrete, *Constr. Build. Mater.* 163 (2018) 571–585. <https://doi.org/10.1016/j.conbuildmat.2017.12.129>.
- [33] R. Serafini, S.R.A. Dantas, D.A.S. Rambo, A.D. de Figueiredo, Pull-out response of steel fiber reinforced concretes exposed to elevated temperatures, in: *Proc. Seventh Int. Colloq. Performance, Prot. Strength. Struct. under Extrem. Load. Events*, The University of British Columbia, Whistler, Canada, 2019: pp. 614–621.
- [34] Federation Internationale du Beton, Model Code for Concrete Structures 2010, in: Ernst & Sohn, Germany, 2013: p. 434.
- [35] D. Choumanidis, E. Badogiannis, P. Nomikos, A. Sofianos, Barcelona test for the evaluation of the mechanical properties of single and hybrid FRC, exposed to elevated temperature, *Constr. Build. Mater.* 138 (2017) 296–305. <https://doi.org/10.1016/j.conbuildmat.2017.01.115>.
- [36] CNR-DT 204, Guide for the Design and Construction of Fibre-Reinforced Concrete Structures, Ital. Natl. Res. Counc. (CNR), Rome, Italy. (2007). <https://doi.org/10.14359/10516>.
- [37] F.B. Varona, F.J. Baeza, D. Bru, S. Ivorra, Influence of high temperature on the mechanical properties of hybrid fibre reinforced normal and high strength concrete, *Constr. Build. Mater.* 159 (2018) 73–82. <https://doi.org/10.1016/j.conbuildmat.2017.10.129>.
- [38] D. Choumanidis, E. Badogiannis, P. Nomikos, A. Sofianos, The effect of different fibres on the flexural behaviour of concrete exposed to normal and elevated temperatures, *Constr. Build. Mater.* 129 (2016) 266–277. <https://doi.org/10.1016/j.conbuildmat.2016.10.089>.
- [39] M. Colombo, M. di Prisco, R. Felicetti, SFRC exposed to high temperature: Hot vs. residual characterization for thin walled elements, *Cem. Concr.*

- Compos. 58 (2015) 81–94. <https://doi.org/10.1016/j.cemconcomp.2015.01.002>.
- [40] C. Soranakom, B. Mobasher, Correlation of tensile and flexural responses of strain softening and strain hardening cement composites, *Cem. Concr. Compos.* 30 (2008) 465–477. <https://doi.org/10.1016/j.cemconcomp.2008.01.007>.
- [41] F. Di Carlo, A. Meda, Z. Rinaldi, Evaluation of the bearing capacity of fiber reinforced concrete sections under fire exposure, *Mater. Struct.* 51 (2018) 154. <https://doi.org/10.1617/s11527-018-1280-2>.
- [42] R.P. Salvador, S.H.P. Cavalaro, I. Segura, A.D. Figueiredo, J. Pérez, Early age hydration of cement pastes with alkaline and alkali-free accelerators for sprayed concrete, *Constr. Build. Mater.* 111 (2016) 386–398. <https://doi.org/10.1016/j.conbuildmat.2016.02.101>.
- [43] N.N. Skoblinskaya, K.G. Krasilnikov, Changes in crystal structure of ettringite on dehydration. 1, *Cem. Concr. Res.* 5 (1975) 381–393. [https://doi.org/10.1016/0008-8846\(75\)90093-9](https://doi.org/10.1016/0008-8846(75)90093-9).
- [44] N.N. Skoblinskaya, K.G. Krasilnikov, L.V. Nikitina, V.P. Varlamov, Changes in crystal structure of ettringite on dehydration. 2, *Cem. Concr. Res.* 5 (1975) 419–431. [https://doi.org/10.1016/0008-8846\(75\)90017-4](https://doi.org/10.1016/0008-8846(75)90017-4).
- [45] Q. Zhou, F.P. Glasser, Thermal stability and decomposition mechanisms of ettringite at $<120^{\circ}\text{C}$, *Cem. Concr. Res.* 31 (2001) 1333–1339. [https://doi.org/10.1016/S0008-8846\(01\)00558-0](https://doi.org/10.1016/S0008-8846(01)00558-0).
- [46] E. Tajuelo Rodriguez, K. Garbev, D. Merz, L. Black, I.G. Richardson, Thermal stability of C-S-H phases and applicability of Richardson and Groves' and Richardson C-(A)-S-H(I) models to synthetic C-S-H, *Cem. Concr. Res.* 93 (2017) 45–56. <https://doi.org/10.1016/j.cemconres.2016.12.005>.
- [47] P. Yu, R.J. Kirkpatrick, Thermal dehydration of tobermorite and jennite, *Concr. Sci. Eng.* 97 (2012) 117–119.
- [48] W.M. Haynes, *CRC handbook of chemistry and physics*, 95th ed., CRC Press, Boca Raton, FL, 2015.

ARTICLE D

Title: Design-oriented assessment of the residual post-fire bearing capacity of precast fiber reinforced concrete tunnel linings

Submit to: Fire Safety Journal

Publication date: Not assigned.

Status: Under review.

DESIGN-ORIENTED ASSESSMENT OF THE RESIDUAL POST-FIRE BEARING
CAPACITY OF PRECAST FIBER REINFORCED CONCRETE TUNNEL
LININGS

Ramoel Serafini^{1,2*}, Sérgio R. A. Dantas^{1,2}, Ronney R. Agra^{1,2}, Albert de
la Fuente³, Antonio F. Berto², Antonio D. de Figueiredo¹

¹Department of Civil Construction Engineering, Polytechnic School of the University of São Paulo |
Avenida Professor Almeida Prado, Travessa 2, 83, 05424-970, São Paulo, Brazil.

² Institute of Technological Research | Avenida Professor Almeida Prado, 532, 05508-901, São Paulo,
Brazil

³ Department of Civil and Environmental Engineering, Polytechnic University of Catalonia | Jordi
Girona, 1-3, 08034, Barcelona, Spain

*corresponding author: rserafini@usp.br

Keywords: fire; tunnel lining; steel fiber reinforced concrete; bearing capacity;
numerical simulation.

ABSTRACT

This study presents a meso-scale experimental program and employs a numerical approach to determine the bearing capacity of steel fiber reinforced concretes (SFRC) tunnel linings after fire exposure. First, the effect of temperature on the mechanical properties of SFRC was determined through a refined experimental campaign. Additionally, the suitability of the bending test and the DEWS test to assess the post-fire tensile properties of the SFRC was verified. Then, a thermo-mechanical model was implemented to assess the changes in the bearing capacity of SFRC for tunnels built with TBM technology. Results show that the thermo-mechanical model

properly estimated the temperature distribution and the mechanical properties as a function of the duration of fire (t) and depth (z). The bearing capacity of the SFRC segments exposed to the ISO 834 and HFC fire curves were comparable when the condition $t_{ISO} = 2 t_{HFC}$ was satisfied. Additionally, a greater bearing capacity reduction was numerically observed when the compressive region of the cross-section is affected by fire. The results obtained aid in the definition of appropriate rehabilitation operations, classifying the degree of damage sustained by the structure, and provides a tool for designers regarding the effect of fire on SFRC structures.

1 Introduction

Tunnel structures are key infrastructure elements that aim to facilitate the mobility of people and goods in modern civilization in which investments may be linked to the reduction in social inequality [1,2]. In the last decades, the production of precast segments for tunnels benefited greatly from the use of discrete steel fibers as partial or total substitution to the conventional rebars in reinforced concrete (RC) [3,4]. The major benefits are related to the improved economic competitiveness, efficiency, and corrosion resistance provided by the steel fibers [5,6]. In this context, the investigation of the damage imposed by fire on steel fiber reinforced concretes (SFRC) is a topic that requires attention from the scientific community.

In this sense, special attention must be given to fire events in tunnel structures since these events may cause social and structural damage. The reduced compartment dimensions and unfavorable ventilation conditions of these structures result in aggravated fire events with severe heating rates and greater temperature values than a surface fire [7]. Therefore, the investigation of the fire safety of tunnels has been driven by the unquantifiable cost associated with the loss of human lives and the high social and economic costs due to the repair and temporary closure of tunnels.

The majority of the mesoscale studies regarding SFRC under high temperature have focused on the evaluation of the compressive strength (f_c), elastic modulus (E_c), and tensile strength (f_{Ft}) of the composite [8–15]. Results show that the increase in temperature tends to negatively affect the compressive and elastic properties of the SFRC, although the increase in fiber content mitigates the reductions in f_c [10]. The reductions in f_{Ft} are comparable to those suffered by plain concrete [13–15], which occurs because the steel fibers are not engaged before the matrix cracks. A

considerable lack of studies focused on the evaluation of the post-crack design parameters was found in literature, which is required to determine the bearing capacity of SFRC under fire exposure [16]. These parameters are key factors for the current analytical and numerical models employed for the design of tunnel linings [17,18].

Although several progenitive full-scale experimental campaigns and numerical models have been developed for RC tunnel linings under fire [19–21], the studies related to SFRC tunnel linings are scarce in literature. A study published by Yan et al. [22] exposed a SFRC pre-cast segment to the hydrocarbon fire curve (HFC) and evaluated the influence of the loading conditions and the presence of lining joints in the global fire performance of the segments. Di Carlo et al. [23] proposed a numerical approach to assess the bearing capacity of SFRC precast segments based on a staggered analysis that detaches the thermal problem from the mechanical one. The model proposed determines the bearing capacity of the SFRC by calculating the distribution of mechanical properties in the cross-section considering a stress-block constitutive law, the temperature-dependent constitutive equation of SFRC, and the translational and the rotational equilibrium conditions.

In this context, the basic concept underlying this study was to propose a meso-scale experimental program and employ a numerical approach to determine the bearing capacity of tunnel linings during a fire event. A comprehensive experimental investigation was conducted aiming to determine the mechanical behavior of the SFRC after exposure to target temperatures. Later, the temperature distribution and mechanical changes in SFRC as a function of the depth in order to determine the contribution of the material to the bearing capacity of the segments. The post-crack design parameters of SFRC were determined for target temperatures ranging between 150 and 750 °C by means of the Double Edge Wedge Splitting (DEWS) test. Moreover, the classical bending test and the DEWS test were evaluated regarding their applicability for the post-fire evaluation of the SFRC. The experimental and numerical analyses were used to characterize the post-crack behavior of SFRC under fire exposure.

The experimental results were employed as input parameters for a thermo-mechanical numerical model to assess the bearing capacity of a SFRC tunnel. The

aforementioned assessment was conducted based on the design parameters of a tunnel to be executed in the city of São Paulo (Brazil). Therefore, the experimental and numerical approach used in this study may serve as a designing tool to determine the structural safety of a tunnel affected by fire, while also providing resources to determine an adequate rehabilitation procedure.

2 Materials and methods

Figure 1 illustrates the scheme adopted for the experimental program and numerical investigation. The experimental campaign was conducted using two different heating procedures. Oven-heated specimens were employed to assess the mechanical properties at target temperatures and the chemical/mineralogical changes ranging between 150 °C and 750 °C, while specimens exposed to fire were used to assess the temperature distribution as a function of time and the post-fire bearing capacity of the SFRC. This paper is part of a Ph.D. research project that aims to evaluate the effect of fire on SFRC structures. Therefore, a detailed description of the materials can be found at Serafini et al. [24]. For the convenience of the reader, a brief description of the materials used in this research is provided.

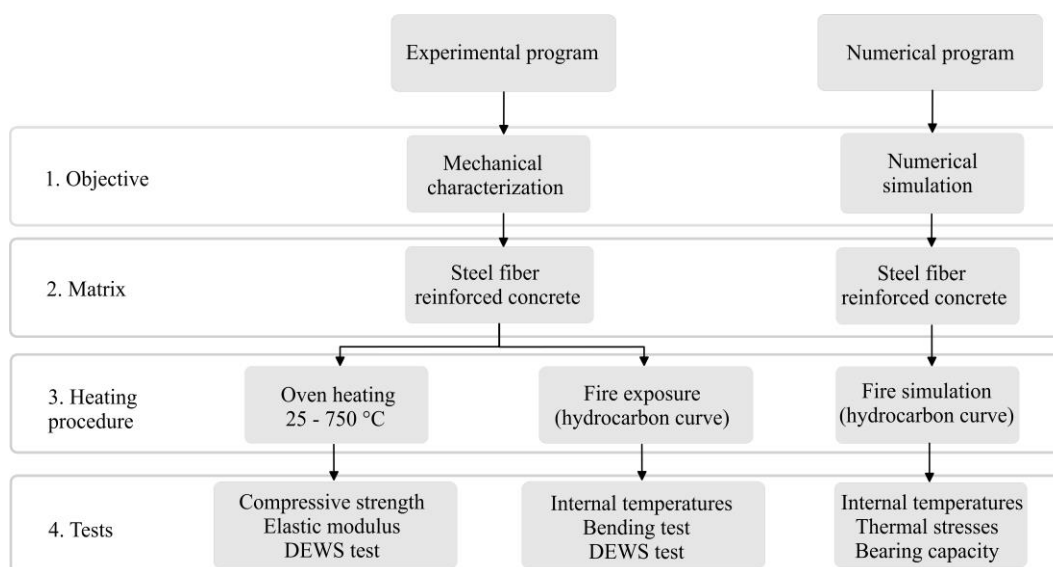


Figure 1 – Scheme adopted for the experimental and numerical programs

2.1 Materials

A cement type CEM I 52.5R and silica fume (98% SiO₂) were used as cementitious materials. River and artificial sand and two coarse granite aggregates were used to increase the particle packing and a polycarboxylate-based superplasticizer was used to provide workability to the mix. The concrete matrix was reinforced using a

commercial hooked-end steel fiber. Polypropylene microfibers were added to the mix to minimize the risk of explosive spalling during the fire test. Table 1 shows the data provided by the manufacturers for both fiber types.

Table 1 – Data provided by the manufacturers for both fiber types

Characteristics	Hooked-end steel fiber	Micro-synthetic fiber
Length (mm)	60	12
Diameter (mm)	0.75	0.03
Aspect ratio (l/d)	80	Not provided
Specific weight (kg/m ³)	7850	910
Specific surface area (m ² /kg)	Not provided	147
Melting point (°C)	Not provided	165
Tensile strength (MPa)	1225	Not provided
Young modulus (GPa)	200	Not provided

2.2 Composition and preparation of SFRC

The SFRC mix design adopted was as close as possible to the concrete mix used in the construction of the Subway Line 6 of the city of São Paulo, Brazil (see Table 2). Contrary to real production conditions, no heat curing was employed for the SFRC due to the technical limitations on a laboratory scale. The steel fiber content adopted was 0.45% of total volume, which aimed to guarantee a minimum flexural bearing capacity, ductility, and crack control for the TBM jack's thrust phase [24]. The micro-synthetic fiber content was kept at 0.09% of total volume to mitigate the occurrence of explosive spalling.

Table 2 – Materials necessary to fabricate one cubic meter of SFRC

Materials	Dosage (kg/m ³)
Cement CEM I 52.5R	400
Silica fume	22
Water	165
Siliceous river sand	403
Artificial granite sand	269
Coarse granite aggregate - d _{max} : 19 mm	770
Coarse granite aggregate - d _{max} : 9.5 mm	330
Superplasticizer	3
Micro-synthetic fiber – anti-spalling	0.80
Hooked-end steel fiber	35

The preparation of concrete followed the same methodology presented by Serafini et al. [24]. In the fresh state, the SFRC presented a specific weight of (2430 ± 52) kg/m³ and a slump value of (50 ± 10) mm. During the casting procedure, thermocouples type K were inserted in one of the prismatic specimens in preset depths of 3, 6, 9, 12,

and 15 cm from the surface exposed to fire. A total of 30 cylindrical specimens ($\text{O}100 \times 200 \text{ mm}$) and 20 prismatic specimens ($150 \times 150 \times 550 \text{ mm}$) were cast, the latter being 7 prismatic specimens for bending test and 13 prismatic specimens that were cut into cubes ($150 \times 150 \text{ mm}$) for the DEWS test. The specimens were cured in a saturated room for the first 72 h after demolding, and later stored at room conditions ($25 \pm 1 \text{ }^\circ\text{C}$) until the age of 150 days.

2.3 Heating procedures

2.3.1 Oven heating

An electric oven with maximum temperature capacity of $1000 \text{ }^\circ\text{C}$ and fix heating rate of $(12 \pm 2) \text{ }^\circ\text{C}/\text{min}$ was employed to heat cubic and cylindrical specimens. Specimens were heated at the temperatures of 150, 300, 450, 600, and $750 \text{ }^\circ\text{C}$ and kept at each temperature during 10, 8, 6, 4, and 4 h, respectively. The duration of the sustained thermal load was determined by numerical simulation based on the work of Carpio et al. [25] and had the objective to ensure uniform temperature of the specimens. After the heat exposure, the chamber was kept closed and cooling occurred during 24 h. Specimens that were not subjected to heating were used for comparative purposes.

2.3.2 Fire exposure

The exposure of specimens to fire was conducted in a vertical fire simulator at the Laboratory of Explosion and Fire Safety (LSFEx) from the Institute of Technological Research (IPT). A more detailed description and illustration of the equipment and the procedure adopted for the test is described in Serafini et al. [24]. A total of eight prismatic specimens were positioned on a masonry structural wall and a single-face fire exposure was induced. The heat regime adopted was the hydrocarbon fire curve (HFC), following the recommended curves for underground structures [26]. Figure 2 shows the HFC compared to the experimental fire curve obtained in this study. The fire test was kept during 120 min and the chamber was kept closed during 24 h for the cooling of specimens after the fire test was finished. During the fire exposure, the temperature inside the SFRC was recorded by thermocouples connected to a data acquisition system every 30 s.

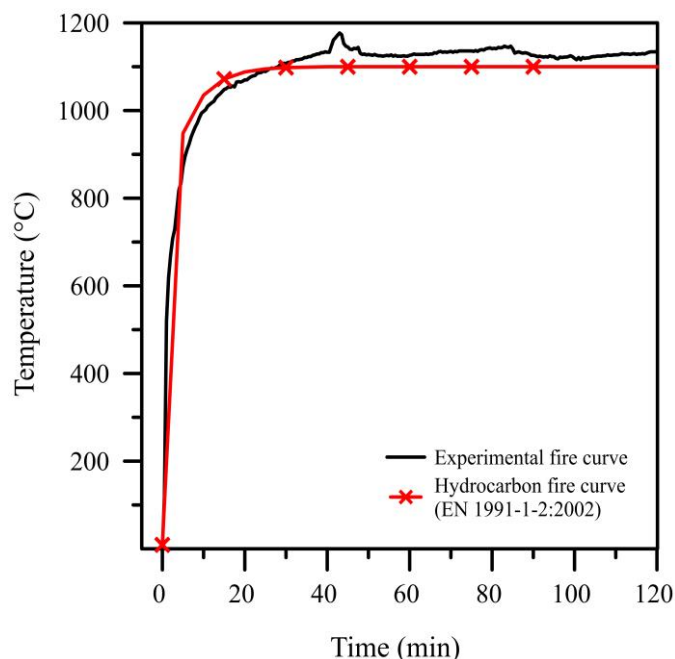


Figure 2 – Comparison between the HFC and the experimental fire curve

2.4 Mechanical characterization

Table 3 summarizes the mechanical tests performed in the experimental program. All the tests for mechanical characterization were conducted with specimens in post-cooling conditions. Analysis of variances (ANOVA) and Tukey tests were employed to evaluate the experimental results statistically.

Table 3 – Summary of the mechanical tests conducted

Test	Property	Specimen type	Heating procedure	Quantity
Compressive test	Compressive strength	Cylindrical	Oven heated $25 \leq T \leq 750 \text{ } ^\circ\text{C}$	30
	Elastic modulus	Cylindrical	Oven heated $25 \leq T \leq 750 \text{ } ^\circ\text{C}$	
DEWS test	Tensile properties	Cubic	Oven heated $25 \leq T \leq 750 \text{ } ^\circ\text{C}$	30
	Tensile properties	Cubic	Fire test (HFC)	8
Bending test	Tensile properties	Prismatic	Fire test (HFC)	7

2.4.1 Compressive strength and elastic modulus

The compressive strength (f_c) and elastic modulus (E_c) of the SFRC were determined following the procedure presented by Serafini et al. [24]. A total of thirty specimens

were evaluated, being five for each target temperature. The compressive and elastic properties were not determined for specimens exposed to the fire test due to the wide range of mechanical properties induced by the unifacial heat exposure. Also, the occurrence of crushing and grinding on the surface directly exposed to fire would compromise the results obtained.

2.4.2 Three-point bending test

The bending tests were performed in a servo-hydraulic universal testing machine, INSTRON 8802, with a load cell of 250 kN and in closed-loop configuration. The Crack Mouth Opening Displacement (CMOD) was controlled in accordance with the rates defined by the EN 14651 standard [27] and the methodology provided by Serafini et al. [24] using a knife-edge clip-gauge with maximum length of 4 mm. The flexural strength (f_j) for each given CMOD was calculated as:

$$f_j = \frac{3F_j \cdot l}{2bh_{sp}^2} \quad (1)$$

where F_j is load at a given CMOD (in N); l is the span (in mm); b is the width of the specimen (in mm); and h_{sp} is the distance between the tip of the notch and the top of the specimen (in mm). The results obtained by the prismatic specimens at room temperature are also verified according to the procedure presented by the *fib* Model Code [28] regarding the verifications for the SFRC to be considered a structural material.

A total of seven prismatic specimens were tested under bending, being three SFRC prismatic specimens taken as reference and four prismatic specimens tested after fire exposure. The fire-exposed specimens were positioned in a way that the flexural tensile stresses were generated in the region closer to the fire (see Fig. 3). This setup was adopted to reduce the punching interaction in the region affected by fire, which also mitigates the occurrence of crushing and grinding interactions.



Figure 3 – The three-point bending test setup for specimens exposed to fire

2.4.3 Double Edge Wedge Splitting (DEWS) test

The DEWS test was employed to assess the tensile properties of oven-heated and fire exposed cubic specimens. The test was performed following the simplified methodology presented by Borges et al. [29]. Cubic specimens with sides measuring 150 mm were produced by cutting the prismatic specimens. Since a mode I fracture is induced during the DEWS test, the influence of crushing or grinding of concrete during the test may be considered negligible [30].

The removal of cubic specimens and execution of the grooves/notches were conducted before the heating procedure for oven-heated specimens and after the heat procedure for fire-exposed specimens. This difference was adopted to mitigate the influence of lateral heating during the fire test, which is discussed in detail in Serafini et al. [24]. For the fire-exposed specimens, the triangular grooves were cut along two opposite sides of the cubes in the face positioned 90° from the face exposed to fire and respecting the same orientation as the oven-heated specimens. Figure 4 illustrates the DEWS test setup for specimens exposed to fire.

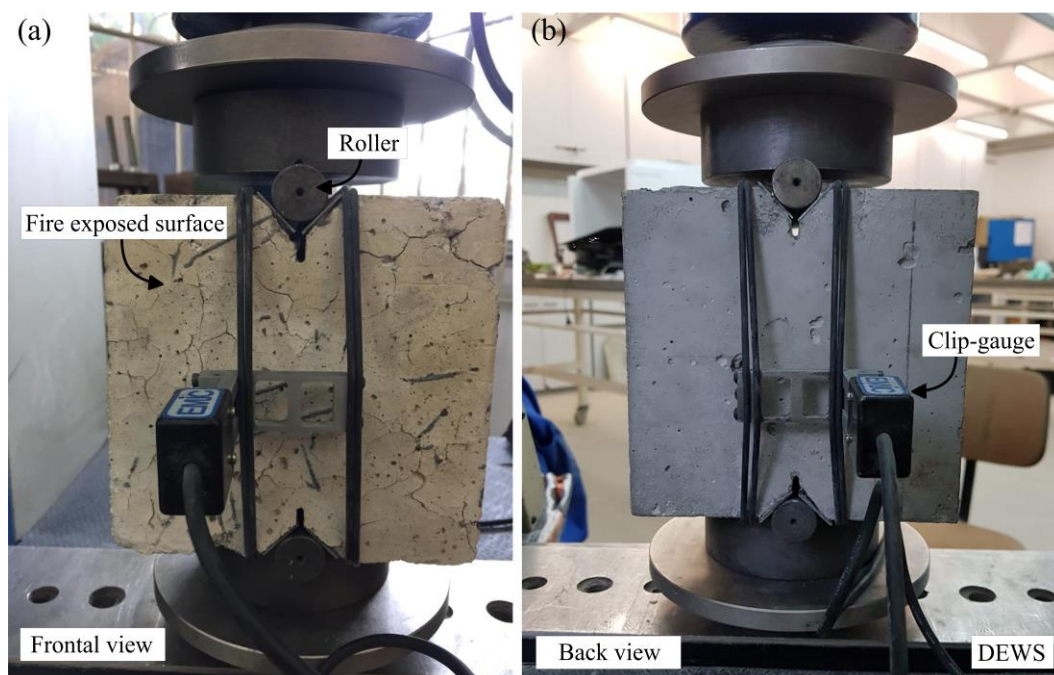


Figure 4 – The (a) frontal view and (b) back view of the DEWS test setup for specimens exposed to fire

Steel plates with thickness of 0.9 mm were glued to the surface of the grooves and graphite powder was used to lubricate the contact between the roller and the plates. This procedure results in reduced frictional interaction in the roller-specimen contact [31]. The tensile strength of the matrix (f_{Ft}) and the post-crack tensile strengths related to serviceability (f_{Fts}) and the ultimate limit state (f_{Ftu}) were determined based on the results. The crack-opening displacement (COD) of 0.25 and 1.25 mm were adopted to determine the f_{Fts} and f_{Ftu} values since they are representative of the serviceability (SLS) and ultimate limit state (ULS) conditions [29]. A total of five prismatic specimens were employed for each target temperature in the oven-heated scenario, while eight cubic specimens were employed for the post-fire scenario.

2.4.4 Coefficient of mechanical degradation

The coefficient of mechanical degradation is a factor calculated based on experimental results that can be applied to reduce the bearing capacity of the layers of SFRC in a structure, as described by the Italian guideline CNR-DT 204 [32]. This coefficient has a particular use for the assessment of fiber reinforced concrete structures by means of cross-sectional analysis [32,33]. The results obtained during the mechanical characterization of oven-heated specimens were used to calculate the coefficient of mechanical degradation for the compressive strength (K_c), tensile

strength (K_{Ft}), elastic modulus (K_{Ec}), and the post-crack tensile strength relative to a COD of 1.25 mm (K_{Ftu}).

The oven-heated results of K_c and K_{Ftu} were chosen to be analyzed since they represent the most important parameters at the ULS condition for SFRC structures. In this sense, the oven-heated results of K_c and K_{Ftu} were paired with the internal temperature distribution calculated by the thermal model to estimate the differential damage due to fire as a function of z and t . The results obtained were compared to the results employing the analytical curve proposed by the Italian guideline CNR-DT 204 [32].

2.5 Numerical simulation

The numerical model first developed by Di Carlo et al. [23] and later reproduced and refined by Carpio et al. [34] was employed. The main aspects related to the numerical model employed are briefly discussed in this paper for the convenience of the reader.

The exposure of concrete to a fire event results in a non-linear distribution of temperatures and affects the physical, thermal, and mechanical properties of the material. In this context, the numerical model solves the thermal problem by means of finite difference method (FDM) applied to the Fourier heat transfer equation. The net heat flux transferred from the fire source to the SFRC surface is determined considering the heat transferred by convection and radiation. The changes in specific heat, density, and thermal conductivity as a function of temperature followed the constitutive equations presented in the EN 1992-1-2:2004 [33].

The thermal model calculates the temperature distribution as a function of time inside the SFRC cross-section, which serves as input for the mechanical problem. Thus, the numerical model adopts a staggered analysis that detaches the thermal problem from the mechanical one. The mechanical problem is solved by considering the temperature-dependent constitutive equation of the material. The stress-strain distribution in the cross-section was calculated based on the non-compliance between the thermal strains and the kinematic requirements of the total strain field imposed by the Navier-Bernoulli hypothesis, as described in detail in Carpio et al. [34]. Lastly, the bearing capacity of the SFRC specimens was evaluated by calculating the distribution of compressive and tensile strength in the cross-section considering a stress-block constitutive law, the temperature-dependent constitutive equation of

SFRC, and the translational and the rotational equilibrium conditions as shown by Di Carlo et al. [23].

The numerical simulation was conducted considering a SFRC density of 2400 kg.m^{-3} , specific heat of $900 \text{ J.kg}^{-1}.\text{K}^{-1}$, thermal conductivity of $1.2 \text{ W.m}^{-1}.\text{K}^{-1}$, emissivity of 0.9, convective coefficient of $25 \text{ W.m}^{-2}.\text{K}^{-1}$, initial temperature of $20 \text{ }^\circ\text{C}$, and a specimen height of 150 mm. Also, the mechanical properties of the SFRC were inputted as $f_c = 83.9 \text{ MPa}$, $f_{LOP} = 6 \text{ MPa}$, $f_{RI} = 4.3 \text{ MPa}$, and $f_{RS} = 3.0 \text{ MPa}$. The average values were used in this simulation in order to better represent the behavior of the material in the meso-scale, and are not employed for design purposes. Moreover, the experimental values of K_c and K_{Ft} were used as input and linearly interpolated in during the numerical simulation. The fire simulation was conducted considering the HFC with the heating procedure applied to the bottom side of the specimen. The aforementioned values and procedures were adopted aiming to better simulate the concrete experimentally tested in this study.

3 Results and discussion

3.1 Oven-heated mechanical properties

Figure 5 shows the coefficients of mechanical degradation for the compressive and tensile properties compared to European standards. The SFRC produced had a f_c of $(83.9 \pm 0.6) \text{ MPa}$ and an E_c of $(36.3 \pm 0.5) \text{ GPa}$ at the age of 150 days. In the temperature range between 150 and $750 \text{ }^\circ\text{C}$, the f_c reduced between 6.3% and 97.7%, while the E_c reduced between 24.6% and 99.7% when compared to room temperature results. The K_c and K_{Ec} values obtained in this study were significantly lower than the values presented by the Eurocode, which may be a result of the increased porosity due to the ignition of micro-synthetic fibers and to differences in the heat regimes employed. Even with those considerations, the K_c and K_{Ec} values are in line with similar studies found in literature [35–37].

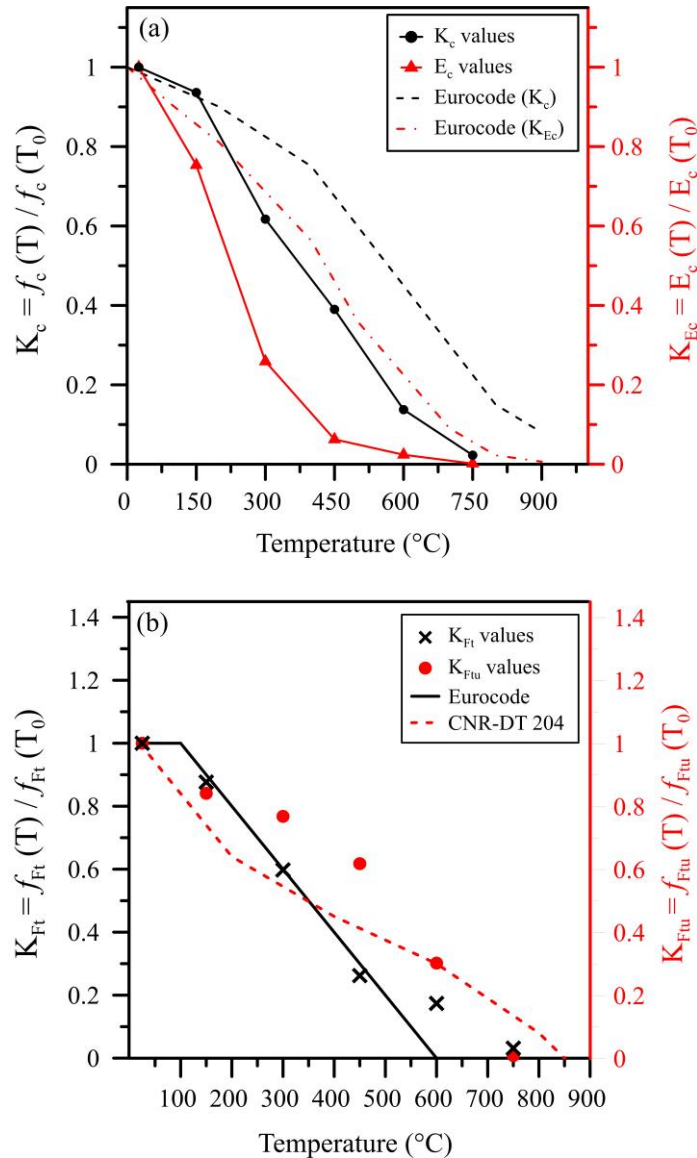


Figure 5 – Coefficients of mechanical degradation for the (a) compressive and (b) tensile properties compared to European standards

A severe reduction in E_c between the temperatures of 150 and 450 °C was observed, which may be attributed to changes in the volume of solids associated to the changes in the pore structure of the matrix [38], the degradation of micro-synthetic fibers [24], and changes in the porosity of aggregates [39]. These factors are also summed to the micro-crack formation in the interfacial transition zone between aggregates and the matrix and the considerable dehydration of hydrated products, which are known to influence the f_c and E_c of the composite [39].

In the temperature range between 150 and 750 °C, the f_{ft} reduced between 12.3% and 96.8% and the f_{ftu} reduced between 15.9% and 99.2% when compared to room temperature results. For temperatures up to ~450 °C the reductions in f_{ft} were more drastic than those in f_{ftu} . This difference arises from the considerable effect imposed

by the dehydration of the cement paste and the thermal-induced cracks on the f_{Ft} [39], while the f_{Ftu} is governed by the bond-slip mechanism of the steel fibers. Therefore, the reductions in terms of f_{Ftu} tend to be lower than those obtained for f_{Ft} , especially since the bond-slip mechanism of steel fibers is not significantly affected up to ~ 400 °C [40–44]. Additionally, the K_{Ft} and K_{Ftu} results agree well with the curve presented by the Italian guideline, CNR-DT 204 [32], as well as with the results obtained by bending tests in literature for a similar class of SFRC [45–47].

3.2 Post-fire results

3.2.1 Qualitative physical evaluation

Figure 6 illustrates the physical changes that occurred on the prismatic specimens after fire exposure. The occurrence of explosive spalling was not verified in any of the specimens tested in this study, which may be attributed to the presence of micro-synthetic fibers in the concrete mix, as also observed by other researchers in literature [48,49]. Moreover, the average mass loss of SFRC prismatic specimens after fire exposure was of 5.7%, which agrees well with literature results since the amount of mass loss of siliceous concretes is relatively low, even for temperatures beyond ~ 600 °C [50,51].

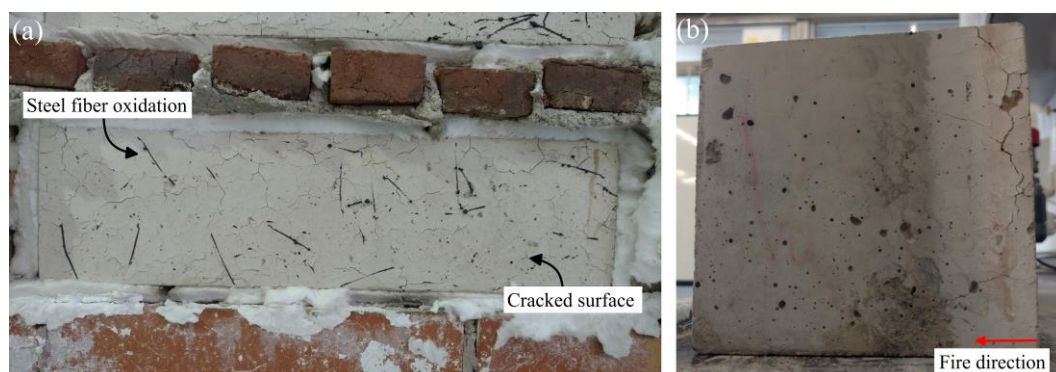


Figure 6 – Physical changes that occurred on the prismatic SFRC specimen after fire exposure

The visual inspection showed the formation of an oxide surrounding the steel fibers that were closer to the fire source. This oxide formation occurs because the oxidizing nature of the atmosphere favors the combination between oxygen and iron at high temperatures. This oxidation process results in the formation of a three-layered scale structure that is friable and does not bring meaningful contribution to the mechanical properties of steel [52,53]. Also, the oxidation of steel fibers increases the total diameter of the fiber (oxide + steel) at the expense of a reduction in the effective cross-sectional area for temperatures greater than ~ 750 °C [54]. Additionally, an

extensive crack network may be verified in the specimens. The extensive cracking verified is a result of the temperature-related deterioration and the non-uniform thermal related stresses generated by fire exposure [39]. Also, the more pronounced formation of cracks closer to the surface affected by fire may be attributed to the elevated temperatures recorded and the consequent degradation of the material.

3.2.2 Internal temperature distribution

Figure 7 shows the experimental and numerical results for the internal temperature distribution in the SFRC as a function of z and t . It is possible to observe that the temperature inside the composite increases drastically for reduced values of z and greater values of t . The temperature readings inside the SFRC have recorded maximum values of 612, 403, 212, 141, and 112 °C for the z values of 3, 6, 9, 12, and 15 cm at $t = 120$ min. In this sense, a wide range of temperatures is generated in the inner layers due to the low thermal conductivity of the composite, which is known to reduce even further with the increase in temperature [51,55]. Moreover, the experimental temperature readings as a function of z and t show good agreement with the thermal model implemented.

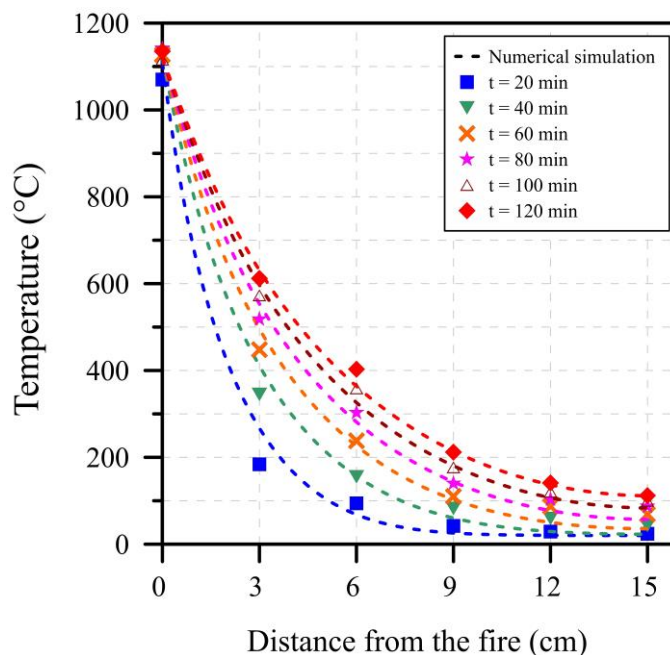


Figure 7 – Experimental and numerical results for the internal temperature distribution in the SFRC

The wide range of temperatures inside the SFRC resulted in a non-linear distribution of thermal strains that do not comply with the kinematic requirements of the total strain field. This strain incompatibility generated compressive stresses at $z = 150$ mm and $z = 0$ mm, while tensile stresses arise in the central portion of the SFRC (see

Fig. 8). At $z = 0$ mm, the compressive stresses reduce with the duration of fire due to the more rapid loss of mechanical strength caused by fire. The maximum compressive stress value of ~ 48 MPa occurred in the region closer to the fire for $t < 1$ min, which represents $\sim 57\%$ of the f_c . Such a considerable compressive stress occurred due to the high heating rate of the HFC and the fact that thermal-creep is not considered in the numerical model implemented [34,39].

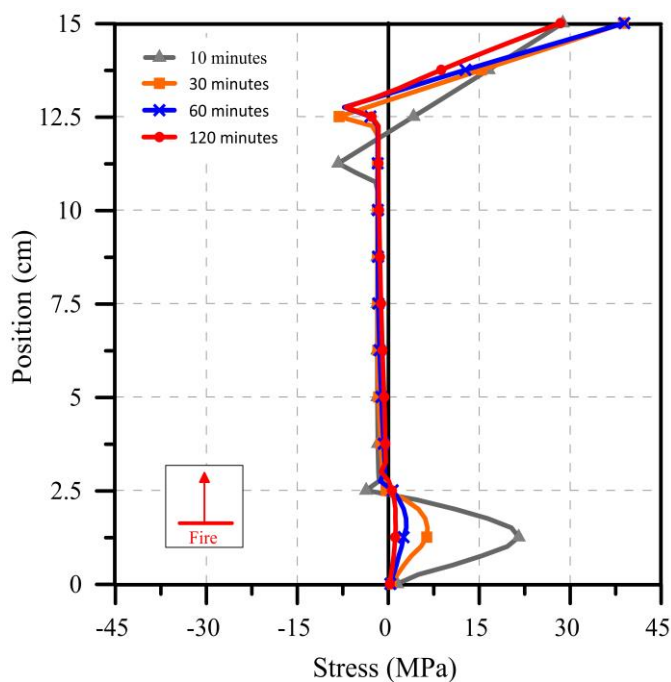


Figure 8 – Numerical simulation of the stress distribution in the SFRC as a function of fire duration

Figure 9 shows the temperature-time linear regression curves based on experimental results, as well as the internal heating rate values as a function of z . The results show that, at a given value of z , the temperature of the composite increases at a constant rate. This can also be observed by the almost constant offset between the temperature-depth curves in Fig. 7, especially for $z \geq 6$ cm. In this sense, the heating rate values calculated by the slope of linear regression curves for z equal to 3, 6, 9, 12, 15 cm were 4.84, 3.36, 1.63, 1.08, and 0.89 °C/min, respectively. Additionally, these internal heating rate values seems to increase logarithmically with the reduction in the values of z (see Fig. 9b).

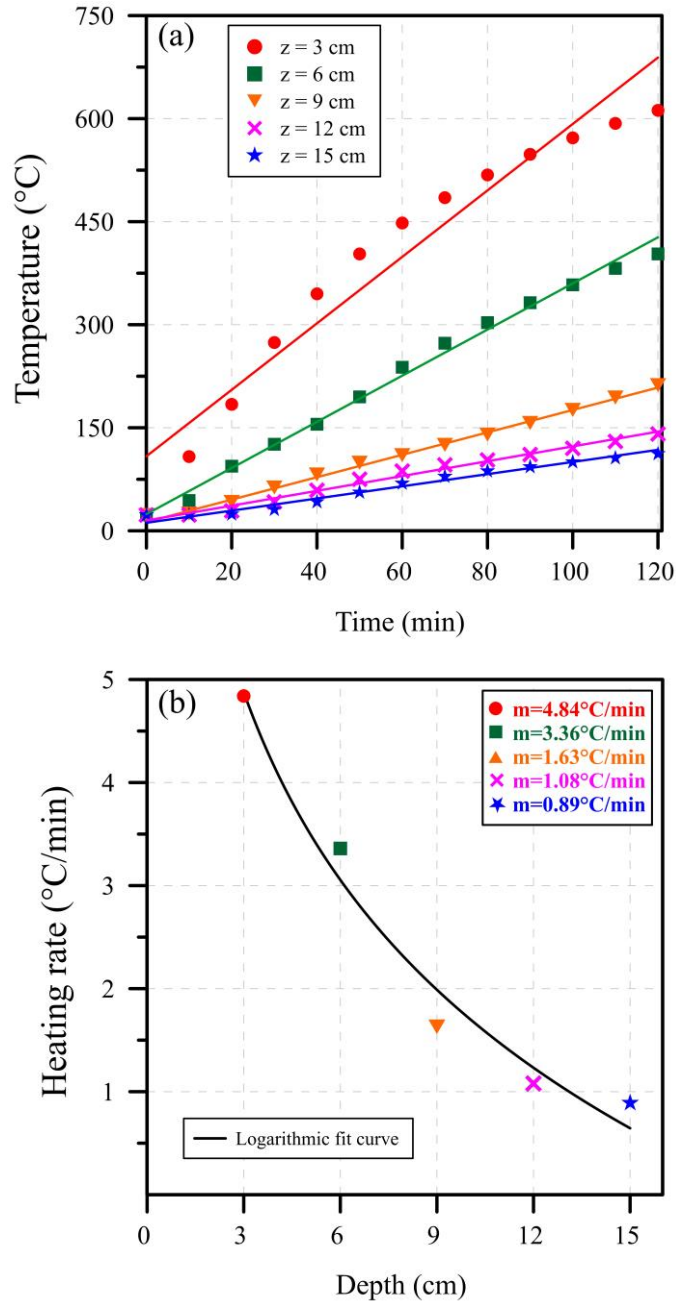


Figure 9 – (a) linear regression for the internal heating rate, and (b) internal heating rate values

The heating rate results obtained in this study agree well with previous results obtained with macro-synthetic fiber reinforced concrete (MSFRC) using the same concrete matrix tested in comparable conditions [24]. This result may indirectly suggest that the thermal conductivity of concrete is more significantly influenced by the properties of the concrete mix (*e.g.* aggregates, w/c ratio, binder type) than by the addition of fibers. Moreover, a study conducted by Liu et al. [55] shows that an increase of 1% in the steel fiber content added to the mix results in an increase of ~ 0.1 W/m.K in the thermal conductivity of SFRC, which is close to negligible when

compared to the influence of other variables, such as type of aggregate, moisture conditions, and the test methodology adopted in experiments [56–58].

3.2.3 Differential damage in the SFRC

Figure 10 shows the values of K_c and $K_{F_{tu}}$ as a function of z and t compared to European standards. The K_c values determined based on experimental results for $t = 120$ min have reached 0.11, 0.52, 0.80, 0.87, and 0.95 for z values of 3, 6, 9, 12, and 15 cm, respectively. This means that the layers at $z \leq 3$ cm provide virtually no compressive strength to the SFRC, which is a result of the considerable dehydration, cracking, and deterioration that occurs in this region [24]. However, the K_c values ranged between 80% and 95% for $z \geq 9$ cm, which may suggest that layers at this depth can retain a considerable portion of the initial f_c value. Additionally, the K_c values are lower than those prescribed by Eurocode [33], which can be attributed to differences in the methodology adopted and the composition of SFRC, as discussed in Section 3.1.

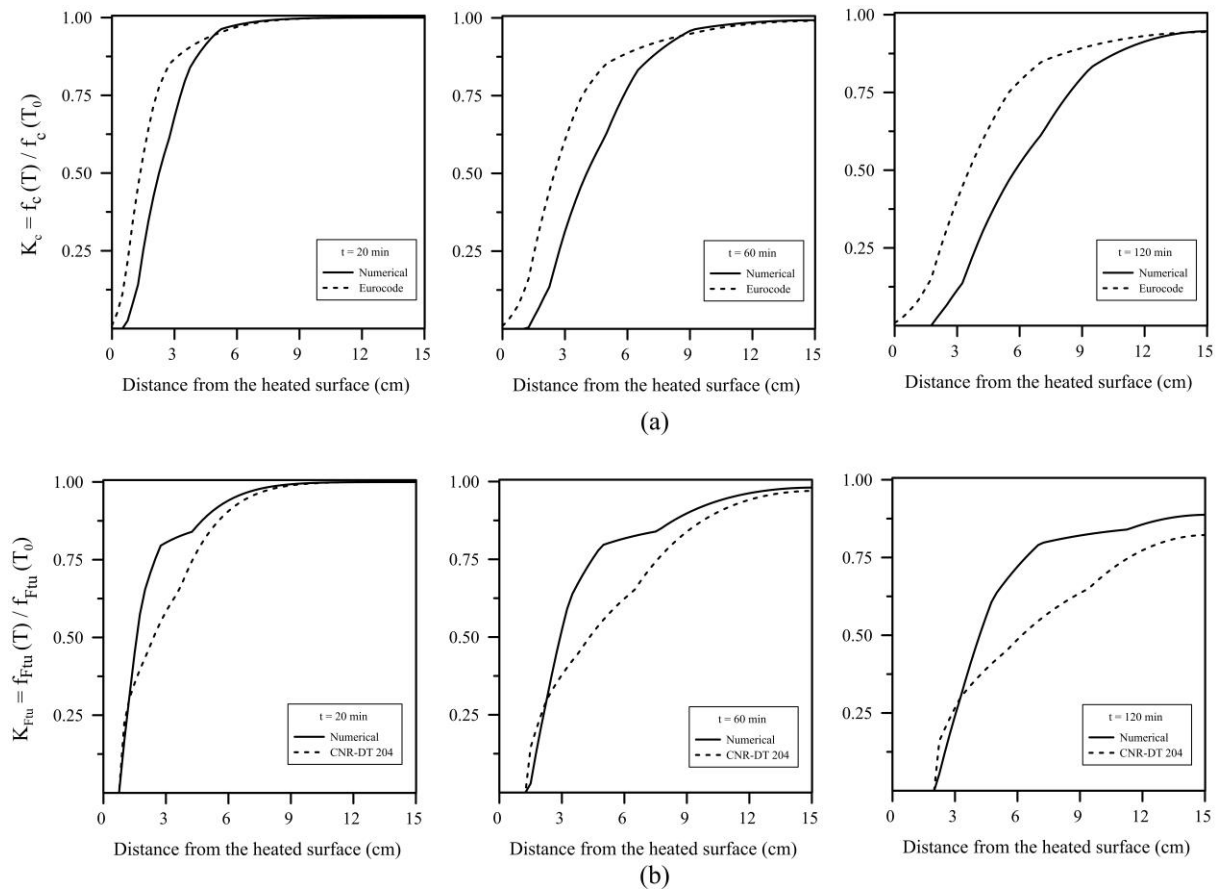


Figure 10 – Values of (a) K_c and (b) $K_{F_{tu}}$ as a function of z compared to European standards

The values of $K_{F_{tu}}$ for $t = 120$ min have reached values of 0.24, 0.72, 0.82, 0.86, and 0.89 for z values of 3, 6, 9, 12, and 15 cm. These results suggest that the layers at z

< 3 cm suffer a severe reduction in f_{Ftu} values, while layers at $z \geq 6$ cm may retain a significant portion of the initial f_{Ftu} value. The lower reductions observed for K_{Ft} compared to K_c can be attributed to the reduced effect of temperature on the bond-slip behavior of steel fibers up to ~ 400 °C [40–44] and, consequently, on the SFRC f_{Ftu} values. Moreover, the results obtained considering the K_{ftu} values presented by CNR DT-204 [32] have shown to be in favor of safety.

Also, the values of K_c and K_{Ftu} reduce non-linearly with the depth, which is directly proportional to the distribution of internal temperatures in the SFRC. However, the experimental results show that the reduction rate tends to be linear for a given value of z , as shown in Fig. 11. This feature may be noticed for K_c and K_{Ftu} for all the evaluated values of z , with exception of $z = 3$ cm for K_c . The non-linear changes in K_c at this specific value of z may be related to the aggressive heating rate provided by HFC and due to the proximity to the fire source. Moreover, the rate of reduction for K_{Ftu} in Fig. 11 seems to be lower than those for K_c , especially considering lower values of z . For every 60 minutes of fire exposure, the K_c reduced by 30.3%, 28.6%, 12.2%, 4.9%, and 3.1% and the K_{Ftu} reduced by 34.5%, 11.5%, 10.9%, 8.9%, and 6.9%, both for the respective z values of 3, 6, 9, 12, and 15 cm.

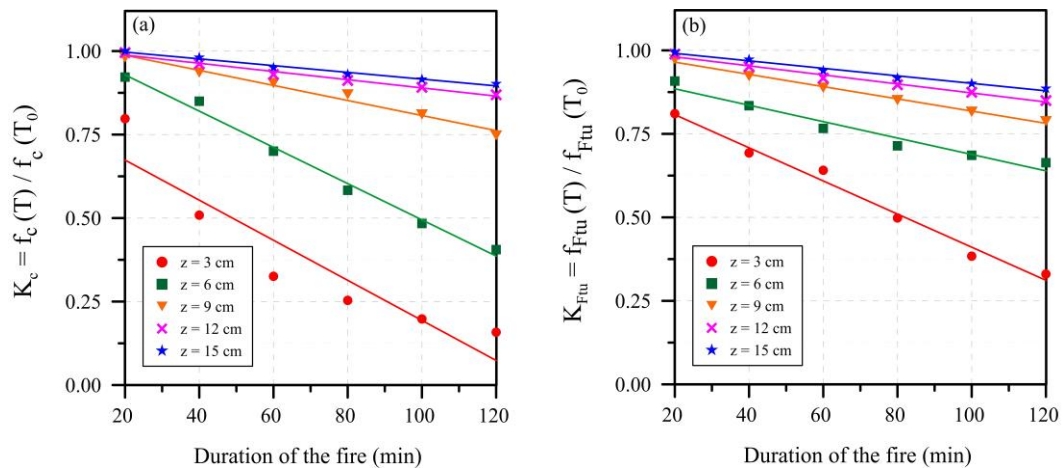


Figure 11 – Evolution of (a) K_c and (b) K_{Ftu} as a function of the duration of fire

3.2.4 Bending test results

Figure 12 shows the stress-CMOD curves for the SFRC before and after fire exposure by means of the three-point bending test. The SFRC tested at room temperature presented a softening behavior which is characteristic of composites with fiber contents lower than the critical fiber volume. In terms of post-crack parameters, the SFRC was classified as 4.0a ($f_{R1k} = 4.0$ MPa; slip softening) and met the minimum

requirements at SLS (f_{R1}/f_{LOP}) and ULS (f_{R3}/f_{R1}) to be considered a structural material according to the methodology proposed by the *fib* Model Code 2010 [16].

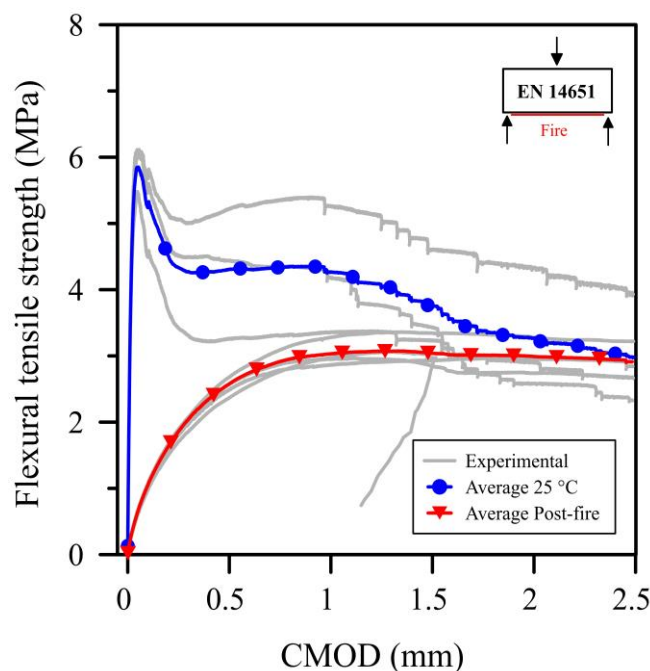


Figure 12 – Post-crack tensile strength for the SFRC before and after fire exposure by means of the three-point bending test

The rupture peak associated with the matrix cracking is absent in specimens after fire exposure, which is justified by the extensive crack network induced by fire (see Section 3.2.1). The post-fire values of f_{LOP} and f_{R1} reduced by 88.9% and 40.1%, respectively, when compared with reference specimens. Contrarily, f_{R3} and f_{R4} values did not show significant differences between the pre- and post-fire values, the slight differences observed being primarily due to the scatter of the bending test itself.

Moreover, the numerical simulation shows that the bearing capacity of the SFRC is slightly reduced when the fire affects the flexural tensile region of the specimens. Contrarily, a great reduction in the bearing capacity is verified when the fire affects the compressive zone of the specimen (see Fig. 13). This occurs because the scalar value of f_c is greater than the scalar value of f_{Ftu} , therefore the temperature-related reductions in f_c tend to affect more significantly the bearing capacity of the cross-section. Secondly, the K_c is greater than K_{Ftu} for the same internal temperature value, which results in a more rapid loss of bearing capacity when the compressive region of the beam is heated.

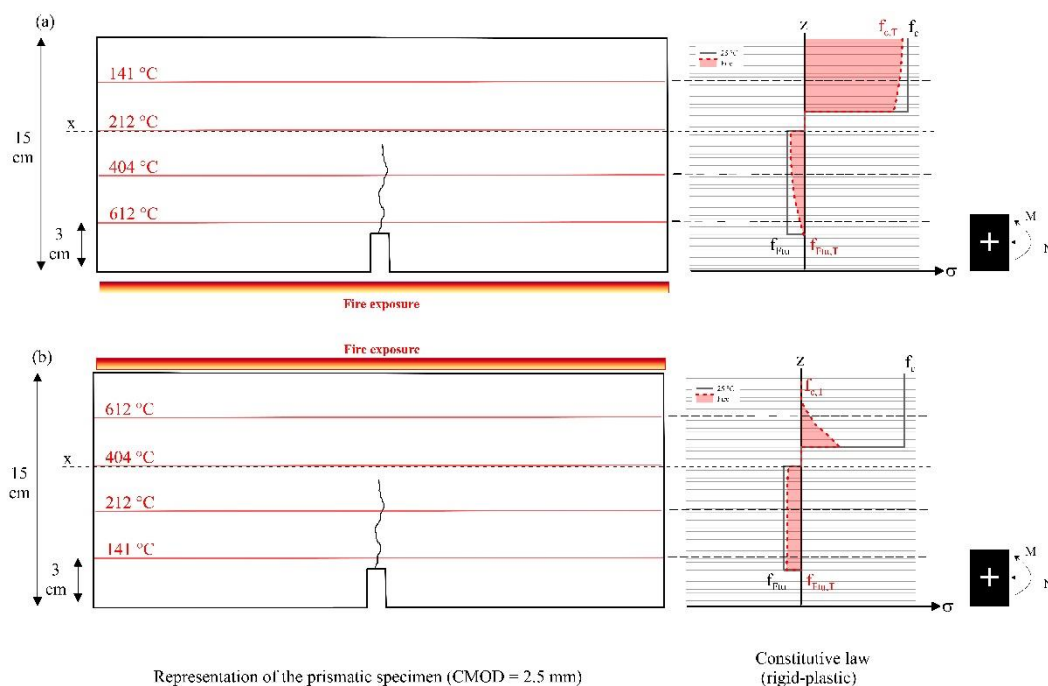


Figure 13 – Bearing capacity under bending with fire effect on the (a) tensile region and (b) compressive region of the SFRC

This means that the results obtained by bending tests tend to be significantly influenced by the compressive portion of the cross-section, especially depending on the orientation of the prismatic specimens related to the surface affected by fire. Therefore, the bending test methodology adopted for the determination of post-fire f_{Ftu} may provide non-representative results of the actual properties of the composite after a fire event, while the investigation of alternative test methods is required. Moreover, the non-significant difference in results at $CMOD = 2.5$ mm may be influenced by the reduced effect of temperature on the bond-slip behavior of hooked-end steel fibers up to ~ 400 °C [40–44].

3.2.5 DEWS test

Figure 14 shows the stress-COD curves before and after fire exposure and the comparison between oven-heated and fire-exposed specimens. The exposure to fire resulted in reductions of 71.4%, 66.7%, and 59.1% for f_{Ft} , f_{Fts} , and f_{Ftu} , respectively. These reductions may be attributed to the severe cracking caused by the dehydration of hydrated products in the cement paste [24], the temperature gradients induced by fire (see Section 3.2.1), and the temperature-related changes in the microstructure and the bond-slip mechanism of the steel fibers [44]. These macro- and microstructural changes are some of the factors that lead to the reduction in the tensile properties of the composite.

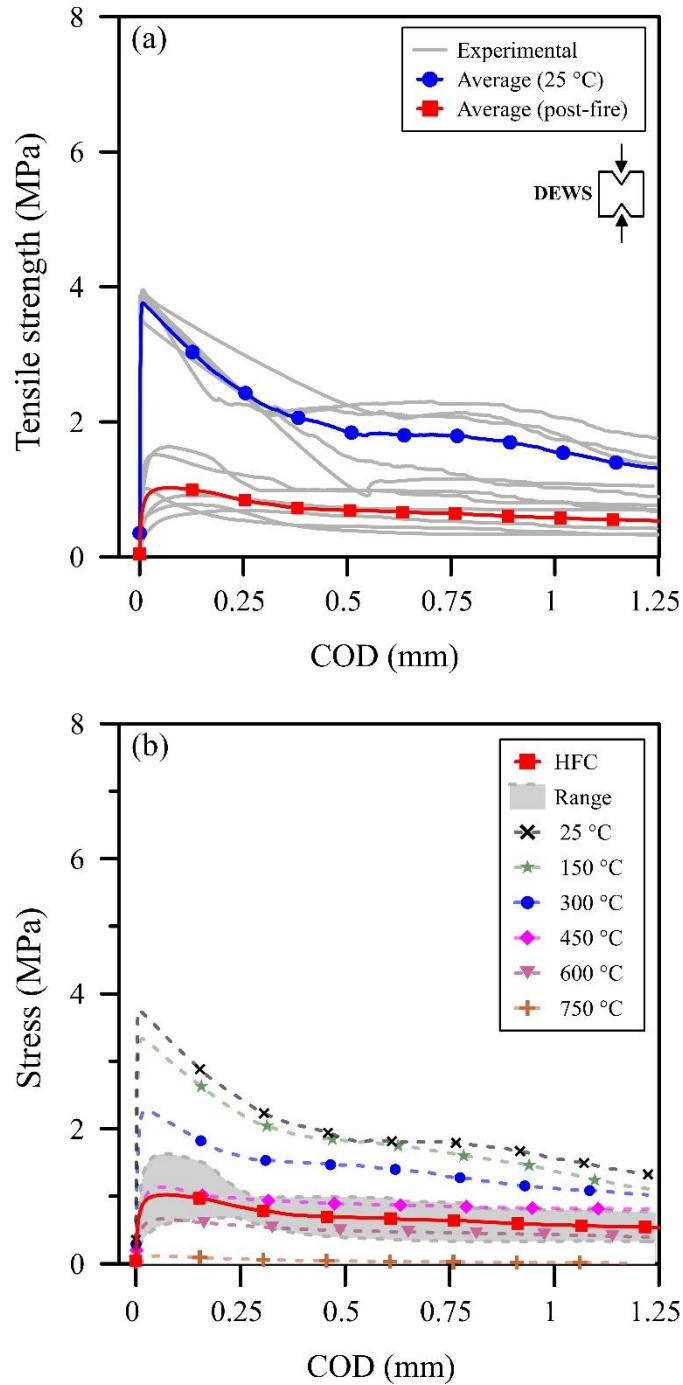


Figure 14 – Tensile properties after fire exposure compared to (a) room temperature and (b) oven-heated results

The post-fire tensile properties obtained by the DEWS test may be compared to the results obtained for oven-heated specimens, which were presented in Section 3.1. In this sense, a comparison between the post-fire stress-COD curves and the results for temperatures ranging between 150 °C and 750 °C are presented in Fig. 14b.

It is possible to observe that the post-fire f_{Ftu} values tend to the average result obtained for temperatures between 450 °C and 600 °C. In this sense, the numerical

simulation was employed as a tool to assess the distribution of f_{Ftu} in the cross-section as a function of z (see Fig. 15). The results show that the post-fire f_{Ftu} is null up to $z = 2$ cm and increases non-linearly up to 85.9% of the initial f_{Ftu} value with the increase in z . Therefore, the average post-fire f_{Ftu} value determined tends to represent the layers closer to the fire, which means that the DEWS test was capable of yielding more representative results than the EN 14651 bending test for the definition of f_{Ftu} .

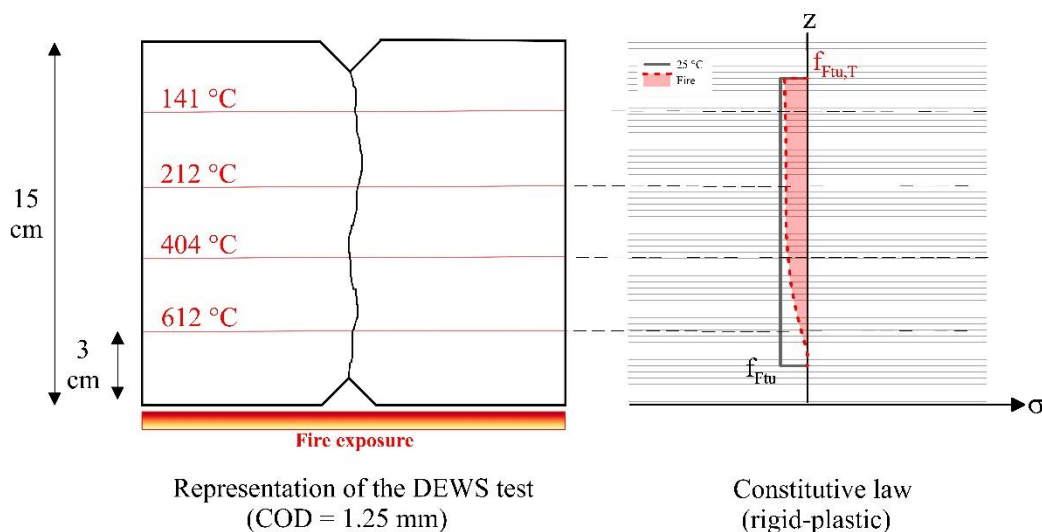


Figure 15 – Distribution of f_{Ftu} as a function of z for the DEWS test

4. Case study: São Paulo subway line

The numerical model implemented in this study was employed to assess the effect of a fire event on the bearing capacity of SFRC segments, taking as basis the design parameters of a tunnel to be executed in the city of São Paulo (Brazil). The steel fiber reinforced concrete law adopted is presented in Figure 16, while the parameters employed in the numerical simulation are presented in Table 4. The values of f_{cd} and f_{R3d} were employed based on the design parameters considering a partial safety factor of $\gamma_F = 1.0$, since fire is an exceptional event. The numerical simulation was conducted considering the ISO 834 and the HFC. These fire curves were adopted to simulate two distinct scenarios with variable heating rate and maximum temperature. The bearing capacity of the cross-section was assessed by means of the Moment-Axial (M-N) interaction envelopes and the results are presented as a function of the fire curve adopted.

Table 4 – Parameters adopted for the subway line numerical simulation

Parameter	Input value
f_{cd} (MPa)	45
f_{R3d} (MPa)	3.0
f_{Ftud} (MPa)	1.0
H (in meters)	0.40
B (in meters)	1.0
Initial temperature ($^{\circ}\text{C}$)	20
Emissivity	0.9
Density ($\text{kg}\cdot\text{m}^{-3}$)	2400
Specific heat ($\text{J}\cdot\text{kg}^{-1}\cdot\text{K}^{-1}$)	900
Thermal conductivity ($\text{W}\cdot\text{m}^{-1}\cdot\text{K}^{-1}$)	1.2
Convective coefficient ($\text{W}\cdot\text{m}^{-2}\cdot\text{K}^{-1}$)	25

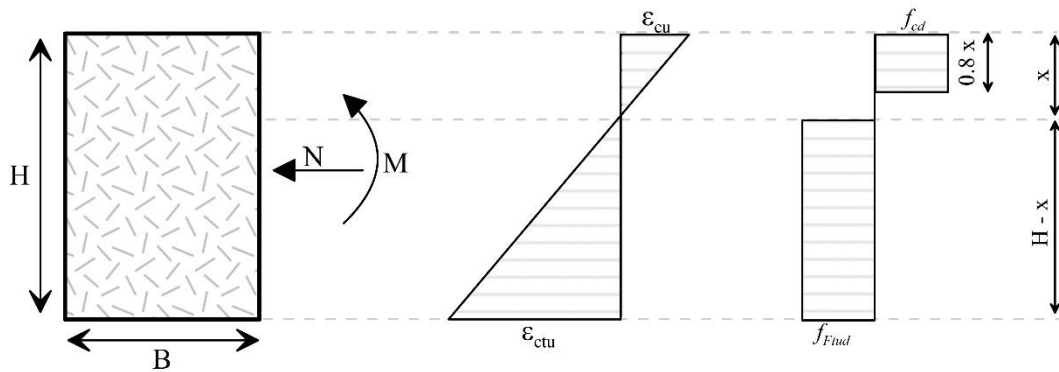


Figure 16 – Steel fiber reinforced concrete law adopted

Figure 17 shows the M-N interaction envelopes for the SFRC exposed to fire following the ISO 834 and the HFC. The results show that the exposure of the segments to a uniaxial fire event resulted in a considerable loss in terms of bearing capacity. In this sense, the reductions in terms of bearing capacity have shown to be greater when the compressive region of the cross-section is closer to the fire (*i.e.* negative flexural moment). This occurs because the f_c represents a greater portion of the total bearing capacity of the segment, while the f_{Ftu} have lower scalar values. This effect was also observed both during the experimental campaign conducted and the numerical simulation, which was discussed in Section 3.2.4.

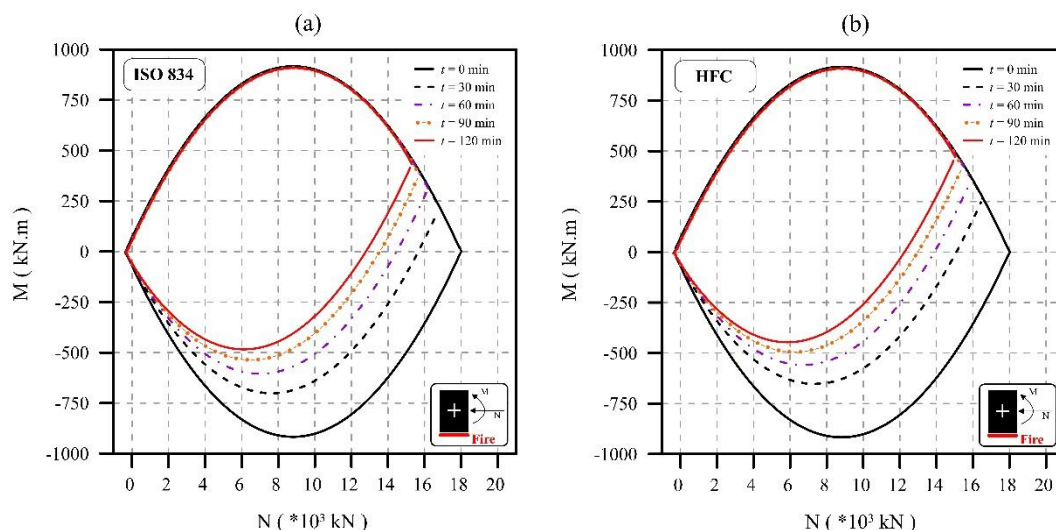


Figure 17 – The M-N envelopes for the SFRC exposed to fire following (a) the ISO 834 and (b) the HFC

Even though the fire curves are different, it can be verified that the bearing capacity of SFRC is considerably reduced in both cases. The bearing capacity of the SFRC segments reduced more rapidly when exposed to the HFC, which is reasonable since the HFC prescribes higher values of maximum temperature and a rapid heating rate at the initial minutes of a fire. An interesting result is that the bearing capacity of the SFRC exposed to the ISO 834 and HFC fire curves were comparable when the condition $t_{(ISO)} = 2 t_{(HFC)}$ is satisfied (see Fig. 18). This condition was also verified in a parametric study conducted by Di Carlo et al. [23], which highlights the importance of determining the adequate fire curve for the proper assessment of tunnels exposed to fire events.

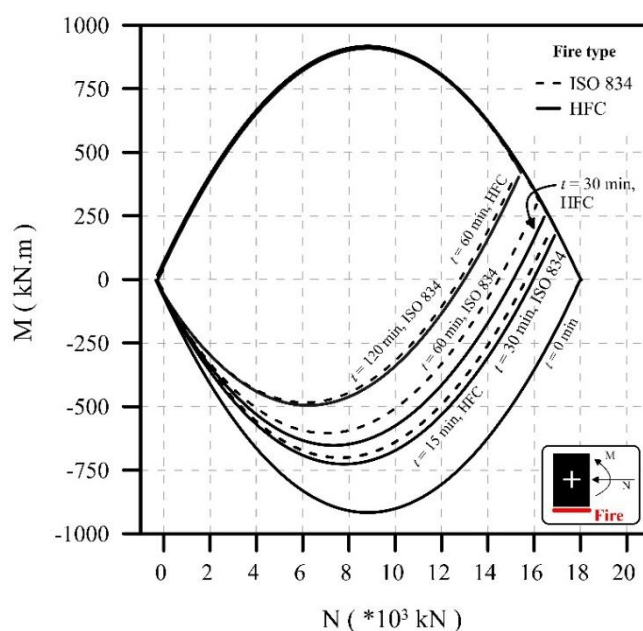


Figure 18 – Comparison between the M-N envelopes generated as a function of the fire curve adopted

In this sense, the M-N interaction envelopes can be employed as useful tools to assess the cross-sectional stability of tunnels built with SFRC under fire exposure. In this particular case, the results presented in this section serve to the specific case of the Subway Line 6 at the city of São Paulo (Brazil). However, the tools presented in this study may be employed for the assessment of other tunnel structures built with SFRC. It is important to remind that validating the numerical simulation with experimental results is beneficial for a representative assessment of the bearing capacity of SFRC tunnel structures.

5 Conclusions

The following conclusions can be drawn from the present study:

- The temperature readings inside the SFRC exposed to fire reached 612, 403, 212, 141, and 112 °C for the z values of 3, 6, 9, 12, and 15 cm at $t = 120$ min. The distribution of temperatures obtained experimentally showed good agreement with the thermal model implemented. Moreover, the incompatibility between the thermal strains and the total strain field results in compressive stresses at $z = 0$ mm and $z = 150$ mm and tensile stresses at the central region of the specimens is subjected to fire.
- The reduction of the compressive (K_c) and post-crack tensile strength for a crack-opening of 1.25 mm (K_{ftu}) were determined as a function of temperature. The results in terms of K_c were lower than those prescribed by European guidelines, which was attributed to the melting of the micro-synthetic fibers and particularities of the heat regime adopted. Contrarily, the K_{ftu} values were greater than those prescribed by the CNR DT-204, which suggests that the guideline is on the safe side when micro-synthetic fibers are used and the explosive spalling is avoided.
- The K_c and K_{ftu} results fed the numerical model implemented and the differential damage inside the SFRC was estimated. The K_c values for $t = 120$ min have reached 0.11, 0.52, 0.80, 0.87, and 0.95 for z values of 3, 6, 9, 12, and 15 cm, respectively. The values of K_{ftu} obtained for $t = 120$ min have reached values of 0.24, 0.72, 0.82, 0.86, and 0.89 for z values of 3, 6, 9, 12, and 15 cm. This means that the layers at $z \leq 3$ cm provide virtually no mechanical contribution, while layers further away (*e.g.* values of $z \geq 6$ cm) may retain over 80% of the initial mechanical property value.

- The post-fire tensile properties of the SFRC were assessed by the bending test and the DEWS test. The post-fire results obtained by means of the bending test showed a reduction of 88.9% and 40.1% in terms of f_{LOP} and f_{RI} , respectively. Contrarily, f_{R3} and f_{R4} values did not show significant differences between the pre- and post-fire values. The post-fire results obtained by means of the DEWS test showed reductions of 71.4%, 66.7%, and 59.1% for f_{Ft} , f_{Fts} , and f_{Ftu} , respectively. In this sense, the results suggest that the bending test may not be adequate to determine the ULS post-crack tensile properties of the composite after a fire, while the DEWS test could yield more representative results.
- The effect of a fire event on the bearing capacity of the SFRC segments was assessed using the numerical model implemented in this study. The results show that the fire exposure resulted in a considerable loss in terms of bearing capacity, which have shown to be greater when the compressive region of the cross-section is closer to the fire (*i.e.* negative flexural moment). This occurs because the f_c represents a greater portion of the cross-sectional bearing capacity, especially for SFRC with strain-softening behavior such as the one employed in this study. Therefore, the M-N interaction envelopes can be employed as useful tools to assess the local stability of tunnels built with SFRC under fire exposure.
- The bearing capacity of the SFRC segments decreased more rapidly when exposed to the HFC than to the ISO 834 fire curve, which is reasonable since the HFC prescribes higher values of maximum temperature and a rapid heating rate. This highlights the importance of determining the adequate fire curve for the proper assessment of tunnels exposed to fire events, which can be estimated based on experimental and numerical programs. An interesting result is that the bearing capacity of the SFRC exposed to the ISO 834 and HFC fire curves were comparable when the condition $t_{ISO} = 2 t_{HFC}$ was satisfied.

Therefore, the results obtained are capable of evaluating the changes in temperature and in mechanical properties of SFRC in the cross-sectional level, as a function of space and time. More than that, the procedure proposed in this paper may be used as a tool to verify the stability SFRC tunnel linings in the design stage, as well as for structures affected by fire that require an adequate rehabilitation procedure.

Acknowledgments

The authors would like to thank the Institute for Technological Research (IPT) and its foundation (FIPT) for their financial and institutional support through the New Talents Program N.01/2017 and N.01/2018. This work was partially supported by the Conselho Nacional de Desenvolvimento Científico e Tecnológico (CNPq) [Grant # 305055/2019-4 (Antonio Domingues de Figueiredo)]. The authors would also like to thank Dr. Renan P. Salvador (USJT) for the technical contributions that improved the quality of this work.

References

- [1] D. Klenert, L. Mattauch, O. Edenhofer, K. Lessmann, Infrastructure and inequality: insights from incorporating key economic facts about household heterogeneity, *Macroecon. Dyn.* 22 (2018) 864–895. <https://doi.org/10.1017/S1365100516000432>.
- [2] I. Josa, A. Aguado, Infrastructure, innovation and industry as solutions for breaking inequality vicious cycles, *IOP Conf. Ser. Earth Environ. Sci.* 297 (2019) 012016. <https://doi.org/10.1088/1755-1315/297/1/012016>.
- [3] A. de la Fuente, A. Blanco, J. Armengou, A. Aguado, Sustainability based-approach to determine the concrete type and reinforcement configuration of TBM tunnels linings. Case study: Extension line to Barcelona Airport T1, *Tunn. Undergr. Sp. Technol.* 61 (2017) 179–188. <https://doi.org/10.1016/j.tust.2016.10.008>.
- [4] L. Liao, A. de la Fuente, S. Cavalaro, A. Aguado, Design of FRC tunnel segments considering the ductility requirements of the Model Code 2010, *Tunn. Undergr. Sp. Technol.* 47 (2015) 200–210. <https://doi.org/10.1016/j.tust.2015.01.006>.
- [5] J.-L. Granju, S. Ullah Balouch, Corrosion of steel fibre reinforced concrete from the cracks, *Cem. Concr. Res.* 35 (2005) 572–577. <https://doi.org/10.1016/j.cemconres.2004.06.032>.
- [6] G.A. Plizzari, G. Tiberti, Steel fibers as reinforcement for precast tunnel segments, *Tunn. Undergr. Sp. Technol.* 21 (2006) 438–439. <https://doi.org/10.1016/j.tust.2005.12.079>.
- [7] B. Yun, Operation Systems in Underground Engineering, in: *Undergr. Eng.*, Elsevier, 2019: pp. 239–259. <https://doi.org/10.1016/B978-0-12-812702-5.00006->

- 2.
- [8] Y.-S. Tai, H.-H. Pan, Y.-N. Kung, Mechanical properties of steel fiber reinforced reactive powder concrete following exposure to high temperature reaching 800°C, *Nucl. Eng. Des.* 241 (2011) 2416–2424. <https://doi.org/10.1016/j.nucengdes.2011.04.008>.
- [9] G.M. Chen, Y.H. He, H. Yang, J.F. Chen, Y.C. Guo, Compressive behavior of steel fiber reinforced recycled aggregate concrete after exposure to elevated temperatures, *Constr. Build. Mater.* 71 (2014) 1–15. <https://doi.org/10.1016/j.conbuildmat.2014.08.012>.
- [10] O. Dügenci, T. Haktanir, F. Altun, Experimental research for the effect of high temperature on the mechanical properties of steel fiber-reinforced concrete, *Constr. Build. Mater.* (2015). <https://doi.org/10.1016/j.conbuildmat.2014.11.005>.
- [11] C.-S. Poon, S. Azhar, M. Anson, Y.-L. Wong, Comparison of the strength and durability performance of normal- and high-strength pozzolanic concretes at elevated temperatures, *Cem. Concr. Res.* 31 (2001) 1291–1300. [https://doi.org/10.1016/S0008-8846\(01\)00580-4](https://doi.org/10.1016/S0008-8846(01)00580-4).
- [12] C.S. Poon, Z.H. Shui, L. Lam, Compressive behavior of fiber reinforced high-performance concrete subjected to elevated temperatures, *Cem. Concr. Res.* 34 (2004) 2215–2222. <https://doi.org/10.1016/j.cemconres.2004.02.011>.
- [13] H. Li, G. Liu, Tensile Properties of Hybrid Fiber-Reinforced Reactive Powder Concrete After Exposure to Elevated Temperatures, *Int. J. Concr. Struct. Mater.* 10 (2016) 29–37. <https://doi.org/10.1007/s40069-016-0125-z>.
- [14] W.Z. Zheng, H.Y. Li, Y. Wang, H.Y. Xie, Tensile Properties of Steel Fiber-Reinforced Reactive Powder Concrete after High Temperature, *Adv. Mater. Res.* 413 (2011) 270–276. <https://doi.org/10.4028/www.scientific.net/AMR.413.270>.
- [15] D. Gao, D. Yan, X. Li, Flexural properties after exposure to elevated temperatures of a ground granulated blast furnace slag concrete incorporating steel fibers and polypropylene fibers, *Fire Mater.* 38 (2014) 576–587. <https://doi.org/10.1002/fam.2198>.
- [16] Federation Internationale du Beton, Model Code for Concrete Structures 2010, in: Ernst & Sohn, Germany, 2013: p. 434.
- [17] Z. Guan, T. Deng, G. Wang, Y. Jiang, Studies on the key parameters in segmental lining design, *J. Rock Mech. Geotech. Eng.* 7 (2015) 674–683.

- <https://doi.org/10.1016/j.jrmge.2015.08.008>.
- [18] Guidelines for the design of shield tunnel lining, *Tunn. Undergr. Sp. Technol.* 15 (2000) 303–331. [https://doi.org/10.1016/S0886-7798\(00\)00058-4](https://doi.org/10.1016/S0886-7798(00)00058-4).
- [19] Z. Yan, H. Zhu, J. Woody Ju, W. Ding, Full-scale fire tests of RC metro shield TBM tunnel linings, *Constr. Build. Mater.* 36 (2012) 484–494. <https://doi.org/10.1016/j.conbuildmat.2012.06.006>.
- [20] F. Yasuda, K. Ono, T. Otsuka, Fire protection for TBM shield tunnel lining, *Tunn. Undergr. Sp. Technol.* 19 (2004) 317. <https://doi.org/10.1016/j.tust.2004.01.018>.
- [21] C. Pichler, R. Lackner, H.A. Mang, Safety Assessment of Concrete Tunnel Linings under Fire Load, *J. Struct. Eng.* 132 (2006) 961–969. [https://doi.org/10.1061/\(ASCE\)0733-9445\(2006\)132:6\(961\)](https://doi.org/10.1061/(ASCE)0733-9445(2006)132:6(961)).
- [22] Z. Yan, H. Zhu, J.W. Ju, Behavior of reinforced concrete and steel fiber reinforced concrete shield TBM tunnel linings exposed to high temperatures, *Constr. Build. Mater.* 38 (2013) 610–618. <https://doi.org/10.1016/j.conbuildmat.2012.09.019>.
- [23] F. Di Carlo, A. Meda, Z. Rinaldi, Evaluation of the bearing capacity of fiber reinforced concrete sections under fire exposure, *Mater. Struct.* 51 (2018) 154. <https://doi.org/10.1617/s11527-018-1280-2>.
- [24] R. Serafini, S.R.A. Dantas, R.P. Salvador, R.R. Agra, D.A.S. Rambo, A.F. Berto, A.D. de Figueiredo, Influence of fire on temperature gradient and physical-mechanical properties of macro-synthetic fiber reinforced concrete for tunnel linings, *Constr. Build. Mater.* 214 (2019) 254–268. <https://doi.org/10.1016/j.conbuildmat.2019.04.133>.
- [25] J.M. Carpio, Numerical model for the thermo-hygro-mechanical analysis of concrete elements from early ages, *Universitat Politècnica de Catalunya*, 2019.
- [26] C.N. Costa, Dimensionamento de elementos de concreto armado em situação de incêndio., *Universidade de São Paulo*, 2008. <https://doi.org/10.11606/T.3.2008.tde-04092008-155911>.
- [27] EN 14651, Test method for metallic fibred concrete — Measuring the flexural tensile strength (limit of proportionality (LOP), residual), United Kingdom, 2007.
- [28] L. Liao, A. de la Fuente, S. Cavalaro, A. Aguado, Design procedure and experimental study on fibre reinforced concrete segmental rings for vertical shafts, *Mater. Des.* 92 (2016) 590–601.

- <https://doi.org/10.1016/j.matdes.2015.12.061>.
- [29] L.A.C. Borges, R. Monte, D.A.S. Rambo, A.D. de Figueiredo, Evaluation of post-cracking behavior of fiber reinforced concrete using indirect tension test, *Constr. Build. Mater.* 204 (2019) 510–519. <https://doi.org/10.1016/j.conbuildmat.2019.01.158>.
- [30] R. Serafini, R.R. Agra, R.P. Salvador, A. de la Fuente, A.D. de Figueiredo, Double Edge Wedge Splitting Test to Characterize the Design Postcracking Parameters of Fiber-Reinforced Concrete Subjected to High Temperatures, *J. Mater. Civ. Eng.* 33 (2021) 04021069. [https://doi.org/10.1061/\(ASCE\)MT.1943-5533.0003701](https://doi.org/10.1061/(ASCE)MT.1943-5533.0003701).
- [31] M. di Prisco, L. Ferrara, M.G.L. Lamperti, Double edge wedge splitting (DEWS): an indirect tension test to identify post-cracking behaviour of fibre reinforced cementitious composites, *Mater. Struct.* 46 (2013) 1893–1918. <https://doi.org/10.1617/s11527-013-0028-2>.
- [32] CNR-DT 204, Guide for the Design and Construction of Fibre-Reinforced Concrete Structures, Ital. Natl. Res. Counc. (CNR), Rome, Italy. (2007). <https://doi.org/10.14359/10516>.
- [33] BS EN 1992-1-2, Eurocode 2 Design of concrete structures - Part 1-2: General rules-Structural fire design, *Des. Concr. Struct. - Part 1-2 Gen. Rules-Structural Fire Des.* (2004).
- [34] J.M. Carpio, R. Serafini, D. Rambo, A. de la Fuente, A.D. De Figueiredo, Assessment of the bearing capacity reduction of FRC elements subjected to fire, in: *Proc. Fib Symp. 2019 Concr. - Innov. Mater. Des. Struct.*, Kraków, Poland, 2019: pp. 1378–1386.
- [35] A. Lau, M. Anson, Effect of high temperatures on high performance steel fibre reinforced concrete, *Cem. Concr. Res.* 36 (2006) 1698–1707. <https://doi.org/10.1016/j.cemconres.2006.03.024>.
- [36] B. Chen, J. Liu, Residual strength of hybrid-fiber-reinforced high-strength concrete after exposure to high temperatures, *Cem. Concr. Res.* 34 (2004) 1065–1069. <https://doi.org/10.1016/j.cemconres.2003.11.010>.
- [37] W. Zheng, H. Li, Y. Wang, Compressive stress–strain relationship of steel fiber-reinforced reactive powder concrete after exposure to elevated temperatures, *Constr. Build. Mater.* 35 (2012) 931–940. <https://doi.org/10.1016/j.conbuildmat.2012.05.031>.
- [38] G.P. Alves, E.I. Jussiani, A.C. Andrello, B.M. Toralles, Effect of temperature

- rise on the microstructure of cementitious materials: A study through X-ray computed microtomography (μ -CT), *Constr. Build. Mater.* 237 (2020) 117446. <https://doi.org/10.1016/j.conbuildmat.2019.117446>.
- [39] Z.P. Bažant, M.F. Kaplan, *Concrete at high temperatures: material properties and mathematical models*, Longman, 1996.
- [40] S. Abdallah, M. Fan, K.A. Cashell, Bond-slip behaviour of steel fibres in concrete after exposure to elevated temperatures, *Constr. Build. Mater.* 140 (2017) 542–551. <https://doi.org/10.1016/j.conbuildmat.2017.02.148>.
- [41] S. Abdallah, M. Fan, D.W.A. Rees, Effect of elevated temperature on pull-out behaviour of 4DH/5DH hooked end steel fibres, *Compos. Struct.* 165 (2017) 180–191. <https://doi.org/https://doi.org/10.1016/j.compstruct.2017.01.005>.
- [42] S. Abdallah, M. Fan, K.A. Cashell, Pull-out behaviour of straight and hooked-end steel fibres under elevated temperatures, *Cem. Concr. Res.* 95 (2017) 132–140. <https://doi.org/10.1016/j.cemconres.2017.02.010>.
- [43] G. Ruano, F. Isla, B. Luccioni, R. Zerbino, G. Giaccio, Steel fibers pull-out after exposure to high temperatures and its contribution to the residual mechanical behavior of high strength concrete, *Constr. Build. Mater.* 163 (2018) 571–585. <https://doi.org/10.1016/j.conbuildmat.2017.12.129>.
- [44] R. Serafini, R.R. Agra, L.A.G. Bitencourt, A. de la Fuente, A.D. de Figueiredo, Bond-slip response of steel fibers after exposure to elevated temperatures: Experimental program and design-oriented constitutive equation, *Compos. Struct.* 255 (2021) 112916. <https://doi.org/10.1016/j.compstruct.2020.112916>.
- [45] F.B. Varona, F.J. Baeza, D. Bru, S. Ivorra, Influence of high temperature on the mechanical properties of hybrid fibre reinforced normal and high strength concrete, *Constr. Build. Mater.* 159 (2018) 73–82. <https://doi.org/10.1016/j.conbuildmat.2017.10.129>.
- [46] D. Choumanidis, E. Badogiannis, P. Nomikos, A. Sofianos, The effect of different fibres on the flexural behaviour of concrete exposed to normal and elevated temperatures, *Constr. Build. Mater.* 129 (2016) 266–277. <https://doi.org/10.1016/j.conbuildmat.2016.10.089>.
- [47] M. Colombo, M. di Prisco, R. Felicetti, SFRC exposed to high temperature: Hot vs. residual characterization for thin walled elements, *Cem. Concr. Compos.* 58 (2015) 81–94. <https://doi.org/10.1016/j.cemconcomp.2015.01.002>.
- [48] C. Maluk, L. Bisby, G.P. Terrasi, Effects of polypropylene fibre type and dose on the propensity for heat-induced concrete spalling, *Eng. Struct.* 141 (2017)

- 584–595. <https://doi.org/10.1016/j.engstruct.2017.03.058>.
- [49] N. Yermak, P. Pliya, A.-L. Beaucour, A. Simon, A. Noumowé, Influence of steel and/or polypropylene fibres on the behaviour of concrete at high temperature: Spalling, transfer and mechanical properties, *Constr. Build. Mater.* 132 (2017) 240–250. <https://doi.org/10.1016/j.conbuildmat.2016.11.120>.
- [50] M.J. Hurley, D. Gottuk, J.R. Hall, K. Harada, E. Kuligowski, M. Puchovsky, J. Torero, J.J.M. Watts, C. Wieczorek, *SFPE handbook of fire protection engineering*, fifth edition, 2016. <https://doi.org/10.1007/978-1-4939-2565-0>.
- [51] V. Kodur, Properties of Concrete at Elevated Temperatures, *ISRN Civ. Eng.* 2014 (2014) 1–15. <https://doi.org/10.1155/2014/468510>.
- [52] R.Y. Chen, W.Y.D. Yuen, Review of the high-temperature oxidation of iron and carbon steels in air or oxygen, *Oxid. Met.* (2003). <https://doi.org/10.1023/A:1023685905159>.
- [53] H. Abuluwefa, The effect of oxygen concentration on the oxidation of low-carbon steel in the temperature range 1000 to 1250°C, *Oxid. Met.* (1996). <https://doi.org/10.1007/BF01048639>.
- [54] R. Serafini, L.M. Mendes, R.P. Salvador, A.D. de Figueiredo, The effect of elevated temperatures on the properties of cold-drawn steel fibers, *Mag. Concr. Res.* (2020) 1–28. <https://doi.org/10.1680/jmacr.19.00498>.
- [55] K. Liu, L. Lu, F. Wang, W. Liang, Theoretical and experimental study on multi-phase model of thermal conductivity for fiber reinforced concrete, *Constr. Build. Mater.* 148 (2017) 465–475. <https://doi.org/10.1016/j.conbuildmat.2017.05.043>.
- [56] K.Y. Shin, S.B. Kim, J.H. Kim, M. Chung, P.S. Jung, Thermo-physical properties and transient heat transfer of concrete at elevated temperatures, *Nucl. Eng. Des.* (2002). [https://doi.org/10.1016/S0029-5493\(01\)00487-3](https://doi.org/10.1016/S0029-5493(01)00487-3).
- [57] L. Phan, *Fire Performance of High-Strength Concrete: A Report of the State-of-the-Art*, *Fire Res.* (1996).
- [58] V.K.R. Kodur, M.A. Sultan, Effect of temperature on thermal properties of high-strength concrete, *J. Mater. Civ. Eng.* (2003). [https://doi.org/10.1061/\(ASCE\)0899-1561\(2003\)15:2\(101\)](https://doi.org/10.1061/(ASCE)0899-1561(2003)15:2(101)).

ARTICLE E

Title: Assessment of the bending capacity of FRC and hybrid RC-FRC tunnel sections subjected to fire including thermal spalling effects

Submit to: Materials and Structures

Publication date: Not assigned.

Status: Under review.

ASSESSMENT OF THE BENDING CAPACITY OF FRC AND HYBRID RC-FRC
TUNNEL SECTIONS SUBJECTED TO FIRE INCLUDING THERMAL
SPALLING EFFECTS

Ramoel Serafini^{1*}, Albert de La Fuente², Antonio D. de Figueiredo¹

¹ Department of Civil Construction Engineering, Polytechnic School of the University of São Paulo |
Avenida Professor Almeida Prado, Travessa 2, 83, 05424-970, São Paulo, Brazil.

² Department of Civil and Environmental Engineering, Polytechnic University of Catalonia | Jordi
Girona, 1-3, 08034, Barcelona, Spain

*corresponding author: rserafini@usp.br

Keywords: fire; fiber reinforced concrete; thermal spalling; bending capacity; tunnel
lining.

ABSTRACT

A design-oriented numerical model for the analysis of RC, FRC, and RC-FRC tunnel sections exposed to fire with different spalling parameters is presented. The numerical model is conceived in two steps: the first is the determination of the temperature field in the cross-section exposed to fire according to the spalling parameters; and the second is the determination of the M-N interaction envelopes based on the thermal field in the section. At last, a parametric study was conducted to evaluate the effect of the fire curve, the spalling parameters, the reinforcement type, and the rebar's concrete cover on the bending capacity of the sections. The results showed that the use of FRC as total or partial substitution to RC mitigates the fire-related reduction in bending capacity of the sections. Moreover, increasing the RC concrete cover is beneficial only if thermal spalling is avoided. When thermal spalling occurs, the FRC and RC-FRC solutions yielded the lowest reductions in the bending capacity among the reinforcement solutions tested.

1 Introduction

Fiber reinforced concrete (FRC) is a composite material that may partially or totally replace the reinforced concrete (RC) in structural applications. In the last decades, a steadily increase trend in the amount of urban tunnels built with FRC pre-cast segments was verified due to the benefits provided by adding randomly distributed fibers into concrete [1]. When comparing the structural behavior of RC and FRC segments, the results of a full-scale experimental campaign show that the same load level conditions may be reached by FRC segments with advantages in terms of performance and cost [2]. The performance benefits are mostly related to the enhanced material's response to impact, diffused, and concentrated loads during the storage, transportation, and assembly of the pre-cast segments, as well as improved corrosion resistance [3–6].

In the last three decades, pernicious effects of fire were reported in several tunnels in Europe [7]. Because of this, researchers focused on evaluating the mechanical properties of FRC as a function of temperature [8–14] and developed progenitive full-scale experimental programs to evaluate the reductions in load bearing capacity and the deformation of the tunnel rings during fire [15]. In 2018, Di Carlo et al. [16] proposed a numerical model capable of assessing the bearing capacity of FRC sections considering different geometries, materials' properties, and fire scenarios. The numerical model employed a staggered analysis in which the thermal model computes the temperature distribution along the cross-section and the mechanical model computes the moment-axial (M-N) interaction envelopes based on the equilibrium equations. The aforementioned model was later implemented by other researchers in literature for the parametric analysis of a FRC subway line tunnel in the city of São Paulo, Brazil [17].

Moreover, advances have been reported in understanding the complex mechanisms governing the occurrence of thermal spalling in concrete, especially related to the influence of the materials' properties, the section geometry, and the fire scenario [18]. This phenomenon negatively affects the bearing capacity of tunnels [19] mostly due to the reduction of cross-sectional area, which may reach more than 50% in severe cases [15,20]. In this sense, some predictive numerical models capable of estimating the occurrence of thermal spalling in plain concrete and FRC have been developed at

micro- and meso-scale [21–24], however engineer-oriented models focused on the design of tunnels are scarce. More than that, the effect of spalling on the temperature distribution in the cross-section is often disregarded and this might lead to unsafe designs.

The current guidelines provide limited amount of information regarding the influence of fire and thermal spalling on the bearing capacity of FRC sections, as in state-of-the-art reports published by the ITA [25] and the *fib* Bulletin 46 [26]. The importance of evaluating the effect of spalling on tunnels is highlighted in the *fib* Bulletin 83, however the state-of-the-art report does not provide any spalling-related parameter to evaluate the fire resistance of tunnels [27]. Moreover, the *fib* MC-10 does not provide parameters oriented to the fire-design of FRC structures with or without the occurrence of thermal spalling [28]. Therefore, it is noticeable the lack of studies and parameters related to the effect of thermal spalling on the bearing capacity of tunnel segments. As a consequence, there are limited design-oriented tools to assess the fire safety conditions of TBM tunnels.

In this sense, the current paper presents a thermal-mechanical model to calculate the bearing capacity of RC, FRC, and hybrid RC-FRC sections exposed to fire considering the occurrence of thermal spalling. The bending bearing capacity is assessed by means of the bending-axial force (M-N) interaction envelopes, which are computed considering the distribution of temperatures and the respective mechanical properties in the cross-section. Finally, a parametric study varying the fire curve, the spalling parameters, the reinforcement type, and the concrete cover was conducted. Therefore, the results represent a valuable reference for standards and guidelines worldwide, as well as for the designer's community concerning the design and rehabilitation of tunnel structures affected by fire.

2. Thermo-mechanical numerical model

This section presents the fundamental concepts for the development of the thermo-mechanical numerical model to assess the bearing capacity of the FRC sections with and without steel bar reinforcement under the occurrence of thermal spalling. The heat transfer model was based on common solution approach to the Fourier heat transfer equation [16,17] and applied to the FRC tunnel segments, while the mechanical model was based on the work of Di Carlo et al. [16]. The numerical model

implemented for this study is based on a staggered analysis that decouples both thermal and mechanical problems, the thermal spalling phenomenon being simulated by imposing spalling (R_{sp}) and section lost (s_L) rates. Even though the model developed simplifies the strongly dependent thermo-hygro-mechanical phenomena, it is valid and suitable for pre-design purposes.

2.1 Heat transfer model

The heat transfer through an isotropic solid body can be described by the Fourier heat transfer equation, as:

$$\nabla(KT) + Q = \rho C \quad (1)$$

where K is the thermal conductivity; c is the specific heat; p is the density; Q is the volumetric heat flux; T is the temperature; and t is the time. The heat transfer through concrete may be described in one-dimension planar conduction with no internal heat generated when considering a concrete fully hardened. This assumption may be considered in the central zone of the segments, which represents the greatest portion of the element. However, the regions of contact between segments may be better described by a two-dimension conduction since lateral heating may influence the temperature distribution [29], which needs to be addressed in future research. Based on this assumption and the discussion provided, Eq.1 reduces to:

$$\alpha \left(\frac{\partial^2 T}{\partial z^2} \right) = \frac{\partial T}{\partial t} \quad (2)$$

where $\alpha = \frac{K}{\rho c}$.

In this sense, a numerical model based on the finite difference method (FDM) was developed to solve the Fourier heat transfer equation. The space-time domain was divided in preset constant values (discrete approach) and the differential equations were approximated by FDM. The numerical model adopted a closed space-time domain \mathfrak{R} :

$$\mathfrak{R} = \{(z, t): 0 \leq z \leq L, 0 \leq t \leq t_{fire}\} \quad (3)$$

where z is the spatial variable; L is the length of the cross-section; t is the time related variable; and t_{fire} is the maximum duration of the fire event. The points within the space-time domain are equidistant and identified according to:

$$z_i = (i - 1)\Delta z, \quad i = 1, 2, \dots, n \quad (4)$$

$$t_j = (j - 1)\Delta t, \quad j = 1, 2, \dots, m \quad (5)$$

where n and m are the number of points and time instants, being $\Delta z = L/(n - 1)$ and $\Delta t = t_{fire}/(m - 1)$.

The computation of the second derivatives of the temperature with respect to the spatial variable at a point $z \in \mathfrak{R}$ were solved by the FDM approach, as:

$$\frac{\partial^2 T}{\partial z^2} = \frac{T(z + \Delta z, t) - 2T(z, t) + T(z - \Delta z, t)}{(\Delta z)^2} \quad (6)$$

while the first derivative of temperature related to time is computed as:

$$\frac{\partial T}{\partial t} = \frac{T(z, t + \Delta t) - T(z, t)}{\Delta t} \quad (7)$$

Substituting the Eqs. (6) and (7) into Eq. (2) it is possible to determine an equation to compute the temperature at $t = j + 1$ given that the temperature at the $t = j$ is known, which is described as:

$$T_{i,j+1} = (1 - 2\bar{k})T_{i,j} + \bar{k}(T_{i+1,j} + T_{i-1,j}) \quad (8)$$

where $\bar{k} = \alpha\Delta t/\Delta z^2$. The FDM results are stable if the condition $2\alpha\Delta t < \Delta z^2$ is satisfied.

2.2 Initial and boundary conditions

The thermal equilibrium between the cross-section and the surroundings is considered to be the initial condition for the numerical simulation. Thus, the numerical model assumes that at $t = 0$ the n layers that compose the cross-section discretization, from the intrados to the extrados, are at $T = 25$ °C. The net heat flux (\dot{h}_{net}) transferred from the fire source to the surface of the FRC segment is the sum of the heat flux components convection (\dot{h}_c) and radiation (\dot{h}_r), according to the Eq. (9):

$$\dot{h}_{net} = \dot{h}_c + \dot{h}_r = \alpha_c(T_f - T_s) + \sigma\varepsilon \left[(T_f + 273)^4 - (T_s + 273)^4 \right] \quad (9)$$

where α_c is the convective heat transfer coefficient (in $\text{W}\cdot\text{m}^{-2}\text{K}^{-1}$); σ is the Stefan-Boltzmann constant (in $\text{W}\cdot\text{m}^{-2}\text{K}^{-4}$); ε is the dimensionless emissivity ranging from 0 (perfect reflector) to 1 (perfect absorber); T_f is the temperature of the fire source at a given t value; and T_s is the temperature at the surface of the FRC segment at given t value. Figure 1 illustrates the heat transfer model developed considering the heat flux transferred and the convection described by the discretized Fourier heat transfer equation.

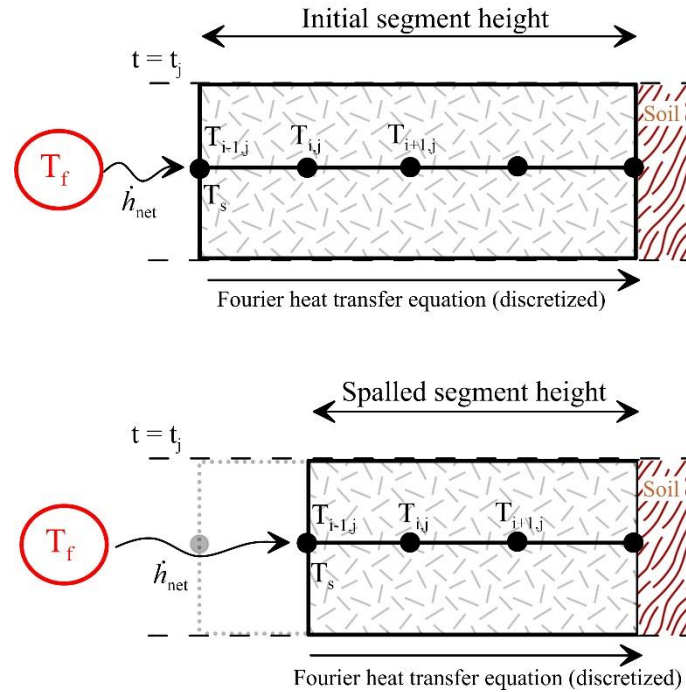


Figure 1 – Illustration of the heat transfer model developed

The effect of spalling is considered in the bearing capacity of FRC segments by reducing the height of the section (H) during the fire event accordingly. This reduction is implemented during the thermal simulation of the composite and results in a cross-section that varies as a function of time. The spalling rate (in mm/h) and the maximum depth of spalling (in mm) are considered the input parameter for simulating the spalling process. These parameters may be determined based on an experimental program using vertical fire simulators and a concrete mix representative of the segment [30]. In these experimental programs, spalling initiation time versus depth diagrams are often used to determine the spalling rate [31]. The spalling rate is established to compute the time required for a concrete thickness (Δz) exposed to elevated temperature to be spalled, by applying the Eq. (10).

$$t_{sp} = \frac{3600 \cdot \Delta z}{R_{sp}} \quad (10)$$

where t_{sp} is the time required for Δz to be spalled (in seconds); and R_{sp} is the experimentally determined rate of spalling (in mm/h). Therefore, the concrete thickness measuring Δz are removed from the thermal analysis every t_{sp} seconds until the maximum depth of spalling is reached. The model takes into account that the heat transferred by the fire source, in the form of \dot{h}_c and \dot{h}_r , begins to affect an inner region of the specimen (see Fig. 1), which influences the temperature distribution in the FRC. Whenever the spalling condition is reached, the reference position

containing $T_{i,j}$ moves one discretized Δz unit toward the interior of the FRC and the spalled layers are disregarded in the thermal model. This process occurs until the maximum depth of spalling accepted by the designer is reached.

2.3 Thermal and physical properties of FRC

The thermal conductivity (K), specific heat (c), and density (ρ) of the FRC are time-dependent properties. In this sense, the changes in K , c , and ρ are assumed to vary similarly to plain concrete by the equations provided by the Eurocode [32]. The specific heat of concretes produced with siliceous and calcareous aggregates vary with temperature according to the Eq. (11).

$$c(T) = \begin{cases} 900, & 20\text{ }^\circ\text{C} \leq T \leq 100\text{ }^\circ\text{C} \\ 900 + (T - 100), & 100\text{ }^\circ\text{C} < T \leq 200\text{ }^\circ\text{C} \\ 1000 + (T - 200), & 200\text{ }^\circ\text{C} < T \leq 400\text{ }^\circ\text{C} \\ 1100, & 400\text{ }^\circ\text{C} < T \leq 1200\text{ }^\circ\text{C} \end{cases} \quad (11)$$

where c is the specific heat of concrete (in $\text{J.kg}^{-1}\text{K}^{-1}$); and T is the temperature (in $^\circ\text{C}$). The changes in density of concrete occurs due to the dehydration of hydrated products and consequent water loss, which may be computed by a multilinear equation as:

$$\rho(T) = \begin{cases} \rho_R, & 20\text{ }^\circ\text{C} \leq T \leq 115\text{ }^\circ\text{C} \\ \rho_R \left[1 - \frac{0.02(T - 115)}{85} \right], & 115\text{ }^\circ\text{C} < T \leq 200\text{ }^\circ\text{C} \\ \rho_R \left[0.98 - \frac{0.03(T - 200)}{200} \right], & 200\text{ }^\circ\text{C} < T \leq 400\text{ }^\circ\text{C} \\ \rho_R \left[0.95 - \frac{0.03(T - 400)}{800} \right], & 400\text{ }^\circ\text{C} < T \leq 1200\text{ }^\circ\text{C} \end{cases} \quad (12)$$

where ρ is the density of concrete as a function of temperature (in kg.m^{-3}); ρ_R is the density of concrete at room temperature (in kg.m^{-3}); and T is the temperature (in $^\circ\text{C}$). The concrete density at room temperature was considered to be 2430 kg/m^3 , based on the work of Serafini et al. [30]. Lastly, the thermal conductivity of normal-weight concretes exposed to temperatures between 20 and $1200\text{ }^\circ\text{C}$ can be determined by the average of lower and upper limit values given by:

$$K_U = 2 - 0.2451 \left(\frac{T}{100} \right) + 0.0107 \left(\frac{T}{100} \right)^2 \quad (13)$$

$$K_L = 1.36 - 0.136 \left(\frac{T}{100} \right) + 0.0057 \left(\frac{T}{100} \right)^2 \quad (14)$$

where K_U is the upper limit for the thermal conductivity (in $\text{W}\cdot\text{m}^{-1}\text{K}^{-1}$); K_L is the lower limit for the thermal conductivity (in $\text{W}\cdot\text{m}^{-1}\text{K}^{-1}$); and T is the temperature (in $^{\circ}\text{C}$).

3. FRC bearing capacity

3.1 Constitutive law

The constitutive law employed is based on a stress-block approach defined by the design compressive strength (f_{cd}) and the design post-crack tensile strength for the ultimate crack-opening (f_{Ftud}), as show in Fig. 2. The mechanical properties of the composite are influenced by the increase in temperature, which is computed by the use of coefficients of mechanical degradation as reduction factors in literature [13] and in design guidelines [32,33].

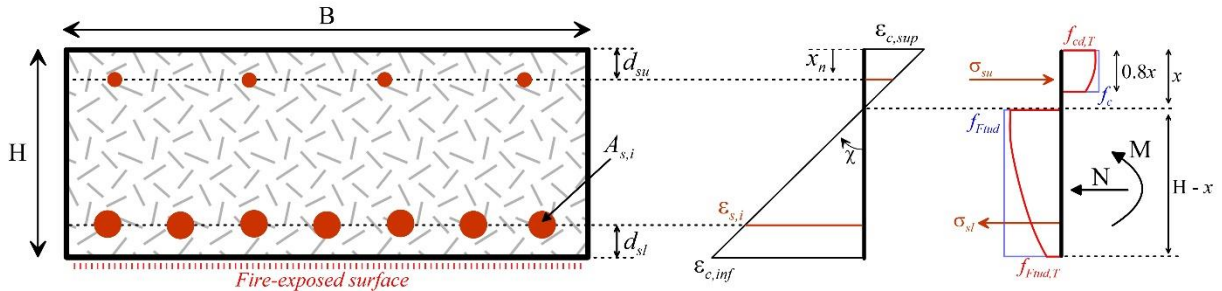


Figure 2 – Stress-block constitutive law adopted for the FRC

In this context, the FRC compressive strength was calculated as a function of temperature based on the cylinder compressive strength and the respective coefficient of mechanical degradation, as:

$$f_{cd,T} = K_c \frac{f_{ck,R}}{\gamma_c} \quad (15)$$

where $f_{cd,T}$ is the design compressive strength at a given temperature (in MPa); K_c is temperature-dependent coefficient of mechanical degradation; $f_{ck,R}$ is the characteristic compressive strength at room temperature (in MPa); and γ_c is the partial safety factor, which is taken as $\gamma_c = 1$ in case of fire events [28]. The mechanical degradation of f_{cd} and f_{sy} are represented by K_c and K_{sy} , respectively, and defined as a function of temperature according to the values prescribed by the Eurocode [32], as shown in Figure 3. The K_{sy} value is based on the reductions in the yield strength of hot rolled steel.

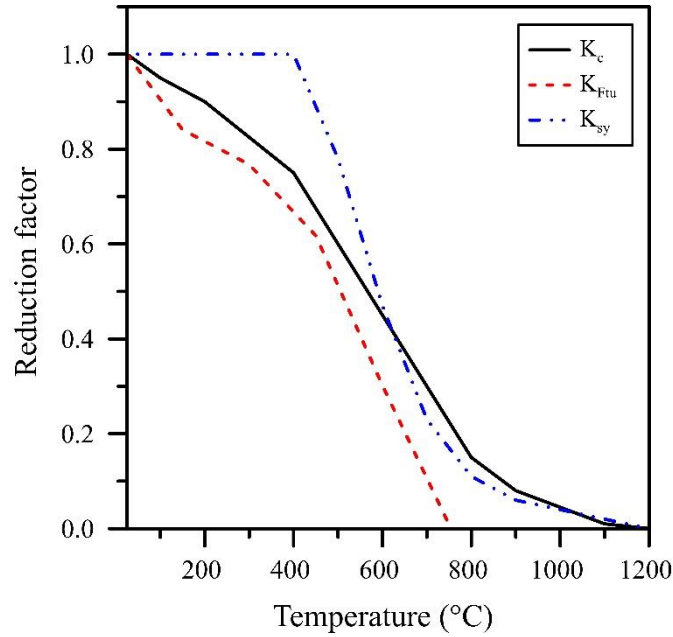


Figure 3 – Temperature-dependent coefficient of mechanical degradation for f_c and f_{Ftu}

The behavior in tension is computed based on the rigid-plastic model presented by the *fib* Model Code 2010 [28] and the tensile strength for ultimate limit state (ULS) condition may be determined by the EN 14651 three-point bending test procedure [34]. The design post-crack tensile strength of the composite can be calculated as a function of temperature, as:

$$f_{Ftud,T} = K_{Ftu} \cdot \frac{f_{R3k}}{3} \cdot \frac{1}{\gamma_F} \quad (16)$$

where $f_{Ftud,T}$ is the design post-crack tensile strength associated with the ultimate crack-opening (in MPa); K_{Ftu} is the coefficient of mechanical degradation for the post-crack tensile strength as a function of temperature; and f_{R3k} is the characteristic flexural tensile strength relative to the ULS at room temperature (in MPa). The mechanical degradation of f_{Ftud} is represented by K_{Ftu} , which is defined as a function of temperature according to the experimental results obtained by Serafini et al. [13] and presented in Figure 3.

In cases where reinforcing steel is considered, the design yield strength of steel (f_{sd}) is reduced according to the yield strength reduction factor (K_{sy}) prescribed by the Eurocode [32], as described in Eq. (17).

$$f_{sd,T} = K_{sy} \cdot f_{sy} \cdot \frac{1}{\gamma_F} \quad (17)$$

where $f_{sd,T}$ is the design yield strength of steel (in MPa); K_{sy} is the coefficient of mechanical degradation for the yield strength of steel as a function of temperature; and f_{syk} is the characteristic steel yield strength at room temperature (in MPa).

3.2 Cross-sectional modelling

The procedure begins with the thermal simulation performed based on the procedure presented in Section 2. After the thermal simulation is completed, the distribution of temperatures is available in the points of the cross-section for every instant of time, respecting the subdivisions adopted in Eq. 4 and Eq. 5. Once the temperature and the constitutive relationship of the FRC at that temperature are known, the equations for the rotational and translational stability of the cross-section can be written as:

$$N = B \cdot \left[\sum_{i=1}^{n_{sc}} f_{cd,(T_i)} \cdot \Delta z + f_{cd,(T_{0.8x})} \cdot (0.8x - n_{sc} \cdot \Delta z) - \sum_{i=1}^{n_{st}} f_{Ftud,(T_{n_s-n_{si}+i})} \cdot \Delta z - f_{Ftud,(T_x)} \cdot (H - x - n_{st} \cdot \Delta z) \right] + n_{su} \cdot A_{su} \cdot f_{sd,(T_{su}\chi)} \cdot \beta_1 - n_{sl} \cdot A_{sl} \cdot f_{sd,(T_{sl}\chi)} \cdot \beta_2 \quad (18)$$

$$M = B \cdot \left[\sum_{i=1}^{n_{sc}} f_{cd,(T_i)} \cdot \Delta z \cdot \left[\frac{H}{2} - \Delta z \cdot \left(i - \frac{1}{2} \right) \right] + f_{cd,(T_{0.8x})} \cdot (0.8x - n_{sc} \cdot \Delta z) \cdot \left[\frac{H}{2} - 0.8x + \frac{0.8x - n_{sc} \cdot \Delta z}{2} \right] + \sum_{i=1}^{n_{st}} f_{Ftud,(T_{n_s-n_{si}+i})} \cdot \Delta z \cdot \left[\frac{H}{2} - \left(n_{st} - i + \frac{1}{2} \right) \cdot \Delta z \right] + f_{Ftud,(T_x)} \cdot (H - x - n_{st} \cdot \Delta z) \cdot \left[\frac{H}{2} - x - \frac{H - x - n_{st} \cdot \Delta z}{2} \right] \right] + n_{su} \cdot A_{su} \cdot f_{sd,(T_{su}\chi)} \cdot \left(\frac{H_i}{2} - d_{su} \right) \cdot \beta_1 + n_{sl} \cdot A_{sl} \cdot f_{sd,(T_{sl}\chi)} \cdot \left(\frac{H_i}{2} - d_{sl} \right) \cdot \beta_2 \quad (19)$$

where n_s is the quantity of subsections in the cross-section; n_{sc} is the quantity of compressed subsections located within $0.8x$; n_{st} is the quantity of subsections subjected to tensile stresses; T_x is the temperature at the position of the neutral axis; $T_{0.8x}$ is the temperature at distance $0.2x$ from the neutral axis; n_{su} is the amount of rebars in the upper region of the section (extrados); n_{sl} is the amount of rebars in the

lower region of the section (intrados); A_{su} is the cross-sectional area of steel (unitary) in the upper region; A_{sl} is the cross-sectional area of steel (unitary) in the lower region; H is the total height at time t ; H_i is the initial height of the segment; d_{su} is the concrete cover at the extrados; d_{sl} is the concrete cover at the intrados; and the β_1 and the β_2 variables compute the signal for the contribution of rebars in the rotational and transitional stability according to Eq. (20) and Eq. (21), respectively. The latter is required since the failure planes are accounted by inputting a vector of neutral axes x contained between the intrados and extrados of the FRC segment, which is posteriorly necessary for assessing the M-N interaction envelopes.

$$\beta_1 = \begin{cases} \frac{d_{su} - x}{|d_{su} - x|} & \text{if } x \neq d_{su} \\ -1 & \text{if } x = d_{su} \end{cases} \quad (20)$$

$$\beta_2 = \begin{cases} \frac{(x - H + d_{sl})}{|x - H + d_{sl}|} & \text{if } x \neq (H - d_{sl}) \\ 1 & \text{if } x = (H - d_{sl}) \end{cases} \quad (21)$$

3.3 Validation of the model

The validation of the thermal model was conducted by exposing steel fiber reinforced concrete (SFRC) prismatic specimens to fire, following the same experimental procedure presented by Serafini et al. [30]. Prismatic specimens measuring 150 x 150 x 550 mm were produced containing thermocouples positioned at preset distances of 3, 6, 9, 12, and 15 cm from the surface subjected to fire. The fire event was simulated by a vertical fire simulator with a height and width of 2.85 m each and a depth of 0.95 m, this containing six industrial methane gas burners that generated the flames.

The prismatic specimens were positioned in structural masonry wall and exposed to a uniaxial heat regime following the HFC (Fig. 4a). It is important to remark that the experimental setup and heating regime aimed to reproduce the heating conditions at the intrados of a tunnel lining. The thermal distribution was acquired in through thermocouple readings in steps of 30 s during the whole test. On the other hand, the validation of the mechanical model was carried out by considering the results on the characterization of the post-fire mechanical properties of the abovementioned SFRC specimens subjected to fire. In this regard, the fire-exposed prismatic specimens were tested according to EN 14651 [34], the region closer to the fire maintained facing downward during the test, in order to characterize the post-cooling bending capacity of the SFRC specimens (Fig. 4b).

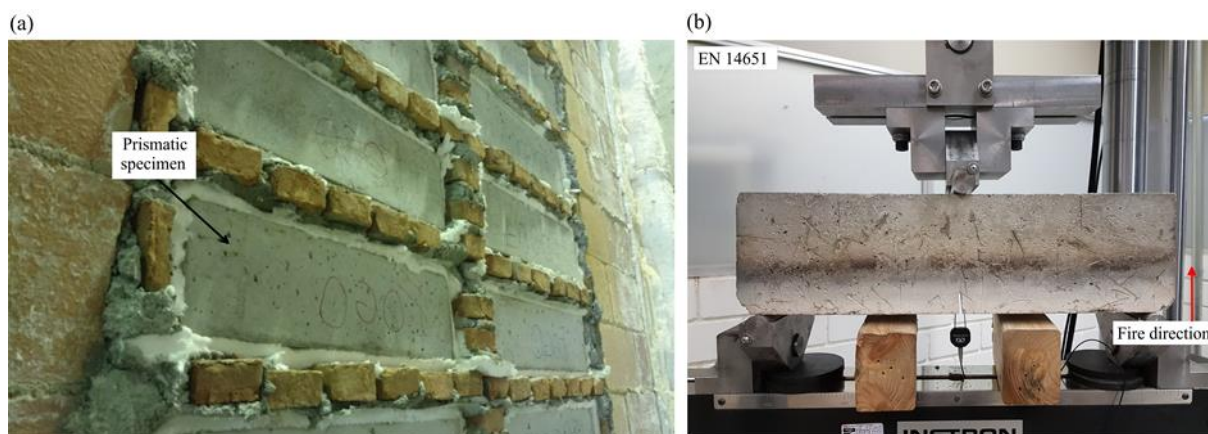


Figure 4 – (a) Prismatic specimens positioned and (b) bending test configuration

Both the experimental and numerical fire-induced temperature distributions are presented in Figure 5a. These results allow confirming that the errors of the thermal model are below 11% for $t = 120$ min, independently of the depth in the SFRC specimen. Likewise, it is to be remarked that errors decrease as the exposure time t increases, the maximum error being below 42% ($t < 20$ min) in all cases. The latter, however, is not significant from the design perspective since the drop of bearing capacity starts to be noticeable for time exposure superior to 15 min, at which the thermal model provides reliable results. Therefore, the thermal model resulted to be capable of predicting the distribution of temperatures within the section, with sufficient accuracy for structural design purposes, especially when considering long-time fire exposures.

For validation purposes, the resisting bending moment at $\text{CMOD} = 2.5$ mm ($M_{u,E}$) was determined based on the load-CMOD curves by imposing equilibrium conditions. The $M_{u,E}$ was then compared to the bending capacity obtained numerically ($M_{u,N}$) by computing the ratio $M_{u,N}/M_{u,E}$ (Fig. 5b), which provides information on both the model accuracy and the margin of safety respect to the experimental results. Likewise, the results presented by Agra [35] were also been included into the database in order to increase the representativeness of this validation. In this regard, it must be remarked that Agra used the same materials and proportions, while also following the experimental procedure exposed in Serafini et al. [30]. However, Agra tested smaller prismatic specimens of 100 x 100 x 350 mm, which does not affect the results of this validation.

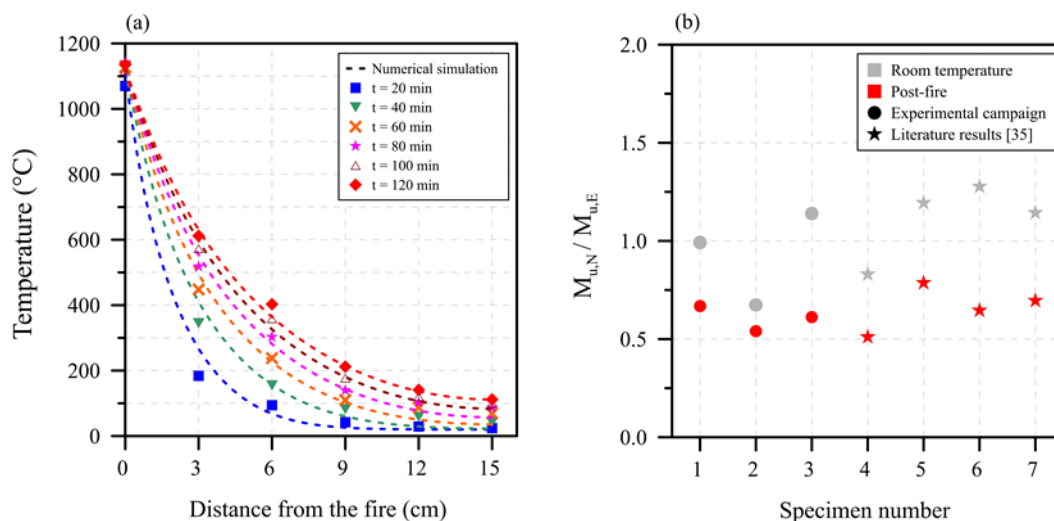


Figure 5 – (a) fire-induced temperature distribution and (b) $M_{u,N}/M_{u,E}$ considering the experimental and numerical results

The results presented in Figure 5b permit to draw the following conclusions regarding the mechanical model validation: (1) the mean $M_{u,N}/M_{u,E}$ for room temperature is 1.04 (CoV = 20.8%), which confirms the capability of the model to predict the bending capacity of SFRC elements subjected to normal temperature. Moreover, this CoV = 20.8% is aligned with the expected variability of both the post-cracking flexural strength of SFRCs and the accuracy of the constitutive equations and material partial safety factors provided in the *fib* MC-2010 for simulating the post-cracking response of SFRC specimens [36]. And (2), for post-fire conditions, the average $M_{u,N}/M_{u,E}$ is 0.64 (CoV = 14.7%), which denotes that the mechanical model yields to conservative results, with rather low dispersion of the results (taking into account the intrinsic scatter of the SFRC post-cracking mechanical properties [37]). This may be justified by the adoption of constitutive equations that may not precisely represent the thermal-related changes in mechanical properties (*i.e.* distribution of the damage along the cross-section), but are in favor of safety and accepted in the design guidelines [27,28]. Based on the outcomes of these validations, the prediction capacity and accuracy of both models were found to be satisfactory and sufficient for the purpose of this research.

4. Numerical investigation

In light of the discussions provided in the previous sections, a parametric investigation was conducted aiming to assess the effect of fire in the bearing capacity of the RC and FRC sections. The following scenarios were employed to assess the deterioration of bending capacity on RC and FRC sections exposed to fire:

- d) A conventional RC with $A_s = 792 \text{ mm}^2$ on the upper region and lower region of the section. This value was chosen since it is minimum longitudinal reinforcement ratio for compressed members according to the *fib* MC-10, which aims to ensure the ductility response in case of cracking due to transient loads related to transportation, stacking, and manipulation of the segments. The sensitivity to fire action was evaluated on a RC section with a concrete cover of $c = 30 \text{ mm}$ (RC30) based on the XC4 exposure class prescribed by the *fib* MC-10 [28], and another RC section with $c = 50 \text{ mm}$ (RC50).
- e) A FRC 45 3c composite without any steel rebar reinforcement. This solution can be used in those lining stretches along which low-moderate forces are expected and minimum amount of reinforcement is required, in which the conventional rebar reinforcement is replaceable by fibers. Likewise, local reinforcement is required to control splitting and spalling cracks due to the thrust of the jacks during excavation.
- f) A FRC 45 3c composite with the same steel reinforcement described in (1), being identified as RC30-FRC for the hybrid option with $c = 30 \text{ mm}$, and RC50-FRC for the one with $c = 50 \text{ mm}$. This hybrid reinforcement approach could be of technical interest in those stretches along which the external forces are demanding in magnitude and/or cracking is expected due to the thrust of the TBM, resulting in the need for additional reinforcement to control cracking.

These possible configurations for the cross-section of the tunnel were analyzed in this paper as a function of the temperature-time pattern numerically obtained, based on the fire curve adopted and the axial load ratio applied. Table 1 shows the input parameters adopted for the thermo-mechanical simulations conducted in this study.

Table 1 – Input parameters adopted for the thermo-mechanical simulation

Property	Input value
H (mm)	400
B (mm)	1000
f_{cd} (MPa)	45
f_{R3d} (MPa)	3.0
f_{sd} (MPa)	434
Initial temperature (°C)	25
Concrete density (kg/m ³)	2400
Specific heat (J.kg ⁻¹ .K ⁻¹)	900
Convective heat coefficient (W.m ⁻² .K ⁻¹)	25
Thermal conductivity (W.m ⁻¹ .K ⁻¹)	1.6
Emissivity	0.9

4.1 Effect of fire curve and reinforcement type

First, the simulation was conducted considering one mild fire scenario and one severe fire scenario, thus following, respectively, the ISO 834 and the HFC fire curves. These fire curves were employed on the RC, FRC, and RC-FRC solutions. Moreover, the reduction in bending capacity is presented for two axial loading conditions: (1) considering simple bending to be representative of lining stretches or sections where the axial load is low in magnitude (*i.e.* $N/A_c \cdot f_{cd,25^\circ\text{C}} = 0$); (2) considering a 0.20 axial load ratio to be representative stretches placed at medium-large buried sections. Figure 6 illustrates the changes in bending capacity of the sections exposed to the HFC and the ISO 834 fire curves. At this moment, the analysis is conducted without considering the occurrence of thermal spalling.

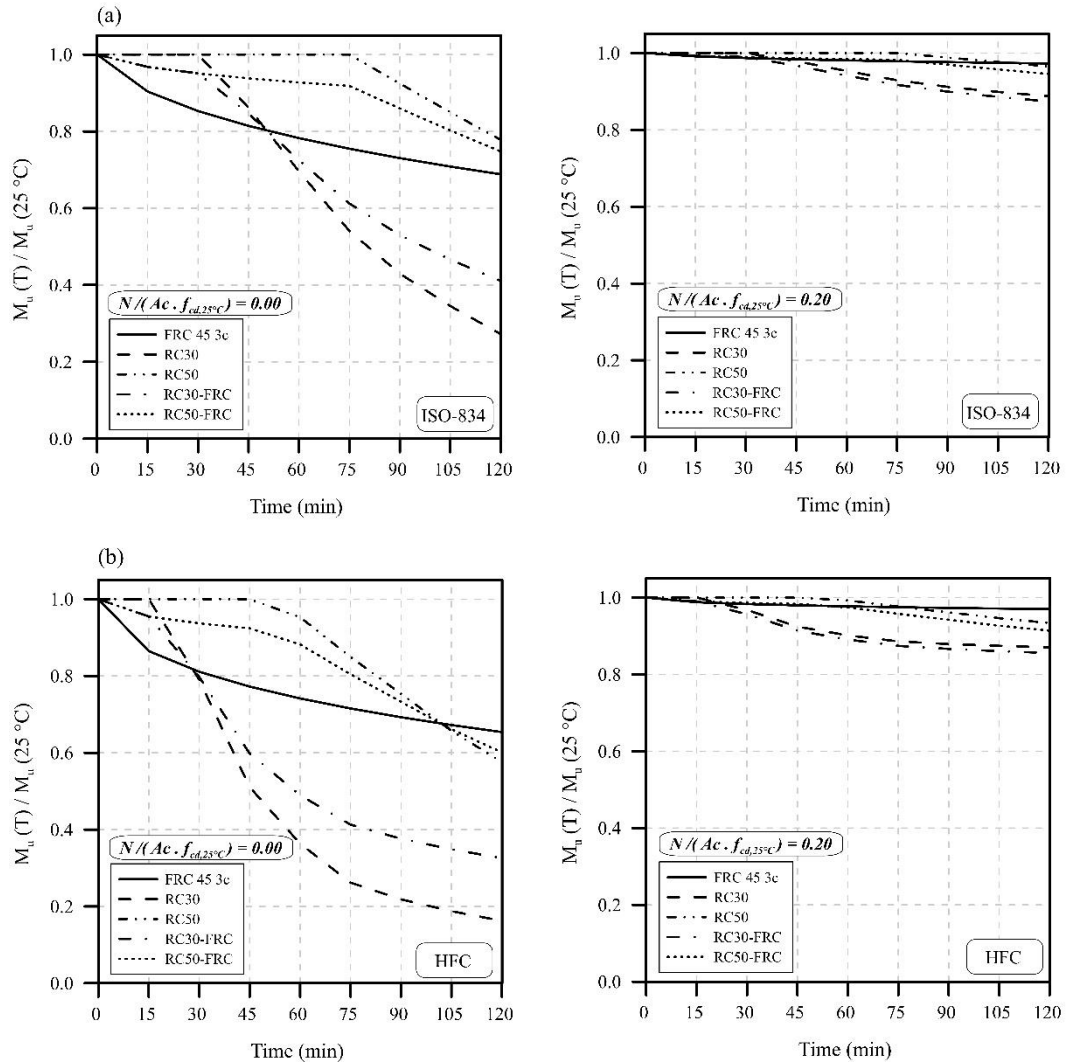


Figure 6 – Changes in bending capacity of the sections exposed to (a) the ISO 834 and (b) the HFC fire curves

For all reinforcement types, the reductions in bending capacity were lower for the sections affected by the ISO-834 than those affected by the HFC, independently of the magnitude of the axial load. This difference is more pronounced for lower values of t , which is reasonable considering that the ISO-834 fire curve prescribes lower heating rate and lower maximum temperature values than the HFC. The reduction in FRC 45 3c bending capacity caused by the HFC was 3.5% to 5.5% greater than the reductions caused by the ISO-834, which shown to be a range valid for all values of t . Therefore, the FRC solution shows very low sensitivity to the characteristics of the fire curves evaluated in this study, which may be attributed to the distributed reinforcement and the reduced contribution of the post-crack tensile properties to the sectional bearing capacity [16]. In this sense, the FRC simple bending capacity

reduced by ~31% and ~35% after $t = 120$ min of ISO 834 and HFC fire curve, respectively.

The RC30 simple bending capacity reduced by ~73% and ~84% when exposed to the respective ISO-834 and HFC fire curves after $t = 120$ min, whereas the RC50 bending capacity reduced by ~22% and ~35%. Therefore, the increase in concrete cover considerably reduced the sensitivity of the RC solution to fire, independently of the fire curve adopted. This decreased fire-sensitivity is associated with the lower temperatures developed in steel and the consequently reduced mechanical deterioration of the rebars, as shown in Figure 7. A more rapid increase in temperature is verified for rebars located at $c = 30$ mm than for $c = 50$ mm, which is also more pronounced when the RC solutions are exposed to HFC than when exposed to the ISO-834 fire curve.

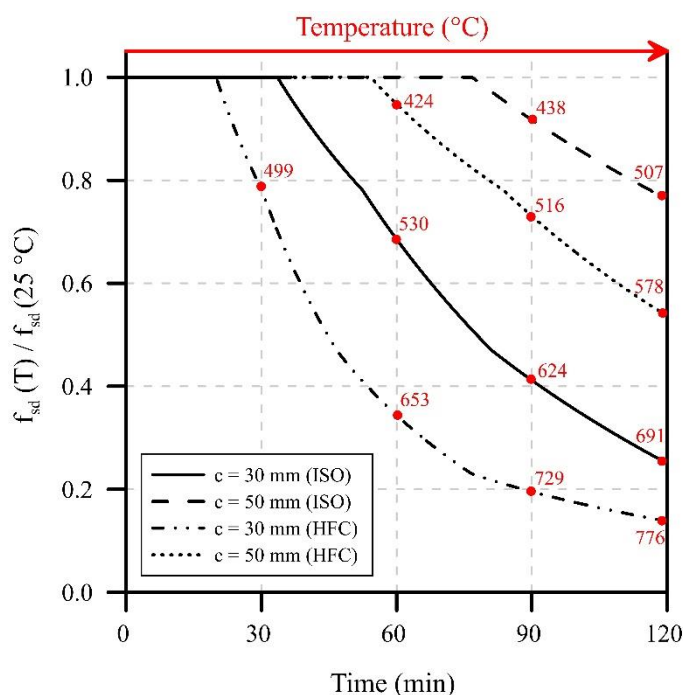


Figure 7 – Distribution of temperatures and the respective reduction in the yield strength of rebars

The hybrid solution RC30-FRC showed a simple bending capacity reduction of ~59% and ~63% when exposed to the respective ISO-834 and HFC fire curves after $t = 120$ min, while the RC50-FRC showed reductions of ~25% and ~40%. In this sense, it is possible to observe that the RC and hybrid RC-FRC solutions are considerably more sensitive to the different fire curves than the FRC solution, which is justified by the considerable contribution of the localized reinforcement provided by rebars to the bearing capacity.

Given the severe nature of the HFC, the analysis henceforth is focused on the results obtained by sections exposed to this particular fire curve. When comparing the RC-FRC and the RC solutions, the RC30-FRC section showed lower reductions than those observed for RC30, especially for $t \geq 30$ min. Contrarily, the reductions in RC50-FRC bending capacity were greater than those obtained by RC50, especially during the first 90 minutes of the fire, reaching a comparable reduction for $t = 120$ min. These results show that the addition of fibers to RC sections is beneficial particularly when the reinforcement provided by rebars is considerably reduced during the fire. However, when the rebars remain relatively unaffected by temperature, a slight reduction in bending capacity is noticed due to the deterioration of the fibrous reinforcement. Therefore, the behavior of RC-FRC sections is highly dependent on the position of rebars and is directly associated with the contribution of fibers to the bending capacity.

The RC50 and RC50-FRC solutions obtained the lowest reductions in bending capacity, except when compared to the FRC at $t = 120$ min. Nevertheless, the RC30 solution was the most fire sensitive option among all the reinforcement solutions and fire scenarios evaluated. When the solutions are subjected to an axial load ratio of 0.20, the reductions in the bending moment capacity are considerably mitigated. This was evidenced for all reinforcement types and it occurs because a failure mode based on the crushing of the compressive layer that is not affected by fire occurs. It is important to remark that the sections subjected to an increased axial load ratio experience greater reductions in bending moment capacity whenever the compressive region is affected by fire, as discussed in detail by di Carlo et al [16].

Moreover, the results proved that the cross-sectional ductility (represented by the curvature, χ) increases with the fire duration, as shown in Fig. 8. This increase was greater for RC30 and RC30-FRC alternatives, independently of the axial load ratio. Among the RC and RC-FRC solutions, the RC50 and RC50-FRC solution have shown similar ductility increments and obtained the lowest increase in ductility due to the lower effective depth of the reinforcement. For simple bending, the FRC obtained the lowest increase in ductility after $t = 120$ min. When the section is subjected to a 0.20 axial load ratio, the RC solutions and the respective hybrid alternatives have shown similar ductility patterns and the FRC solution had the lowest increase in ductility, which occurs due to the failure being governed by concrete crushing.

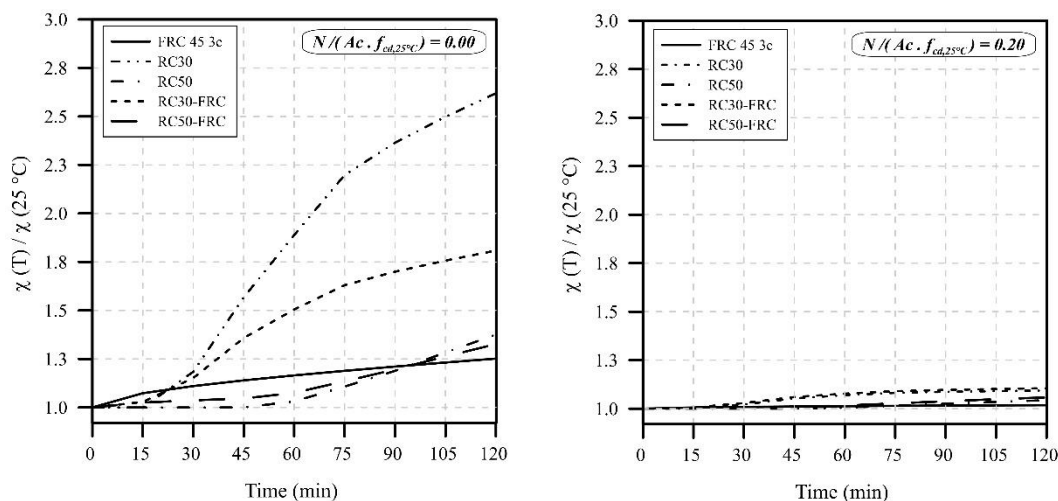


Figure 8 – Effect of fire on the ductility of the reinforcing solutions when affected by HFC

4.2 Effect of thermal spalling

In light of the bending capacity reductions presented in Section 4.1, the effect of thermal spalling was evaluated considering the HFC since it has proven to be the worst fire scenario evaluated in this study. Experimental results in literature demonstrated the dependance between the onset of thermal spalling and the thermal gradients in normal-strength concrete without micro-fibers, in which spalling began at $t = 2$ min when exposed to RWS fire curve [31]. In order to ensure a conservative approach, the spalling was considered to begin at $t = 0$ min for simulation purposes.

The reduction in bending capacity of the sections is evaluated considering two spalling parameters: the spalling rate (R_{sp}) and the percentage of section lost (s_L). These parameters may be determined by measuring the spalling depth as a function of time in experimental campaigns using fire simulators and a concrete representative of the structure [30]. Considering the parametric nature of this study, R_{sp} values of 100 mm/h and 300 mm/h were adopted as moderate and severe spalling rates based on parameters of a normal-strength concrete without microfibers and with different moisture contents [31]. The s_L values of 5%, 10%, and 20% were arbitrarily adopted based on the hypothesis that greater section losses would represent extremely severe cases [15,20]. In this sense, the changes in the height of the section as a function of time and the spalling parameters is presented in Fig. 9.

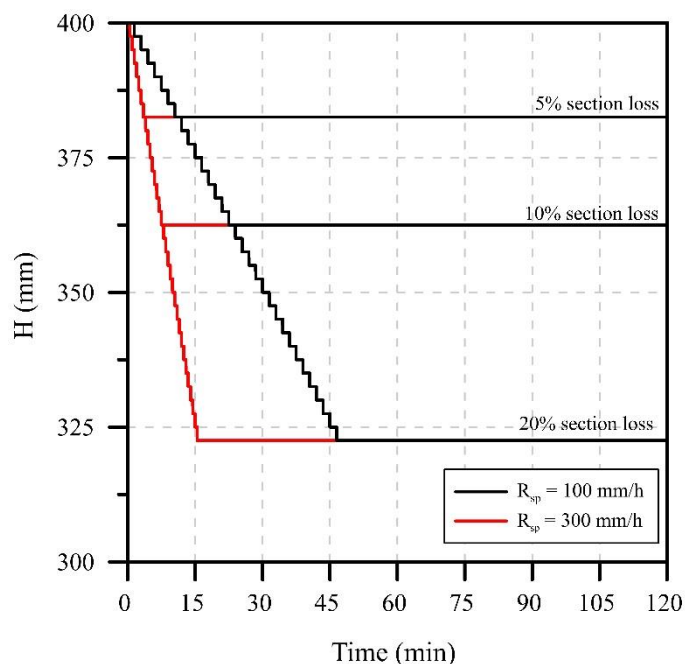


Figure 9 – Change in the height of the section as a function of time and the spalling parameters

Considering the aforementioned parameters, the deterioration of the FRC section as a function of R_{sp} and s_L is presented in Figure 10. The simulations considering the thermal-spalling yielded lower residual bending capacity than the scenario without the occurrence of thermal spalling – which is recognized by the NS identifier (*e.g.* FRC 45 3c - NS). For a fire duration of $t = 120$ min, the post-fire bending capacity seems to be greatly influenced by reductions in s_L and less influenced by the increase in R_{sp} . This can be observed for simple bending, as well for sections with an axial load ratio of 0.20. However, the increase in R_{sp} considerably influences the rate of reduction in the bending capacity for the initial moments of fire, with exception of $s_L = 5\%$. Regarding the FRC simple bending scenario, reductions of $\sim 40\%$, $\sim 49\%$, and $\sim 60\%$ occurred for the respective s_L values of 5%, 10%, and 20% after $t = 120$ min. For sections with 0.20 axial load ratio, reductions of $\sim 9\%$, 15%, and $\sim 27\%$ occurred for the respective s_L values of 5%, 10%, and 20% after $t = 120$ min.

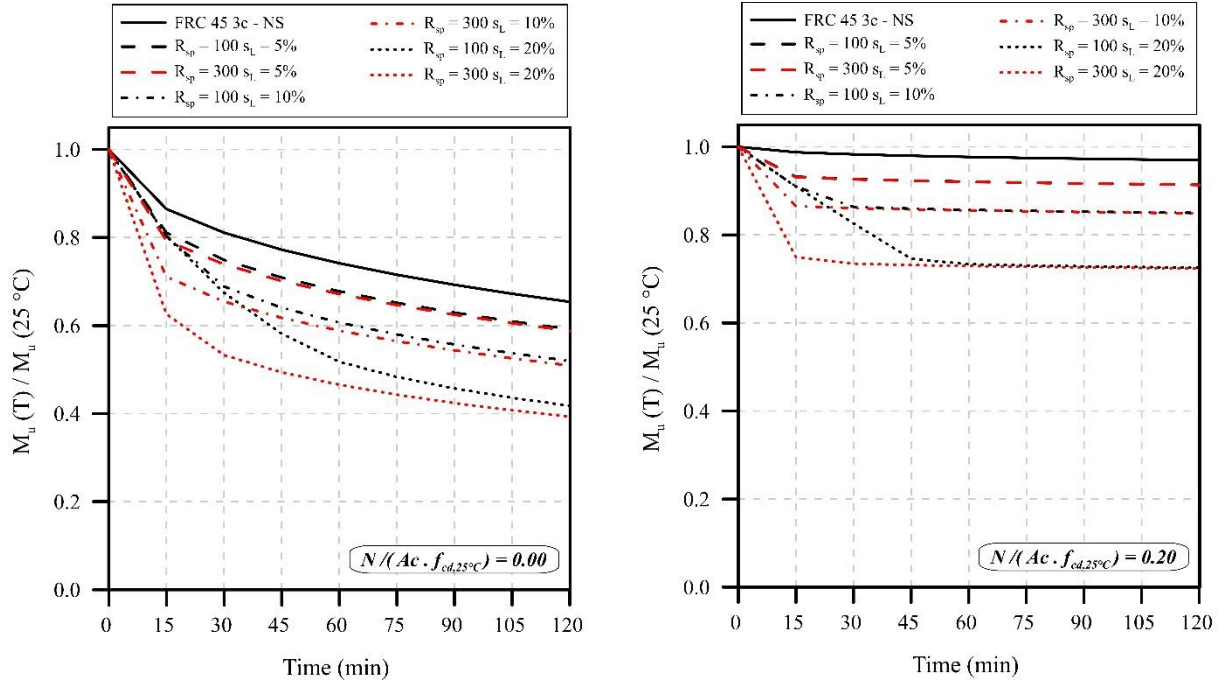


Figure 10 –Reductions in bending capacity of FRC 45 3c section as a function of R_{sp} and s_L

Figure 11 illustrates the reductions in bending capacity of RC30 and RC30-FRC solutions as a function of R_{sp} and s_L . Regarding the RC30 section, the occurrence of thermal spalling reduced the simple bending capacity by over 90% within the first 30 minutes of fire, with minimal influence of R_{sp} and s_L . This occurs because the temperature on the rebars increase rapidly given the proximity with the heated surface and the occurrence of thermal spalling, as depicted in Fig. 12. Regarding the RC30-FRC section, the results indicate that the addition of fibers resulted in a solution that is less sensitive to thermal-spalling than the RC30 counterpart. The RC30-FRC simple bending capacity reduced by ~76%, 82%, and 87% for the respective s_L values of 5%, 10%, and 20% after $t = 120$ min. Even with this consideration, the bending capacity of both the RC30 and RC30-FRC sections are reduced to drastically low values when thermal spalling occurs. For sections subjected to an axial load ratio of 0.20 the reductions are considerably lower due to the failure being governed by concrete crushing.

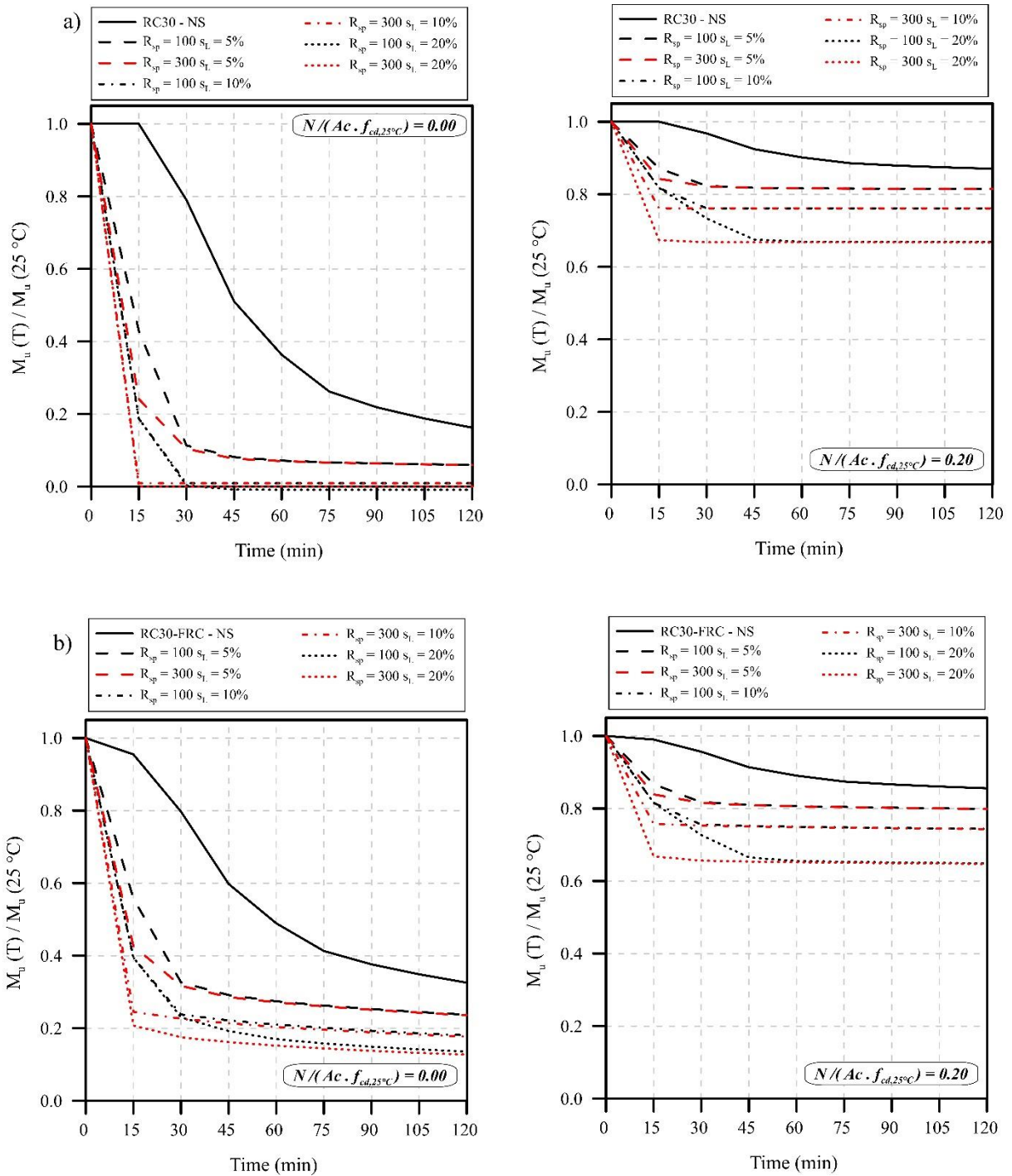


Figure 11 – Reductions in bending capacity of (a) RC30 and (b) RC30-FRC solutions as a function of R_{sp} and s_L

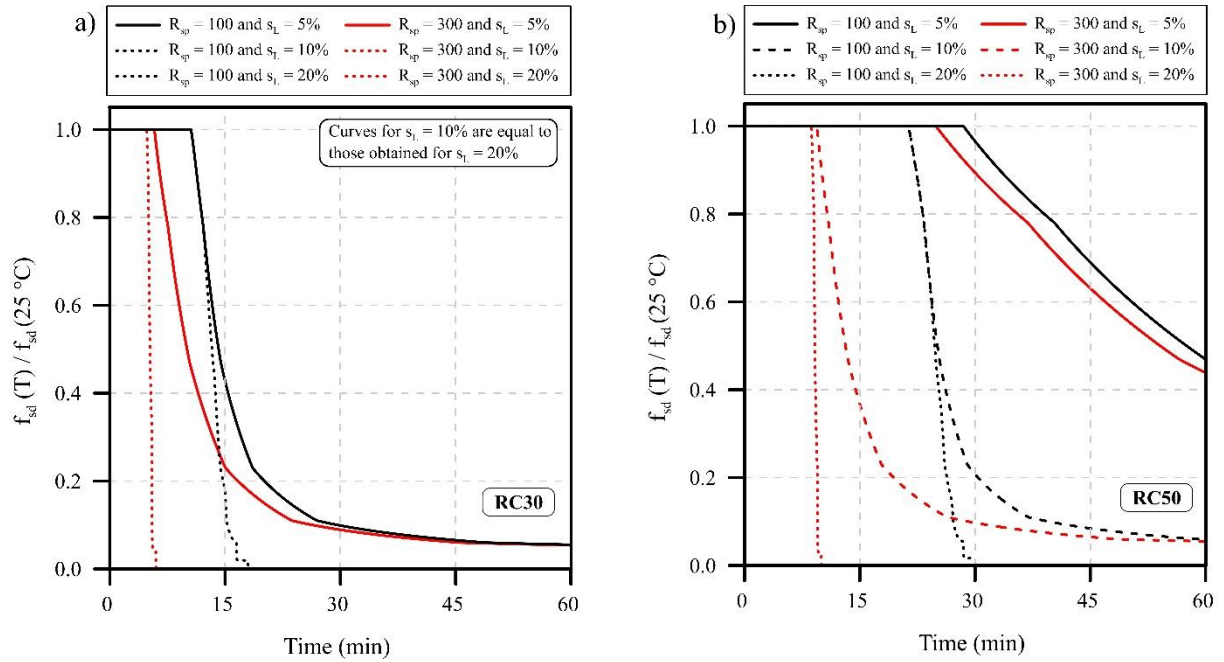


Figure 12 – Effect of R_{sp} and s_L on the tensile strength of rebars in (a) RC30 and (b) RC50 sections

Figure 13 illustrates the reductions in bending capacity of RC50 and RC50-FRC solutions. Considering $t = 120$ min, the occurrence of thermal spalling reduced the simple bending capacity of RC50 sections by over 88% independently of the s_L value. However, when $s_L = 5\%$ the rate of reduction in bending capacity is slightly lower than for greater s_L values. For greater s_L values, reductions of over $\sim 80\%$ are registered within the first 30 minutes of fire. These drastic reductions are a result of the rapid increase in temperature of the rebars due to the reductions in H and the aggravated thermal field induced in the section (see Fig. 12). Although the RC50-FRC solution seems to be slightly less sensitive than RC50, the reductions bending capacity were greater than 65% after $t = 120$ min. For sections with 0.20 axial load ratio, reductions of $\sim 35\%$ and $\sim 57\%$ occurred for the respective s_L values of 20% and 40% after $t = 120$ min, independently of the position of the rebars.

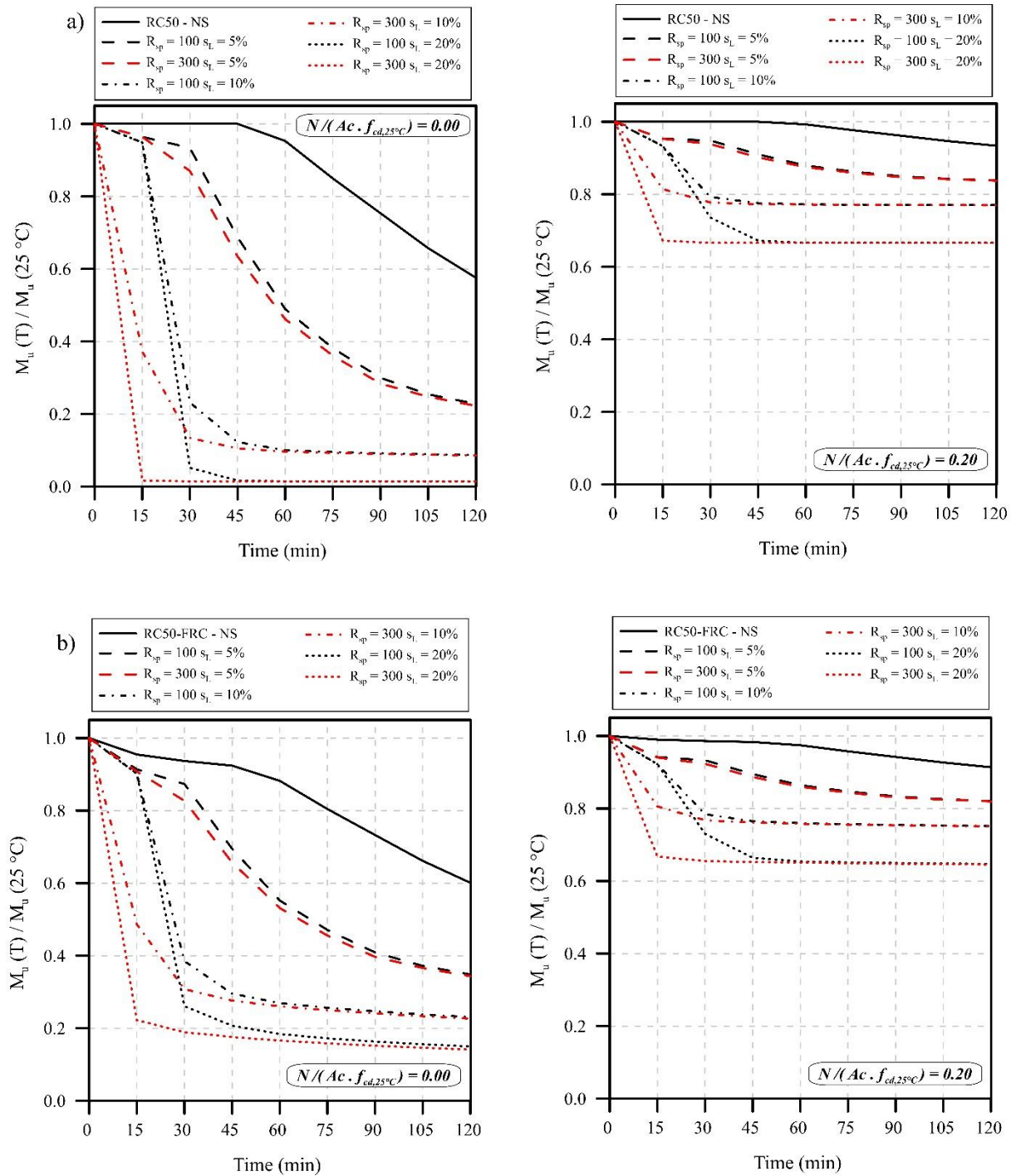


Figure 13 – Reductions in bending capacity of (a) RC50 and (b) RC50-FRC solutions as a function of R_{sp} and s_L

Therefore, the results obtained in this parametric study are indicative that the occurrence of spalling considerably affects the bearing capacity of FRC, RC, and hybrid RC-FRC sections. The RC30 and RC50 and their respective hybrid options have shown to be very sensitive to the occurrence of thermal spalling, since the reductions in H resulted in a more pronounced exposure of the rebars and aggravated thermal field. Additionally, the increase in concrete cover has a minor influence in

mitigating the reductions in bearing capacity caused by mild or severe thermal spalling scenarios. Moreover, the RC-FRC solutions have shown slightly lower bending reductions than the respective RC solution. This means that the addition of fibers may mitigate the reductions in bending capacity of RC sections. Lastly, the FRC solution have shown to be the least sensitive option evaluated, especially for lower s_L values. This occurred because of the contribution of fibers to the sectional bending capacity and the distributed nature of the fibrous reinforcement.

5. Conclusions

In this research paper, a numerical model for the evaluation of the bearing capacity of cross-sections subjected to fire loads and the thermal spalling effects was implemented. Posteriorly, the model was used to perform an extensive parametric analysis for which reinforced concrete (RC), fiber reinforced concrete (FRC), and the hybrid solution (RC-FRC) were analyzed involving different axial load levels, fire curves, concrete cover and thermal spalling parameters. In this context, based on the results obtained, the following conclusions could be drawn:

- Sections exposed to the hydrocarbon fire curve suffered greater bending capacity reductions than those exposed to the ISO 834 fire curve, independently of the magnitude of axial load. When spalling is inexistent, both FRC and RC50-FRC solutions proved to be less sensitive to fire respect in comparison with the conventional RC30 solution.
- The cross-sectional ductility, represented by the curvature (χ), increases with the fire duration. The increase was greater for RC30 and RC30-FRC alternatives, independently of the axial load ratio. For simple bending, the RC50 and RC50-FRC have shown similar ductility increments, while the FRC obtained the lowest increase in ductility at $t = 120$ min. When the section is subjected to a 0.20 axial load ratio, the RC solutions and the respective hybrid alternatives have shown similar ductility patterns and the FRC solution had the lowest increase in ductility.
- The increase in spalling rate (R_{sp}) influences the rate of reduction in the bending capacity at the early stage of the fire, while the increase in section lost ratio (s_L) influence the bending capacity at intermediate-final stages of the fire. This influence was evidenced for all reinforcing strategies and axial load ratios evaluated in this parametric study.

- The RC sections analyzed experienced a drastic bending capacity reduction with the occurrence of thermal spalling, being greater than ~90% for RC30 and ~80% for RC50. The increase in concrete cover had a minor role in mitigating the reductions of bearing capacity caused by mild or severe thermal spalling scenarios, especially for lower values of section lost. Although a considerable deterioration is observed, the FRC solution yielded the lower reductions in bending capacity among all the reinforcing solutions tested.
- The reductions in bending capacity are lower for cross-section subjected to axial load. This was evidenced for all the reinforcement solutions evaluated in this study, with and without thermal spalling. This occurs because the mode of failure changes to crushing of the most compressive concrete layer, which is further from the heating surface and, thus, less affected by fire.

Therefore, the results show that the thermal-mechanical model and the spalling subroutine implemented in this study may be employed to determine the bending capacity of RC, FRC, and hybrid RC-FRC solutions. At this end, the results represent a valuable reference for standards and guidelines worldwide, as well as for the engineering community given that the procedure serves as a tool for the design and rehabilitation of tunnel structures affected by fire.

Funding

This work was funded by the Institute for Technological Research (IPT) and its foundation (FIPT) through the New Talents Program [grant #N.01/2017 (Ramoel Serafini)] and partially funded the Conselho Nacional de Desenvolvimento Científico e Tecnológico (CNPq) [Grant # 305055/2019-4 (Antonio Domingues de Figueiredo)].

References

- [1] A. de la Fuente, P. Pujadas, A. Blanco, A. Aguado, Experiences in Barcelona with the use of fibres in segmental linings, *Tunn. Undergr. Sp. Technol.* (2012). <https://doi.org/10.1016/j.tust.2011.07.001>.
- [2] A. Caratelli, A. Meda, Z. Rinaldi, P. Romualdi, Structural behaviour of precast tunnel segments in fiber reinforced concrete, *Tunn. Undergr. Sp. Technol.* 26 (2011) 284–291. <https://doi.org/10.1016/j.tust.2010.10.003>.
- [3] A. de la Fuente, A. Blanco, J. Armengou, A. Aguado, Sustainability based-approach to determine the concrete type and reinforcement configuration of

- TBM tunnels linings. Case study: Extension line to Barcelona Airport T1, *Tunn. Undergr. Sp. Technol.* 61 (2017) 179–188. <https://doi.org/10.1016/j.tust.2016.10.008>.
- [4] J.-L. Granju, S. Ullah Balouch, Corrosion of steel fibre reinforced concrete from the cracks, *Cem. Concr. Res.* 35 (2005) 572–577. <https://doi.org/10.1016/j.cemconres.2004.06.032>.
- [5] L. Liao, A. de la Fuente, S. Cavalaro, A. Aguado, Design procedure and experimental study on fibre reinforced concrete segmental rings for vertical shafts, *Mater. Des.* 92 (2016) 590–601. <https://doi.org/10.1016/j.matdes.2015.12.061>.
- [6] L. Liao, A. de la Fuente, S. Cavalaro, A. Aguado, Design of FRC tunnel segments considering the ductility requirements of the Model Code 2010, *Tunn. Undergr. Sp. Technol.* 47 (2015) 200–210. <https://doi.org/10.1016/j.tust.2015.01.006>.
- [7] I.Y. Maevski, *Design Fires in Road Tunnels*, National Academies Press, Washington, D.C., 2011. <https://doi.org/10.17226/14562>.
- [8] W.Z. Zheng, H.Y. Li, Y. Wang, H.Y. Xie, Tensile Properties of Steel Fiber-Reinforced Reactive Powder Concrete after High Temperature, *Adv. Mater. Res.* 413 (2011) 270–276. <https://doi.org/10.4028/www.scientific.net/AMR.413.270>.
- [9] Y.-S. Tai, H.-H. Pan, Y.-N. Kung, Mechanical properties of steel fiber reinforced reactive powder concrete following exposure to high temperature reaching 800°C, *Nucl. Eng. Des.* 241 (2011) 2416–2424. <https://doi.org/10.1016/j.nucengdes.2011.04.008>.
- [10] C.S. Poon, Z.H. Shui, L. Lam, Compressive behavior of fiber reinforced high-performance concrete subjected to elevated temperatures, *Cem. Concr. Res.* 34 (2004) 2215–2222. <https://doi.org/10.1016/j.cemconres.2004.02.011>.
- [11] R. Serafini, F.P. Santos, R.R. Agra, A. De la Fuente, A.D. de Figueiredo, Effect of specimen shape on the compressive parameters of steel fiber reinforced concrete after temperature exposure, *J. Urban Technol. Sustain.* 1 (2018) 10–20. <https://doi.org/10.47842/juts.v1i1.7>.
- [12] P. Sukontasukkul, W. Pomchiengpin, S. Songpiriyakij, Post-crack (or post-peak) flexural response and toughness of fiber reinforced concrete after exposure to high temperature, *Constr. Build. Mater.* 24 (2010) 1967–1974. <https://doi.org/10.1016/j.conbuildmat.2010.04.003>.

- [13] R. Serafini, R.R. Agra, R.P. Salvador, A. de la Fuente, A.D. de Figueiredo, Double Edge Wedge Splitting Test to Characterize the Design Postcracking Parameters of Fiber-Reinforced Concrete Subjected to High Temperatures, *J. Mater. Civ. Eng.* **33** (2021) 04021069. [https://doi.org/10.1061/\(ASCE\)MT.1943-5533.0003701](https://doi.org/10.1061/(ASCE)MT.1943-5533.0003701).
- [14] D.A.S. Rambo, A. Blanco, A.D. de Figueiredo, E.R.F. dos Santos, R.D. Toledo, O. da F.M. Gomes, Study of temperature effect on macro-synthetic fiber reinforced concretes by means of Barcelona tests: An approach focused on tunnels assessment, *Constr. Build. Mater.* **158** (2018) 443–453. <https://doi.org/10.1016/j.conbuildmat.2017.10.046>.
- [15] Z. Yan, H. Zhu, J.W. Ju, Behavior of reinforced concrete and steel fiber reinforced concrete shield TBM tunnel linings exposed to high temperatures, *Constr. Build. Mater.* **38** (2013) 610–618. <https://doi.org/10.1016/j.conbuildmat.2012.09.019>.
- [16] F. Di Carlo, A. Meda, Z. Rinaldi, Evaluation of the bearing capacity of fiber reinforced concrete sections under fire exposure, *Mater. Struct.* **51** (2018) 154. <https://doi.org/10.1617/s11527-018-1280-2>.
- [17] J.M. Carpio, R. Serafini, D. Rambo, A. de la Fuente, A.D. De Figueiredo, Assessment of the bearing capacity reduction of FRC elements subjected to fire, in: *Proc. Fib Symp. 2019 Concr. - Innov. Mater. Des. Struct.*, Kraków, Poland, 2019: pp. 1378–1386.
- [18] Y. Fu, L. Li, Study on mechanism of thermal spalling in concrete exposed to elevated temperatures, *Mater. Struct.* **44** (2011) 361–376. <https://doi.org/10.1617/s11527-010-9632-6>.
- [19] F. Yasuda, K. Ono, T. Otsuka, Fire protection for TBM shield tunnel lining, *Tunn. Undergr. Sp. Technol.* **19** (2004) 317. <https://doi.org/10.1016/j.tust.2004.01.018>.
- [20] Z. Yan, H. Zhu, J. Woody Ju, W. Ding, Full-scale fire tests of RC metro shield TBM tunnel linings, *Constr. Build. Mater.* **36** (2012) 484–494. <https://doi.org/10.1016/j.conbuildmat.2012.06.006>.
- [21] Y. Zhang, J.W. Ju, H. Zhu, Z. Yan, A novel multi-scale model for predicting the thermal damage of hybrid fiber-reinforced concrete, *Int. J. Damage Mech.* **29** (2020) 19–44. <https://doi.org/10.1177/1056789519831554>.
- [22] J. Bosnjak, Explosive spalling and permeability of high performance concrete under fire: numerical and experimental investigations, University of Stuttgart,

2014. <https://doi.org/10.18419/opus-529>.
- [23] G. Periskic, Development of a 3D thermo-hygro-mechanical model for concrete under fire and application to fastenings loaded in tension, University of Stuttgart, 2009. <https://doi.org/10.18419/opus-340>.
- [24] J. Ozbolt, G. Periskic, H.-W. Reinhardt, R. Eligehausen, Numerical analysis of spalling of concrete cover at high temperature, *Comput. Concr.* 5 (2008) 279–293. <https://doi.org/10.12989/cac.2008.5.4.279>.
- [25] International Tunnelling and Underground Space Association, ITAtech Report n°7 - Design guidance for precast fibre reinforced concrete segments, 2016.
- [26] Fédération Internationale du Béton, Bulletin 46 - Fire design of concrete structures - structural behaviour and assessment, Switzerland, 2008.
- [27] Fédération Internationale du Béton, Bulletin 83 - Precast Tunnel Segments in Fibre-Reinforced Concrete, Switzerland, 2017.
- [28] Federation Internationale du Beton, Model Code for Concrete Structures 2010, in: Ernst & Sohn, Germany, 2013: p. 434.
- [29] M.D. Crespo, C. Molins, A.R. Mari, Effect of variations in thermal-curing cycle on the cracking risk of precast segmental tunnel lining, *Constr. Build. Mater.* 49 (2013) 201–213. <https://doi.org/10.1016/j.conbuildmat.2013.07.078>.
- [30] R. Serafini, S.R.A. Dantas, R.P. Salvador, R.R. Agra, D.A.S. Rambo, A.F. Berto, A.D. de Figueiredo, Influence of fire on temperature gradient and physical-mechanical properties of macro-synthetic fiber reinforced concrete for tunnel linings, *Constr. Build. Mater.* 214 (2019) 254–268. <https://doi.org/10.1016/j.conbuildmat.2019.04.133>.
- [31] W. Kusterle, W. Lindbauer, G. Hampejs, A. Heel, P.F. Donauer, M. Zeiml, W. Brunnsteiner, R. Dietze, W. Hermann, H. Viechtbauer, M. Schreiner, Technical Report 544: Fire resistance of fibre-reinforced, reinforced and prestressed concrete, Vienna: Bundesministerium für Verkehr, Innovation und Technologie [in German], 2004.
- [32] BS EN 1992-1-2, Eurocode 2 Design of concrete structures - Part 1-2: General rules-Structural fire design, *Des. Concr. Struct.* - Part 1-2 Gen. Rules-Structural Fire Des. (2004).
- [33] CNR-DT 204, Guide for the Design and Construction of Fibre-Reinforced Concrete Structures, Ital. Natl. Res. Counc. (CNR), Rome, Italy. (2007). <https://doi.org/10.14359/10516>.
- [34] EN 14651, Test method for metallic fibred concrete — Measuring the flexural

- tensile strength (limit of proportionality (LOP), residual), United Kingdom, 2007.
- [35] R.R. Agra, Influence of steel fiber content on the behavior of concrete exposed to elevated temperatures (in Portuguese), Universidade de São Paulo, 2020. <https://doi.org/10.11606/D.3.2020.tde-04032021-110133>.
- [36] V. Cugat, S.H.P. Cavalaro, J.M. Bairán, A. de la Fuente, Safety format for the flexural design of tunnel fibre reinforced concrete precast segmental linings, *Tunn. Undergr. Sp. Technol.* 103 (2020) 103500. <https://doi.org/10.1016/j.tust.2020.103500>.
- [37] S.H.P. Cavalaro, A. Aguado, Intrinsic scatter of FRC: an alternative philosophy to estimate characteristic values, *Mater. Struct.* 48 (2015) 3537–3555. <https://doi.org/10.1617/s11527-014-0420-6>.

APPENDIX A

Solution of the thermal model by FDM

The first important concept for the implementation of the thermal model is that the problem is solved using a discrete approach. Therefore, the second order differential equation is solved by using the FDM. The mathematical approach using the FDM is used to determine the second derivative as being:

$$f'(x_o) = \frac{f\left(x_o + \frac{\Delta x}{2}\right) - f\left(x_o - \frac{\Delta x}{2}\right)}{\Delta x} \quad (A1)$$

$$f''(x_o) = \frac{f(x_o + \Delta x) - 2f(x_o) + f(x_o - \Delta x)}{[\Delta x]^2} \quad (A2)$$

Considering a discrete approach to the problem according to the closed space-time presented in Eq. 13 – 15 of the main body of this thesis and using Eq. A2, the second derivatives of the temperature with respect to the spatial variable may be defined as:

$$\frac{\partial^2 T}{\partial z^2} = \frac{T_{i+1,j} - 2T_{i,j} + T_{i-1,j}}{[\Delta z]^2} \quad (A3)$$

The first derivative of temperature related to time was computed as:

$$\frac{\partial T}{\partial t} = \frac{T_{i,j+1} - T_{i,j}}{\Delta t} \quad (A4)$$

Once the FDM equations are defined, they may be applied to the thermal problem in order to solve the differential equation. The Fourier heat transfer law for one-direction conduction can be defined as:

$$\rho(T).C(T).\frac{\partial T}{\partial t} = K(T).\frac{\partial^2 T}{\partial z^2} \quad (A5)$$

Substituting A3 and A4 into A5, a discrete solution to the Fourier heat transfer law based on the FDM equations can be achieved, as:

$$\rho \cdot C \cdot \left[\frac{T_{i,j+1} - T_{i,j}}{\Delta t} \right] = K \cdot \left[\frac{T_{i+1,j} - 2T_{i,j} + T_{i-1,j}}{[\Delta z]^2} \right] \quad (\text{A6})$$

$$\left[\frac{T_{i,j+1} - T_{i,j}}{\Delta t} \right] = \frac{K}{\rho \cdot C} \left[\frac{T_{i+1,j} - 2T_{i,j} + T_{i-1,j}}{[\Delta z]^2} \right] \quad (\text{A7})$$

$$T_{i,j+1} - T_{i,j} = \frac{K}{\rho \cdot C} \cdot \frac{\Delta t}{[\Delta z]^2} [T_{i+1,j} - 2T_{i,j} + T_{i-1,j}] \quad (\text{A8})$$

$$T_{i,j+1} = \frac{K}{\rho \cdot C} \cdot \frac{\Delta t}{[\Delta z]^2} [T_{i+1,j} - 2T_{i,j} + T_{i-1,j}] + T_{i,j} \quad (\text{A9})$$

For simplification purposes, we consider $\bar{k} = \frac{K}{\rho \cdot C} \cdot \frac{\Delta t}{[\Delta z]^2}$ before following on with the operations, as:

$$T_{i,j+1} = \bar{k} [T_{i+1,j} + T_{i-1,j}] + T_{i,j} - 2 \cdot \bar{k} \cdot T_{i,j} \quad (\text{A10})$$

$$T_{i,j+1} = \bar{k} [T_{i+1,j} + T_{i-1,j}] + (1 - 2\bar{k})T_{i,j} \quad (\text{A11})$$

Therefore, using Eq. A11 it is possible to calculate the temperature for the next moment of the fire simulation ($t = j + 1$) based on the temperature distribution of the segment at the previous time ($t = j$). The initial boundary condition of thermal stability of SFRC at room temperature (for $t = 0$ min) is employed as starting parameter for the iterative method implemented. The boundary conditions and the net heat flux from the fire source to the surface of concrete are explained in detail in Section 3.6.2.